Optimization of metal oxides for the realization of electrode in adequacy with the photosensitive material in the infrared range

Louis David Mohgouk Zouknak

To cite this version:

Louis David Mohgouk Zouknak. Optimization of metal oxides for the realization of electrode in adequacy with the photosensitive material in the infrared range. Micro and nanotechnologies/Microelectronics. Université Grenoble Alpes [2020-..], 2024. English. NNT : 2024GRALT031 . tel-04679769

HAL Id: tel-04679769
https://theses.hal.science/tel-04679769v1

Submitted on 28 Aug 2024

THÈSE

Pour obtenir le grade de

DOCTEUR DE L'UNIVERSITÉ GRENOBLE ALPES

École doctorale : EEATS - Electronique, Electrotechnique, Automatique, Traitement du Signal (EEATS)
Spécialité : Nano électronique et Nano technologies
Unité de recherche : Centre de Radiofréquences, Optique et Micro-nanoélectronique des Alpes

Optimisation d'oxydes métalliques pour la réalisation d'électrode en adéquation avec le matériau photosensible dans l'infrarouge.

Optimization of metal oxides for the realization of electrode in adequacy with the photosensitive material in the infrared range

Présentée par :

Louis David MOHGOUK ZOUKNAK

Direction de thèse :

Charles LEROUX Expert Senior E6, CEA Leti	Directeur de thèse
Gérard GHIBAUDO Directeur de recherche émérite, Université Grenoble Alpes	Co-directeur de thèse
Serge BLONKOWSKI Ingénieur Docteur, CEA-Leti	Co-encadrant de thèse
Mickael GROS-JEAN Manager R&D, STMicroelectronics	Co-encadrant de thèse

Rapporteurs :

Brice GAUTIER
PROFESSEUR DES UNIVERSITES, INSA Lyon
Marie-Paule BESLAND
DIRECTRICE DE RECHERCHE, CNRS BRETAGNE ET PAYS DE LA LOIRE

Thèse soutenue publiquement le **5 avril 2024**, devant le jury composé de :

Ahmad BSIESY, PROFESSEUR DES UNIVERSITES, Université Grenoble Alpes	Président
Charles LEROUX, INGENIEUR HDR, CEA CENTRE DE GRENOBLE	Directeur de thèse
Brice GAUTIER, PROFESSEUR DES UNIVERSITES, INSA Lyon	Rapporteur
Marie-Paule BESLAND, DIRECTRICE DE RECHERCHE, CNRS BRETAGNE ET PAYS DE LA LOIRE	Rapporteure
Laurence RESSIER, PROFESSEURE DES UNIVERSITES, INSA Toulouse	Examinatrice

Invités :

Gérard GHIBAUDO
Directeur de recherche émérite, CNRS

Acknowledgements(French)

Tout d'abord, je remercie chaleureusement mes directeurs de thèse, Charles LEROUX (CEA LETI) et Gerard GHIBAUDO (anciennement IMEP, aujourd'hui CROMA). Charles, votre soutien moral, vos conseils avisés, votre encouragement constant, vos commentaires critiques et constructifs ont été indispensables tout au long de ce parcours. Vous avez su me guider avec patience, me permettant de surmonter les défis rencontrés et d'avancer avec confiance. Je vous remercie également pour l'initiation aux mesures et aux caractérisations électriques. Gerard, vos conseils académiques, votre expertise et votre rigueur scientifique ont enrichi considérablement ce travail de recherche. Votre vision claire et vos retours constructifs ont été essentiels pour structurer et approfondir cette thèse. Je voudrais exprimer ma profonde gratitude à mon encadrant industriel (STMicroelectronics Crolles) pour l'opportunité qu'il m'a offerte en me recrutant en thèse CIFRE, pour son soutien constant durant ces trois années, sa patience et nos différentes discussions. Vos contributions ont été déterminantes pour la réussite de cette thèse. Je souhaite également remercier mon encadrant principal Serge BLONKOWSKI (CEA LETI) pour ses qualités scientifiques et humaines. Je n'oublierai jamais nos discussions variées allant de la physique théorique aux sujets de l'actualité et de la géopolitique.

Les principaux travaux de cette thèse ont été réalisés au CEA-LETI, au sein du service de dépôts. Je tiens à remercier Philippe Rodriguez pour m'y avoir accepté et accueilli. Un remerciement spécial à Thierry FARJOT (CEA LETI) pour son aide technique, son soutien et mon intégration dans les équipes de dépôt en salle blanche. J'exprime ma gratitude à toutes les personnes dont la collaboration, l'expertise et les conseils ont contribué à l'aboutissement de cette thèse. Mes remerciements vont également à l'ensemble des membres du laboratoire LDJ (CEA LETI) pour leur aide et leur environnement de recherche stimulant. Votre collaboration et vos échanges ont été source d?inspiration et de motivation.

Je tiens à remercier particulièrement les institutions CEA LETI et STMicroelectronics Crolles pour avoir mis à disposition les ressources nécessaires à la réalisation de cette thèse. Je remercie également l'ANRT pour le financement de cette thèse, sans lequel ce travail n'aurait pas été possible.

Je tiens à exprimer ma reconnaissance à mes collègues doctorants Roméo, Tadeu, Julien, Anthony, Bohb, Matthieu, Kilian et les collègues du laboratoire Nicolas, Benjamin... pour leur camaraderie et leur soutien quotidien. Nos échanges et votre présence ont rendu ce parcours doctoral plus agréable et motivant.

Je souhaite également exprimer ma profonde gratitude aux membres du jury pour leur précieuse contribution à cette thèse. Merci à Ahmad Bsiesy, Professeur des Universités à l'Université Grenoble Alpes, pour avoir accepté de présider et d'examiner cette thèse. Un grand merci à Brice Gautier, Professeur des Universités à l'INSA Lyon, et à Marie-Paule Besland, Directrice de Recherche au CNRS, pour avoir accepté de rapporter ce travail. Je tiens à exprimer une reconnaissance particulière à Marie-Paule Besland pour son aide précieuse dans la correction du manuscrit. Enfin, merci à Laurence Ressier, Professeure des Universités à l'INSA Toulouse, pour avoir accepté d'évaluer cette thèse.

Enfin, un immense merci à ma famille et à mes amis pour leur amour, leur patience et leur soutien moral. Votre présence à mes côtés, même dans les moments les plus difficiles, a été une source de motivation constante. Cette thèse est dédiée à toutes les personnes qui ont cru en moi et m'ont soutenu tout au long de ce voyage intellectuel et personnel.

Merci infiniment.

Contents

Table 1: Physical Constants

Symbol	Value	Definition
c	$299792458\,\mathrm{m.s^{-1}}$	Speed of light in a vacuum
e	$\simeq 1.6 \times 10^{-19}$ C	Elementary charge
h	$\simeq 6.62 \times 10^{-34}$ J.s	Planck constant
$\hbar$	$\simeq 1.05 \times 10^{-34}$ J.s	Reduced Planck constant
k	$\simeq 1.38 \times 10^{-23}\,\mathrm{J.K^{-1}}$	Boltzmann constant
m_0	$\simeq 9.11 \times 10^{-31}$ kg	Electron mass
ε_0	$\simeq 8.85 \times 10^{-12}\,\mathrm{m^3.kg^{-1}.s^4.A}$	Vacuum permittivity

0.1 Notations and abbreviations

Table 2: Notations and Abbreviations

Symbol	Definition
TCO	Transparent conductive oxide
TMO	Transition metal oxide
ETL	Electron transport layer
HTL	Holes transport layer
ITO	Tin doped indium oxide
H-ITO	Hydrogen doped indium tin oxide
ZnO	Zinc oxide
QD	Quantum dot
PbS	Lead sulfide
MoO_x	Molybdenum oxide
NiO_x	Nickel oxide
SiO_2	Silicon oxide
XPS	X-ray photoemission spectroscopy
E_F	Fermi energy level
E_g	Band gap energy
E_{gopt}	Optical band gap energy
E_V or VB or VBM	Valence band maximum energy
E_C or CB or CBM	Conduction band minimum energy
MOS	Metal Oxide Semiconductor
FGA	Forming Gas Annealing
RCA	Standard cleaning process before high temperature oxidation
V_{bf}	Flat band voltage
Dit	Interface density of states
ε_r	Relative permittivity
ϕ_m *or* WF_m	Work Function of Material **m**
NIR	Near infrared ($0.8\mu m < \lambda < 1\mu m$)
SWIR	Short wave infrared ($1\mu m < \lambda < 1.7\mu m$)
IR	Infrared
MWIR	Middle wave infrared ($3\mu m < \lambda < 5\mu m$)
Vis	Visible range (400 nm < λ <780 nm)
sccm	Standard cubic centimeters per minute (gas flow rate)
u.a	Arbitrary units
EQE	External quantum efficiency
λ	Wavelength
m_e	Electron effective mass
m_h	Hole effective mass
m^*	Effective mass

Chapter 1

Introduction

1.1 Motivation and Objectives

Infrared (IR) photodetectors are considered as the "eyes" of many optoelectronic devices, capable of converting IR light signals into an electrical response. The emergence of new applications based on IR photodetectors and the fast growing demand for innovative solutions in the fields of automation, optical fiber communication, machine vision, military industry, food inspection, remote sensing and metrology, agriculture and medical imaging, pose new challenges. The fabrication of most current IR photodetectors is based on the epitaxial growth of III-V semiconductors (such as InGaAs), which is difficult to scale up due to high material costs and technological difficulties. Problems such as mismatch of lattice parameters, high thermal budget and contamination make integration on CMOS readout circuits difficult[1, 2]. These technological issues generally lead to devices with poor performance, such as a high operating bias or high dark currents (noise). On the other hand, despite the fact that they benefit from advances in CMOS technology, Ge-based IR photodetectors still have high production costs and a limited operating spectral range due to the limited absorption of Si, with absorption maximum edge at $\approx$ 1100 nm (indirect gap) and Ge, with absorption maximum edge at $\approx$ 1600 nm (direct gap) [3, 4]. To overcome above mentioned issues, related to the high cost of semiconductors, the challenges of integrating III-V semiconductors and the limitation of Si and Ge photodetectors, intensive research has been carried out on various alternatives.

In recent decades, the development of zero-dimensional (0D) materials or quantum dots (QDs) has experienced significant growth (Nobel Prize of Chemistry 2023, A. Ekimov, L. Brus and M. Bawendi). Among these, PbS QDs have received special attention due to their outstanding properties, including tunable optical absorption from 600 to 2600 nm (size-dependent band gap) and ease of synthesis in solution. PbS QDs are considered one of the most promising materials for the next generation of IR sensors. Hence, there is a growing interest in their use in industrial sectors. In parallel to QDs, perovskite materials are also promising candidates for IR photodetectors due to their excellent electrical properties, such as high carrier mobility and long carrier diffusion length, their good optical properties, i.e. light absorption capacity and tunable bandgap (depending on composition), and above all their cost-effective synthesis process in solution under non-vacuum conditions[5]. The fabrication of high-performance photodiodes based on these materials (QDs and perovskites) requires, on the one hand, the realisation of efficient holes extraction contact or HTL (electrons blocking layer) and electrons extraction contact or ETL (holes blocking layer) and, on the other hand, the realisation of an electrical transparent contact adapted for the IR spectrum, that allows an efficient collection of the extracted charges from the active material at the top electrode of the device.

This thesis is part of a project focusing on the development by STMicroelectronics of the next generation of infrared sensors with low manufacturing costs and improved performance compared to current devices[6, 7]. The thesis was carried out within the collaboration between STMicroelectronics and CEA-Leti in Grenoble. The deposition of metal oxide thin films and TCO as well as the various characterizations were carried out in Leti's clean rooms and laboratories within the DPFT/SDEP/LDJ and DCOS/SCCS/LCEF departments. The deposition and optimization of the PbS QD films was carried out by STMicroelectronics (Crolles 300). For the fabrication of the photodiodes, the 300 mm Si/Ta/TiN/ZnO/PbS substrates, i.e. the PbS QD films deposited on an optimised electron extraction electrode, were supplied by Crolles 300 mm. In order to be processed on 200 mm tools, these substrates were cut into several smaller samples, and our photodiode devices were fabricated by depositing the hole extraction layer (HTL) and the transparent electrical contact (TCO). One of the difficulties with QD-based technologies is their stability, and our studies were significantly impacted by the transfer of wafers between CEA-Leti and STMicroelectronics Crolles. This is because PbS QDs can be rapidly oxidised or degraded when exposed to oxygen or moisture (in the ambient atmosphere)[8]. The quality of PbS QDs film surfaces must therefore be carefully monitored in order to achieve high performance devices.

The main objective of this research work is to realise a novel top electrode adapted to the IR spectrum by sputtering at room temperature, thus adapted to fragile PbS QDs and perovskite materials. This top electrode will consist of a HTL and a transparent electrical contact (TCO). The TCO and HTL layers will first be studied individually and then integrated together in photodiode structures. These materials will be prepared by DC and RF sputtering on an equipment compatible with industrial developments.
For this purpose, inorganic semiconductors based on n- and p-type metal oxides were investigated as HTL. MoO_x, an n-type semiconductor with an appropriate choice of stoichiometry is the traditionally and the most commonly used material as HTL on PbS QD films. The use of MoO_x brings a number of challenges, such as optimising the stoichiometry for efficient holes transport. In addition to the difficulties of optimising the MoO_x stoichiometry on PbS QDs films, it is very often necessary to use an additional layer of p-type PbS QDs film between the n-type PbS QDs films and the MoO_x film to achieve high performance devices[9, 10, 11]. Besides MoO_x, we have also investigated other HTL materials known in the literature, in particular NiO_x, which is a p-type material. We have compared different materials and have showed that ultrathin NiO_x film could be a better alternative to MoO_x film as hole extraction layer. The optimization of the HTL electrical and optical properties as well as their band structures during the deposition process and at room temperature is necessary to obtain devices with the best performances. We will be focused on the change of the properties of the different HTL as a function of their chemical composition, and the the chemical composition has been varied by tuning the deposition parameters.

For transparent electrical contact, we will focus on In_2O_3-based TCO, of which ITO is the best known. It is well known that the optical transmission of ITO decreases strongly in the IR region due to plasmonic absorption[12]. In this work, we will study the effects of deposition conditions as well as Sn and hydrogen doping to define the most suitable TCO in the IR region, i.e. a material that favours the transmission of IR photons and the collection of holes photogenerated by the active material (perovskite or PbS QDs).

1.2 Outline

This thesis document is divided into five chapters. The first chapter is devoted to the state of the art. It begins with the history of photodetectors, in particular IR photodetectors. The different photodetector architectures are presented, with a focus on photodiodes. We present some interesting applications for IR sensors as well as the development of the market for IR sensors between 2021 and 2031. Secondly, we present the electrical, electronic, structural and optical properties of nanocrystals, with a particular focus on PbS QDs. The various synthesis methods for PbS QDs are also presented. Next, we have presented the theoretical elements to understand and optimise the electrical, electronic and optical properties of TCO, especially in the case of In_2O_3 TCO. Based on classical calculations, we have shown that there is a trade-off between the optical and electrical properties of TCO. Finally, we reviewed the optical, electrical and electronic properties of inorganic HTLs based on transition metal oxides, focusing on MoO_x and NiO_x.

In the second chapter, we present in detail the technique we used to prepare our OCT films. We have presented in detail the PVD deposition technique as well as the tool used to prepare the different metal oxide and TCO films studied in this thesis. We have presented the rapid characterization techniques available in clean rooms such as X-ray reflectometry (XRR) and the 04-point resistivity measurement method. The principles of in-depth characterisation techniques such as spectral ellipsometry, optical transmission and reflection, XPS-UPS, X-ray diffraction are also presented. Other analysis techniques such as AFM and Hall effect measurements are also described. In the last part of this chapter, we review the theory of MOS capacitance, the characterization and in-depth analysis of which will enable us to determine the work function of some of the materials studied here.

The third chapter is devoted to the study of the properties of In_2O_3 TCO. We report the structural, electrical and optical properties of In_2O_3 TCO. We have also demonstrated the value of hydrogen doping for the optimisation of In_2O_3 and Sn-doped In_2O_3 films for applications in the IR region of the electromagnetic spectrum. We then determined the work function of hydrogen-doped ITO (H-ITO) by MOS capacitance measurements and analysis. Finally, we present the damaging effect of ITO sputtering on H-ITO/SiO_2/Si structures.

In the fourth chapter, we present the properties of MoO_x and NiO_x as a function of stoichiometry. First, we describe the procedure for the preparation of NiOx and MoOx films. We then report on the various studies that have been carried out on the structural, electrical and optical properties of these materials. We present the work function of NiOx and MoOx measured by UPS. Also, for the first time, we have determined the work function of MoOx as a function of stoichiometry by measuring and analysing the MOS capacitances of Al/MoOx/SiO2/Si. Part of this chapter is also dedicated to the thermal stability and ambient atmosphere of these materials.

The fifth chapter will be devoted to photodiode devices based on PbS QDs and perovskites. Firstly, we will present a simplified fabrication method for PbS QD-based photodiodes. Secondly, we will study the properties of the transparent H-ITO contact on photodiode performance. We will then study the different HTL layers (NiO_x and MoO_x), and show the importance of the surface quality of the PbS film on photodiode performance. Finally, we will demonstrate the possibility of making superior transparent electrical contacts on perovskite-based photodiodes, validating their possible integration on CMOS readout circuits. We will also summarise the main results obtained in this work and outline some important perspectives to be explored in the continuation of this thesis.

Chapter 2

State of art

2.1 Image sensors and light detectors

2.1.1 History of image sensors

The history of image sensors began in France in the 19^{th} century. Between 1816 and 1839, inventors Nicephore Niepce and Louis Daguerre developed a photographic technique called the daguerreotype, in which copper plates were coated with a thin layer of polished, light-sensitized silver. After exposure, the image was made visible by exposing the plate to mercury vapor, creating a unique positive black-and-white image[13, 14]. In 1848, the physicist Edmond Becquerel (who was the son of the father of radioactivity, Henri Becquerel), known for his work in the field of electricity and especially for the discovery of the photovoltaic effect, made an important contribution to color photography (short-lived image) [15]. In 1855, Maxwell published his article entitled *Experiments on Color, as Perceived by the Eye, with Remarks on Color-Blindness* in which he proposed that colors can be reproduced by combining three primary colors (red, green, and blue), known as *Maxwell's trichromatic theory*, and he also developed the first mathematical model describing the properties of trichromatic colors [16]. In 1861, he made the first color photograph of a rainbow using his method of three primary colors, making an important breakthrough in the field of color photography. In 1903, the Lumière brothers invented the *Autochrome* camera, the first commercially available color camera, in which glass plates were coated with colored potato starch grains in red-orange, green, and blue-violet. During exposure, the starch grains acted as color filters, recording the various color components on the plate[17]. In the 1920s and 1930s, American musicians and inventors Godowsky and Mannes, who worked for Eastman Kodak, developed an innovative process that became known as *Kodachrome* [18]. The Kodachrome process consisted of gelatin layers containing dyes that recorded the three primary colors separately. During development, these layers were treated with special chemical reagents to produce color images. This process, based on color reversal or slide films, revolutionized color photography at the time and continued to be used until 2009. The era of digital imaging began with the creation of the first digital image by Russell Kirsch in 1957[19], followed by the invention of the CCD sensor by Willard Boyle and George E. Smith in 1969[20]. In 1973, Steven Sasson developed the first digital camera[21], and in 1981 Sony introduced the first consumer digital camera, the *Sony Mavica*, which stored images on floppy disks. The advent of user-friendly graphical interfaces, such as those introduced by Apple in 1984, made it easier to edit and manipulate digital images. Adobe played an important role with the introduction of Photoshop in 1990, which has become the industry standard for image editing. CMOS sensors, originally developed in the 1960s by Mohamed Atalla and Dawon Kahng[22], have become increasingly popular due to their advantages such as low power consumption, lower manufacturing costs, and the ability to integrate image processing circuits. It is important to point out that the emergence of IR detectors dates back to World War II, when, thanks to the work of Theodore Case and Albert Chapin, the thermo-bolometer emerged. The first IR diode detectors (IR) appeared in the 1950s, while in the 1970s the first IR CMOS image sensors were introduced by Eric Fossum and George Smith. In the early 2000s, CMOS sensors became a popular alternative to CCD sensors, facilitating the miniaturization of digital cameras and their widespread adoption. Today, CMOS sensors are widely used in digital cameras, smartphones, and other digital imaging devices[23, 24].

Among these photodetectors, infrared (IR) image sensors play a significant role in various fields, including military applications, thermal imaging, surveillance, medical imaging, and consumer electronics. The development of IR image sensors has seen significant advancements over the years, including the utilization of indium gallium arsenide (InGaAs) and quantum dot (QD) materials. IR imaging has its roots in the late 19^{th} century when William Herschel discovered the existence of IR radiation [9]. The first practical application of IR imaging was during World War II when IR detectors were used for night vision The early IR detectors utilized thermal principles, such as bolometers and thermopiles, to detect and convert IR radiation into electrical signals [25]. In the 1960s, the development of photovoltaic detectors, also known as photovoltaic or PV cells, marked a significant milestone in IR sensing technology. PV cells were typically made of materials like lead sulfide (PbS) or lead selenide (PbSe), which were sensitive to the mid-wavelength infrared (MWIR) and long-wavelength infrared (LWIR) regions [26]. In the 1970s, the introduction of HgCdTe (Mercury Cadmium Telluride) detectors revolutionized the field of IR imaging. HgCdTe offered a wide spectral range, including MWIR, LWIR, and even the SWIR regions. HgCdTe detectors provided high sensitivity, low noise, and high frame rates, making them suitable for a wide range of applications [27]. In the 1990s, indium gallium arsenide (InGaAs) detectors gained attention due to their sensitivity in the SWIR region. InGaAs detectors were particularly suitable for telecommunications applications, as they could operate in the 1000-1700 nm wavelength range. The sensitivity of these detectors based on III-V compound semi-conductors was achieved through band gap engineering by adjusting the indium and gallium composition ratios [26]. In recent decades, quantum dot (QDs) materials have emerged as a promising alternative for IR sensing applications [25, 28]. QDs are nanoscale semiconductor crystals that exhibit quantum confinement effects, enabling precise tuning of their bandgaps [3]. QDs materials, such as lead sulfide (PbS) and lead selenide (PbSe), have been investigated for their potential in IR imaging [28, 29]. In this thesis, we will be particularly interested on PbS-based IR image sensors. The increasing availability of digital visible and IR cameras plays an important role in popularising digital imaging. The era of digital imaging has brought constant advances in image quality, storage capacity, and sharing capabilities, changing the way we capture, process, and share images. New technological developments will undoubtedly lower the cost of IR photodetectors and make their use accessible to the general public.

2.1.2 Primary types of IR light detectors and image sensors operating principle

Photodetectors are semiconductor devices that electrically detect and convert optical signals into electrical signals. At its operating wavelength, the photodetector should have high sensitivity, high response speed, minimum noise, small size, low voltage, and high reliability under operating conditions. There are several different architectures of photodetectors, including photodiodes, phototransistors, solar cells, and photoconductors. Each architecture has its own unique characteristics and operating principles. Here is an overview of these different photodetector architectures:

2.1.2.1 Photoconductors or photoresistors

Photoconductor devices operate on the principle of measuring a temporary change in conductivity of the semiconductor under illumination (**Figure** 2.1.a). Commercial bulk PbS photoconductors are commonly used for the detection of IR light in the range of 1 - 3 μm. In this range, they exhibit a typical detectivity of 10^{10} Jones (cm $Hz^{1/2}.W^{1}$), which peaks at 10^{10} Jones at 2.2 μm at 25°C when biassed at 100 V and with a rise time of 200 μs [3]. The photoconductivity arises mainly from the generation of a primary photocurrent. These currents result directly from the absorption of photons and subsequent extraction of photoexcited charge carriers and determine the EQE of the device. Photoconductivity can also result from the generation of a secondary photocurrent due to the injection and transit of charge carriers from the device electrodes and determines the photoconductive gain (G), which is expressed as:

$$G = \frac{\tau_{lt}}{\tau_{tt}} = \frac{\tau_{lt}\mu V}{l^2}; \qquad \left(\tau_{tt} = \frac{l}{\mu E} = \frac{l^2}{\mu V}\right) \tag{2.1.1}$$

where τ_{lt} is the lifetime of the main charge carrier, τ_{tt} is the transit time of the main charge carrier, μ is the mobility of the main charge carrier, l is the distance between the electrodes, and V is the applied voltage to generate the electric field E = (V/l). It can be observed that a gain (G > 1) can be achieved in the device when $\tau_{lt} > \tau_{tt}$. The dark current is a key factor for these devices. It depends primarily on the applied electric field, the mobility of the charge carriers, the quality of the QDs layer (dispersion and size distribution of the QDs), and the relative band alignment of the metal electrode to the conducting band. Most PbS QDs light guides are fabricated with gold contacts. Gold has a work function of $\phi = 5.1$ eV. Therefore, the gold contact can inject holes into the VB of the PbS QDs (since the work function of gold matches the VB energy level of the PbS QDs), this significantly increases the hole concentration n_h, leading to p-type transport [30].

2.1.2.2 Phototransitors

Phototransistors are electronic devices that combine the characteristics of a transistor and a photodetector. The operating principle of phototransistor is similar to that of a conventional transistor, but it is photosensitive and can convert incident light into an electric current. They consist of three electrical contacts, gate, source and drain (**Figure** 2.1.b), this allows better control of the semiconductor's conductivity, as the gate voltage can be varied in addition to the source-drain voltage and illumination intensity. For example, applying a negative gate voltage induces charge carriers (holes) in a p-type PbS QDs layer, thus increasing the conductivity. The gate electrode can therefore be used as a switch or amplifier and can also control the position of the Fermi level, thereby establishing or removing trap states. Phototransistors based on QDs have very low quantum efficiencies in addition to high dark currents (noise) due to low mobility in QDs films. Therefore, they are rarely used in industrial applications. However, hybrid 0D-2D structures (PbS-QDs on graphene or 2D-MoS_2) can lead to improved performance of QDs -based phototransistors, where the 2D material facilitates the electrical transport of charges generated by light [31].

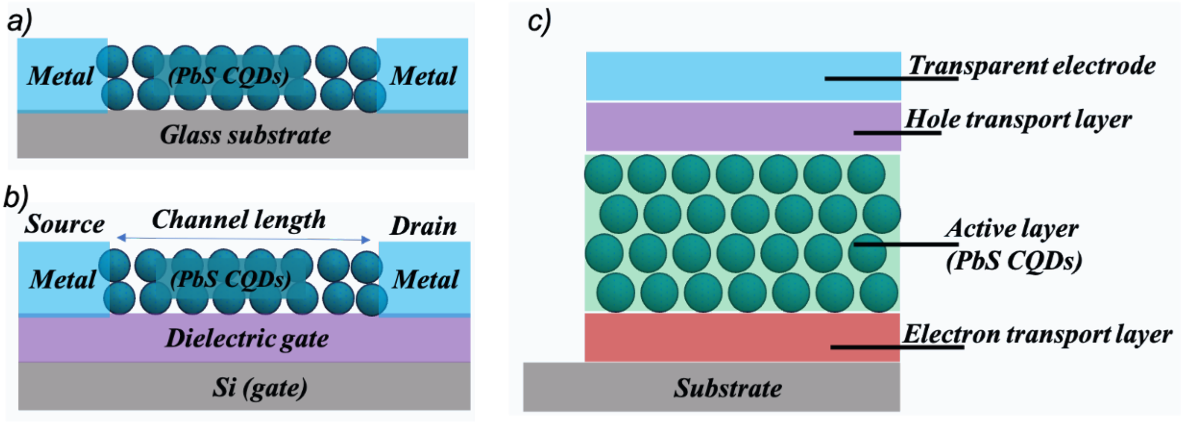

Figure 2.1: PbS QDs-based Photodetectors architecture: a) schematic image describing a simple photoconductor architecture, b) phototransistor device, c) p-i-n, p-n photodiode or solar cell device vertically stacked. HTL and ETL layers are generally transition metal oxide thin film materials with relatively low work function $\phi \approx 4$ eV such as ZnO or TiO_2 are used as ETL, while MoO_x, NiO_x, V_2O_x or WO_x with work function $\phi > 5$ eV outputs are used as HTL. The transparent electrode is a TCO, usually ITO.

2.1.2.3 Photodiodes

Photodiodes can be classified into several types, including Schottky, heterojunction, p-n, and p-i-n types. The main architectures of photodiodes are p-i-n and p-n photodiodes. p-i-n photodiodes consist of p-type and n-type regions separated by more or less long intrinsic region, while p-n photodiodes consist exclusively of a p-n junction. They operate on the principle of the internal photoelectric effect. When exposed to appropriate light, photon absorption produces excitons (electron-hole pairs), and separation of these electron-hole pairs by an electric field produces a photocurrent. **Figure** 2.1.c shows a p-n photodiode, which can be considered as a p-i-n architecture when the PbS-QDs layer is an intrinsic semiconductor. The HTL and ETL layers have respectively the function of hole extraction and electron transport (electron blocking) and electron extraction and electron transport (hole blocking). The alignment of the energy levels of the materials used facilitates the collection of electrons and holes at opposing contacts while limiting the passage of opposite charges (reducing dark current). Photodiodes can be operated with zero bias (photovoltaic mode), but are typically used with reverse bias (photoconductive mode), which allows for wide bandwidth and wide linear dynamic range. p-i-n photodiodes offer several advantages, such as high quantum efficiency, low dark current, and fast response time. They are mainly used in optical communication systems, imaging applications and light detection applications.

2.1.2.4 Solar cells

Solar cells typically consist of single or multiple p-n junctions, with different band gaps to efficiently capture a wider range of the solar spectrum.

2.1.2.5 Figures of merit or performance metrics

Photodetector figures of merit provide information about theirs performances and light detection capability. These parameters allow characterization and comparison of different types of photodetectors. The most commonly used performance metrics include external quantum efficiency, detectivity, responsivity, linearity, bandwidth, response time, and signal-to-noise ratio.

External quantum efficiency EQE(λ):
The external quantum efficiency EQE(λ) is the number of electron-hole pairs collected for each absorbed incident photon.

$$EQE(\lambda) = \left(\frac{I_{ph}(\lambda)}{e}\right)\left(\frac{I_{opt}(\lambda)}{hc/\lambda}\right)^{-1} \qquad (unit, \quad \%) \tag{2.1.2}$$

where $I_{ph}(\lambda) = I_{light}(\lambda) - I_{dark}(\lambda)$ is the photogenerated current in amperes, with I_{light} the total current under illumination, I_{dark} the dark current, $I_{opt}(\lambda)$ is the incident optical power in watts at a wavelength λ, h is Planck's constant, c is the speed of light and e is the elementary charge. It is important to have a high EQE over the entire wavelength range of the photodetector. In the particular case of QDs, the EQE spectrum is a quasi-Gaussian curve whose maximum and half-maximum width (FWHM) are determined by the band gap and size distribution, respectively. The EQE can be improved by optimizing the alignment of the band levels of the contacts with the active material to facilitate the extraction of the generated electron-hole pairs, it can also be improved by photomultiplication, i.e., collection of multiple charge carriers per incident photon well known as a multiple exciton generation [32, 33]. The EQE can also be tuned to a specific wavelength using an optical filter.

Responsivity $R(\lambda)$:
The responsivity is the ratio of photogenerated current to the incident optical power falling on the detector at a given wavelength λ.

$$R(\lambda) = \frac{I_{ph}}{I_{opt}(\lambda)} \qquad (unit, \quad A.W^{-1}) \tag{2.1.3}$$

The spectral response of the photodetector is obtained by plotting the responsivity against the wavelength, and usually follows the absorption spectrum of the photosensitive semiconductor material used for the fabrication of the photodetector[3].

Signal to noise ratio SNR and noise equivalent power NEP(λ):
The SNR is the measure of the relative strength of the desired signal compared to the background noise level. It quantifies the quality of a signal by comparing the magnitude of the signal to the magnitude of the noise.

$$SNR = 20log\left(\frac{Signal}{Noise}\right) \tag{2.1.4}$$

where Signal represents the power or amplitude of the desired signal, and Noise represents the power or amplitude of the background noise. A higher SNR indicates a stronger and more distinguishable signal compared to the noise, resulting in better signal quality and easier detection.

The NEP(λ) is the minimum detectable optical power at which the electrical SNR in the photodetector is equal to unity.

$$NEP(\lambda) = \frac{\sqrt{\bar{I}_n^2}}{R(\lambda)} \tag{2.1.5}$$

where I_n is the noise current spectral density, and $NEP(\lambda)$ is in units of W.Hz$^{-0.5}$. Total noise current in a detector is the sum of all the noise sources. These include $1/f$ low-frequency flicker noise, I_{gr} (generation-recombination noise) , the thermal noise I_{th} and the shot noise I_{sh}.

Detectivity $D^*(\lambda)$:
The detectivity is the most important figure of merit for photodetectors, it is used to quantify the sensitivity of a photodetector in detecting weak optical signals in the presence of noise. It provides a measure of the smallest detectable signal that can be reliably distinguished from the

noise[34]. As the detectivity of a photodetector is directly proportional to the responsivity, it is indirectly a function of wavelength, modulation frequency and applied electric field.

$$D^*(\lambda) = \frac{\sqrt{A}}{NEP(\lambda)} \tag{2.1.6}$$

where A is the active area of the photodetector.

Response time:
The response time is the time required to collect the photogenerated charge carriers (electrons and holes) by the photons absorbed at the contacts with the active layer under the effect of an applied electric field, i.e., the time required for the output signal of the photodetector to reach $(1 - e^{-1}) \approx 63\%$ of its steady-state maximum value in response to an incident optical signal. he response time determines the detector's ability to capture fast optical events or signals (ability to acquire high-frequency images). This is an essential parameter for applications such as LIDAR (Light Detection and Ranging) or the detection of hot objects against a cold background. It is generally measured by using a "pulse' or 'slot' source and by studying the photodetector's response to rapid changes in the signal.

Dynamic range DR(λ):
The DR of a photodetector refers to the range of input signal power levels over which the detector can provide a useful and reliable output. It represents the ratio between the maximum detectable signal power and the minimum detectable signal power without saturation or excessive noise, it is the range over which the photocurrent increases with increasing incident optical power, and the linear dynamic range is the range over which photocurrent increases linearly with increasing optical power. The dynamic range is typically expressed in decibels (dB) and is calculated using the formula:

$$DR(\lambda) = 10log\left(\frac{P_{max}(\lambda)}{P_{min}(\lambda)}\right) \tag{2.1.7}$$

where DR is the dynamic range, $P_{max}(\lambda)$ and $P_{min}(\lambda)$ are the maximum and minimum detectable signal powers respectively. A larger dynamic range indicates a photodetector's ability to handle a wide range of signal powers, from weak signals to strong signals, without losing accuracy.

Dark current density J_d:
Dark current is the electrical current that flows through a photodetector under an applied reverse bias voltage even when no light is incident on it. It is primarily caused by the thermal generation of charge carriers within the active material. The dark current in PbS-QDs based photodetectors can originate from various sources, including trap-assisted tunneling due to defect states or traps within the material bandgap, leakage current caused by the device structure imperfections (material defects or interface states), surface recombination, PbS-QDs typically have surface ligands, incomplete surface passivation can lead to important surface recombination processes that contribute to dark current. Dark current can limit the sensitivity and other performances of photodetectors, especially in low-light or high-precision applications. Minimizing dark current in PbS-QDs based photodetectors is critical to achieve high sensitivity and good signal-to-noise ratio. Several strategies can be used to reduce dark current, including surface passivation and band-level engineering[35]. Improving device structure and interfaces, such as optimizing electrode materials and interfaces[36, 37, 38, 39], can help reduce leakage currents and improve dark current. In recent years, considerable effort has been made to reduce the dark current density in PbS-based IR photodiodes. The most recent photodetectors have ultra low values, of the order of $\approx 10^{-9}$ A.cm^{-2} for IR photodetetors and of $\approx 25.10^{-8}$ A.cm^{-2} for SWIR photodetectors, at T = 60°C and at high bias V = -2 V [6]. Georgitzikis et al also reported ultra low dark current density less than $25.10^{-8} A.cm^{-2}$ at room temperature and at reverse bias V = -1 V [40].

2.1.3 Main applications

IR photodetectors are widely used in a variety of applications. The **Figure**. 2.2 shows the applications in each wavelength range of the IR spectrum, NIR[41, 42], SWIR[43], MWIR[44] and LWIR [45]. In surveillance and security applications, they are used to detect motion and monitor areas even in complete darkness [29, 46], the **Figure** 2.3.**a** shows the difference between a Vis and SWIR detector of a scene taken in a foggy atmosphere. In thermography, IR detectors are used to measure the temperature of objects without contact and have applications in building inspection and preventive maintenance of equipment. Another area where IR detectors convert IR radiation into visible signals is thermal imaging, which enables fire monitoring, search and rescue, and night vision [47, 48]. In the military and defence sectors, IR detectors are used for target detection, night vision, and heat warning detection[1]. They also play an important role in controlling industrial processes by monitoring parameters such as temperature and gas concentration[3]. In medicine and bioimaging, IR photodetectors are used for tumour detection, medical thermography, and vital signs monitoring [50]. Moisture is a key indicator of process control and quality in agriculture and and food industry, IR photodetectors can be used for sorting and inspection of products, thanks to selective imaging at the wavelengths where water absorption is strongest, items with a high water content appear darker than drier tissues, because water is opaque to SWIR illumination, detecting its presence or absence can be useful for assessing the health of plants and the maturity or dryness of produces (see **Figure** 2.3.**b** and **d**).

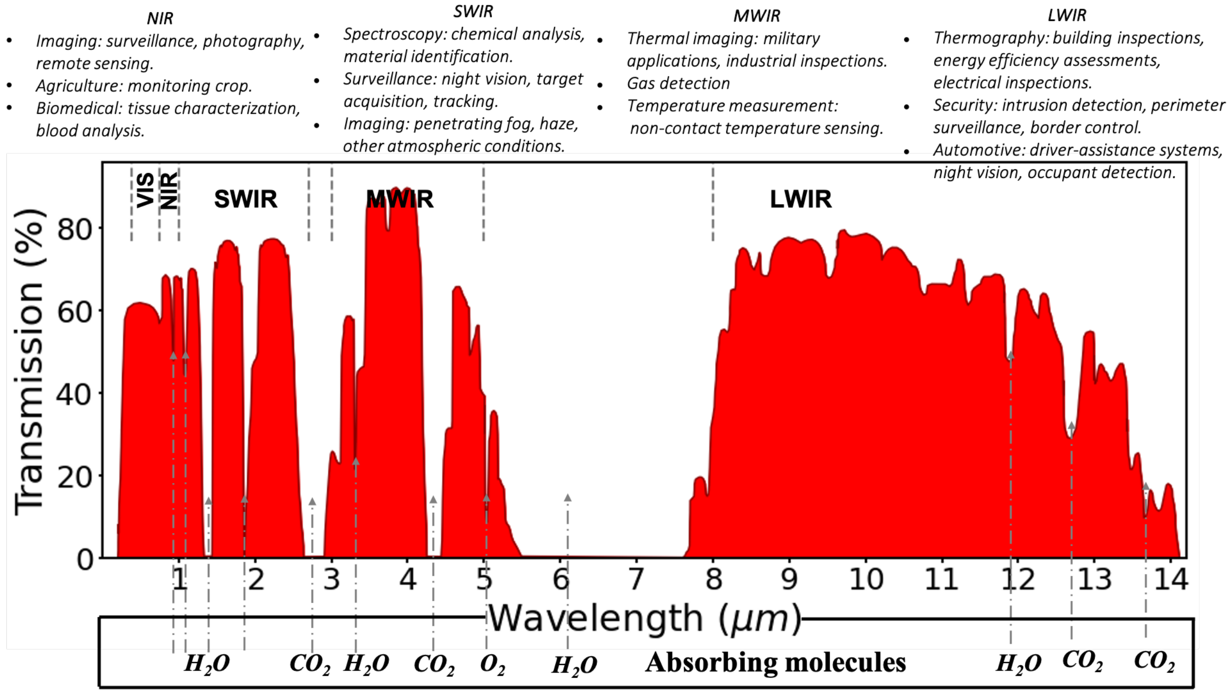

Figure 2.2: Atmospheric transmittance and absorbing molecules versus wavelength[49], possible IR sensors applications in different spectral bands

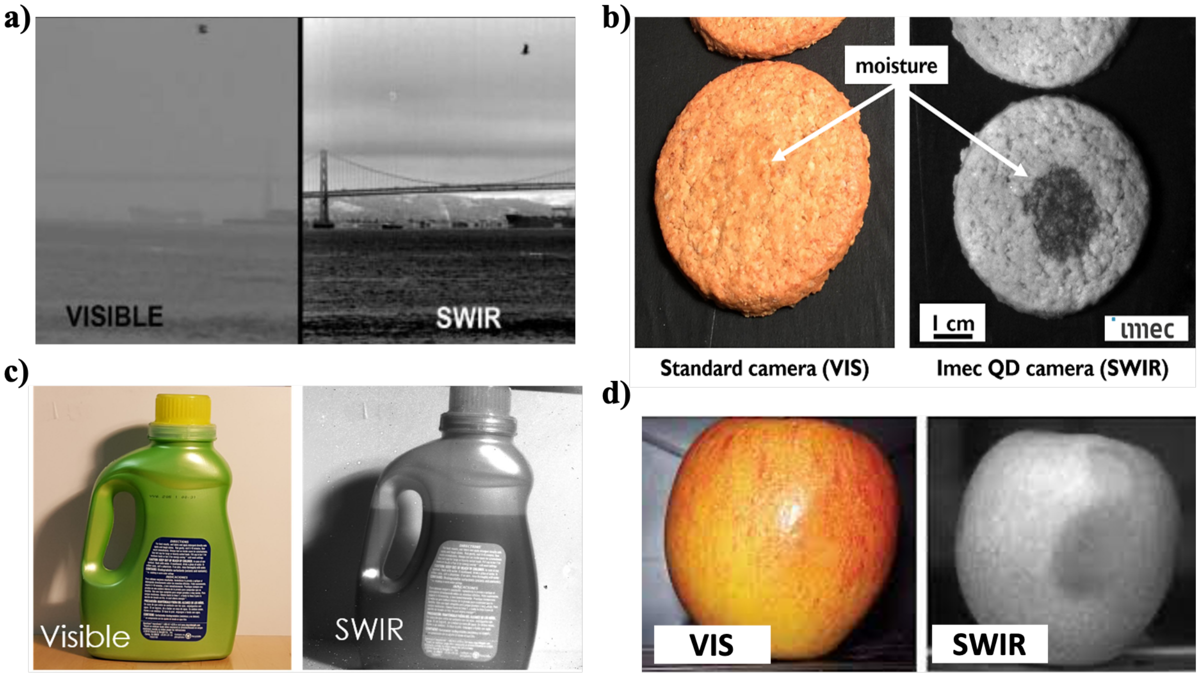

Figure 2.3: Examples of IR photodetector applications:**a)** Surveillance, artificial vision or night vision, SWIR cameras reduce the effect of fog or smoke, allowing scenes not present in the visible realm to be seen, source: *Courtesy of NASA*. **b)**Food inspection, images of cookies acquired with a visual sensor (left) and with Imec's quantum dot-based SWIR sensor at 1,450nm (right), the bottom cookie had a drop of water applied to its surface, which can be only distinguished under SWIR light, source: *Imec*. **c)** Checking of liquid fill levels, the fill level in the plastic bottle is not revealed with a visible camera, whereas a SWIR camera clearly shows the fill level, source: *SWIR Vision Systems*. **d)** Agricultural food product sorting and inspection systems, the visible image of apple shows no bruising, while the SWIR image on right shows the fruit is clearly damaged source: *UTC Aerospace Systems*.

In industrial automation, infrared sensors are used in a variety of applications, such as detecting proximity, level (**Figure** 2.3.**c**), motion, position, and more. They enable accurate and reliable monitoring and control of industrial processes. Common applications such as LIDAR use IR light sensing to accurately measure the distance between the emitter and surrounding objects, creating accurate and detailed 3D point clouds of the environment, this data can then be used for a variety of applications in a wide range of fields[51, 52]. These applications are just a few of many that demonstrate the versatility and importance of IR photodetectors in a variety of fields.

2.1.4 Market of IR sensors

The IR sensors market is a rapidly growing industry that focuses on the development, production, and distribution of photodetectors capable of detecting and measuring IR radiation. The market for IR sensors has witnessed significant advancements in recent years, driven by technological innovations and increasing demand for non-contact temperature measurement, night vision, gas detection, and motion sensing. IR sensors offer several advantages, such as high sensitivity, fast response time, and the ability to operate in harsh environments. Key factors contributing to the growth of the photodetectors market include the expanding adoption of IR sensing technology in surveillance systems, the rising need for automation and safety in industries, and the growing demand for consumer electronics with IR capabilities. Prominent players in the IR sensors market include companies like STMicroelectronics[7], Omron Corporation, Texas Instruments, Murata Manufacturing[53], etc... These companies focus on product innovations, strategic partnerships,

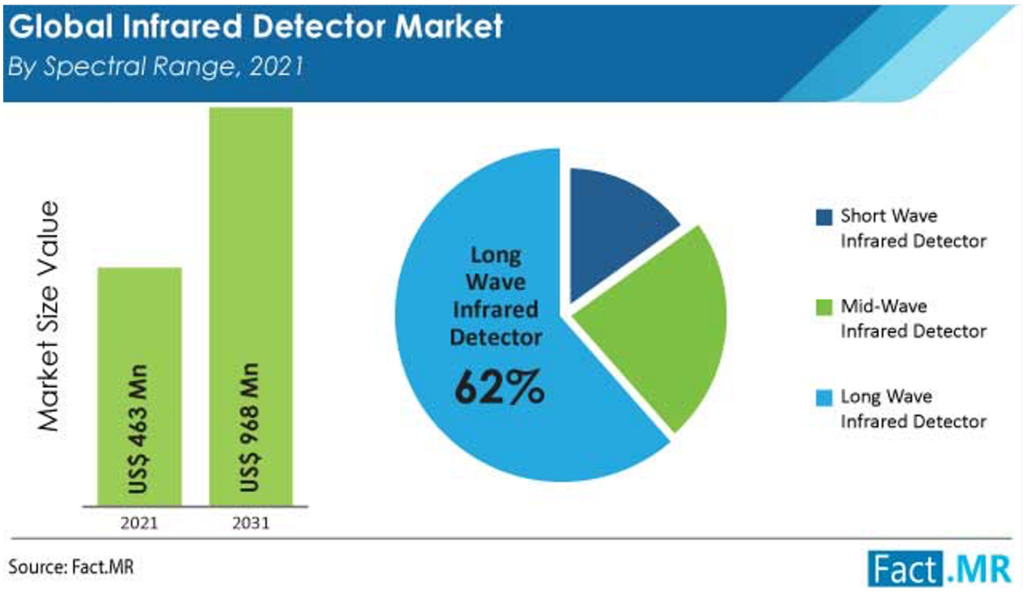

Figure 2.4: Infrared imaging market size, share by spectral band, and forecast trends for 2021-2031

and mergers and acquisitions to strengthen their market position and gain a competitive edge. Overall, the IR sensors market is poised for continued growth in the coming years as advancements in technology drive the development of more advanced and versatile sensors to meet the evolving needs of various industries. **Figure** 2.4 shows the growth of the photodetector market IR according to *Fact.MR*, which is expected to double in the next ten years and reach a value of 1 billion dollars in 2031.

2.2 Lead Sulphide (PbS) colloidal quantum dots (QDs), from engineered functionalities to applications

2.2.1 Colloidal quantum dot and basic materials physics

QDs were first synthesised in the 1980s by Louis E. Brus [54] and have attracted the interest of various fields, especially in optoelectronics. QDs are solid semiconductor nanostructures consisting of several hundred to thousands of atoms and have a diameter of 2 to 10 nm, corresponding to a size range of 10 to 50 atomic lengths. QDs surface is controlled by adding surfacee ligands by the surface ligand, to preserve the particle size and to avoids defects, which provides optical and electronic properties controlled by surface. The small size of QDs results in a high surface-to-volume ratio, such that their properties are intermediate between those of single molecules and bulk semiconductors, a significant fraction of the atoms making up the quantum dots are therefore located on the surface. QDs surface states therefore play a key role in determining the properties of these materials, by influencing luminescence, defect energy levels , doping type and charge density. These materials have unique optical and electronic properties that depend strongly on their size. Due to quantum confinement, they exhibit interesting phenomena, particularly a narrow absorption peak. QDs are generally compounds of the type II-VI (HgTe, ...), III -V (InSb, ...) or IV-VI (PbS ...), although there are also QDs in the form of single elements (Ge, Si ...). In this section, as in this work, we will focus specifically on the case of PbS.

Quantum confinement is a very essential aspect of QDs semiconductors. It occurs in all semiconductors where at least one of the dimensions is smaller than its Bohr radius of the exciton (Wannier exciton) or the bound electron-hole pair. PbS bulk is a semiconductor with a direct band gap of about 0.41 eV, when an electron is excited (photon absorption), the Coulomb interaction between the electron and the created hole is such that, the Bohr radius a_h (distance between the electron-hole pair) given by the following equation is ≈ 18 nm [3].

$$a_h = \frac{\hbar^2 \varepsilon_0 \varepsilon_r}{m^* e^2 \pi}, \qquad \frac{1}{m^*} = \frac{1}{m_h^*} + \frac{1}{m_e^*} \tag{2.2.1}$$

Due to the small dimensions of PbS QDs, similar to the de Broglie wavelength (spatial extension of atomic orbitals), ≈ 9 nm, which is approximately twice the Borhr radius of the exciton, there is strong quantum confinement of electrons and holes in all three spatial dimensions, leading to discrete quantized energy states (as in 3D quantum well or spherical quantum box) observable in optical absorption spectrum. The confinement of the wave function leads to a tunable band gap of the QDs over a broad energy range between 0.6 -1.6 eV, depending on the average QDs size. For a spherical quantum well with zero potential inside the box and infinite outside, the Hamiltonian gives eigenergies as:

$$E_{n,1} = \frac{\hbar^2 \Phi_{n,l}^2}{2m^* R^2} \tag{2.2.2}$$

where, m^* is the effective mass of the particle, and R is the radius of the nanocrystal. The coefficient $\Phi_{n,l}$ is the n^{th} zero of the l^{th} spherical Bessel function. numbers n, 1 and m are the same as used in the atomic notation of states, for example, n = 1, 1 = 0 would be the 1S state. The following experimentally determined relationship is useful to determine the band gap width E_g as a function of the diameter d of the QDs and vice versa [55].

$$E_g = 0.41 + \frac{1}{0.0392 d^2 + 0.114 d} \tag{2.2.3}$$

As direct band gap semiconductors, PbS QDs also have a large molar absorption coefficient, reaching ≈ 10^6 $M^{-1}.cm^{-1}$ at 400 nm [56].

2.2.2 Optical, electronic properties and charge transport in QDs film

In QDs, electron states in the conduction band and the hole states in the valence band are quantized. **Figure.**2.5 shows the density of states for a bulk semiconductor compared to semiconductor QDs. Starting from a continuum of the density of states in the bulk, as the size of the dot decreases, the separation between energy levels increases, and it increases more dramatically near the band edge. The states near the center of the band are still close enough to be considered continuous. The absorption spectrum of a bulk semiconductor is continuous, but in QDs, it consists of a series of discrete transitions with very high absorption intensity at the transition wavelengths (energies).

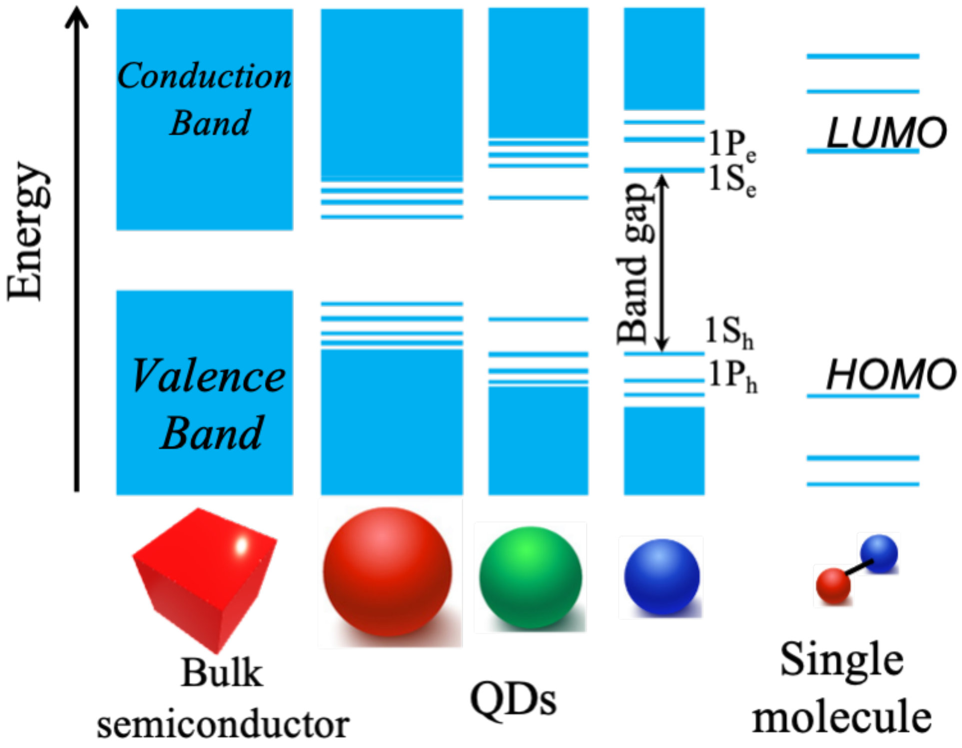

Figure 2.5: Change in energy levels as a function of QDs size. The QDs materials show the individual energy levels which can be calculated using the particle-in-a-box model. As the crystal grows large it approaches the bulk semiconductor state with energy bands separated by the bandgap energy Eg

Although there are no real bands in QDs, the term interband is used to refer to a transition between a level from the valence band and a level from the conduction band, and intraband to refer to a transition between two levels from the same band. Thus, the smallest interband transition energy is the energy difference between the last level of the valence band 1S$_h$ and the first level of the conduction band 1S$_e$ is:

$$1S_e - 1S_h \approx E_g + \frac{\pi^2\hbar^2}{2R^2}\left(\frac{1}{m_e^*} + \frac{1}{m_h^*}\right) + E_c \tag{2.2.4}$$

Where R is the radius of the nanocrystal and E_c is the Coulomb interaction energy between the hole and the electron, also known as the exciton binding energy. Thus, for the $1S_e - 1S_h$ interband transition with the lowest energy, quantum confinement adds the energy $\frac{\pi^2\hbar^2}{2R^2}\left(\frac{1}{m_e^*} + \frac{1}{m_h^*}\right) + E_c$ to the band gap energy of the bulk material. The band gap energy Eg is directly related to the size of the QDs by the **Equation** 2.2.3.

The electronic properties of QDs are defined in terms of the energy levels of the individual dots, the coupling between dots, and their structural arrangement. Silver nanoparticles of 4 nm separated by 0.5 nm or gold nanoparticles of 5 nm separated by butane dithiol ligands or by shorter ligands were reported to be metallic. In contrast, semiconducting QDs with similar or higher monodispersivity initially did not even exhibit ohmic transport. By controlling the Fermi level with charge transfer doping and an efficient ligand exchange procedure, ohmic conductivity can be achieve in some monodisperse QDs with mobilities up to 10^{-2} cm^2.V^{-1}.s^{-1}[57]. However, this conductivity decreases with temperature, indicating insulating behaviour unlike metal nanocrystals, even with very short ligands[58]. The conductivity in QDs must follow certain rules, there must be partial state occupancy in QDs, and charges must be able to move from one state to another between QDs on a reasonable timescale. In addition, the disorder in the QD films must be taken into account. The charge transport in QDs film can be described by a combination of several mechanisms:

Band transport-hopping transport: In QDs film, electrons and holes are confined within a discrete energy level structure due to their small size. The charge transport can occur through the energy bands, similar to bulk semiconductors. In this case, the charge carriers move by hopping between neighbouring QDs, and the transport behaviour is influenced by the energy levels, density of states, carrier concentrations and the distance between neighbouring QDs. Due to disorder, it is difficult to obtain band conduction in QDs. Band formation requires coupling greater than disorder energy. Even in ordered systems, sufficient electron-electron repulsion can split the band, leading to the Mott insulator[59], but more often disorder localises the electrons, as in Anderson localisation[60]. Weak transmission due to variations in confinement energy, electron-electron repulsion and variations in coupling and thermal broadening leads instead to hopping conductivity, the mobility in the hopping regime derived from Einstein-Smoluchowsky equation is given by[57]:

$$\mu_{hop} = \frac{ed^2E_a}{3hkT}exp\left(-\beta l - \frac{E_a}{kT}\right) \tag{2.2.5}$$

where **d** is center to center distance between two neighbouring dots, E$_a$ is the activation energy (E$_a$ $\sim$ 0.02 - 0.05 eV, depending on ordering in QDs film), β is the attenuation of the wave function ($\beta \sim$ 0.9 - 1.2 Å^{-1}, l is dot separation(edge-to-edge spacing), h and k are the Planck and the Boltzmann constants respectively.

Trap-assisted transport: QDs generally have surface defects and trap states that can capture and release charge carriers. These trap states act as localized energy levels within the band gap, and charge carriers can be trapped and transported between the QDs via these states. Trap-assisted transport can significantly affect the charge carrier mobility and overall transport characteristics in QDs film.

Tunnelling transport: Quantum tunnelling is a phenomenon where charge carriers can cross an energy barrier by exploiting their wave-like nature. In QDs, charge carriers can tunnel through potential barriers, allowing them to move between neighbouring quantum dots. Tunnelling mechanism becomes more significant when the inter-dot spacing is small and the the energy barriers. The tunnelling rate between two orbitals of QDs neighbors can be approximated by[61]:

$$\Gamma \sim exp\{-2(2m^*\Delta E/\hbar^2)^{1/2}\Delta x\} \tag{2.2.6}$$

where m* is the electron effective mass, ΔE is the the height of the tunnelling barrier and Δx are and width of the tunnelling barrier or the shortest edge-to-edge distance between the dots. If the barriers between dots are sufficiently small, the quantum dot array is analogous to a covalently bonded solid, even though the coupling ligand itself is much more complex than a single bond.

Surface ligands contribution: QDs are typically coated with organic ligands or inorganic surface passivators to protect the QDs and control their electronic properties. These ligands can influence charge transport by affecting the carrier mobility, inter-dot coupling, and energy level alignment[61]. Ligands may form a tunnelling barrier or provide an additional charge transport pathway.

Additionally, in the case of PbS QDs, the type of ligand controls the type of electrical conduction (p-type or n-type). **Figure** 2.6 shows the tunability of the band gap energy levels (CB and VB energy levels measured by UPS and optical absorption) of PbS QDs capped with different ligands. The QD films used all have the first excitonic peak at λ = 963 nm, i.e. they are QDs with the same diameter or bandgap E$_g$. Starting with Br- and proceeding clockwise (**Figure** 2.6 left panel), the effect of tuning the energy levels is shown on **Figure** 2.6 right panel. The halide ligands lead to a low VBM, while the thiol ligands have the opposite effect[62]. The observed shift in energy levels is expected to have a significant impact on the operation of electronic devices fabricated with PbS QDs.

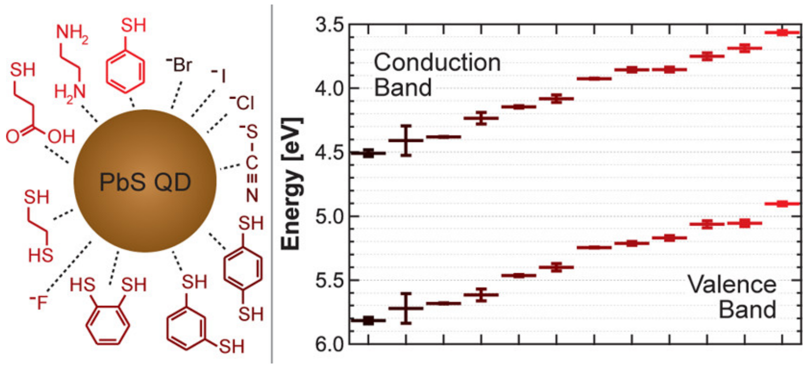

Figure 2.6: Tuning the energy level of the band gap (control of CB and VB energy levels) of PbS QDs using different ligands[62]

2.2.3 Synthesis and deposition of QDs

The synthesis and deposition of quantum dots (QDs) are crucial steps in the fabrication of materials or devices based on QDs. There are several synthesis methods, including colloidal synthesis, sol-gel synthesis, self-assembly, assisted lithography and plasma synthesis. In this section, we will focus solely on colloidal synthesis, which is the most commonly used method. Colloidal synthesis of QDs involves the use of chemical precursors containing the constituent elements of QDs, such as $PbCl_2$ or PbI_2 and Na_2S for PbS QDs, along with a suitable solvent and ligands like oleic acid. The precursors, dissolved in organic solvents such as tetrahydrofuran, hexane, or octadecene, are mixed and heated at an appropriate temperature under an inert atmosphere (N_2). The nucleation phase is initiated by adding nucleating agents or catalysts, typically a weak base like triethylamine, where atoms cluster to form very small PbS QD nuclei. QD growth is continued by adding growth agents such as dodecylamine and additional precursors. Precise control over the size of PbS QDs can be achieved by adjusting reaction parameters such as precursor concentration, temperature, reaction time, and precursor-to-growth-agent ratio. Longer reaction times and higher reaction temperatures result in larger nanocrystals. Characterization techniques such as absorption spectroscopy and dynamic light scattering can be employed to evaluate the size and distribution of the obtained QDs. Once the desired-sized PbS QDs are formed, a quenching solution, containing an excess of ligands (typically oleic acid), is injected into the solution, and the reaction medium's temperature is rapidly reduced to ambient temperature to halt further reaction. The ligand solution helps stabilize the QD surface and prevent particle aggregation, resulting in a colloidal suspension. Colloidal synthesis of QDs offers several advantages, including relative simplicity, high flexibility in QD design, and the ability to produce QDs in large quantities. The synthesis of QDs is based on the use of long alkyl chains (oleic acid or oleylamine). Ligand exchange plays an important role in the functionalization and integration of QDs in various applications. Ligand exchange consists of replacing the original ligands on the surface of QDs with new ligands to achieve better electrical properties and higher stability of QDs (surface passivation). A ligand exchange process consists of replacing long-chain ligands with single-element ligands or shorter molecules[63, 64, 65]. The main ligand exchange methods are:

Solid-state ligand exchange: QDs with long alkyl chains are first deposited on the substrate by spin coating, then a solution containing an excess of short ligands (thiol ligands) is added, followed by a short soaking and removal of the solution by spin coating, then a protic solvent (polar solvent with at least one hydrogen that can interfere with hydrogen bonds or solvent that can release an H^+ proton) is spin-coated onto the QDs film to remove the alkyl chains and excess

short ligands[66]. To achieve complete ligand exchange, the concentration of QDs is adjusted to film thickness of several tens of nm.
Solution-phase ligand exchange: QDs encapsulated with long alkyl chains and dispersed in a nonpolar solvent are dissolved in a polar solvent containing short hydrophilic ligands. The long ligands are replaced by short hydrophilic ligands, and the QDs then migrate into the polar solvent. The polar phase containing QDs with exchanged ligands can be easily separated from the nonpolar phase. The QDs solution can then be used as an ink, enabling a one-step film-making process such as spin coating or spray coating without the need for further exchange steps.

Currently, most QDs-based applications use solid-phase ligand exchange because this method can be better controlled and produces smooth, compact QDs films from which long alkyl ligands are largely removed. The strong bonding between the thiol ligands and the QDs enables fast and efficient exchange[66]. Commonly used ligands for surface modification of QDs include are:

- Organic ligands used in the synthesis of QDs (organic alkyl chains, etc...).
- Inorganic ligands such as metal chalcogenide complexes designed to increase charge carrier mobility[67]. To increase carrier mobility, inorganic metal chalcogenide complexes (MCC) ligands have been developed. Unlike organic alkyl chains, metal chalcogenide complexes ligands generally provide a net charge, allowing dispersion in polar solvents. As with QD inks based on organic ligands solution, one-step spin coating can be considered for film formation directly from metal chalcogenide complexes-ligated QDs. Organic components such as ammonium can be removed by gentle post-annealing. After removal of the organic ligands, the mobility and conductivity of the carriers are significantly improved, making it possible to demonstrate the efficiency of QD-based field-effect transistors[66].
- Halide ligands, used to achieve low defect density while maintaining high charge carrier mobility. Despite the improvement in charge carrier mobility in QD films achieved by using MCC ligands, the performance of devices based on these ligands remains poor due to the high defect density in these solids. Therefore, halogenated ligands have been investigated for QD passivation, offering both efficient carrier transport between QDs due to their atomic size and enhanced surface passivation due to their strong bonding with QDs. In comparison to chloride and bromide ligands, iodide ligands can form a stronger coupling with the surface atoms of QDs, resulting in a lower defect density in the film. The iodine, as a strong base, strongly couples with the weak acid, Pb atoms of PbS QDs, whereas the strong acid, H^+, forms a strong coupling with the chlorine base. Chlorine ligands are easily removed from the surface by protic solvents. DFT calculations demonstrate that the energy required to remove iodine ligands is higher than that of chlorine ligands. The binding of oxygen atoms leads to the formation of defect states within the energy gap, while the adsorption of halogen ligands prevents the adsorption of oxygen[64, 68]. Halogenated ligands have shown promising advantages in reducing defect density and improving charge carrier mobility, reaching values exceeding 10^{-2} $cm^2.V^{-1}.s^{-1}$. Furthermore, The use of halogenated ligands has proven effective in preventing oxygen adsorption on QD surfaces, contributing to device stability and performance.

The choice of ligands also makes it possible to define the doping type of the QDs film. For example, the use of iodide ligands leads to an n-type, whereas PbS+EDT(Ethane-1,2-dithiol) is p-type.
There is also a hybrid ligand exchange process, which combines organic cross-linkers and inorganic passivators. The hybrid ligand passivation process comprises two stages: an exchange of halogenated ligands in the solution phase followed by an exchange of organic ligands in the solid state. Halogenated anions are introduced in situ or during the final stages of the synthesis process, enabling passivation of sites inaccessible to larger organic ligands. Small organic ligands such as EDT are then used in the solid state to replace the long organic ligands.

2.3 In_2O_3 based TCO

2.3.1 Introduction

Numerous technologies, such as screens, organic light-emitting diodes (OLEDs), photovoltaic panels and smart windows, require the use of transparent electrodes. Metals such as nickel (Ni), gold (Au), or silver (Ag) thin films, with a thickness of less than 10 nm can exhibit optical transparency of over 40% in the visible (Vis) and near-infrared (NIR) domains[69, 70] and a relatively high sheet resistance on the order of several hundred $\Omega/\Box$. This increased sheet resistance is attributed to the scattering diffusion of conduction electrons at the film's surface[71]. For metal films thicker than a few tens of nanometers, good electrical resistance is achieved, however, the optical transmission gets close to zero. Therefore, thin metal films cannot fully play the role of transparent electrodes. There is another class of materials that simultaneously exhibit good optical transmission (in the Vis and NIR domains of the electromagnetic spectrum) and low electrical resistivity, known as transparent conductive oxides (TCO). The primary TCO are M_mO_n type materials, where M is usually a post-transition metal atom (In, Sn, Zn, Cd ...) and O represents the oxygen atom. The extraordinary combination between electrical and optical properties was first observed in 1907 by K. Baedeker on thermally evaporated cadmium oxides (CdO)[72]. In 1947, the optical transmission and electrical conductivity properties of chlorine-doped tin oxide (SnO_2:Cl) [73] and antimony-doped tin oxide (SnO2:Sb) [74], as well as tin-doped indium oxide ($In_{2-x}O_3$:Sn_x or ITO) [75], were discovered. Later, in 1971, aluminum-doped zinc oxide (ZnO:Al) was also identified as TCO [76]. Table-1 shows the most important TCO and various possible dopants[77].

Materials	Dopants
In_2O_3	**Sn**, Ge, Mo, F, Ti, Zr, Mo, Hf, Nb, Ta, W, Te
SnO_2	Sb, **F**, As, Nb, Ta
ZnO	**Al**, Ga, B, In, Y, Sc, F, V, S, Ge, Ti, Zr, Hf

Table 2.1: Doping of main TCO materials.

From the 1990s onward, the development of transparent conductors has progressed rapidly, with the discovery of several new materials every year and the improvement of existing materials' properties. Research efforts have expanded the family of transparent conductors to include sulfides, selenides, nitrides, graphene, and carbon nanotubes [77]. Among these materials, ITO is considered the best transparent conductor and is therefore the most widely used. **Figure**.2.7 shows the resistivities of the main TCO-based materials that have been reported between the 1970s and 2000 [78].

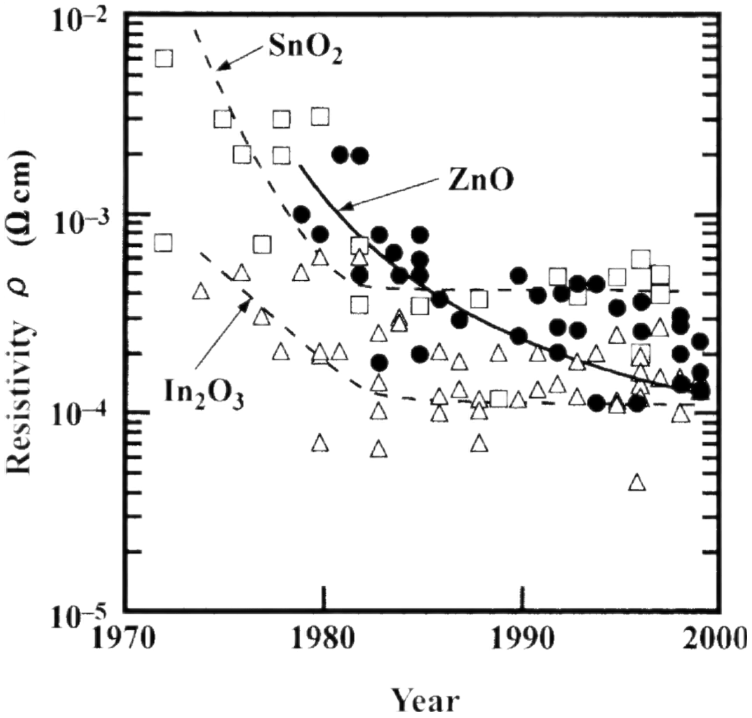

Figure 2.7: Reported (1970-2000) resistivities of binary transparent conducting oxide (TCO) materials: undoped and impurity-doped SnO_2 (□), In_2O_3 (△), and ZnO (●). lowest restivities are observed for In_2O_3-based TCO.

The main limitation of TCO is related to the inherent trade-off between transparency and electrical conductivity from a physical point of view. A conductor tends to be opaque like metal, while a visibly transparent material like glass tends to be insulating. This limitation is critical for certain applications. For example, as displays get larger and write speeds increase, it is necessary to reduce electrical resistance while maintaining good optical transmission[79]. In the IR region, optical transmittance tends to decrease sharply, and simply reducing film thickness to increase optical transmittance would result in an increase in resistivity. However, the requirements are not limited to the combination of conductivity and transparency. Other properties of transparent conductors such as work function and morphology are also important. The knowledge of the work function of TCO is necessary to understand band alignment and optimize contact resistance with other materials when used in tandem solar cell stacks or photodiodes. With the increasing demand for TCO and the development of more complex devices, a deep understanding of the physics of TCO materials is needed to optimize new properties compatible with increasingly complex applications. The ever-growing interest in TCO is reflected in an extensive literature on various materials, their properties, and deposition techniques, which reflects several decades of intensive scientific research and technical applications. **Figure**.2.8 shows the evolution of the number of publications referring to the three most important TCO over the last two decades [80]. The guiding principles for the design of TCO materials and their integration into new applications still represents a challenging tasks nowadays. The basic physics of their rarest electrical and optical properties (electronic conduction in a transparent solid), is now reasonably well understood[81].

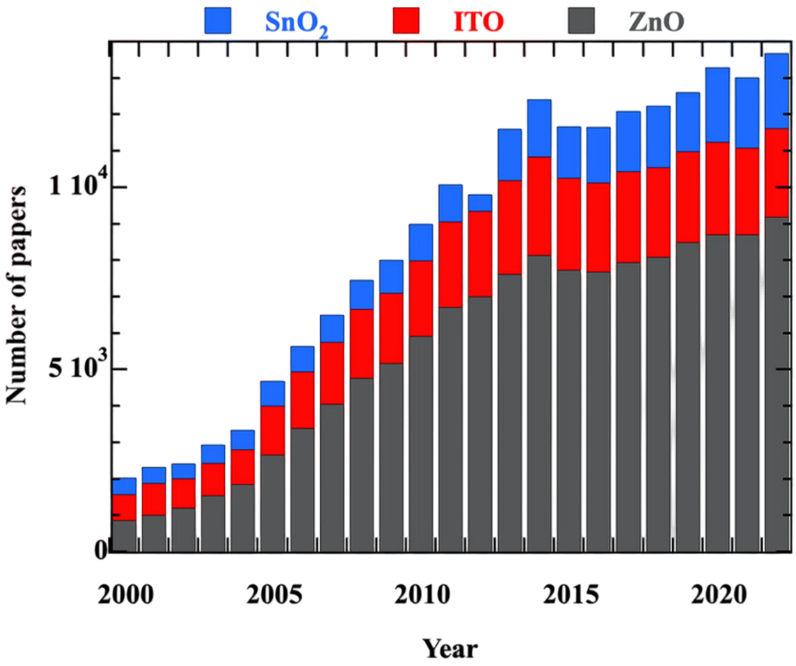

Figure 2.8: Number of publications devoted to ZnO, SnO$_2$ and In$_2$O$_3$ based-TCO over the last two decades

This section will present the main fundamental aspects of TCO-based semiconductor physics. In Sections 2.3.2 and 2.3.3, we will discuss the electronic structure, electronic and optical properties of TCO, and the criteria for selecting a TCO as a transparent conductor. Special attention will be given to In$_2$O$_3$-based materials, although most of the considerations can be generalized to all other n-type TCO and some p-type materials.

2.3.2 Basic physics of TCO

2.3.2.1 Structural properties

TCO based on In$_2$O$_3$, such as ITO, crystallizes in a complex structure closely resembling that of bixbyite (space group symmetry: Ia3, lattice constant: 1.0117 nm, cubic crystal), which corresponds to In$_2$O$_3$ crystal lattice (**Figure**.2.9). The structure of bixbyite can be regarded as an imperfect crystal of the fluorite structure obtained by extracting 16 oxygen atoms (empty anion sites) for a unit cell of bixbyite. The unit cell of In$_2$O$_3$ consists of 80 atoms, with 32 indium atoms occupying b-sites and 24 occupying d-sites, while oxygen atoms occupy Wyckoff positions 48e [82, 83]

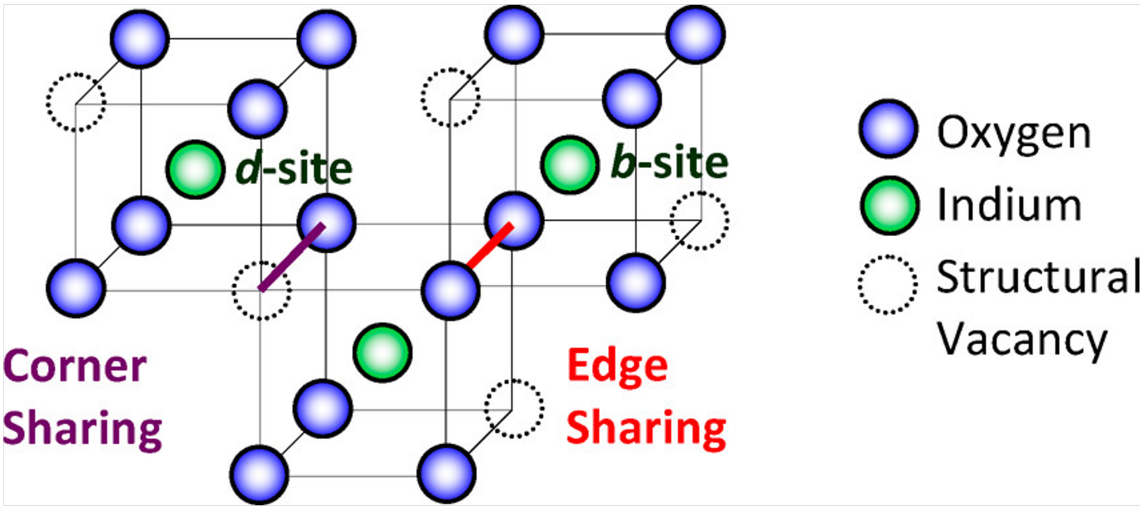

Figure 2.9: Schematic representation of the crystal structure of In_2O_3, the open circles indicate the oxygen vacancies, the blue spheres indicate the oxygen atoms, and the green spheres indicate the indium atoms. In the ideal structure, one quarter of the anionic sites are empty (oxygen atom position), 80 atoms per unit cell, 48 anions, 8 cations in b-position and 24 cations in d-position.

Sn-doped In_2O_3 or ITO is a heavily doped n-type semiconductor with a wide band gap, which has a relatively low electrical resistivity due to its density of free charge carriers. In intrinsic stoichiometric oxides, electrical conductivity and transparency in the visible cannot coexist, however doping can create free charge carriers. The density of free charge carriers in ITO results from two different types of electron donor sites:

➢ Oxygen vacancies (V_O), which act as n-type double electron donors (**Equation** 2.3.1).

$$O_O^{\times} \rightleftharpoons V_O^{\bullet\bullet} + \frac{1}{2}O_2(g) + 2e' \tag{2.3.1}$$

Where, $O_O^{\times}$ is the neutral oxygn atom in it normal lattice site, $V_O^{\bullet\bullet}$ is a oxygn vacancy, with double positive charges and e' is an electron in Kröger-Vink notation.

➢ Doping with Sn, a metal with a higher valence than In (In: $[Kr]5s^2 4d^{10} 5p^1$ and Sn: $[Kr]5s^2 4d^{10} 5p^2$), primarily occurs through the substitution of In atoms with Sn atoms (In^{3+} by Sn^{4+}). The state where all Sn ions have released their conduction electrons can be described as $In_{2-\delta}Sn^{\bullet}O_3e'_{\delta}$, neglecting the density of oxygen vacancies ($\delta \gg$ x) ,where x is the concentration of oxygen vacancies in substoichiometric indium oxide of the formula In_2O_{3-x}[84].

It is generally considered that each V_O site is surrounded by the 5s orbitals of In^{3+} ions. These orbitals are stabilized compared to the In 5s conduction band due to the absence of covalent bonding with the missing oxygen O^{2-}. Thus, the In 5s orbitals at each V_O site form shallow donor states below the conduction band, at around 30 meV for low **x** values. At high concentrations of V_O, a impurity band is expected to form, overlapping the lower conduction band of $In_2O_{3-x}(V_O^{\bullet\bullet})_x e'_{2x}$, leading to an electronic transition towards a heavily doped semiconductor with itinerant electrons [81, 84]. The electronic band structure of ITO with low and high oxygen vacancy concentrations, adapted from Fan and Goodenough [85] is represented in **Figure** 2.10.

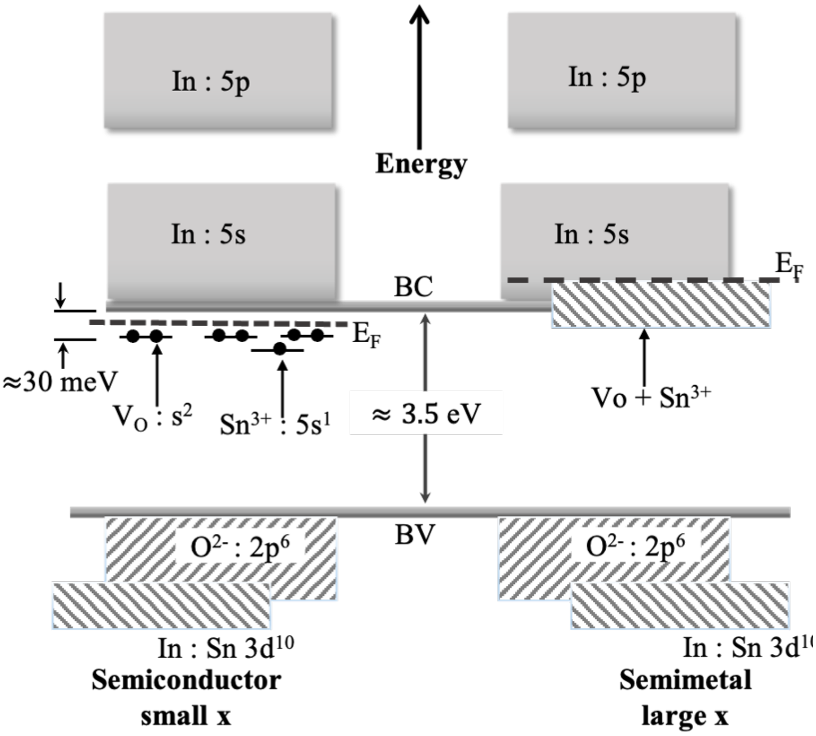

Figure 2.10: Schematic electronic band structure of Sn-doped In_2O_3, for small x (left) and for large x (right).

The density of electrons can be controlled by ITO's chemical composition in several ways, including:

➢ The concentration of Sn through the choice of the deposition target, by adjusting the initial composition of the ITO target with Sn (1-10 at.%.) [77].

➢ The choice of oxygen partial pressure (p_{O_2}) and total pressure. A low p_{O_2} promotes the formation of oxygen vacancies, while high deposition pressure will lead to the opposite effect.

➢ Post-deposition annealing treatments. Annealing under oxygen atmosphere reduces the density of oxygen vacancies, while annealing under a non-oxidizing atmosphere leads to oxygen desorption or an activation of doping through the reduction of $(2Sn^{\bullet}InO_i'')^{\times}$ known as Frank and Köstlin defects , according to the following equation [84, 86]

$$(2Sn^{\bullet}InO_i'')^{\times} \rightleftharpoons \frac{1}{2}O_2(g) + 2Sn_{In}^{\bullet} + 2e' \tag{2.3.2}$$

The density of free carriers in ITO can reach 1-2$\times 10^{21} \cdot cm^{-3}$ depending on the process. We will discuss the impact of electron density on ITO's electrical and optical properties in the following sections.

2.3.2.2 Electrical properties

Mott criterion given by **Equation** 2.3.3 provides the free charge carriers density n_c at which the transition from non-metal to metal conductivity (itinerant-electron) occurs.

$$n_c a_H^* = 0.26 \pm 0.05 \tag{2.3.3}$$

$$a_H^* = \frac{\hbar}{m^*(e^2/\varepsilon_r)} = \frac{a_0\varepsilon_r}{m^*/m_0} \tag{2.3.4}$$

where a_H^* is the Bohr radius of the material, a_0 is the hydrogen Bohr radius, m^* is an appropriate effective mass and ε_r the relative permittivity. The data collected in the literature on ITO films give: $m^* = 0.35m_0$, $\varepsilon_r = 4$, which gives $a_H^* = 13$Å and $n_c = 6.4 \times 10^{18} cm^{-3}$. The free carriers density in ITO films, as well as in other TCO, is generally higher the critical density n_c. Therefore, this criterion justifies the application of free electrons model to TCO. The Boltzmann theory of classical electron gas and the Drude model are two important tools used to describe electron transport in conductive materials.

Within the Boltzmann formulation, conductivity σ (resistivity ρ) depends on both the mobility μ of free charge carriers and their density n:

$$\sigma = ne\mu = \frac{ne^2\tau}{m*} = \frac{1}{\rho} \tag{2.3.5}$$

where $m*$ is the effective mass and $\tau$is the charge carrier lifetime. For thin films with uniform thickness t, the electrical resistance is expressed as sheet resistance:

$$R_s = \rho/t \tag{2.3.6}$$

This quantity only depends on the film thickness t. If t is known, the resistivity (conductivity) can be easily determined using the four-point probe measurement technique (Van der Pauw) which will be described later.

Equation 2.3.5 also shows that electrical conductivity can be improved by increasing the free charge carriers through doping. Increasing conductivity can also be achieved by improving charge mobility. In ITO films, mobility depends on several scattering mechanisms, namely scattering through neutral and ionized impurities (oxygen vacancies), electron-phonon interaction, and scattering at grain boundaries.

Grain boundaries scattering: grain boundaries behave as charge traps, creating an energy barrier E_b. They reduces the mobility of charge carriers between grains. The grain boundary mobility μ_{gb} is given by the **Equation** 2.3.7 [87, 88].

$$\mu_{gb} = \frac{L}{\sqrt{2\pi m^* kT}} exp\left(-\frac{E_b}{kT}\right) \tag{2.3.7}$$

where L is the grain size.
This model applied to ITO gives an $E_b \approx$10 meV [89]. The grain boundaries have a significant impact on mobility when the grain size is comparable to the electron mean free path λ_{mfp}, the electron mean free path in a solid is given by the following equation:

$$= \nu_F \tau \tag{2.3.8}$$

where $\nu_F = \hbar k_F / m^*$ is the Fermi velocity and $\tau = \mu m^*/e$ the resistivity relaxation time or free carriers live time. For ITO film with a free carriers density of 5 $\times 10^{20}$ cm^{-3} and a mobility of 50 cm^2.V^{-1}.s^{-1}, the mean free path of electrons $\lambda_{mfp} \approx$ 8 nm, whereas the typical grain sizes are on the order of 50 - 100 nm [77]. Therefore, we expect that an electron moving under the influence of an applied d.c. electric field will be scattered many times within a grain before reaching a grain boundary. Thus this mechanism is not as relevant in the TCO materials.

Ionized impurities scattering: It is characterized by short or long-range Coulomb interactions between the ionized impurities and the free electrons in the film. This interaction reduces the mobility μ_{ii} of free carriers in the background formed by fixed ionized impurities. This mechanism is intrinsic to the doped material and can therefore set the lower limit of the resistivity. Using the Coulomb interaction between the electrons and the impurities, Brooks calculated in 1955 the mobility for an electron gas of density n as[90**?**]:

$$\mu_{ii} = \frac{8\pi(\varepsilon_0\varepsilon_r)^2\hbar^2 n}{N_i Z^2 e^2 m_e^{*2}} \frac{1}{f(k_F)} \tag{2.3.9}$$

where N_i is the number of scattering centers per unit volume and Z is the charge of the impurity, ε_0 is the dielectric constant of free space, while ε_r is the relative dielectric constant at low frequencies. $f(k_F)$ is the screening function and depends on the Thomas-Fermi screening wave vector.

When the free carriers density is above 10^{19} cm^{-3} (high density of oxygen vacancies), the interaction between free charges and grain ionized impurities become the most important scattering mechanism in TCO. Considering only ionized impurities scattering, the mobility limit of ITO has been estimated between 90-100 $cm^2.V^{-1}.s^{-1}$[91, 92]. However, in practice, this value is rarely achieved, and the total mobilities of ITO films range from 10-50 cm $^2.V^{-1}.s^{-1}$ depending on the processes[93]. Nevertheless, hydrogen-doped indium oxide can exhibit mobilities higher than 100 $cm^2.V^{-1}.s^{-1}$[94].

Neutral impurity scattering: In ITO films with high Sn doping, non-activated defects such as Sn_2O_4 or Sn_3O_4 groups are formed[84]. These non-activated defects are related to the limited solubility of Sn in ITO. The solubility values of $\approx 60-80\%$ were reported by Kostlin et al for ITO[95]. Even if these defects are neutral, they can interact with free electrons by means of collisions when they are in the path of an electron. The impact of these defects on the mobility μ_N is given by the following equation[96, 97].

$$\mu_N = \frac{m^* e^3}{20\varepsilon_0\varepsilon_r n_N \hbar^3} \tag{2.3.10}$$

Where, n_N is the concentration (per cm^3) of neutral impurities. This value is often estimated from the difference between the measured carrier density and the carrier concentration.

The total mobility can be estimated using the Matthiessen formula.

$$\frac{1}{\mu_{tot}} = \frac{1}{\mu_{gb}} + \frac{1}{\mu_{ii}} + \frac{1}{\mu_N} \tag{2.3.11}$$

The mobility of TCO can be controlled through the precise selection of parameters or conditions during the film preparation process. Specifically, by carefully adjusting the partial pressure of oxygen, one can effectively regulate the density of free charge carriers. A higher p_{O_2} results in a lower density of oxygen vacancies, which consequently corresponds to a reduced density of free charge carriers, in turn, leads to an increased mobility (limited ionized impurities scattering). Similarly, a high density of oxygen vacancies leads to low mobility and high free carrier density, resulting in a trade-off between the two quantities. Thus, the maximum conductivity of TCO is limited by the theoretical upper limit of mobility.

2.3.2.3 Optical properties

The second interesting property of TCO is their optical transmission in the Vis and NIR regions of the electromagnetic spectrum. The optical transmission can be simply defined by the Beer-Lambert law, which is the ratio of the transmitted intensity I_T trough a material of thickness t to the incident light intensity I_0, see the **Figure**2.11**.a**, The optical transmission of a semiconductor film of thickness t and absorption α is described by **Equation** 2.3.12

$$\begin{cases} I_T = (I_0 - I_R)e^{-\alpha t} \\ T = \dfrac{I_T}{I_0}, R = \dfrac{I_R}{I_0} \end{cases} \implies \quad T = (1-R)e^{-\alpha t} \tag{2.3.12}$$

Where R is the reflection coefficient and α is the optical absorption. The optical absorption is an intrinsic property of semiconductor materials, it depends on the extinction coefficient k and the wavelength λ and is described by:

$$\alpha = \frac{4\pi k}{\lambda} \tag{2.3.13}$$

The reflection coefficients R and extinction coefficients k will be calculated in the sections below using the classical Drude theory of free electrons. The variation of optical transmission of TCO as a function of wavelength is shown in **Figure** 2.11.**b**[98, 99].

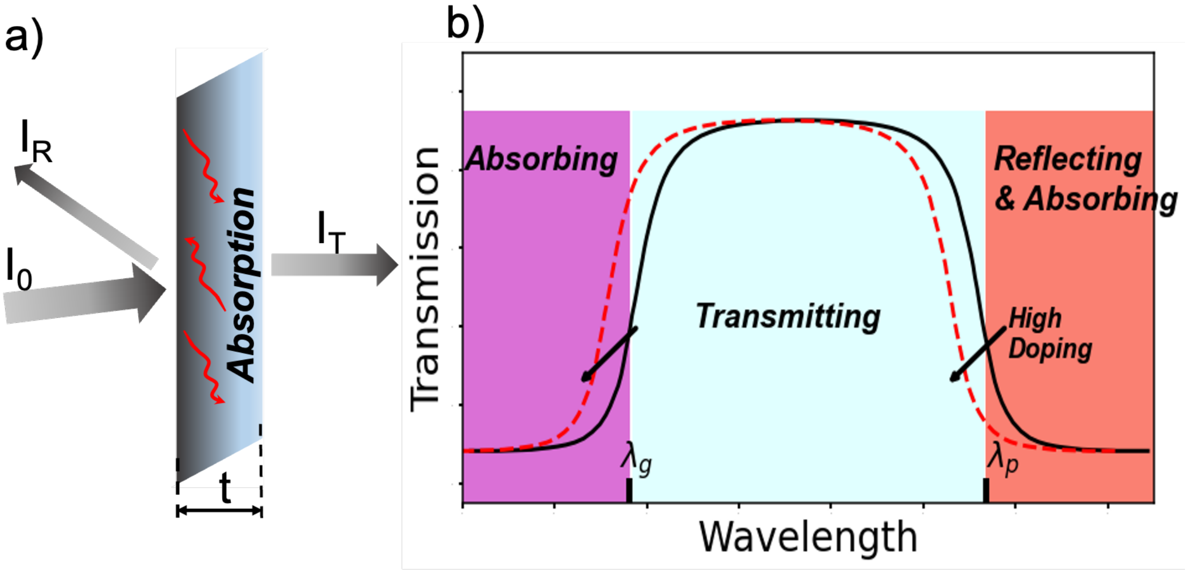

Figure 2.11: **a)** Illustration of the phenomena of reflection, absorption and transmission of light through a semiconductor, **b)** Spectral transmittance of a thin film of TCO material, band gap and absorption below λ_g and free electrons plasma absorption above λ_p.

At shorter wavelengths (ultraviolet or region below λ_g), the transmission is limited by the energy band gap of the material ($E_g > 3$ eV). The energy of the photons is high enough to allow band-to-band transitions, resulting in absorption of the incident light in the material. The width of the transmission window $\lambda_g <$ wavelength $< \lambda_p$ of TCO depends on the optical gap, which is directly related to the free carriers density. In heavily doped n-type TCO, a gradual shift of the band gap toward higher energy is generally observed as the electron density increases. This is well-known as the Moss-Burstein shift [100, 101]. In heavily doped semiconductors, the lowest states in the conduction band are occupied. Therefore, the allowing transitions occur at energies above the Fermi level E_F (**Figure** 2.12), increasing the optical band gap E_g^{opt}.

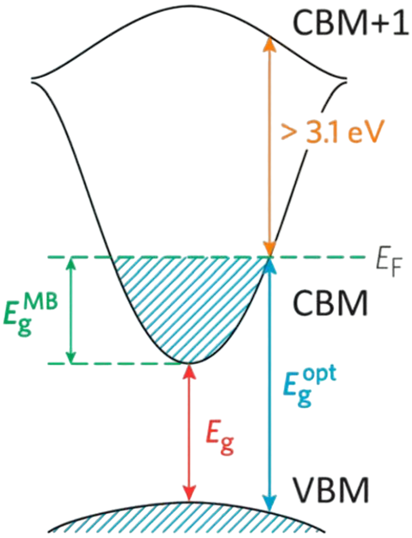

Figure 2.12: Diagram of the optical widening effect of the Moss-Burstein shift [102]

where E$_g$ is the fundamental energy gap separating the VBM and CBM (intrinsic band gap), E$_g^{opt}$ is the optical band gap corresponding to the smallest allowed optical transition from the VB to the CB, E$_g^{MB}$ is the Moss-Burstein shift and E$_F$ is the Fermi level. At high free carrier densities, the band gap narrowing phenomenon can also occur in TCO due to electron-electron and electron-ion interactions [103]. This mechanism competes with the Moss-Burstein effect and may be predominant in certain cases of films with significant densities of impurities within the band gap prior to annealing [104]. The energy gap between the maximum of the valence band and the lowest empty state in the conduction band is given as follows:

$$E_g^{opt} = E_g + E_g^{MB} - \Delta E_g \tag{2.3.14}$$

where E_g is the fundamental band gap, shown in **Figure** 2.12 is direct gap and estimated by first-principles calculations and X-rays spectroscopy to be $E_g \approx 2.8 \pm 0.2eV$ [105]; E_g^{MB} is the MB shift given by:

$$E_g^{MB} = \frac{\hbar^2}{2m_r^*}\left(3\pi^2 n\right)^{2/3} \tag{2.3.15}$$

In this relation m_r^* is the reduced effective mass $1/m_r^* = 1/m_e^* + 1/m_h^*$ where m_e^* and m_h^* are effective mass of the carriers in the conduction and valence band respectively, the value of $m_h^* \approx 0.65m_0$ for ITO [106].

From the absorption coefficient α (2.3.13), in which the expression for k will be specified in the following sections, the optical gap E_g^{opt} value of polycrystalline films can be estimated using the Tauc diagram [107, 108, 109]. Considering direct band-to-band transitions and in the parabolic band approximation, we have:

$$(\alpha h\nu) = \left(h\nu - E_g^{opt}\right)^{1/2} \tag{2.3.16}$$

E_g^{opt} is then obtained by plotting $(\alpha h\nu)^2$ as a function of energy $h\nu$ and performing a linear regression on the lower part of the curve to find the intersection with the energy-axis. This optical gap extraction technique will be then used to make relative comparisons of volume absorption properties between samples. In particular, given the predominance of the Moss-Burstein effect over the band gap narrowing effect, the change in optical gap gives a qualitative indication of the evolution of the doping of the materials as well as their work function.

In the NIR , optical transmission is limited by the photon-plasmon interaction, and the skin depth effect preventing light penetration into the material. The interaction between incident light and a semiconductor includes the phenomena of transmission, reflection, and absorption; the relationship between these three phenomena is given by the following energy conservation yields equation at each wavelength:

$$A(\lambda) + R(\lambda) + T(\lambda) = 1 \tag{2.3.17}$$

Within the framework of free electrons, the optical properties of TCO can be described by the Drude theory. The electric conductivity σ is also defined as the response of free charge carriers in metallic materials to the electric component of an electromagnetic field. This establishes the relationship between current density and electric field:

$$\mathbf{J} = ne\mu\mathbf{E} = \sigma\mathbf{E} \tag{2.3.18}$$

In classical mechanics, current is generally defined as the flow of charged particles with charge e through an elemental surface per unit time. The expression for current density **J** derived from this definition is:

$$\mathbf{J} = -ne\mathbf{v} \tag{2.3.19}$$

Here, **v** represents the statistical average velocity of electrons. The Drude theory describes electrons in conducting materials as a collection of free and independent particles, neglecting electron-electron interactions. According to this theory, electrons oscillate in response to an time-dependent electric field **E** while undergoing collisions with lattice ions during their motion. The collision probability is proportional to the average time between two collisions. The dynamics of electrons can be described by the following Newton's equation:

$$\frac{d\mathbf{p}}{dt} = -\frac{\mathbf{p}}{\tau} - e\mathbf{E} \tag{2.3.20}$$

Where, $\mathbf{p} = m^*\mathbf{v}$ is the average momentum of electrons under the electric field, and τ is the average time between two collisions (relaxation time). By incorporating the aforementioned current density relationships, For the specific case of ITO $m^* = 0.35m_e$, with m_e the electron mass. The free electrons motion equation can be written as:

$$\frac{d\mathbf{J}}{dt} + \frac{\mathbf{J}}{\tau} = \frac{ne^2}{m^*}\mathbf{E} \tag{2.3.21}$$

Writing the frequency-dependent relation from **Equation** 2.3.18 $J(\omega) = \sigma(\omega)E(\omega)$, we derive the dynamic conductivity $\sigma(\omega)$:

$$\sigma(\omega) = \left(\frac{ne^2}{m * \varepsilon_0}\right)\left(\frac{1}{1 + i\omega\tau}\right) \tag{2.3.22}$$

Introducing the Maxwell-Ampere equation:

$$\nabla \times \mathbf{H} = \mathbf{J} + i\omega\varepsilon_0\varepsilon_r\mathbf{E}(\omega) \equiv i\omega\varepsilon_0\varepsilon(\omega)\mathbf{E}\ (\omega) \tag{2.3.23}$$

The frequency-dependent dielectric function $\varepsilon(\omega) = \varepsilon_1(\omega) - i\varepsilon_2(\omega)$ is:

$$\varepsilon(\omega) = \varepsilon_r - \frac{\sigma_0\tau}{1 + \omega^2\tau^2} - i\frac{\sigma_0}{\omega(1 + \omega^2\tau^2)} \tag{2.3.24}$$

where ε_r is the relative permittivity of the TCO lattice, for ITO $\varepsilon_r = 4$, and $\sigma_0 = \dfrac{ne^2\tau}{m^*\varepsilon_0}$ is the dc conductivity. The real and imaginary parts of the frequency-dependent dielectric permittivity are given:

$$\varepsilon_1 = \varepsilon_r - \frac{\sigma_0 \tau}{1+\omega^2\tau^2} \tag{2.3.25}$$

and

$$\varepsilon_2 = \frac{\sigma_0}{\omega(1+\omega^2\tau^2)} \tag{2.3.26}$$

The real parts ε_1 of the dielectric permittivity is the difference of two terms, which means that it is zero at some combination of values of the parameters and frequency, the corresponding frequency is known as plasma frequency ω_p:

$$\omega_p = \left(\frac{ne^2}{m^\star \varepsilon_0 \varepsilon_r} - \frac{1}{\tau^2}\right)^{1/2} \tag{2.3.27}$$

In TCO, the plasma wavelength λ_p, which corresponds to the plasma frequency ω_p, divides the optical properties (**Figure** 2.11.**b**). At wavelengths shorter than λ_p, free electrons cannot respond to the electric field, and the material behaves like a transparent dielectric, and the optical absorption is given by the $\alpha = \dfrac{4\pi k}{\lambda}$. At wavelengths longer than λ_p, TCO reflect and absorb (intra-band) the incident radiation. For most TCO materials, the plasma frequency is in the NIR region of the spectrum ($\lambda_p > 1$ μm).
For ITO in the limit of high electron density (n > 10^{21} cm^{-3}) and high mobility ($\mu > 20$ cm^2.V^{-1}.s^{-1}), $\dfrac{ne^2\tau^2}{m^\star\varepsilon_0} \gg 1$, then, the plasma frequency becomes:

$$\omega_p = \left(\frac{ne^2}{m^\star \varepsilon_0 \varepsilon_r}\right)^{1/2} \tag{2.3.28}$$

The **Equation** 2.3.28 means that for a TCO film to be non-reflective to light of wavelength λ ($\omega_p < \dfrac{2\pi c}{\lambda}$), the electron density n must satisfy the following relation:

$$n < \frac{4\pi^2 m^\star \varepsilon_r}{\mu_0 e^2 \lambda^2} \tag{2.3.29}$$

ε_1 and ε_2 are related to the optical constants and by the following two equations:

$$\begin{cases} \tilde{n} = n - ik \\ \tilde{n}^2 = \varepsilon_1 - i\varepsilon_2 \equiv \varepsilon \end{cases} \Longrightarrow \begin{cases} \varepsilon_1 = n^2 - k^2 \\ \varepsilon_2 = 2nk \end{cases} \tag{2.3.30}$$

where ñ is the complex refractive index and n the refractive index **Equation** 2.3.30 may be used to obtain expressions for the refractive index and the extinction coefficient:

$$\begin{cases} n = \sqrt{\frac{1}{2}(\varepsilon_1^2 + \varepsilon_2^2)^{1/2} + \frac{1}{2}\varepsilon_1} \\ k = \sqrt{\frac{1}{2}(\varepsilon_1^2 + \varepsilon_2^2)^{1/2} - \frac{1}{2}\varepsilon_1} \end{cases} \tag{2.3.31}$$

Figures 2.13 and 2.14 shows the modelled reflectance, transmittance, and absorption of a 100-nm-thick film of the modelled material.

The reflection coefficient R in the equation (2.3.17) at an interface between an ITO layer and free space can be calculated from n and k (2.3.31) using the Fresnel relation:

$$R = \frac{(n-1)^2 + k^2}{(n+1)^2 + k^2} \tag{2.3.32}$$

Figures 2.13**.a** and 2.13**.b** show the reflection and transmission coefficients of a 100 nm thick ITO film, modelled as a function of electron mobility and density values. The reflection coefficient R (Figures 2.13**.a**) is determined from **Equation** (2.3.32) and the transmission coefficient T is computed from **Equation** (2.3.12). The increase of charge density leads to a shift of the reflection wavelength onset, which corresponds to a shift of λ_p (increase of plasma frequency ω_p) to short wavelengths, resulting in a degradation of optical transmission in the NIR region, see Figures 2.13**.b**.

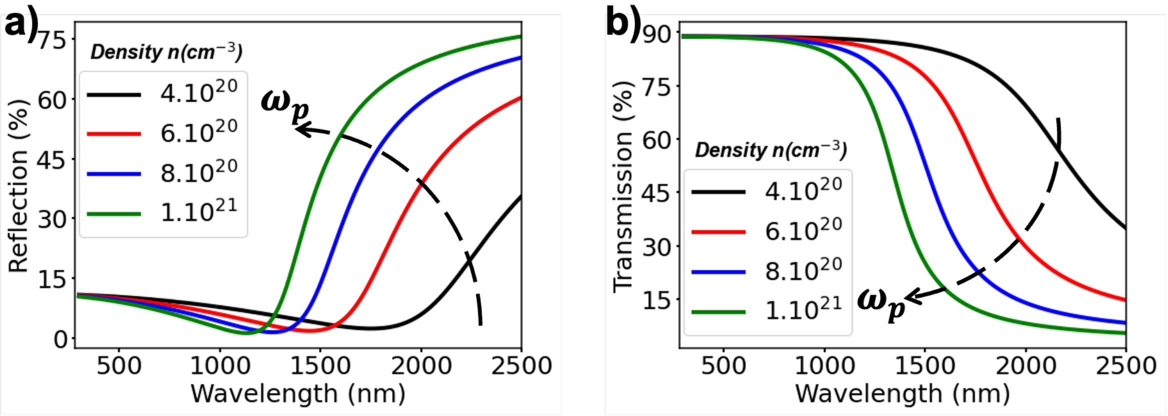

Figure 2.13: Modelled reflection **a)** and transmittance **b)** of ITO film as function of wavelength and various electron density . The effective mass was 0.4m$_e$, the permittivity was ε_r=4, and mobility was 50 cm^2.V^{-1}.s^{-1} and the film thickness was taken as 100 nm

We show the absorption as a function of carrier concentration in Figure 2.14**.a**, the absorption peak shift to shorter wavelengths and the height of the absorption band increases as the carrier concentration increases, leading to a degradation of the transmission. On the other hand, the variation of mobility does not affect the position of the absorption peak, but absorption decreases with increasing electron mobility (Figure 2.14**.b**).

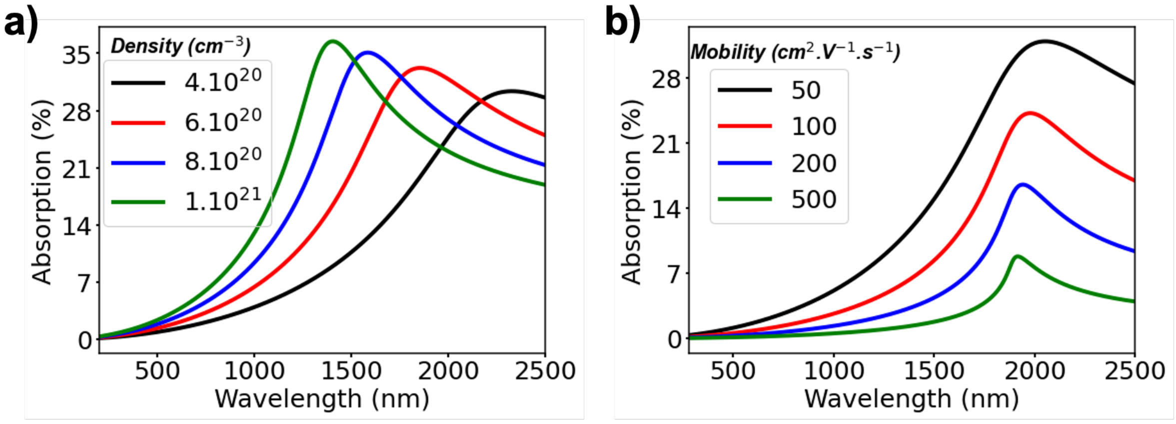

Figure 2.14: Modelled ITO absorption as a function of wavelength: **a)** with different electron densities, electron mobility was 50 cm^2.V^{-1}s.$^{-1}$; **b)** with different variable electron mobility, the carrier density was 5×10^{20} cm^{-3}. The effective mass was 0.4m$_e$, the permittivity was ε_r=4 and the film thickness was fixed at 100 nm.

This result has an important consequence when highly transparent films with very low sheet resistance Rs are required at specific wavelength. Figure 2.14**.a** and **b** shows that this is best achieved by increasing mobility μ rather than the free carriers density n, since increasing n leads to an increase of the absorption as plasma frequency increases. For example, if the mobility could be doubled while maintaining a high n, then assuming that $\mu > 10$ cm^2.V^{-1}s.$^{-1}$ initially, a film could in principle be grown to twice the thickness while maintaining the same optical transmission; therefore, Rs for this film could be reduced by a factor of four, which is a very significant result illustrating the importance of maximising μ . This could be achieved by improving the processing conditions of the film so that μ approaches its intrinsic limit, which is less than 100 cm^2.V^{-1}s.$^{-1}$ for ITO films due to ionised impurities scattering[91].

2.3.2.4 Transparent electrodes: figure of merit

Since there is a trade-off between the optical transmission and conductivity of TCO, the quality of a transparent electrode can be evaluated using performance metrics commonly known as figures of merit (FOM). These figures of merit define the trade-off between conductivity and optical transmission. The best known and most widely used figure of merit is the Haacke figure [110], which is given as a function of transmission T and the sheet resistance $R_\square$ by the following equation:

$$\Phi = \frac{T^x}{R_\square} \tag{2.3.33}$$

Values of x equal to 10, 20 and 100 correspond to transmittances of 90%, 95% and 99% respectively. This method is used in the literature with x = 10 to characterise ITO thin films. This FOM is more suitable for optoelectronic applications, because it favours the optical transmittance of the film while taking into account its resistivity. Φ is expressed in Ω^{-1} and high values indicate good quality TCO film. Gordon[111] proposed another index, independent of film thickness, based on sheet resistance $R_\square$, total visible transmittance T and total visible reflectance R.

$$\Phi \approx \frac{\sigma}{\alpha} = -\left[R_\square ln(T+R)\right]^{-1} = \frac{4\pi\varepsilon_0 c^2 n(m^*\mu_e)^2}{(\lambda e)^2} \tag{2.3.34}$$

where ε_0 is the permittivity of free space, c is the speed of light in vacuum, n is the refractive index of the film, m^* is the effective mass of the conduction electrons, μ_e is the mobility, λ is a visible wavelength of light, and e is the electronic charge. In the literature,very different values for the merit factor are given for ITO, depending on the film processing conditions, Haccke's formula gives values of the order of 10^{-4} to 10^{-1} Ω^{-1} [112, 113] and Gordon's equation gives values of the order of 1-10 Ω^{-1} [111]. These FOM are based solely on the optical transmission and conductivity of TCO. However, structural properties such as film composition and impurities type, morphology and uniformity of film thickness are also important. All these factors are influenced by the process parameters of the different various methods. In addition to these qualities, other criteria such as etching properties, production cost, toxicity, mechanical hardness (flexible devices), thermal and chemical stability may influence the choice of a TCO. For some applications, another important criterion when choosing a transparent electrode is its work function. For metals, the work function is clearly defined as the energy required to remove an electron from the Fermi level to the vacuum level (energy difference between the Fermi level and vacuum level). This definition is still correct in the case of degenerate semiconductors, which is generally the case for TCO and particularly for ITO, However, for a non-degenerate semiconductor it is ambiguous since there are no electrons at the Fermi level. We therefore consider the work function of a semiconductor to be the energy required to extract an electron from its surface and move it away from the material, so that the interaction between the extracted electron and the material becomes negligible. See the book by M. Yoshitake[114] (page 7 to 21) for illustration of these definitions. We will refer to the latter definition when we talk about semiconductors based on transition metal oxides (NiOx and MoOx). There are several techniques for determining the work function value, the most widely used being UPS, but it is very sensitive to the measurement conditions and surface preparation, which may explain the discrepancies

in work function values observed in the literature for certain semiconductors (typical case of transition metal oxides). Another technique is the use of MOS capacitance, which is well suited to determining the work function of metals or degenerate semiconductors. We will discuss these different methods in the next section.
Gordon's work [111] provides an overview of the figures of merit for basic TCO and criteria for choosing a transparent electrode depending on the intended application.

2.4 Hole extraction materials, metal oxides for PbS QDs devices

2.4.1 Transition metal oxides and HTL

In numerous optoelectronic devices based on QDs, perovskite or organic semiconductors such as photodiodes, LEDs or solar cells, hole extraction or transport layers (HTL) play an essential role in the efficient collection and transport of charges. In the photodiode structures we studied, the HTL and ETL layers are inserted between the electrodes and the photosensitive material to control the electrons and holes transport. The ETL must facilitate the passage of electrons and block holes, while the HTL must facilitate the transfer of electrons and block holes. Therefore, they help reduce contact resistances at the interfaces between the different materials making up these devices, and the dark current of devices. The choice of HTL depends on a number of factors, including the specific device architecture, the ability of band levels alignment, and charge transport properties, which can influence the efficiency and stability of the device. It is therefore important to take these factors into account and optimise the device design accordingly. HTL play a central role in efficient hole extraction and transport from the HTL/active interface to the anode TCO/HTL interface, thereby increasing device efficiency. To achieve high-performance devices, materials used for HTL need to have specific characteristics, including a high WF matching the VBM energy level of the donor material and the anode (HTL) energy level, transparency to increase light absorption by the active layer, high hole mobility to reduce charge accumulation and recombination, a large band gap to block electron carriers, and chemical resistance to external factors[115].
Initially, organic semiconductors or conductive polymers such as PEDOT:PSS (poly(3, 4 - ethylenedioxythiophene) polystyrene sulphonate) were used as HTL because of their high conductivity and ease of synthesis in solution[116, 117]. However, organic materials are not an ideal HTL due to their inefficient electron-blocking capability, corrosive nature and hygroscopic behavior, which limit their use in many devices [118, 119]. In particular, the low work function (WF) of PEDOT:PSS (about -5.0 eV) can lead to the formation of labile and mismatched energy level alignments with the active layer (e.g 4.8 - 5.4 eV for PbS QDs films depending on the cross-linkers), resulting in poor device performances[120, 121, 122, 123].
Due to these limitations, other HTL materials have been developed. High work function transition metal oxides are now recognised as efficient HTL in a variety of devices including photodiodes, OFETS and solar cells. These oxides can efficiently extract holes from the PbS QDs layer[11] and facilitate their transport to the electrode. They provide good charge selectivity and can enhance the overall device performance. Metal oxides offer chemical and electronic properties that can be adjusted (wide range work functions) to enable charge exchange with a wide variety of semiconductors. The ability of two materials to exchange charges requires a close alignment of donor and acceptor states of either material. The Figure 2.15.**a** shows an ideal band alignment between a QDs film and a HTL for efficient charge extraction from holes and electron blocking. The example of energy level diagram of an oxide/semiconductor interface revealed by photoelectron spectroscopy is illustrated in Figure 2.15.**b**[124]. Important parameters for energy level alignment, such as the oxide's work function ϕ, the vacuum level, the VBM, the energy level offset ΔE_H, and the ionization energy of the active layer IE. Roughly speaking, one of the goals of HTL optimization is to reduce the energy mismatch ΔE_H.

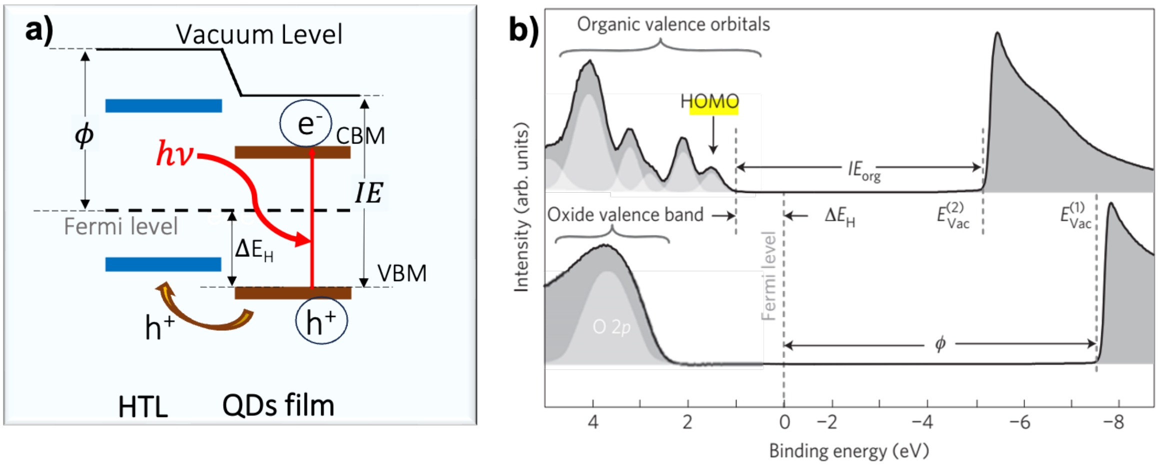

Figure 2.15: Energy levels at oxide-semiconductor interfaces: **a)** picture of suitable energy-level alignment between QDs film and the HTL, **b)** schematic energy-level diagram of an oxide-active layer (organic semiconductor 2T-NATA) interface revealed by UPS.

In recent decades, much work has gone into understanding energy alignment in devices such as OLEDs, solar cells, and photodiodes. Metal/organic interfaces were the first to be considered. Researchers initially assumed that vacuum levels align at the interface. They therefore assumed that the difference between the work function of a metal and the CBM and VBM levels of the semiconductor would determine the charge extraction barriers. The researchers soon realised that the vacuum levels rarely align[125], and the role of the work function in energy alignment became uncertain. Several developments of the interface energy alignment model emerged, such as the Fermi level pinning at the interface (alignment between the VBM and the Fermi level remains constant as the electrode work function increases), the concept of induced density of interface states, interfacial dipoles[126], the push-back or pillow effect[127], the concept of the charge neutrality level[128] and charge transfer model[129]. These concepts help reconcile some of the initial discrepancies in the energy alignment model, but they are not all consistent with each other. Although many scientists and engineers commonly use the work function as an assessment of energy alignment, the reason for doing so is often considered self-evident. The way in which energy alignment is established remains uncertain, and no comprehensive and quantitative predictive model has been developed.

Work function was initially considered to affect energy alignment only in the sense that it determines the positions of the valence and conduction bands of an oxide relative to the vacuum level. Many of the concepts developed for energy alignment at metal/organic semiconductor interfaces are not necessarily valid for semiconductor interfaces with metal oxides. For example, most oxides do not have electronic states at the Fermi level that allow charge exchange. Charge transfer must therefore generally take place via the valence or conduction bands of an oxide[130]. Indeed, several works have convincingly shown that electrons can transfer from the VBM of a semiconductor to the low conduction bands of some d^0 oxides (the spectroscopic notation d^x simply refers to the filling of the core level d of the main metal that makes up the oxide), such as MoO_3 and WO_3[131]. This has led many to believe that the energy alignment characteristics of MoO_3 and WO_3 are the result of their low conduction bands. Although a Fermi-level-pinning transition had been demonstrated previously[132], it was unclear whether this trend was truly universal, as it had been demonstrated using a limited set of samples prepared ex-situ. Later Greiner et al demonstrated, using a wide variety of oxides prepared in-situ, that such a Fermi-level-pinning alignment transition is a universal trend, and that it is the result of an energy alignment principle for non-reactive oxides[124]. This trend is observed with large variety of semiconductor materials. It is generally assumed that, for an electron to move from a semiconductor to an oxide, it must move from the VBM level of the semiconductor to the conduction band of the oxide, and that the conduction band position of an oxide should therefore be very important for energy alignment. However, the tendency towards Fermi pinning level implies that energy levels alignment can occur independently of the oxide's conduction and valence band positions.

Understanding and optimising band alignment requires a knowledge of the electronic properties of transition metal oxides.

The main factor controlling the electronic structures and properties of transition metal oxides is d-band occupancy, consequently, transition metal oxides can broadly classified into different classes[133, 134]. We focus only on some of the oxides with high work function, while noting that there are other oxide families such as TiO_2, ZnO or ZrO_2 with relatively low work function and they are generally used as electron transport layers.

The different kinds of materials are the following

n-type d^0 oxides with a wide band gap like MoO_3, V_2O_5, WO_3 are insulators in their stoichiometric forms, but they naturally tend to be n-type materials due to the presence of oxygen vacancy defects[11, 135]. Their conduction band minima are mainly composed of empty metal d states, and their valence band maxima are mainly composed of O 2p states.

Sub-stoichiometric (defective) n-type oxides: MoO_{3-x}, WO_x, V_2O_{5-x} and CrO_{3-x}: This is the subset of oxygen-deficient d^0 oxides. Oxygen vacancies generate a high density of occupied defective states close to the Fermi level as in In_2O_3-based TCO, which makes these oxides n-type semiconductors. The defect states arise from the filling of empty metallic d-states and can be observed in the valence band XPS spectra.

p-type semiconducting oxides like Cu_2O, Cr_2O_3 are oxides whose d-bands are completely filled (d^{10} oxides). They tend to be semiconductors because of the gap between the d band and the next higher energy band (generally derived from the metal's **s** orbitals).

Conductive metal oxides: MoO_2, WO_2: Oxides whose d-bands are partially occupied, but with a low number of electrons (d^1, d^2 and d^3). These oxides tend to form when the d^0 oxides are chemically reduced. They are n-type semiconductors (with high electrical conductivity) with the presence of a density of states near the Fermi level observable in the valence band XPS spectra.

p-type Mott-Hubbard insulators: CuO, NiO: Oxides whose d-bands are partially occupied by a large number of electrons (d^7, d^8 and d^9): These oxides tend to be Mott-Hubbard/charge-transfer insulators because of their strong electronic correlation [136, 137]. Their electronic properties are dominated by electron-electron correlations. The valence photoemission spectra of these oxides are not as simple to interpret as those of $d^{x} oxides$ $(0 \leq x \leq 4)$, because there is often significant hybridisation between the d states of the metal and the p states of the oxygen, so that it is not easy to divide the valence density of states between the d regions of the metal and the p regions of the oxygen. Their electronic properties cannot be correctly predicted by the simple independent electron model because of the strong Coulomb repulsion between electrons and site exchange interactions. These materials, which should be metallic conductors according to the independent electron model, are instead insulators. In the Mott-Hubbard model, d-electrons localise to metal cations because of a strong repulsion energy in narrow d-bands. Conduction occurs via d-electrons jumping from one metal site to another, and the Coulomb repulsion and exchange interactions introduce an energy penalty for the placement of two d-electrons on the same site. The presence of vacant states at energy levels slightly higher than the most occupied state is a characteristic of metallic materials.

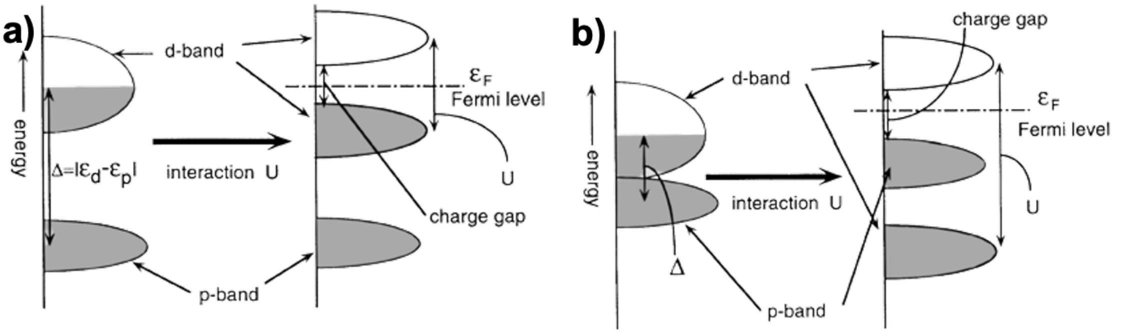

Figure 2.16: Schematic illustration of energy levels for (a) a Mott-Hubbard insulator and (b) a charge-transfer insulator generated by the d-site interaction effect[137].

However, Coulomb repulsion increases the energy of the lowest unoccupied state, resulting in the formation of an energy gap in the d-band, leading to the lower and upper Hubbard bands, separated by the Hubbard term U (see Figure 2.16.**a**). Strong electronic correlation can also give rise to charge transfer insulators, where the lowest energy excitation involves a transition from a ligand site to a metal site, such as from oxygen to a metallic d-state. The energy required to excite an electron from the highest occupied state of an oxygen atom to the lowest unoccupied d state of the metal is represented by the charge transfer term Δ. If the Hubbard shift U is much larger than the charge transfer energy Δ, as shown in Figure 2.16.**b**, the oxide is considered to be a charge transfer insulator, rather than a Mott-Hubbard insulator[137].
Similar to how the n-type conductivity of d^0 oxides is attributed to oxygen vacancies, the p-type nature of these oxides is commonly accepted to be due to the presence of cation vacancies or cation-substituted oxygen atoms, these defects behave as electron acceptors[138]. We will restrict ourselves to the case of MoO_3 with $0 < x \leq 3$ and NiOx. MoOx is chosen first, as it is considered to be the n-type metal oxide with the highest work function[139] and by far one of the most widely used HTL materials. As for NiO_x, it is the HTL of reference in solar cell devices, it is p-type and may have a different hole extraction mechanism to MoO_x. In the following sections, we will present their electronic structures, structural, electrical and optical properties.

2.4.2 Molybdenium oxide (MoO_x)

2.4.2.1 Molybdenum oxide structural properties

Molybdenum (Mo: $[Kr]4d^5 5s^1$) can form two stable binary oxides, namely MoO_3 (Mo: $4d^2$ oxidation state VI+) and MoO_2 (Mo: $4d^0$ oxidation state IV+). The sub-stoichiometric oxides MoO_x ($2 \leq x \leq 3$), initially considered as p-type semiconductors, are now well known as n-type semiconductors. Molybdenum oxide in its stoichiometric form MoO_3 can crystallise in two forms. The thermodynamically stable α-MoO_3 phase has an orthorhombic crystal structure (Figure 2.17.**a**), with lattice parameters a=3.963 Å, b= 13.855 Å, c=3.699 Åand belongs to the space group Pbnm. It has a layered structure perpendicular to the vertical b-direction and linked together by non-covalent van der Waals bonds, resulting in stratification. Internal interactions in octahedra are dominated by strong covalent and ionic bonds. The layers consist of an atomically thin bilayer about 0.7 nm thick. Each bilayer consists of two sub-layers of deformed MoO_6 octahedra. The distance between Mo atoms in two layers is 1.4 nm[140]. The planar sheets of double-layered MoO_6 octahedra are arranged in a zigzag pattern of shared edges along the c-direction and shared corner rows along the a-direction. The metastable β-MoO_3 phase (Figure 2.17.**b**) has a monoclinic crystal structure with lattice parameters a=7.122 Å, b= 5.366 Å, c=5.566 Åand $\alpha = \gamma = 90$, $\beta = 91.990°$ (space group $P2_1/c$), similar to that of ReO_3 or WO_3, with MoO_6 octahedra sharing corners in all three dimensions. Unlike α-MoO_3, MoO_6 octahedra in the β-MoO_3 crystal structure do not form double layers and do not form zigzag rows along the plane [001]. The lack of plane formation in β-MoO_3 makes it non-layered. On each octahedron, the central Mo(VI+) cation is surrounded by six oxygen atoms that occupy three crystallographically non-equivalent sites (Figure 2.18). These are the single-coordinated O(1) oxygen, the double-coordinated O(2) oxygen and the triple-coordinated O(3) oxygen. Each O(1) oxygen is linked to a single Mo atom by a very short Mo-O bond of 1.67 Å. The O(2) oxygen is doubly co-ordinated and located asymmetrically between two Mo centres with bond lengths of 1.73 and 2.25 Å. Finally, oxygen O(3) is symmetrically located between two Mo centres in one sub-layer with a bond distance of 1.94 Å and is also connected to another Mo centre in the other sub-layer with a bond length of 2.33 Å [135]. Monoclinic MoO_2 has a distorted rutile structure. Oxygen vacancies in MoO_x can be controlled during fabrication processes or can be created by the reduction of higher oxides (annealing in a controlled atmosphere). Oxygen vacancies play a crucial role in modifying the electronic and optical properties of semiconducting oxides. Band gap states caused by oxygen vacancies have been identified in single crystals of MoO_3 (structural defect). Oxygen vacancies are energetically more favourable than Mo vacancies and can induce gap states in the MoO_x band gap, which is exploited for band engineering in devices such as solar cells, LEDs or photodiodes. Various synthetic methods have been used to produce sub-stoichiometric molybdenum oxide with oxygen vacancies. In our study, we will use reactive plasma deposition to produce amorphous sub-stoichiometric oxides. Amorphous MoO_x also features the octahedral building block, connected by vertices to their six neighbouring octahedra, similar to that of amorphous tungsten oxide[142, 143].

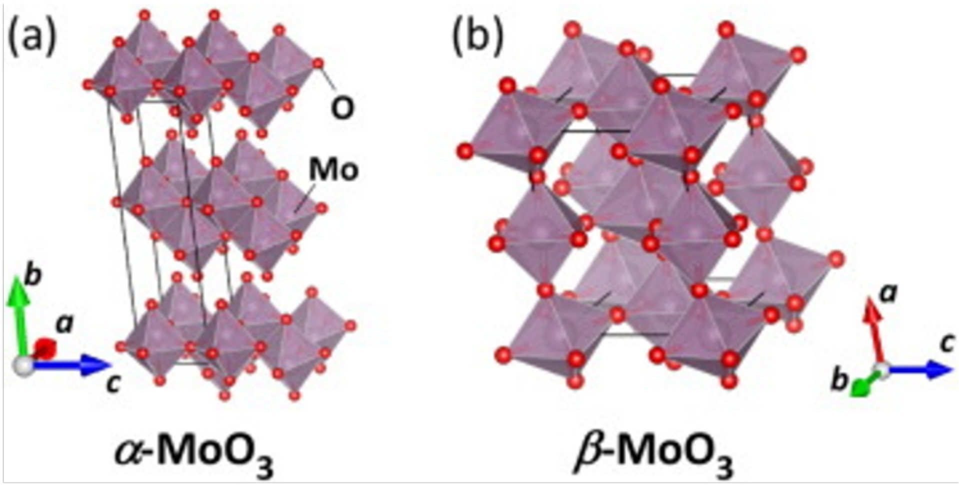

Figure 2.17: Schematic illustration of crystal structures of (a) orthorhombic layered α-MoO_3, and (b) monoclinic distorted-ReO_3-like β-MoO_3. The gray and red balls correspond to Mo and O atoms, respectively. The black lines show each unit cell[141]

In practice, stoichiometric molybdenum oxides are the most widely used, as they provide the best performance devices. Although hole extraction requires materials with a large work function, *Greiner et al* have shown that efficient hole extraction is not obtained with MoO_3, but with $MoO_x(2<x<3)$ which has a smaller work function than MoO_3 [144]. The evolution of work function as a function of stoichiometry will be discussed more clearly in the following sections. Mixed amorphous or crystalline molybdenum oxide structures (known as molybdenum oxide bronzes or Magnelli[145] phases for the crystalline forms) are formed by a mixture of Mo(VI+) and Mo(IV+) as well as intermediate Mo(V+) states. These sub-stoichiometric or mixed forms offer a wide range of electronic, optical and electrical properties. XPS measurements are well suited to determining the stoichiometry of these molybdenum sub-oxides, in particular by analysing the Mo 3d and O 1s spectra. The positions of the peaks and the relative area and theirs full width half maximum (FWHM) provide quantitative information on the stoichiometry of the MoO_x, for example, the binding energy of the peaks increases with the oxidation state of

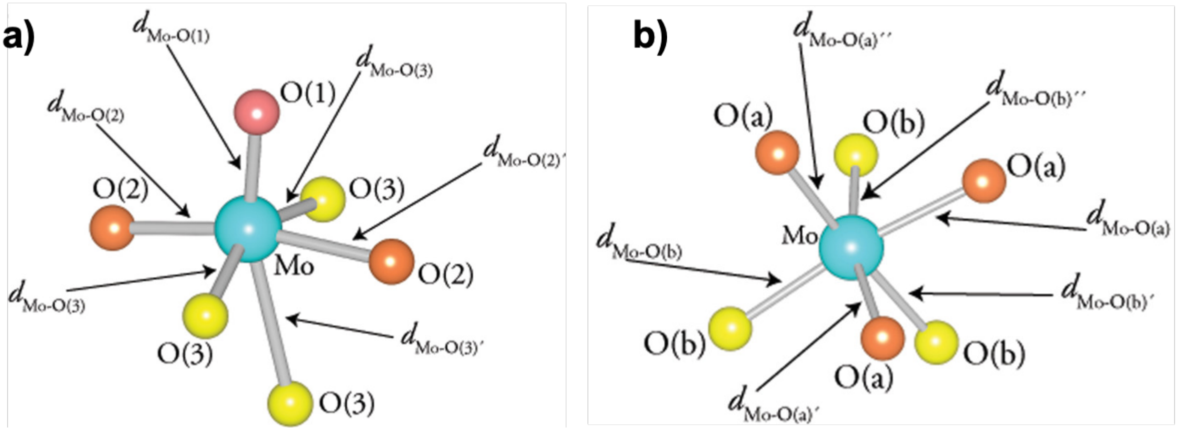

Figure 2.18: Cation coordination in stoichiometric molybdenum oxides, **a)** MoO_6 distorted octahedra of MoO_3 unit cell **b)** MoO_6 distorted octahedra of MoO_2 unit cell[135]

the molybdenum. The band gap states that can be measured in the XPS spectra of the valence band (O 2p) also give an indication of the level of sub-stoichiometry.

2.4.2.2 Molybdenum oxide electronic structure

The electronic properties of molybdenum oxide are highly dependent on its stoichiometry. MoO_3 unintentionally n-type doped wide band gap semiconductor, with a valence band edge around 2.5-3 eV below the Fermi level and a conduction band closer to the Fermi level, with electron affinity greater than 6 eV, and ionisation energy greater than 9 eV [115]. The work function of MoO_x is about WF = 7 eV for x = 3, and this value decreases with the x stoichiometry of MoO_x films. DFT calculations (Perdew-Burke-Ernzerhof method) have shown that the valence band of

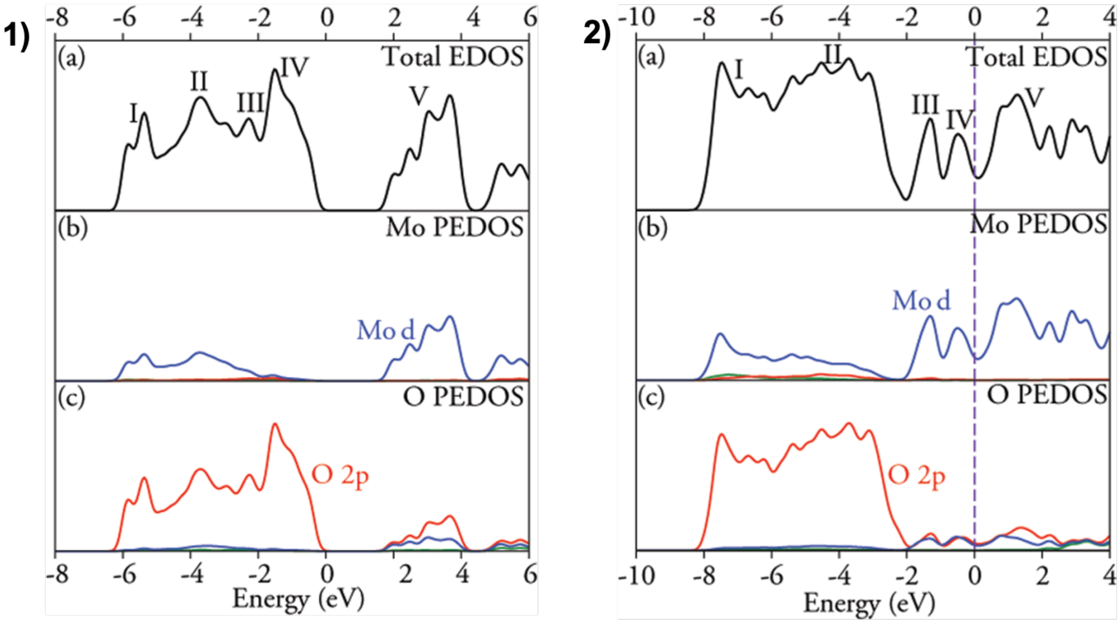

Figure 2.19: Electronic density of states of MoO_3 **(1)** and MoO_2**(2)**, (a) Total EDOS, (b) Mo PEDOS, and (c) O PEDOS. The blue lines represent d states, green s states, and red p states. The dashed line denotes the Fermi energy and correspond to the Γ direction in the first Brillouin zone.[135]

MoO_3 consists of the O 2p oxygen orbitals, while the conduction band is formed by the Mo 4d orbitals (Figure 2.19.**1**). We also note the absence of any electronic state from 0 eV up to about 2 eV. Although this is characteristic of the presence of a band gap, its value is underestimated by this method, and the actual value of the experimental gap has been measured to be well above 3 eV[146]. Recently, ab initio calculations using the hybrid functional and the Becke-Jonhson potential methods have provided a correct calculation of 3 eV for the band gap. The electronic structure of MoO_2 (Figure 2.19.**2**) calculated by DFT (Perdew-Burke-Ernzerhof method) shows a metallic nature, with the presence of Mo 4d states just below the Fermi level and a lack of band gap. The discussion on the metallic nature of MoO_2 remains open in the literature, but when we consider thin films tens of nanometes thick, we can achieve optical transmittances in over 50% in the visible region. If MoO_2 were completely metallic, film thicker than 10 nm would have to be completely opaque to visible and IR light.

2.4.2.3 Molybdenum oxide electrical properties

In most metal oxide-based n-type semiconductors, oxygen vacancies play an important role because they behave as electron donors and contribute significantly to the free electron density. The resistivity of semiconductors depends on the density of N_D^+ ionised donors, structural parameters such as grain size, film thickness and crystalline phases. Therefore, the electrical properties of MoO_x are strongly determined by the x-stoichiometry. Due to the high vacancy density, mobilities are generally very low ($\approx 10^{-2}\text{cm}^2.\text{V}^{-1}.\text{s}^{-1}$) , and resistivity is mainly determined by electron density. The electrical resistivity of MoO_x decreases from MoO_3 to MoO_2. The literature also reports a lower resistivity in the α-MoO_3 phase (10^2 to 10^4 Ω.cm)[147], compared to the β-MoO_3 phase (10^7 Ω.cm)[148]. It should be noted that MoO_3 is rarely used in devices, since the introduction of a certain density of oxygen vacancies is necessary to reduce resistivity and improve charge transport.

2.4.2.4 Molybdenum oxide optical properties

The optical properties of MoO_x films are strongly influenced by their stoichiometry and crystalline structure. Fully stoichiometric MoO_3 films are transparent in the visible and IR light spectrum, similar to insulating materials with a wide band gap, more than 3 eV. In contrast, MoO_2 films, which is semi-metallic in nature, show significant absorption in the visible and IR spectrum. The mixed valence states of MoO_x, which involve the presence of Mo(V+) ions, contribute to the remarkable optical changes observed in the material, such as *chromism* [149, 150] where the yellowish transparent MoO_3 takes on a blue colouration when exposed to ultraviolet light or when small positive ions (Li^+, Na^+, K^+, Cs^+, and H^+) are intercalated, similar to WO_3[143]. These optical changes are closely linked to the electronic structure, where the presence of Mo(V+) states plays a crucial role. The small polaron model[151] is used to explain the chromic response of MoO_x. This model involves oxidation state transitions between neighbouring metal atoms, resulting in an extra electron localised on the reduced metal atom, Mo(VI+) to Mo(V+), causing a local perturbation of the structure, with the system gaining energy (strain energy). When photons of sufficient energy interact with the material, the localised electron can overcome the deformation energy or lattice distortion and transfer to an adjacent metal atom with a higher oxidation state (transferring from the reduced Mo(V+) oxidation state and lattice distortion to this adjacent atom), resulting in colouration[152].

2.4.2.5 Molybdenum oxide stability

The stability of molybdenum oxide is one of the parameters that must be considered when incorporating it into devices. Sub-stoichiometric molybdenum oxide MoO_x (x<3) exhibit very high surface reactivity to oxidizing or reducing atmospheres. Figure 2.20.**a** shows the evolution of the valence band structure (O 2p) of MoO_x deposited by sputtering as a function of air exposure time. The density of states seen below the Fermi level (0 eV) is directly related to the density of oxygen vacancies in the superficial layer of the MoO_x film. This density of states decreases as a function of exposure time, reflecting oxidization of the film surface. Figure 2.20.**b** shows the evolution of the work function measured by UPS (surface analysis method, probing only a few nanometres) as a function of the time exposure to air or oxygen. We also note a strong oxidization of the MoO_x films(deposited by thermal evaporation), resulting in an initial significant increase in the work function of more than 1 eV (shift in Fermi level with n-type doping by oxygen vacancies). The later decrease in work function is a signature of surface contamination by carbon, moisture or other molecules. This degradation of work function due to surface contamination is well-known and generally leads to a deterioration in device performance[154].

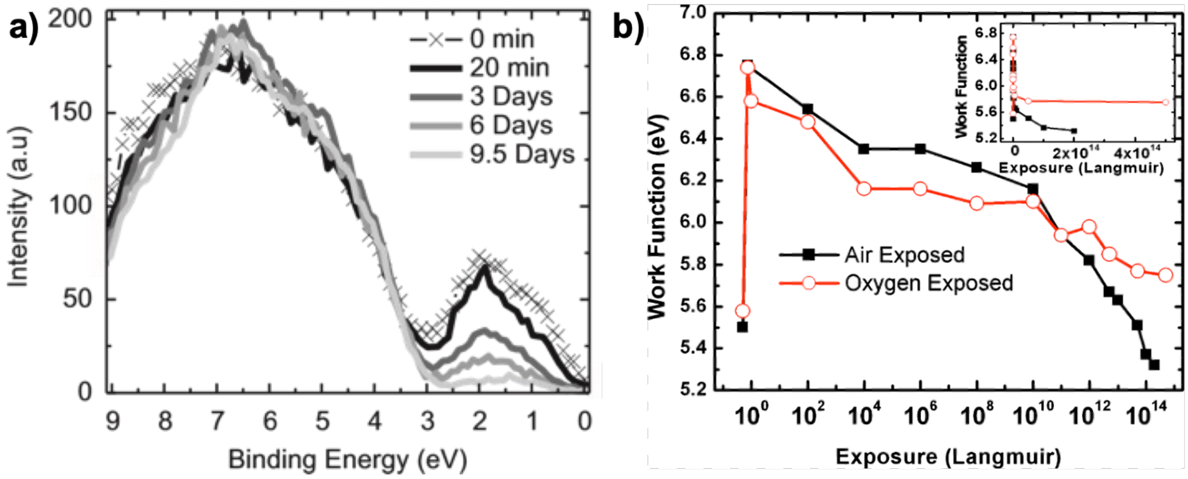

Figure 2.20: MoO_x stability, **a)** Valence band spectra (O 2p) of sputtered MoO_3 films and representative evolution with exposure durations, **b)** The surface work function in eV of thermally evaporated MoO_3 vs air an oxygen exposure[153]

2.4.3 Nickel oxide (NiO_x)

2.4.3.1 NiO_x, structural properties and electronic structure

Nickel oxide (NiO_x or NiO) is a well-studied transition metal oxide with a variety of interesting properties and applications. Due to its unique structural properties, it is widely used as a catalyst, electrode material in lithium-ion batteries and in gas sensors. In addition, because of its electrical and optical properties, NiO_x is of great interest as a new functional material in many electronic and optoelectronic devices. In particular, it is being studied and used as a hole extraction and transport layer (HTL) in organic semiconductor or perovskite-based solar cells and photodiodes. In particular, NiO_x as an HTL has to achieve PCE (power conversion efficiency) record values of over 24% in a single-junction perovskite solar cells[155]. These various applications take advantage of the high work function of NiO_x , which can be tuned to between 5-6.5eV, depending on the material preparation conditions [133, 156, 157]. NiO_x is generally green to black in colour, depending on particle size and charge density or stoichiometry, and appears as a greenish-black powder in its raw form. NiO_x is an antiferromagnetic material (antiparallel alignment of magnetic moments between adjacent nickel ions) with a Néel temperature T_N = 526±3 K. It is also stable at high temperatures, with a high melting point of about 2257 K[158]. NiO_x has different crystalline structures determined by temperature and pressure conditions. At low temperature, NiO_x crystallises in a NaCl-like structure, with Ni^{2+} ions occupying face-centred cubic (FCC) positions, O^{2-} ions occupying the octahedral sites formed by Ni atoms and vice versa [159]. It belongs to the space group ***Fm3m*** with a lattice parameter a = 4.1769 Å.

Conventional band theory, which focuses on the delocalised nature of electrons, cannot be applied to systems with strongly correlated electrons such as NiO_x. In fact the gap between the

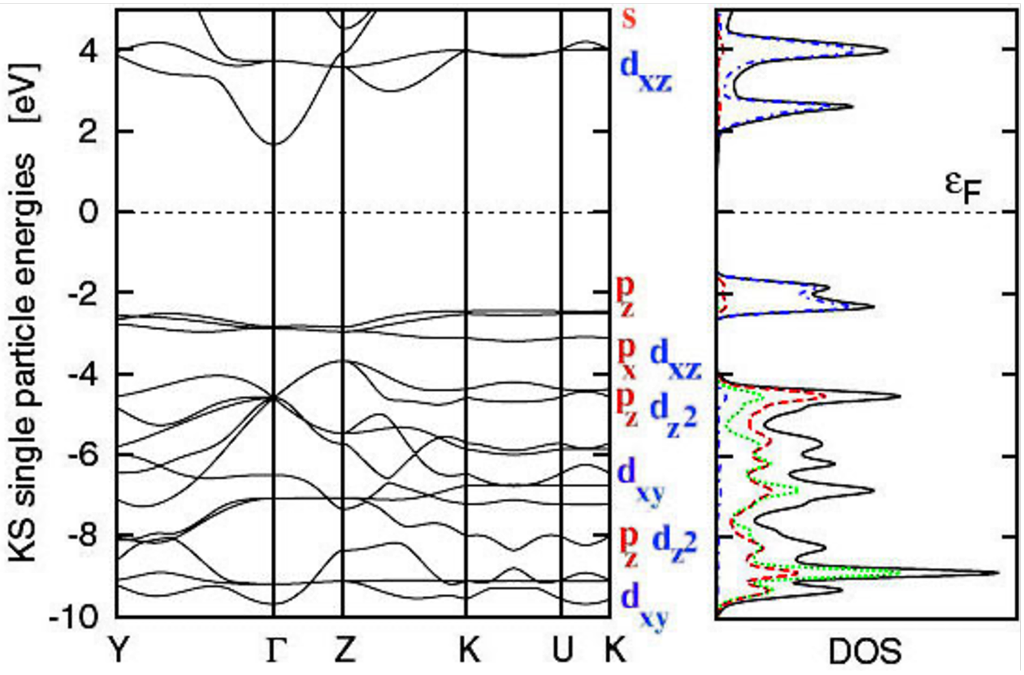

Figure 2.21: Band structure of NiO$_x$ obtained by plane-wave pseudo-potential calculation with the exact exchange in combination with LDA correlation, using the full optimized potential method for the evaluation of the exchange potential. Also shown are the total (solid, black line) and partial densities of states (DOS): O2 p-dashed, red line; Ni 3d with majority ↑-dotted, green line; Ni 3d with majority ↓-dash-dotted, blue line[160].

bands (0.4 eV) is much smaller than the experimental values (> 3 eV). Conventional band theory cannot explain the large gap and predicts that NiO$_x$ is metallic in nature[159, 161]. The electronic structure of NiO$_x$ is complex from an experimental theoretical point of view. Approaches, such as calculations based on the local spin density approximation (LSDA) or the exact exchange technique, have shown better agreement with experimental results, predicting an insulating and anti-ferromagnetic ground state for NiO$_x$, but leading to a smaller gap than the experimental values. More sophisticated techniques have succeeded in reproducing band gap and magnetic moments in agreement with experimental measurements [160, 162, 163, 164]. It should be noted, however, that some results may differ significantly in detail, highlighting the complexity of the system studied and confirming the irrelevance the application of conventional band theory to NiO$_x$. Engel et al calculated a band structure and densities of states (DOS) for NiO$_x$, shown in **Figure** 2.21. They used the exact exchange technique and obtained insulating ground states, predicted band gap and magnetic moments in good agreement with the experiment.

The DOS spectrum (see **Figure** 2.21) shows that the majority-spin d-bands are almost full and the minority-spin d-bands are about half full, and that the direct gap E_g is about 4.3 eV (Centre of the first Brillouin zone or Γ direction), which is in agreement with some photoemission experiments [165]. The optical spectra are defined by the transitions between the p-orbitals of the oxygen ligand and the Ni 3d states, which corresponds to charge-transfer excitation. The maximum of the valence band is dominated by oxygen p-states, while the bottom of the conduction band consists mainly of Ni d-states. So the initial state is the combination of the O 2p and Ni 3d states and the final state is mainly Ni 3d. We also note the presence of d orbitals at the top of the valence band, in the **K** direction of the first Brillouin zone. The singlet at the top of the valence band is almost purely p$_z$, while the degenerate doublet at the top of the valence band comes from hybridisation between (p$_x$, p$_y$), which contribute about 80%, and ($d^{\uparrow}_{xz}$, $d^{\uparrow}_{yz}$), which contribute 20% [164]. Because of this significant hybridisation between the d states of the metal and the p states of the oxygen, so that it is not easy to divide the valence DOS into d regions of the metal and p regions of the oxygen, the interpretation of photoemission spectra (XPS) of the valence band of NiOx is extremely complex. This hybridisation between the p orbitals of the oxygen and the d orbitals of the metal also makes it difficult to quantify the Ni and O atoms using XPS measurements and analyses (more on this discussion in the section on XPS measurements on NiO_x).

2.4.3.2 NiO_x electrical properties

According to the conventional theory of electronic band structure, NiO_x with the external electronic configuration Ni3d^8 O2p^6 should be a metal because of unfilled d-shell, whereas experimentally, NiO_x is a semiconductor or "insulator" with a gap greater than 3 eV (the radius of 3d orbitals $\approx$ 0.6 Å is much smaller than the metal-metal distance $\approx$3 Å, so that the effective d-d hopping which actually goes via an intermediate oxygen is much smaller than the on-site Coulomb repulsion). It is often referred to as a Mott-Hubbard insulator, to indicate that its non-metallic nature is a consequence of the strong electronic correlations between the Ni 3d electrons. In reality it is a charge-transfer insulator and not a Mot-Hubbard insulator. Namely, when the charge transfer energy term Δ between a Ni metal d-site and an oxygen ligand p-site ($d^n p^6$ to the excited configuration $d^{n+1}p^5$) is greater than the Hubbard term U (Coulomb repulsion between electrons on neighbouring atomic orbitals), the electrons remain localised on the atomic sites, resulting in an absence of electrical conduction [166].
Recall **Figure.**2.16, this type of transition-metal oxide where $\Delta = |\varepsilon_d - \varepsilon_p|$ is assumed to be larger than U is called a Mott-Hubbard insulator. Because of $U < \Delta$, the charge gap in the Mott insulating phase is mainly determined by U. On the other hand, if $\Delta = |\varepsilon_d - \varepsilon_p|$ is smaller than U, the charge excitation in the insulating phase is mainly determined by the charge-transfer type where an added hole in the material mainly occupies the oxygen-ps band. The importance of the oxygen-ps band in this class of material is pointed out by Fujimori et al[167]. This type of compound is referred to as the charge-transfer insulator [168].
The room temperature resistivity values of NiO_x films reported in the literature vary by several orders of magnitude depending on the defect densities and the preparation methods used to fabricate the films[169]. The Hall mobility of holes in NiO_x films varies from 10^{-1} to 10^2 $cm^2V.^{-1}.s^{-1}$. NiO_x is considered to be one of the transition metal oxides with good electrical properties compared with d^0 oxides and others.

2.4.3.3 NiO_x optical properties

Like most transition metal oxides, NiO_x has a defective structure, generally an excess of oxygen and Ni [170], leading to the oxidation of Ni^{2+} to Ni^{3+}. These defects behave as acceptors (p-type doping) and lead to a shift Fermi level close to the valence band maximum, so NiO_x is considered to be a p-type semiconductor with an optical gap > 3eV. NiO_x is a transparent material in the visible and IR. The optical absorption is due to p-d transitions in Ni atoms or d-d transitions between two adjacent Ni atoms[171, 172]. Absorption increases with defect density, and experimentally a visual darkening of NiO_x films deposited on glass is observed with increase oxygen concentration.

Chapter 3

Processes and characterizations

3.1 Vacuum thin film synthesis methods

3.1.1 Overview of the different vacuum thin film deposition methods

There are several vacuum deposition methods to obtain thin films with specific properties such as thickness, chemical composition and crystalline structure. Each of these methods has its advantages and limitations, and the choice of method depends on several factors such as industrial constraints (vacuum operation, need for cooling systems, deposition time or speed, cost of deposition, etc.), the desired properties of the thin film and the target materials.

Thin film synthesis methods can be grouped into two main groups, chemical vapour deposition (CVD) and physical vapour deposition (PVD). PVD includes a variety of vacuum processes in which thin films are produced by condensing a vapour of the desired chemical composition onto the substrate. There are a large number of PVD processes[173], including:

Sputtering (DC/RF) with/without magnetron

This technique uses a plasma to eject atoms from the target material (cathode) by bombarding them with ions. The ejected atoms are then deposited on the substrate, forming the thin film. It offers the possibility of relatively easy sputtering of materials with very high melting points and high densities. Any type of material (conducting, semiconducting or insulating) can be deposited on any type of substrate (insulating or conductive), at low or high temperatures. This technique is also considered "environmentally friendly", as it generally generates less chemical and toxic waste. On the other hand, costs are high because reactors are expensive, targets must be cooled due to high-energy ion bombardment, and deposition rates are relatively low.

Ion beam sputtering (IBD)

IBD, also known as ion beam sputtering, is an advanced thin film deposition technique based on the acceleration and focusing of ions onto a solid target. In this process, an ion beam is generated by electric or magnetic fields to accelerate the ions.

These ions are directed on a solid target, where they impact the surface with sufficient energy to eject atoms from the target. These ejected atoms form a stream of particles that deposit on a substrate to form a thin film. The IBD technique offers precise control over the composition, thickness and structure of the thin film by modulating ion beam parameters such as energy and angle of incidence.

Thermal evaporation (by joule effect, electron beam or electric arc)

In this method, the starting material (in solid form) is heated in a vacuum environment so that it sublimes. The atoms or molecules released in the process are deposited on the substrate, where they form a thin film.

Pulsed Laser Ablation (PLD):

Pulsed laser deposition (PLD) is a growth technique in which photonic energy is coupled to the bulk starting material via electronic processes. An intense laser pulse is focused onto a solid target, where it is partially absorbed. Above a certain power density, significant material removal occurs in the form of an ejected luminous plume (plasma). The threshold power density needed to produce such a plume depends on the target material, its morphology, and the laser pulse wavelength and duration. Material from the plume is then re-condensed on a substrate, where film growth occurs. The growth process may be supplemented by a passive or reactive gas or ion source, which may affect the ablation plume species in the gas phase or the surface reaction, in which case one talks of reactive PLD [174, 175]. Pulsed laser deposition preserves the intrinsic properties of the target material in the deposited layer, it enables precise control of thickness, composition, and crystallinity.

Additionally, molecular beam epitaxy (MBE) can be added:

Molecular Beam Epitaxy (MBE) refers to the technique of epitaxial growth of semiconductor compound films by a process involving the reaction of one or more thermal molecular beams with a crystalline surface under ultra-high vacuum conditions. The MBE technique is related to vacuum evaporation, but offers much improved control of the incident atomic or molecular fluxes so that sticking coefficient differences may be taken into account, and allows rapid changing of beam species. MBE is widely used in devices requiring precise control of crystal growth (such as semiconductor lasers) to achieve optimal performance [176]. For example, MBE can be used to produce 'superlattice' structures consisting of many alternating layers of GaAs and $Al_xGa_{1-x}As$ with layer thickness as low as 10 Å[177].

The other major family of thin film synthesis is Chemical Vapor Deposition (CVD), encompassing all deposition techniques where one or more chemical compounds, referred to as precursors, react and/or decompose on a substrate to produce the desired deposit with specific properties [173]. CVD processes can be carried out at low or atmospheric pressure. In some cases, plasma or light is used to activate certain reactants or initiate specific chemical reactions, known as Plasma Enhanced CVD (PECVD) and Photo-CVD (Photon-enhanced CVD), respectively. PECVD or Photo-CVD allows for reduced temperatures and increased deposition rates. Additionally, the family of CVD techniques includes Atomic Layer Deposition (ALD). ALD is a sophisticated thin film deposition technique that enables extremely precise control over the thickness, composition, and structure of deposited films. In this process, materials are deposited layer by layer using sequential chemical reactions between gaseous precursors. Each layer is deposited sequentially and controlled with atomic precision, by alternately exposing the substrate surface to a reactive chemical precursor (surface activation), followed by a reactant that purifies (saturates) the surface and readies it for the next layer. ALD enables the creation of ultra-thin, conformal, and uniform layers, even on complex surfaces. This technique is now extensively employed in microelectronic device fabrication and the synthesis of two-dimensional (2D) materials, owing to its ability to produce precise and reproducible layers while minimizing defects and offering exceptional control over the properties of resulting thin films [178].

Some of the properties of TCO deposited by different techniques are reported in the **Table** 3.1 .

	Method	ρ **(Ω.cm)**	**T(%)**	**E$_g$(eV)**	**n(cm^{-3})**	μ **(cm^2.(Vs)$^{-1}$)**	**Ref**
In_2O_3	**Evaporation**	**2×10^{-4}**	**>90%**	**3.56**	**4×10^{20}**	**70**	[179]
In_2O_3	**PLD**	···	**86%**	**3.5**	···	···	[180]
ITO	**CVD**	**1.7×10^{-4}**	**90%**	**3.9**	**8.8×10^{20}**	**43**	[181]
ITO	**IBD**	**2.4×10^{-4}**	**90%**	**3.85**	**8×10^{20}**	**30**	[182]
ITO	**PLD**	**8.5×10^{-5}**	**85%**	···	**1.4×10^{21}**	**53.5**	[183]
ITO	**PVD**	**2.4×10^{-4}**	**95%**	**4**	**1×10^{20}**	**12**	[184]
ITO	**ALD**	**5×10^{-3}**	**>90%**	**3.5-3.7**	**4-7.6×10^{20}**	**23-49**	[185, 186]

Table 3.1: Reported of properties of In_2O_3 based TCO deposited by different techniques.

In this thesis we will mainly use the DC and RF PVD technique for almost all thin film deposition.

3.1.2 DC/RF magnetron sputtering.

The sputtering effect was first observed by W. R. Grove in 1852[187]. He observed the formation of a thin layer of the metal of the cathode on the surface of the anode and the walls of an electric discharge tube when an electric discharge is applied between the two electrodes of the tube in the presence of an inert gas under low pressure. However, the first applications of this discovery did not occur until a century later with the development of pumping systems. The first industrial applications occurred in 1965 (production of the first films), followed by the invention of the magnetron cathode in 1972. Today, sputtering is one of the most widely used techniques for the synthesis of thin film materials and metallic or ceramic coatings.

3.1.2.1 The principle of sputtering

Sputtering is divided into three main phases:

- Generation of the vapour consisting of species of the material to be synthesised from a target and reactive gases (O_2, N_2, S_2).
- Transport of these species to the substrate in the gas phase.
- Condensation of the vapour on the substrate (nucleation or nucleation and growth).

Figure 3.1 illustrates the sputtering processes. The sputtering chamber is first pumped to a secondary vacuum on the order of 10^{-8} mbar using a turbomolecular and/or cryogenic pump, after a primary pump initially lowers the pressure to limit the introduction of atmospheric contaminants. The sputtering gas (usually Ar) is introduced into the chamber at a flow rate monitored by flow metres and gauges to regulate the working pressure.

By applying a sufficient potential difference ($\sim$100 - 1000 V) between the cathode, which consists of the target (negatively polarised), and the anode, which consists of the reactor walls, a cold plasma or electric filament discharge is generated in a rarefied argon atmosphere at a pressure of the order of 10^{-3} - 10^{-1} mbar, consisting of electrons e^-, positive Ar^+ ions, photons, and neutral Ar atoms. The substrate holder is electrically isolated from the rest of the cathode and anode. Under the action of the electric field, the positive species of the plasma, (Ar^+) ions, are accelerated on the cathode (the target), resulting in its ablation by releasing the energy gained upon impact with the surface of the target. The target atoms in the form of neutral species are ejected by the ballistic effect and condense on the substrate. The momentum of the Ar^+ ions is not only used to eject the target atoms, but also phenomena such as implantation of the incident ion, elastic reflection of the neutralised ion, and emission of secondary electrons may occur[188, 189]. Secondary electrons are added to the free electrons produced during the generation of Ar^+ cations. These electrons are accelerated under the action of the electric field and in turn ionise the (neutral) argon atoms by collisions, forming Ar^+ ions. This mechanism maintains the plasma (maintenance of the electric discharge).

3.1.2.2 The magnetron effect

Two main problems arise in diode sputtering, the low ionisation rate of the plasma, which leads to low deposition rates (< 0.1 μm.h^{-1}) and the high thermalization of the sputtered atoms, which leads to the formation of porous layers: To achieve discharge at lower pressure (10^{-3} - 10^{-2} mbar), a higher ion density, with higher energy incident species, while maintaining a high deposition rate, it is necessary to equip the cathode with a magnetron system (see **Figure**.3.1.**b**). The advantage of magnetron is also to allow to maintain a discharge at lower pressure (pressure is limited in classical sputtering). These magnets create a magnetic field parallel to the surface of the target, perpendicular to the electric field. The electrons emitted by the cathode (secondary electrons) and present in the gas are then trapped by the Lorentz force (e$\mathbf{E}\times$ $\mathbf{B}$). The probability of

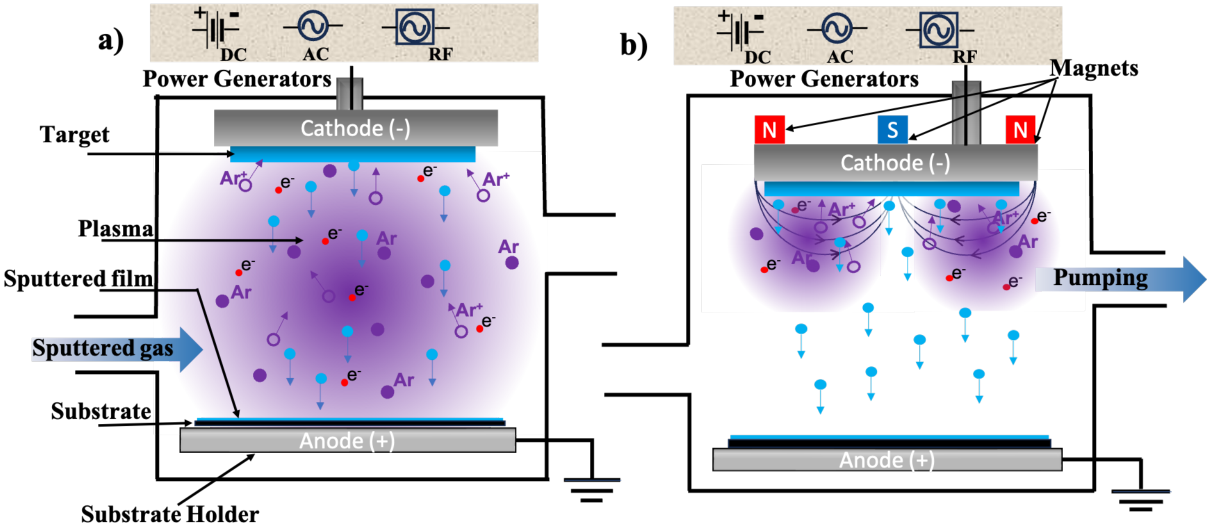

Figure 3.1: Schematic sputtering set-up: **a)** without magnetron system and, **b)** with magnetron, the field lines confine the plasma near the target and force the electrons in a solenoidal movement.

collisions between electrons and argon atoms is therefore increased, leading to a higher ionisation rate, easier maintenance of the plasma at low pressure and improved sputtering yields. This enables the production of denser films[190].

3.1.2.3 Reactive sputtering.

The diode sputtering process with a DC supply is suitable for the deposition of metallic or conductive materials. During the sputtering process with weakly conductive targets, a significant current of positive charges can flow into the target, resulting in over-voltages or electrical discharges and plasma instability, which are detrimental to the process[191]. There are two processes for the deposition of metal oxides:

- Radio frequency (RF) sputtering from compound targets (the metal oxide in question).
- Reactive sputtering from a metal target with the metal oxide being added via the reactive gas (O_2, N_2, S_2 or H_2).

In RF sputtering, an RF generator (13.6 or 27.2 MHz) creates a modulation of the cathode potential, which limits the accumulation of charges on the surface of the target, leading to the maintenance of a stable plasma. Another alternative to RF sputtering is DC-pulsed sputtering (with frequencies between 10 and 100 kHz), which is known to be effective in limiting plasma instabilities. During the polarisation period T_{ON}, the target is negatively polarised, leading to an accumulation of positive charges on the target surface, while during the non-polarisation or positive polarisation period T_{OFF} (see **Figure**.3.2), the plasma is attracted to the target surface and neutralises the accumulated positive charges. But the metal oxides deposited by RF sputtering are often of better quality than those made by DC-pulsed sputtering, because the voltage RF is not perceived by the low-mobility ions in the plasma,, so the potential is not screened and remains uniform between the two electrodes[192].

Reactive sputtering also offers the possibility of producing oxides with different stoichiometry, which can be controlled by the flow rates of the reactive gases and the working pressure during the process. This is important for certain optoelectronic applications where certain specific properties of the material are required, such as work function or defined free carrier densities and mobilities. This is particularly the case for charge extraction and transport layers based

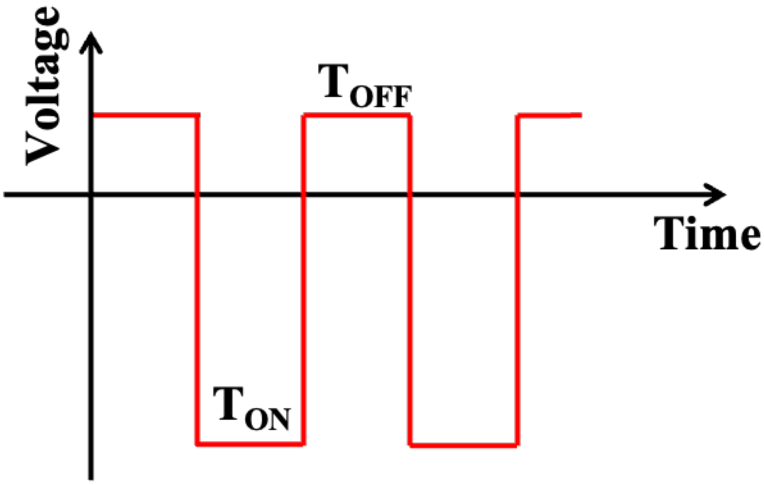

Figure 3.2: Schematic representation of the target voltage waveform for a pulsed DC power supply operating in asymmetric bipolar pulse mode [190]

on transition metal oxides, where the work function depends on the oxygen concentration, or for transparent electrodes (TCO) where the optical and electrical properties are defined by the density of oxygen vacancies. Reactive sputtering from metal targets has other advantages:

- The targets are often of better chemical quality and the deposited films are generally characterised by very low amounts of impurities.
- Metallic targets are thermally conductive and can therefore be cooled efficiently. This means that the possible range of power applied can be extended, for example to a value close to 50 W.cm^{-2}, without the risk of cracking or melting the target.

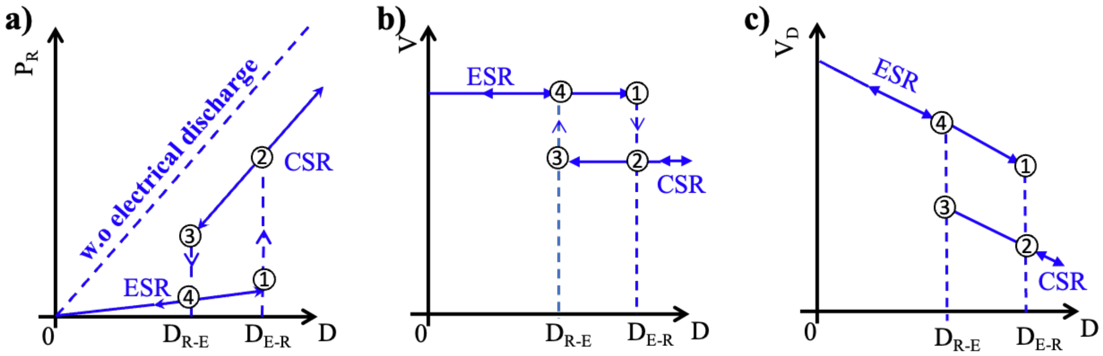

Figure 3.3: **a)** Changes in the partial pressure of the reactive gas , **b)** the discharge voltage and, **c)** the deposition rate as a function of the reactive gas flow rate[192].

3.1.2.4 Thin film growth

In reactive sputtering, the flow of reactive gas O_2 can lead to the appearance of an unstable transition zone between two different sputtering regimes (elemental and compound sputtering regimes). In the absence of electrical discharge, the pressure increases linearly with the flow rate of gas introduced into the sputtering chamber (**Figure** 3.3**a**) The same pressure decreases when the electrical discharge is turned on. The instability of the sputtering regime is generally observed when the surface area of the target is very small compared with the dimensions of the sputtering chamber or when the pumping rate is low. This instability is presented by a hysteresis phenomenon that is widely studied in the literature [193]. This phenomenon results from the competition between the oxidation rate of the target and its sputtering rate. **Figures** 3.3 **a**, **b** and **c** [194] show the hysteresis phenomenon on the reactive gas partial pressure P_R, the discharge voltage V and the deposition rate V_D as a function of the reactive gas flow rate introduced D respectively. When a reactive gas such as oxygen is introduced into the chamber in small quantities, it is essentially consumed by the metal vapour on the reactor walls through the Getter effect and the interaction with the target surface is relatively week. If the partial pressure of the reactive gas is increased to *point 1*, the system is in the ESR (elementary sputtering regime), hence the contamination of the target is greater (the target is mainly covered with the most stable material compound resulting from the reaction between the metal of the target and the reactive gas), in this situation the sputtering rate of the target is lower than that of the metal. If the flow rate of the reactive gas flow rate increases above a critical value D_{E-R} (up to *point 2*), the wall surfaces are completely saturated with metalloid, resulting in a sudden increase in the partial pressure of the reagent and a significant increase in the discharge voltage. A decrease in sputtering efficiency and deposition rate is observed. The system switches from the ESR to the compound sputtering regime (CSR). In CSR, the evolution of the partial pressure of the reactive gas as a function of the reactive gas flow rate parallels the "no discharge" line. The difference between the curves with and without discharge reflects the ability of the reactor to consume reactive gas molecules through the getter effect. When the reactive gas pressure changes little, the cathode discharge voltage remains constant and the deposition rate remains high. The decrease of the reactive gas flow does not immediately lead to a return to the ESR. This difference between the CSR and ESR tipping points is due to the fact that the target is still completely covered by the insulating compound, which generally has a lower sputtering rate than the pure metal from which it was obtained[195]. It is therefore more difficult to completely decontaminate the target to switch back to ESR. For the growth of sub-stoichiometric metal oxide films, we need to place ourselves between ESR and CSR. The formation of a film occurs in several phases: Adsorption and agglomeration of atoms on the substrate, incorporation of deposited atoms by nucleation growth and coalescence or grain boundary migration. Several kinetic and thermodynamic factors influence the different phases of the deposition process. This leads to differences in morphology and microstructure. The morphology of thin films is highly dependent on the deposition conditions and can be predicted by the zone structure model (SZM) [196]. According to this model, the most important deposition parameters in metal film synthesis are the total deposition pressure and the generalised homologous temperature (ratio between the deposition temperature and the absolute melting temperature of the target material). The SZM model was generalised by Anders (**Figure** 3.4) [197]. The Anders zone structure model predicts the morphology of thin films as a function of temperature and plasma ion energy. Controlling the structural properties of materials may be necessary for certain applications. Reactive sputtering offers the possibility to control the structural properties of metal oxides by adjusting gas flow rates and deposition conditions or parameters. The morphology obtained is defined by the film thickness $t^\star$, the generalised homologous temperature $T^\star$ and the normalised kinetic energy flux $E^\star$ of the particles arriving on the target surface. The parameters $T^\star$ and $E^\star$ are mainly influenced by the substrate temperature and the working pressure. During the deposition process, the substrate temperature influences the mobility of atoms on the surface. An increase in substrate temperature leads to an increase in the mobility of the species adsorbed on the substrate surface, but also to an increase in volume diffusion, and therefore to the formation of a denser layer. The deposition pressure influences the energy and angles between the normal to the substrate and the trajectory of the incident particles. As a function of the parameters $t^\star$, $E^\star$ and $T^\star$, the Anders diagram shows 4 zones with different morphologies.

- **Zone 1**

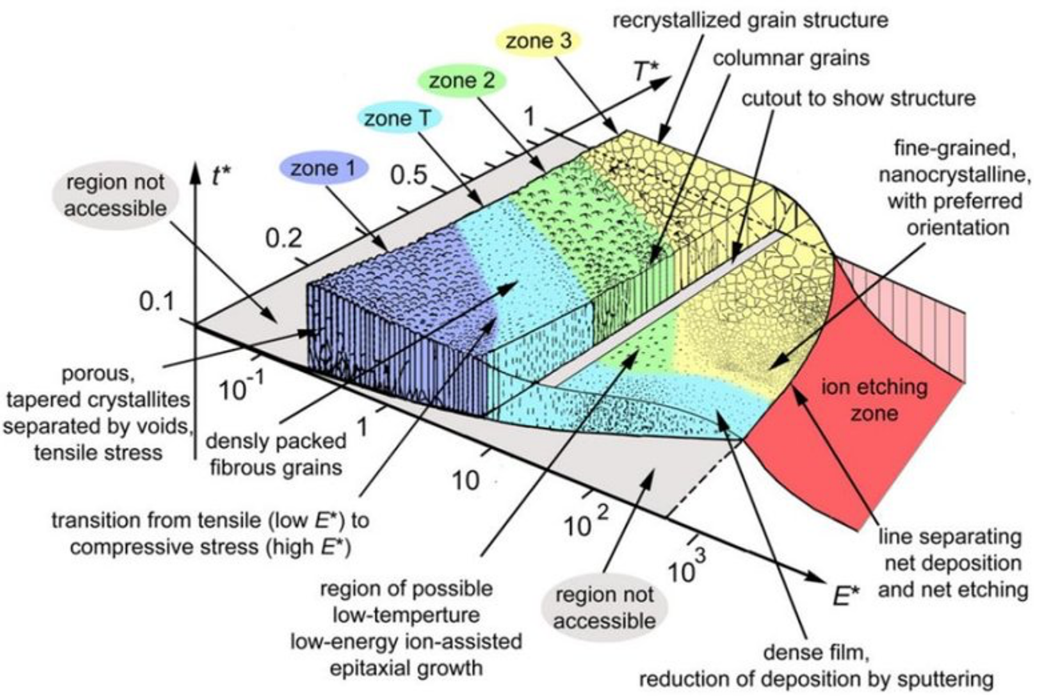

Figure 3.4: A structure zone diagram including plasma-based deposition and ion etching [197]

Columnar morphology, porous and rough, with low diffusion of atoms. The structure is amorphous or consists of few grains. At lower values of E* (high pressure), the argon adsorbed on the surface of the film limits the surface diffusion, maintaining the columnar structure. At lower pressures, the incident particles are more energetic, which increases the mobility of the atoms and leads to the loss of the columnar structure.

- **Zone T**
  Surface diffusion increases significantly, and the empty spaces between the columns can be filled. The result is a structure of fibrous grains separated by dense gaps.

- **Zone 2**
  This zone is formed when the deposition temperature is higher. The structure consists of columnar grains extending through the entire thickness of the layer and separated by dense grain boundaries.

- **Zone 3**
  Dense, coarse grains (volume diffusion) Some zones are not accessible when using a diode system. At T* near the melting temperature of the coating, volume diffusion is significant, resulting in a polycrystalline film (dense films with coarse grain size).

3.1.3 Description of the equipment used: Alliance Concept Cluster Tool 200 (AC CT200)

In this work, our thin films were mainly deposited using a 200 mm multi-chamber PVD coater, the Alliance Concept Cluster Tool 200 (AC CT200). The AC CT200 consists of a load lock (the load lock allows substrates to be loaded and vacuumed before being transferred by a robotic arm to the various process chambers), a transfer chamber, a pre-cleaning chamber for cleaning or de-oxidizing the substrate (Ar etching), two planar chambers (single target in DC sputtering) and a co-sputtering chamber (multi-cathode). Our depositions were performed in this multi-cathode chamber. It is equipped with three magnetron cathodes, one DC and two RF /DC, which can accommodate metal or ceramic targets with a diameter of 101 mm and a usually thickness of 6 mm (thickness of the target material), fixed on a copper disc of 107.5 mm in diameter and 3 mm thick using indium. The use of low melting point materials such as indium ($T_m = 430$ K) makes it easier to cool the target during the sputtering process. The targets, located 30 cm from the substrate holder (equipped with a rotation and translation system), are tilted at 22 degrees to the horizontal in order to promote homogeneous and uniform films. The maximum possible power is 200 W for the DC cathode target and 250 W for the two DC /RF targets. With a target of 101 mm diameter, a power density of 2.5 $W.cm^{-2}$ and a sputtering rate > 1 $Å.s^{-1}$ and 5 $Å.s^{-1}$ with metallic and ceramic targets, respectively, can be achieved with these powers. To obtain high quality deposits and limit excessive heating that could damage the targets, we stayed well below the power limits.

The co-sputtering chamber is connected to different gas lines, an argon line with the possibility

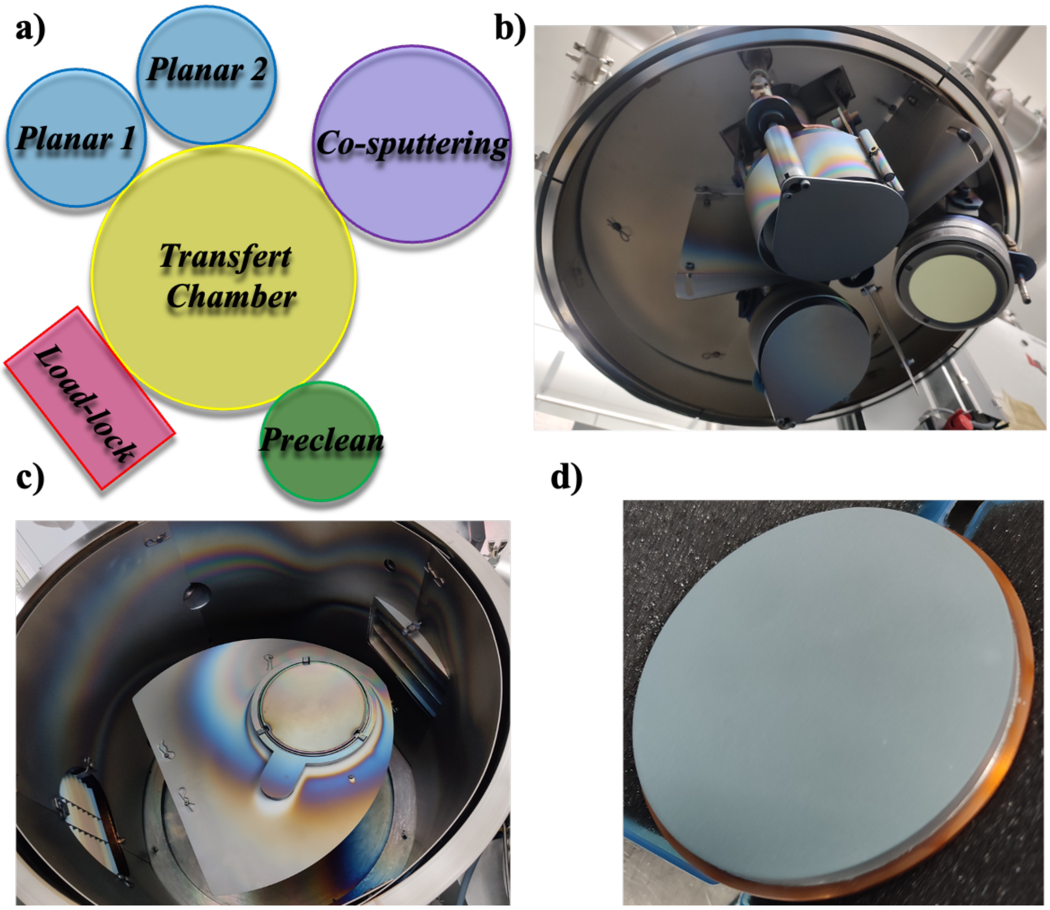

Figure 3.5: Description of the equipment: **a)** sketch of the AC CT200 in a clean room, the different chambers are under vacuum, in the transfer chamber there is a robotic articulated arm responsible for transporting the substrates between the different chambers of the equipment, **b)** picture of the multi-cathode chamber, where the different TCO and TMO depositions were made, **c)** substrate holder equipped with a rotation and translation motor that allows uniform and homogeneous depositions, **d)** new molybdenum oxide (MoO_3 target bonded with indium on a copper disc.

to switch to hydrogenated argon (Ar + 3% H_2) for depositions involving hydrogen doping, with a flow rate between 0 - 100 sccm (standard cubic centimeters per minute), a nitrogen line (0 - 20 sccm) and two oxygen lines, one operating between 0 - 5 sccm for low O_2 concentration control and a second between 0 - 20 sccm. A butterfly valve connected to the cryopump allows the working pressure to be controlled independently of the gas flow. The residual pressure in the AC CT200 is of the order of 10 × 10^{-8} mbar and can vary between 1.8×10^{-3} and 5×10^{-1} mbar during deposition. It is also possible to apply a bias voltage to the substrate holder of the AC CT200, but the large distance (30 cm) between the target and the substrate holder limits the effect, as there will be no ionised species near the substrate. The substrate is biassed via a power-controlled RF generator with voltage response (the physical parameter of post-ionization). A tuning box with a motorised RLC circuit is used to adjust the impedance (set point and return) of the system to limit the reflected power, which is especially important for ceramic targets. The substrate holder in the co-sputter chamber is equipped with a heating resistor. It is possible to reach up to 873,15 K. We did not use this feature during our studies.

3.2 Method and characterizations

3.2.1 X-rays reflectivity

X-ray reflectometry (XRR) is a simple, rapid and non-destructive technique for characterising thin films, multilayer structures and surfaces by measuring the intensity of reflected x-rays as a function of the angle of incidence. This technique provides valuable information about the composition, thickness, density, and roughness of the various layers of a stack of metallic and/or dielectric materials. XRR is based on scattering by a layered medium, as opposed to x-ray diffraction where scattering occurs by reticular planes. XRR uses the reflection of monochromatic x-rays at grazing incidence on a surface or interface. An angular $\omega = 2\theta$ scan is used to measure the reflected intensity as a function of incident angle (the scan range is measured from below the critical angle to the angle at which the measured reflection intensity reaches the background level, the scan range is between $2\theta = 0.1$ - 0.2 degree and 4 - 12 degree, the scan speed is set to the speed at which statistical fluctuations can be suppressed to the extent that the oscillation of the reflection intensity can be observed clearly and without noise, e.g. 0,01 - 2 degree.min^{-1}). The analysis of the reflected intensity makes it possible to determine the thickness, roughness and density of the thin layers or stacks under investigation with extreme accuracy, **Figure** 3.6. **a)** and **b)** illustrate the principle of XRR measurement. **Figure** 3.6. **a)** shows that at angles less than the angle of incidence θ_c, the x-rays are totally reflected and do not propagate inside the material. At angles of incidence greater than θ_c and at material thickness's less than 200 nm, refraction and reflection occur and the x-rays beam propagates through the material, resulting

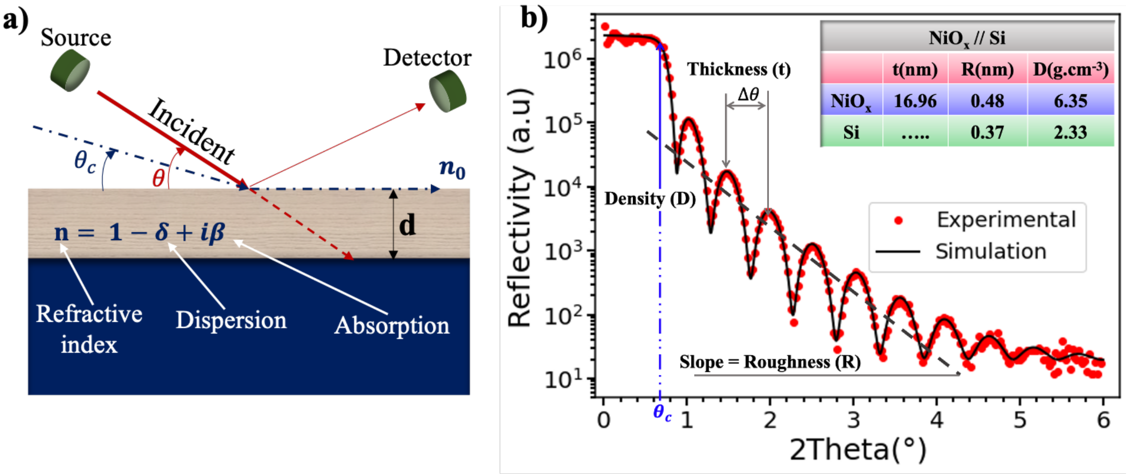

Figure 3.6: Illustration of the principle of XRR measurement: **a)** interaction between the sample and the x-rays as a function of the angle of incidence. **b)** determination of thickness, density and roughness by reconstruction of the reflectivity curve as a function of the angle of incidence (real case of a NiO$_x$ thin film deposited by sputtering on Si substrate).

in the formation of interference fringes called Kiessig fringes (**Figure** 3.6. **b)**). These fringes are due to interference between the reflections at the surface/interface of the substrate and the reflections at the surface of the film, the period of these oscillations can be used to determine the thickness of the film. The amplitude of the oscillation and the critical angle for total reflection θ_c provide information about the film density. This angle depends on the electron density of the film, which in turn depends on its density[198].

The amplitude of the oscillation depends on the difference between the densities of the film and the substrate; the greater the difference in film density, the greater the amplitude of the oscillation.

Most dense materials have a refractive index of less than 1, so total reflection is possible at very small angles of incidence of 0.2 to 1 degree. The refractive index n of a material for x-rays can be calculated using the following equations[198]:

$$n = 1 - \delta + i\beta \tag{3.2.1}$$

where,

$$\delta = \left(\frac{r_0\lambda^2}{2\pi}\right) N_0\rho \sum_{i=1} x_i(Z_i + f_i^{'}) / \sum_{i=1} x_i M_i \tag{3.2.2}$$

$$\beta = \left(\frac{r_0\lambda^2}{2\pi}\right) N_0\rho \sum_{i=1} x_i(Z_i + f_i^{''}) / \sum_{i=1} x_i M_i \tag{3.2.3}$$

Where r_0 is the classical radius of an electron ($\sim 2.8\times10^{-15}$m), N_0 is the Avogadro number, λ is the X-ray wavelength, ρ is the density (g.cm³), Z_i, M_i, x_i, $f_i^{'}$ and $f_i^{''}$ are respectively the atomic number, atomic weight, atomic ratio (molar ratio), atomic scattering factors(anomalous dispersion term) of the ith atom. The term δ corresponds to dispersion and its value depends on the wavelength of the X-rays and on the density and composition of the material. The parameter β is related to the absorption of X-rays, which is expressed by the linear absorption coefficient μ, as shown in the following equations [198]:

$$\beta = \frac{\lambda\mu}{4\pi} \tag{3.2.4}$$

The critical angle θ_c for total reflection is given by the **Equation** 3.2.5, from the critical angle for total reflection, the density of the film can be derived.

$$\theta_c = \sqrt{2\delta} = \lambda\sqrt{\frac{r_0\rho}{\pi}} \simeq 0.1 - 1\, degree \tag{3.2.5}$$

The thickness t of the film is determined from the period $\Delta\theta$ of the Kiessig strips and the wavelength λ of the incident X-rays according to the following equation:

$$t = \frac{\lambda}{2\Delta\theta} \tag{3.2.6}$$

During this thesis, all measurements of the thicknesses and densities of the thin films (TCO and TMO) were performed in a clean room using the Bruker D8 Fabline reflectometer in 200 and 300 mm. Bruker's Leptos software, which uses Fast Fourier Transforms and the Monte Carlo method, was used to analyse the data. Thickness, density and roughness are determined by fitting the experimental data (reflectogram reconstruction) as shown in **Figure** 3.6 for the case of a thin NiOx film.

3.2.2 Optical characterizations

3.2.2.1 Transmission and reflection

Optical transmission and reflection measurements were carried out using a Cary 7000 UMS UV-Vis-NIR version 2.24 dual-beam spectrophotometer operating in the ultraviolet, visible, and near-infrared (NIR) regions between 190 and 3300 nm (deuterium lamp: 190 - 350 nm and halogen lamp: 350 - 3300 nm). The dual-beam operation allows the correction of intensity fluctuations from the source and the environment. The instrument is equipped with the Universal Measurement Accessory (UMA) system, which automatically measures absolute specular reflection, transmission and scattering over a wide range of angles and polarizations. For transmission measurements, angles of 0 and 180 deg were used for the source and detector (collimator), respectively, while for reflection measurements, angles of 7 and 17 deg were used for the detector and collimator. **Figure** 3.7 illustrates the principle of transmission and reflection measurements. We used a measurement step of 1 nm with a selected scan rate of 600 nm.min^{-1}. The measurements were performed on materials on a 25×25 mm^2 glass substrate. A baseline was carried out before measurements on a bare substrate. Optical absorption α for a thin film of thickness t is determined from the transmission and reflection values using the following equation[199]:

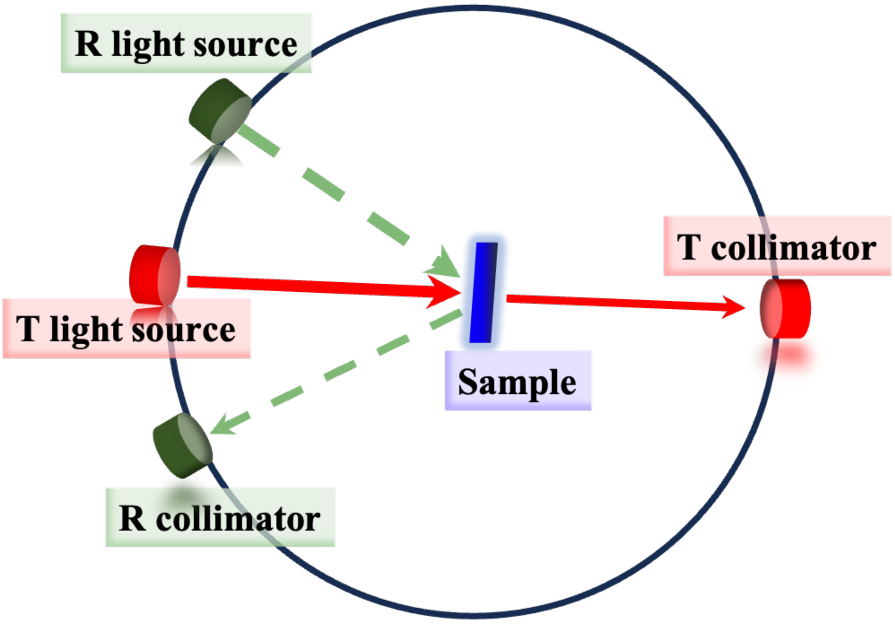

Figure 3.7: Illustration of the optical reflection and transmission measurement principle

$$\alpha = -\frac{1}{t} ln\left(\frac{\sqrt{(1-R)^4 + 4T^2R^2} - (1-R)^2}{2TR^2}\right) \sim -\frac{1}{t} lnT \ (R \ll 1) \qquad (3.2.7)$$

3.2.2.2 Optical characterization by spectral ellipsometry

Ellipsometry is a non-destructive technique based on measuring the change in polarisation of light reflected from a surface. Ellipsometry is considered as an impedance measurement, while reflection or transmission can be considered as power measurement (impedance measurement provides both amplitude and phase, while a power measurement provides only amplitudes). Ellipsometry is mainly used to determine the thickness and optical indices n and k of thin dielectric or transparent films deposited on absorbing substrates (e.g. Si). The basic principle of ellipsometry is based on the analysis of the polarisation state of light reflected by a sample. When light strikes a surface, its polarisation can change due to interactions with electrons in the material. The amplitude of light reflected from a single surface is generally decreased while its phase is shifted. In the case of multiple reflecting surfaces, the different reflecting rays interact and produce maxima and minima depending on the wavelength or angle of incidence. **Figure** 3.8 illustrates the basic principle of ellipsometry, where incident polarised light consists of a p-component parallel to the plane of incidence and an s-component perpendicular to the plane of incidence. For a material with zero absorption, only the amplitude of the reflected wave is affected. Linearly polarised light is reflected as linearly polarised light. However, for absorbing materials and for multiple reflections in a thin layer between the air and the substrate, the two components experience different amplitude changes and phase shifts during reflection. The reflection of the parallel component is always lower than that of the vertical component at angles of incidence other than 0 and 90 deg. Phase shift introduces an additional 90 deg polarised component into the incident beam, making the reflected light elliptically polarised. The key property of ellipsometric measurement is based on the change from linearly polarised to elliptically polarised light or from elliptically polarised to linearly polarised light upon reflection. The reflection coefficients R$_p$ and R$_s$ of the parallel and perpendicular components of the electric field allow us to define the ellipsometric angles Ψ and Δ[200]:

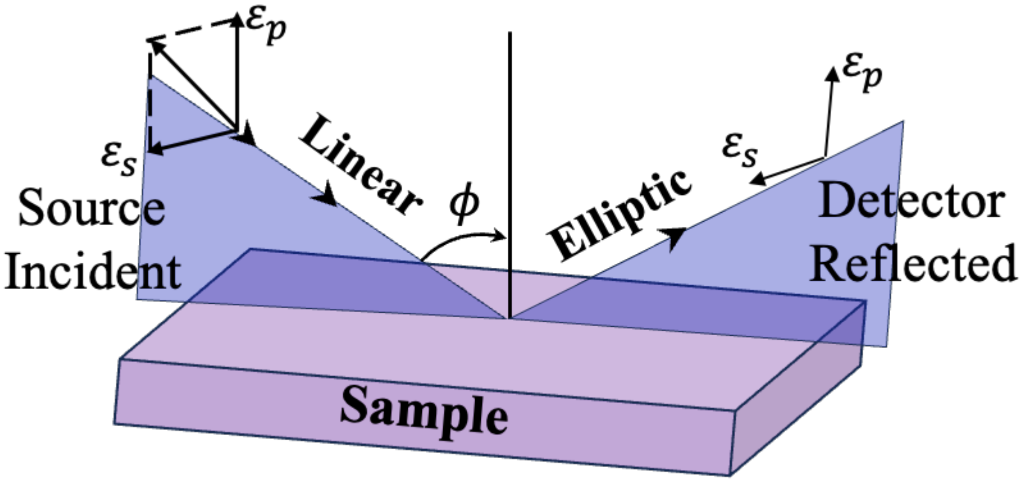

Figure 3.8: Ellipsometry measurement, reflection of polarised light on a flat surface, ϕ is the angle of incidence.

$$R_p = \frac{\varepsilon_p(incident)}{\varepsilon_p(reflected)};\ R_s = \frac{\varepsilon_s(incident)}{\varepsilon_s(reflected)} \tag{3.2.8}$$

and,

$$\frac{R_p}{R_s} = tan\Psi e^{i\Delta} \begin{cases} 0^\circ \leq \Psi \leq 90^\circ \\ 0^\circ \leq \Delta \leq 360^\circ \end{cases} \tag{3.2.9}$$

where,

$$\begin{cases} tan\Psi = \dfrac{|R_p|}{|R_s|} \\ \Delta = \Delta_p - \Delta_s \end{cases} \tag{3.2.10}$$

The refractive index of the material n and the extinction coefficient k of the sample can be expressed as a function of the ellipsometric angles and the incident angle ϕ using the following equations:

$$\begin{cases} n^2 - k^2 = & n_0^2 sin^2\phi \left[1 + \dfrac{tan^2\phi(cos^2 2\Psi - sin^2 2\Psi sin^2\Delta)}{(1 + sin2\Psi cos\Delta)^2} \right] \\ nk = & \dfrac{n_0^2 sin^2\phi tan^2\phi sin4\Psi sin\Delta}{(1 + sin2\Psi cos\Delta)^2} \end{cases} \tag{3.2.11}$$

Ellipsometry is complementary to transmission and reflection measurements. The absorption coefficient can also be defined as a function of the extinction coefficient k by $\alpha = 4\pi k/\lambda$. Briefly, in ellipsometry, the ellipsometric angles Ψ and Δ are measured at different ϕ angles as a function of wavelength. The measured Ψ and Δ parameters are then compared with optical models and simulations to determine material properties such as refractive index, extinction coefficient, and film thickness. **Figure** 3.9.**a** shows the two ellipsometric angles Ψ and Δ measured (dashed black lines) and fitted (solid colour lines) at different incidence angles ϕ for a PbS QD film deposited on a Si//Ta//TiN//ZnO stack. **Figure** 3.9.**b** shows the optical indices n and k resulting from modelling these two angles. It can be clearly seen that the QD absorption peak is at 940 nm as expected. It should be noted that ellipsometry has one major drawback, different optical models can be used to reconstruct the psi and delta curves as a function of wavelength with good accuracy. Therefore, some knowledge of the samples under study is required, or a combination of ellipsometry and another technique such as XRR may be useful (prior measurement of sample thickness with XRR reduces the number of parameters that need to be determined by modelling).

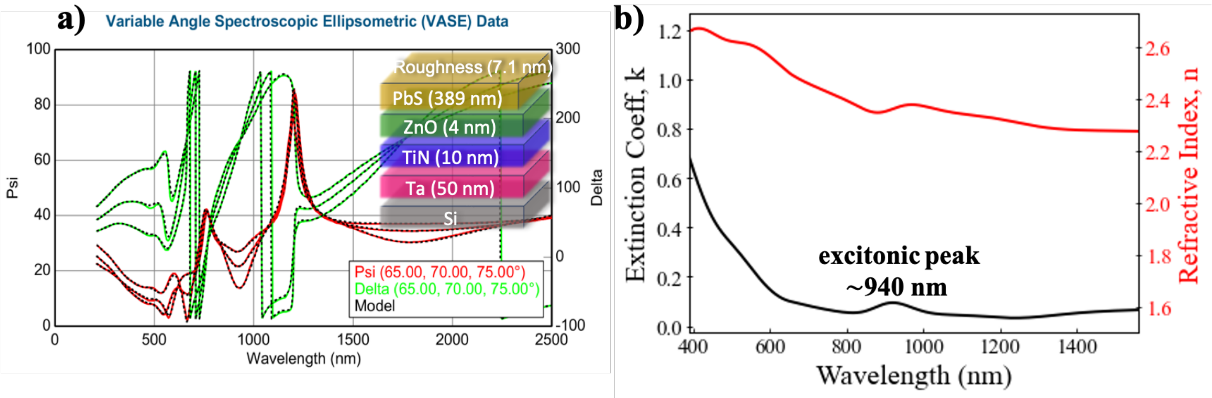

Figure 3.9: **a)** ellipsometry raw data and model fit for ∼ 400 nm of PbS QD), **b)** Optical indices determined by modelling the ellipsometric angles as a function of wavelength for a PbS QD film of ∼400 nm absorbing at 940 nm.

3.2.3 Four probes electrical measurements, VDP and Hall effect

Electrical resistivity measurements were performed in a clean room at room temperature using the standard four-point probe technique on thin films deposited on thermal oxides with a thickness of 500 nm (on 200 mm substrates, the probe is pressed directly onto the surface of the film). The simplest model is obtained when the four tips are aligned and separated by equal distances (see **Figure** 3.10**a**), a small current **I** is applied between the two outer probes, and the voltage is measured between the two inner probes. The four probes technique minimises the effects of contact resistance and voltage drops in the leads (the current flowing in the V measuring branch is negligible because the impedance of the voltmeter is very high, so voltage drops across the contacts are negligible and the measured voltage is actually the voltage between the contacts. Using the voltage and current readings from the probes, the resistivity is given by [199]:

$$\rho = \frac{\pi d}{ln(2)} \frac{V}{I} \tag{3.2.12}$$

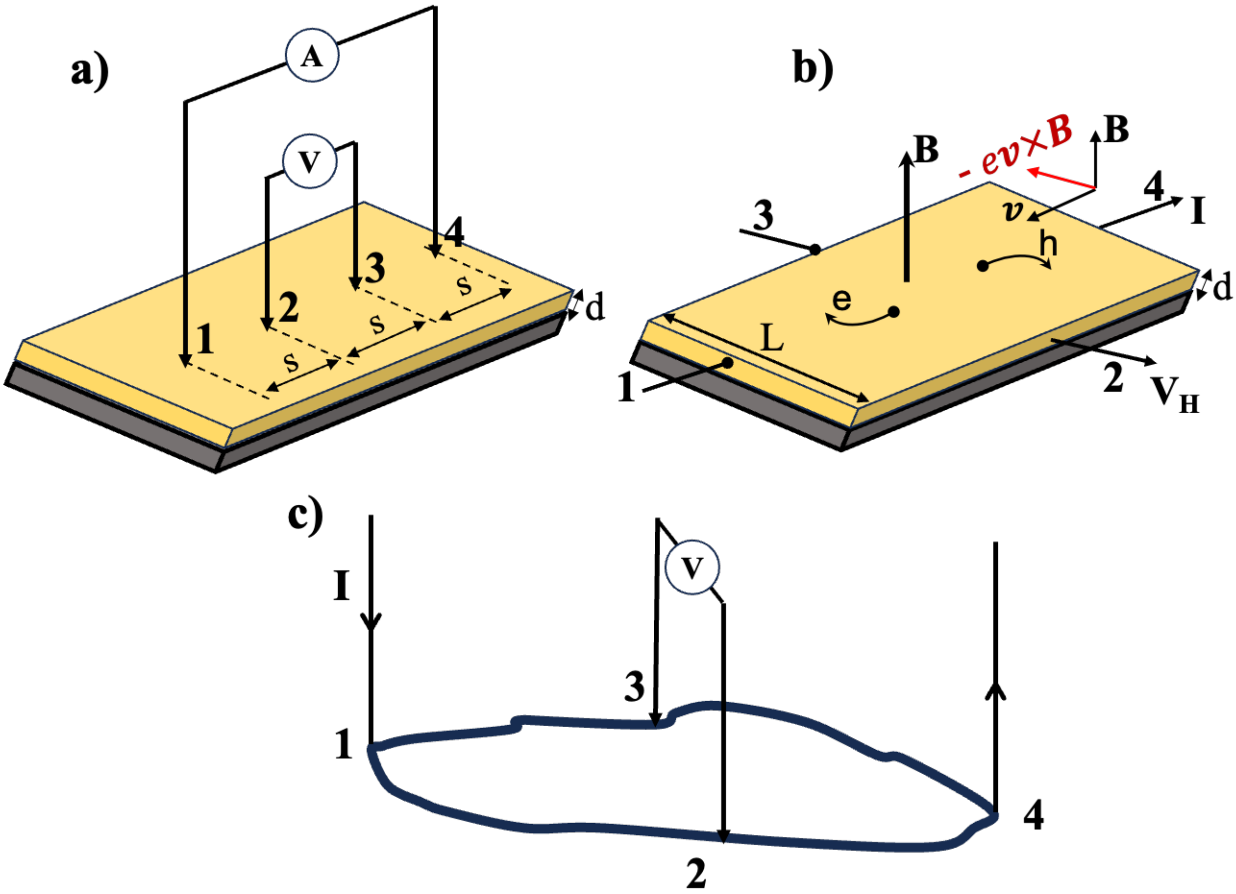

Figure 3.10: **a**) Four-point-probe resistivity measurements configuration (four probes in line), **b)** Hall effect measurement configuration for thin films on insulating substrate, **c)**Van der Pauw (VDP) resistivity measurement (suitable for arbitrary four probes configuration.

This formula assumes that the thickness of the sample is much less than the distance between the probes, d $\leq$ s/2.

For arbitrary shape (**Figure** 3.10.**c**), the resistivity can be calculated using the following equation[199]:

$$\rho = \frac{\pi d}{ln(2)} \frac{(R_{14,23} + R_{42,31})}{2} F \tag{3.2.13}$$

where $R_{14,23} = V_{23}/I_{14}$ and **F** is the correction factor and depends on the ratio $R_r = R_{14,23}/R_{42,31}$. It is close to 1 for all symmetrical shapes. The VDP measurement does not provide information about the density or mobility of free charge carriers in a material (metal or semiconductor). These quantities can be measured by the Hall effect, which was discovered by E. Hall in 1879[201]. The Hall effect is based on the principle that a magnetic field applied to a conducting or semiconducting material through which a current flows leads to the creation of a potential difference that is perpendicular to the direction of the current and the magnetic field (see **Figure** 3.10.**b**). The potential difference produced, also known as the Hall voltage, is related to the deflection of the charge carriers by the Lorentz force -e**v**×**B**, where v is the electron velocity. The Hall voltage V_H is directly proportional to the charge carriers density and their mobility. The Hall voltage is given by the following expression:

$$V_H = R_H I B \tag{3.2.14}$$

Where R_H is the Hall coefficient and the scattering factor r, R_H is given by:

$$\begin{cases} R_H = & \dfrac{r(p - b^2 n)}{e(p + bn)^2} \\ b = & \dfrac{\mu_n}{\mu_p} \end{cases} \tag{3.2.15}$$

When the conduction is dominated by one type of charge carriers, e.g., of type n, the equation is largely simplified as:

$$R_H = \frac{r}{en} \tag{3.2.16}$$

The sign of R_H indicates the type of carrier. The diffusion factor varies between 1 and 2 and depends on the diffusion mechanism in the semiconductor, the magnetic field intensity and the temperature. In the limit of high magnetic fields, $r \longrightarrow 1$ and $R_H = \frac{1}{en}$ for n-type material. The high fields required for r to approach unity are not achievable in most laboratories. Typical magnetic fields are between 0.5 and 1 T (0.5 T for our measurements), so $r > 1$ for typical Hall measurements. Since r is generally not known, it is often assumed to be equal to one. Knowledge of the Hall coefficient, together with measurement of resistivity, allows determination of the carrier type and carrier mobility density.

3.2.4 X-ray Photoelectron Spectroscopy (XPS) and Ultraviolet Photoelectron Spectroscopy (UPS)

3.2.4.1 XPS

Definition and principle

X-ray photoelectron spectroscopy (XPS), also known as ESCA (Electron Spectroscopy for Chemical Analysis), is a powerful analytical technique used to study the surface chemistry of materials. XPS is based on the photoelectric effect described by A. Einstein (1905). Photoemission using x-rays was first observed by Robinson and Rawlinson in 1914, and the first application of photoemission as an analytical method was described by Steinhardt and Serfass in 1951. However, the development of XPS as we know it today was pioneered by K. Siegbahn in the 1960s. The photoelectron emission process is illustrated in **Figure** 3.11, A monochromatic soft x-ray beam (h$\nu < \sim$ 6 keV) with a specific energy (e.g., Al K$_\alpha$ 1486.6 eV) is used to irradiate the sample surface. The interaction of the x-ray photons with the surface of the sample can cause the ejection of photoelectrons from the outermost atomic layers and core levels of the material.

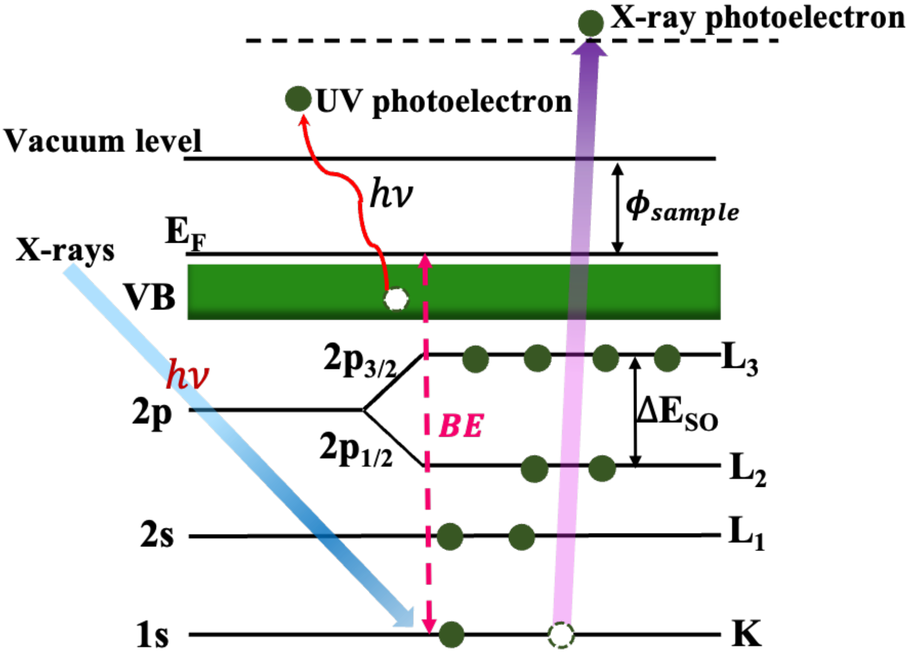

Figure 3.11: Photoelectron emission process

The kinetic energy and the number of electrons ejected provide useful information about the elemental composition (each atom generally has its own binding energy) and the chemical state of the atoms on the surface. The vacuum level refers to the energy level of an ejected electron at rest (a position where the interaction between the ejected electron and the sample is negligible), and the work function of a material is the difference between this and the Fermi energy level. By measuring the kinetic energy $\mathrm{KE}_{measured}$ of the photoelectrons, we can determine their origin and their binding energies BE (see the energy diagram, **Figure** 3.12).

$$BE = h\nu - KE_{measured} - \phi_{spectrometer} \tag{3.2.17}$$

Where hν is the x-ray energy and $\phi_{spectrometer}$ is the spectrometer work function.
All elements except hydrogen and helium can be detected (with a detection limit of 0.1-1 at. %, and in some cases, e.g., for light elements in a matrix of heavy elements, the detection limit may exceed 10% at.); XPS can be used to study the surface of almost any material, conductive or not. The large majority of XPS peaks originate from electrons at specific core levels that have not suffered energy loss or inelastic collisions on their way to the surface (main peaks). Electrons that have undergone inelastic scattering processes lose some of their energy and information about their origin. These inelastically scattered electrons contribute to the continuous background of the spectrum.

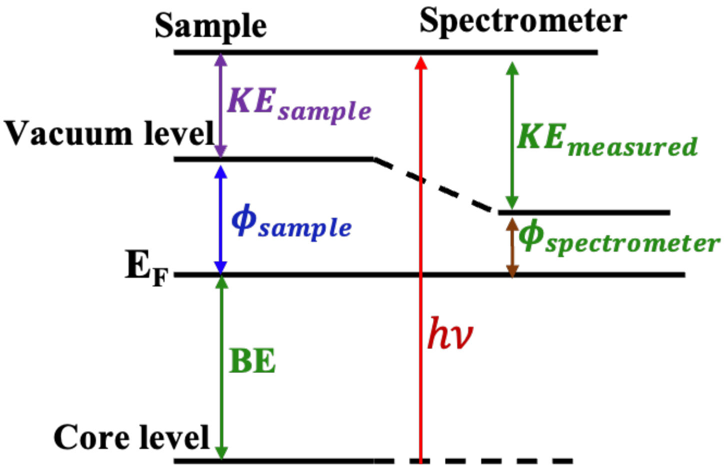

Figure 3.12: XPS basic principle, energy level diagram illustrates schematically the basic XPS equation, including the x-ray source energy hν, the binding energy of the electron BE, the measured kinetic energy of the electron $KE_{measured}$, and the work function of the spectrometer $\phi_{spectrometer}$[202]

The main peaks are described with the spectroscopic notation $\mathbf{Xnl}_j$, where X stands for the element, n is the main quantum number (n = 1, 2, 3, ...), l stands for the orbital angular momentum, s, p, d, f are notated corresponding to l = 0, 1, 2, ..., n - 1, j = l+s is the total angular momentum and corresponds to the sum of the orbital angular momentum and the projection of the spin magnetic spin moment s = ±1/2. For example, Mo $3d_{5/2}$ corresponds to electrons of Mo atoms with n = 3, l = 2, and s = 1/2. For values of $l \geq 1$, the peaks appear as $p_{3/2}$-$p_{1/2}$, $d_{5/2}$-$d_{3/2}$ and $f_{7/2}$-$f_{5/2}$ doublets separated by the ΔE_{SO} spin-orbit coupling (see **Figure** 3.11). The area ratios between the peaks in the doublet are determined by the degeneracy of the electronic levels (2j + 1), e.g., this ratio is equal to 3:2 for levels $d_{5/2}$ and $d_{3/2}$. The spin-orbit coupling may be so important that the in-depth analysis focuses only on the spin-1/2 component, as is the case for Ni 2p, where generally only the Ni $2p_{3/2}$ state is analysed. The position, shape, and the full width at half maximum of the peaks provide useful information about the chemical environment of the atoms. For transition metal oxides, the peaks of the metallic element (e.g. Mo(0) for molybdenum oxides) are generally asymmetric, the full width at half maximum of these peaks decreases as the oxidation state of the metal increases and the binding energies are shifted towards higher values (**Table** 3.2 for the specific case of MoO_x), while for the oxide in its stoichiometric form such as MoO_3, the peaks of the metallic element become symmetric.

Compounds	Main oxidation states	Binding Energy (eV)	
		Mo $3d_{5/2}$	Mo $3d_{3/2}$
Mo	Mo(0)	228.3	231.5
MoO_2	Mo(IV+)	230.0	233.1
MoO_3	Mo(VI+)	232.5	235.6

Table 3.2: Reported values of binding energies of the chemical states of molybdenum and their stoichiometric oxides[203].

One of the keys to XPS measurement is its high surface sensitivity. In measurements with an Al K_α source, the interaction of x-rays with the core levels is mainly due to inelastic collisions, and the distance λ (mean free path) travelled by photoelectrons between two inelastic collisions is less than 2-3 nm. This mean free path length depends on the kinetic energy of the electrons and the density of the free electrons and is of the same order in all solids except alkali metals[204]. Surface sensitivity is related to the attenuation of the x-rays as they pass through the sample. The probing depth d of the x-rays corresponding to the surface layer, which accounts for 95% of the total recorded signal intensity, is about $3\lambda cos\theta$, where θ is the emission angle of the electrons relative to the sample normal, so that d varies between 6-9 nm in the case of electrons collected at the surface normal [202, 204]. For emission angle θ (referred to the surface normal) and an incident energy intensity I_0, the intensity contribution of a surface layer of thickness d to the total intensity of an XPS signal is determined by the following equation:

$$I = I_0 exp(-d/\lambda cos\theta) \tag{3.2.18}$$

Increasing the probing depth can be beneficial to minimise the relative contribution of surface oxides and impurities, especially for samples sensitive to sputtering damage (where the use of low energy Ar ions or Ar cluster etching will alter or degrade the sample). Surface sensitivity is a problem when studying certain materials. In particular, for transition metals or transition metal oxides, which are very sensitive to oxygen, the chemical composition may not be representative of the entire layer after an air exposure.

The difficulties associated with surface sensitivity can be overcome by etching with low energy Ar ions (where this is not limiting) or at the expense of lower energy resolution by using higher energy X-rays (the lower resolution is due to the larger linewidths of Ag L_α and Cr K_α sources [204]. Another problem with XPS can be the charging effect; in some situations, the surface of the samples can become charged during XPS analysis, leading to shifts and distortions of the peak shape, as the loss of negative charge from the surface region due to the photoelectric effect is no longer sufficiently compensated by electrons from the sample bulk, substrate, or surrounding environment. This leads to a positive charging of the sample surface and it becomes more difficult to remove other electrons and the binding energies become greater, causing the peaks shift towards higher binding energies (decrease in the kinetic energy of the photoelectrons due to the Coulombic interaction). This effect can also lead to broadening of the peaks, similar to reduction in the case of metal oxides. The analysis of non-conducting samples requires the use of a low energy electron or electron/ion gun (1-5 eV for electrons or $<$ 5 eV for ions), called a flood gun. However, this type of compensation does not always guarantee the electrical neutrality of the surface.

Another alternative to address peak shifts due to charge effects is energy scaling correction, where the lowest C 1s peak is often used as an internal standard for energy calibration. However, there is debate in the literature about the appropriate binding energy of this peak, with values varying between 284.6 and 285 eV. The effects of these variations in the carbon source, interactions with different substrates, and coupling of the adsorbed layer to the substrate limit the validity of using the C 1s peak as an accurate and universal reference[205, 206, 207].

XPS instrument

In this work, our measurements were performed off-line using a PHI500 VersaProbe II x-ray microscope spectrometer. Its schematic diagram is shown in **Figure** 3.13. It uses electrons generated by the thermoelectric effect with a LaB_6 filament. These electrons are accelerated by a high voltage onto an Al anode to produce an x-ray radiation source consisting of a characteristic spectral line (radiative interaction between the electrons and the core levels of the atoms of the anode) and a continuous spectrum resulting from the deceleration of the electrons on the anode (bremsstrahlung). These x-rays are then passed over an ellipsoidal quartz crystal monochromator that selects the K_α 1 line. The monochromatic x-ray beam obtained is focused on the sample, and the ejected photoelectrons are collected and analysed using a multichannel detector. The analyzer consists of two concentric hemispheres with different radius R_{in} and R_{out}, covered with a conductive layer and subjected to a potential difference U. The geometry of the analyzer can

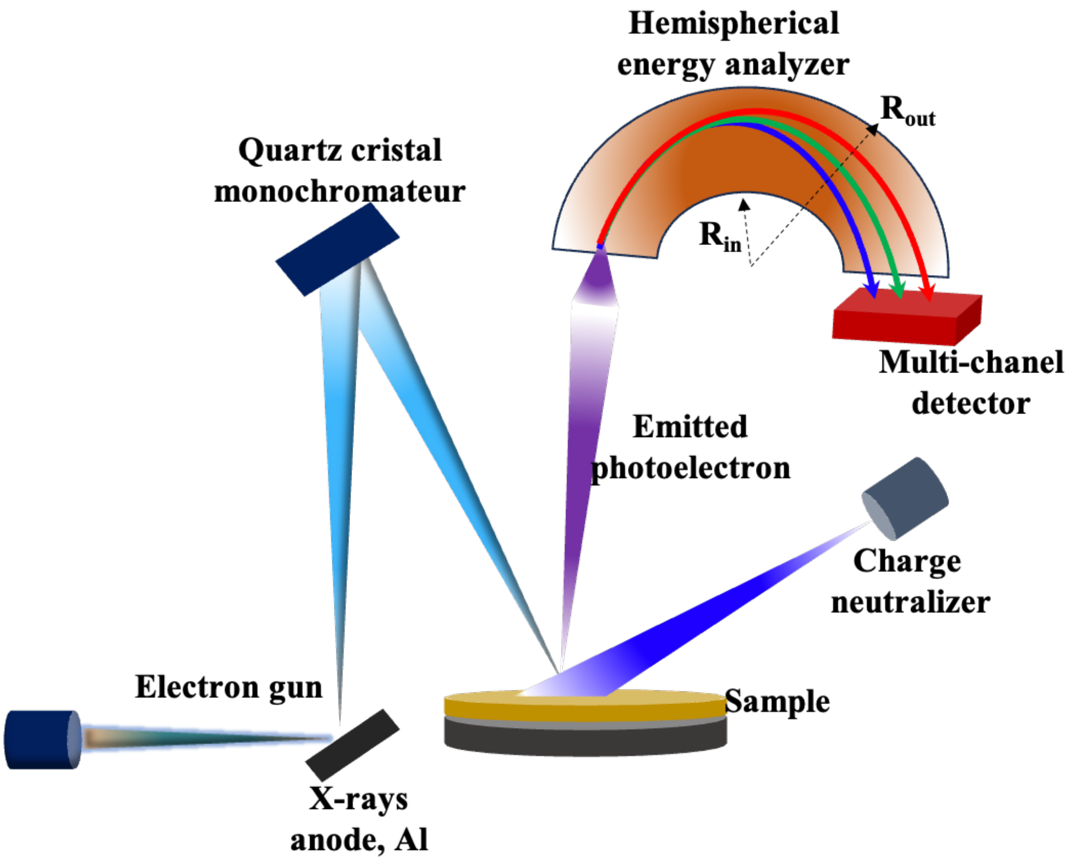

Figure 3.13: Schematic diagram showing the major components of an XPS instrument and monochromator.

be used to determine the characteristic energy E_p of the analyzer, also known as the energy pass[205]:

$$E_p = e.U\left(\frac{R_{out}R_{in}}{R_{out}^2 - R_{in}^2}\right) \tag{3.2.19}$$

E_p corresponds to the energy that an electron entering the analyzer must have to escape on an intermediate radius trajectory. Only electrons with energies near E_p can be detected; electrons with energies much higher or much lower than E_p will be deflected from the outer or inner hemisphere, respectively. Since the kinetic energies of the emitted photoelectrons are not equal, a delay potential is applied to the input of the analyzer so that the energy of E_p is identical to the kinetic energy of all photoelectrons. The variation of this potential is used to construct the XPS spectrum. This method allows to work with a constant energy resolution over the entire kinetic energy range studied.

Analysis of XPS spectra

Survey scans

Survey scans can be used to quickly obtain primary information about the composition of the sample. They are elemental, qualitative analyses that can be used to determine the various elements present in the sample without giving any indication about their concentration. Survey scans are generally acquired at a relatively high energy step to ensure a high signal-to-noise ratio so that even weak signals can be detected. The wide energy range ensures that the peaks of all core electron levels that can be excited by incident photons are acquired. Since the electronic structure is element specific, it is easy to verify which elements are present in the sample by comparing the recorded binding energy values to the XPS manuals. Survey scan analysis must

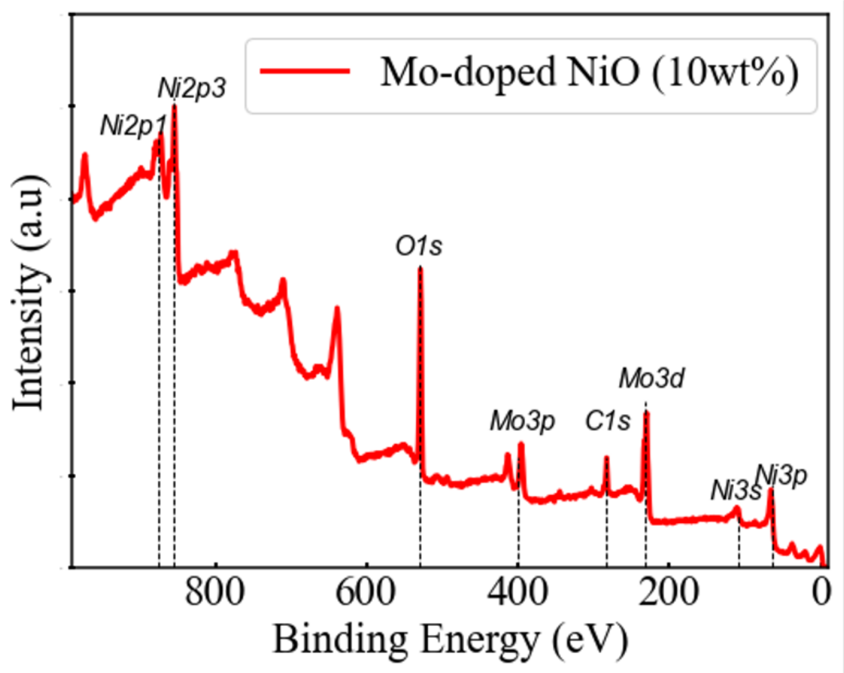

Figure 3.14: XPS survey scan spectra of Mo-doped NiO$_x$

be performed prior to recording narrow range resolution spectra. As example, the **Figure** 3.14 shows the survey scans spectrum of Mo-doped NiO$_x$, showing the different peaks that are present in the material. The presence of C (C 1s around 284.5 eV) is due to surface contamination resulting from air exposure.

High resolution spectra (narrow range)

Spectra over narrow energy ranges are obtained with a very small energy step, resulting in high energy resolution. These spectra provide more accurate information about the surface chemistry of the sample. In our studies, we used the CasaXPS software [208] to analyse the high-resolution spectra. This tool provides different peak shapes, including Gaussian and Lorentzian and their mixtures, as well as different backgrounds such as linear Shirley or Tougaard functions. **Figure** 3.15 shows an example of quantitative analysis of the high-resolution O 1s peak in a NiO$_x$ sample deposited from a NiO target by reactive sputtering (Ar + O_2). A Shirley background function and a mixture of Gaussian and Lorentz peaks are used for the fit. There are two different environments around the Ni atoms: NiO corresponds to the oxide in its stoichiometric form, while Ni_2O_3 describes a more oxidised environment, NiOOH refers to contamination or hydroxylation of the surface. XPS quantification is based on the evaluation of the ratio of the areas under the main peaks of the core levels of all elements present in the sample. In the case of signal overlap, the peaks must first be adjusted to obtain an accurate estimate of the peak areas. The peak area is normalised by the relative sensitivity factor (RSF) of each corresponding electronic level.The RSF takes into account the fact that the number of electrons detected from a given core level of an atom depends on several factors, including the excitation source, the effective photoionization cross section, the inelastic mean free path of the electrons, the angle between the incident x-rays, etc. For the quantification of MoOx, for example, we will use 3. 32 and 2.93 for Mo 3d and O 1s, respectively, and the stoichiometry **x** of MoO$_x$ is defined by the ratio of the area under the peaks of O 1s and Mo 3d.

The order of magnitude of the error is $\sim 5\%$ and the corresponding quantification accuracy in XPS is considered to be poor compared to other techniques such as Auger electron spectroscopy (AES), energy dispersive X-ray spectrometry (EDX or EDS), Rutherford backscatter spectrometry (RBS)[209, 210, 211].

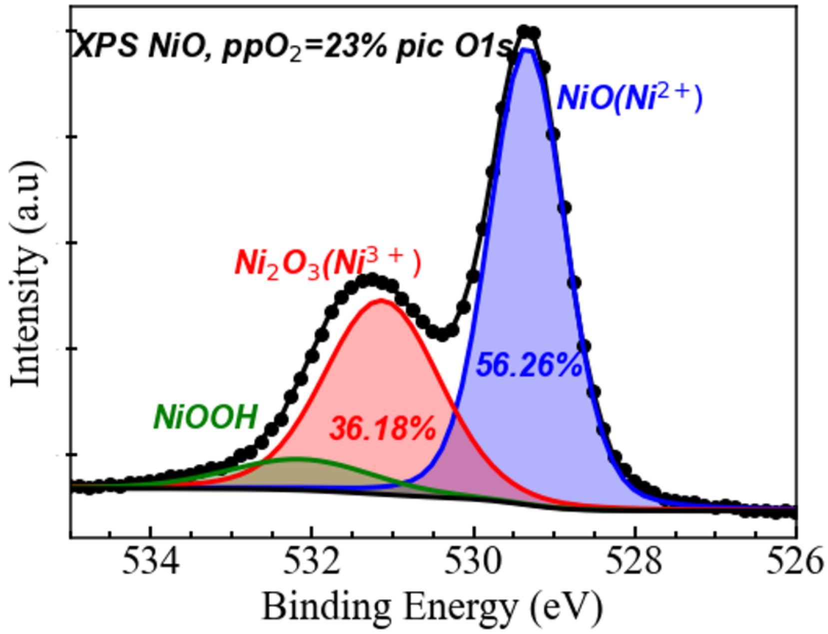

Figure 3.15: High-resolution spectra O 1s pic obtained from NiO$_x$ films, compositions of NiO$_x$ by O 1s XPS spectra divided into NiO lattice (blue), Ni$_2$O$_3$ lattice (red) and bound hydroxide related group NiOOH (green) concentrations

3.2.4.2 UPS

Ultraviolet photoelectron spectroscopy (UPS) is a surface analysis technique similar in principle to XPS. It uses a monochromatic UV photon source, generally with an energy of hν = 21.2 eV (He-I discharge lamp or synchrotron radiation with absolute calibration of photon energy), instead of x-rays, to probe the valence region of the material (binding energy below 30 eV) and can be used to determine the surface work function of metallic and semiconductor materials as well as the ionisation energy or the energy between the vacuum level and the first valence level in a semiconductor. The low energy of the UV source makes this technique even more surface sensitive than XPS, since only the uppermost ~2-3 nm are analysed, which means that surface contamination is even more problematic. **Figure** 3.16 illustrates the principle of the measurement UPS. The binding energies are given relative to the Fermi level (BE = 0), electrons with higher binding energies are not probed, this part of the spectrum is called the secondary electron cut-off (E$_{cut-off}$). The work function and ionisation energy can be determined by the following equations:

$$\begin{cases} \phi = h\nu - (E_{cutoff} - E_F) \\ IE = h\nu - (E_{cutoff} - E_{VB}). \end{cases} \tag{3.2.20}$$

This characterization technique is difficult to apply to weakly conducting or insulating materials. However, in the special case where the very thin insulating layer is deposited on a metal substrate and no charging effect occurs, the work function of the weakly conducting or insulating film can be measured.

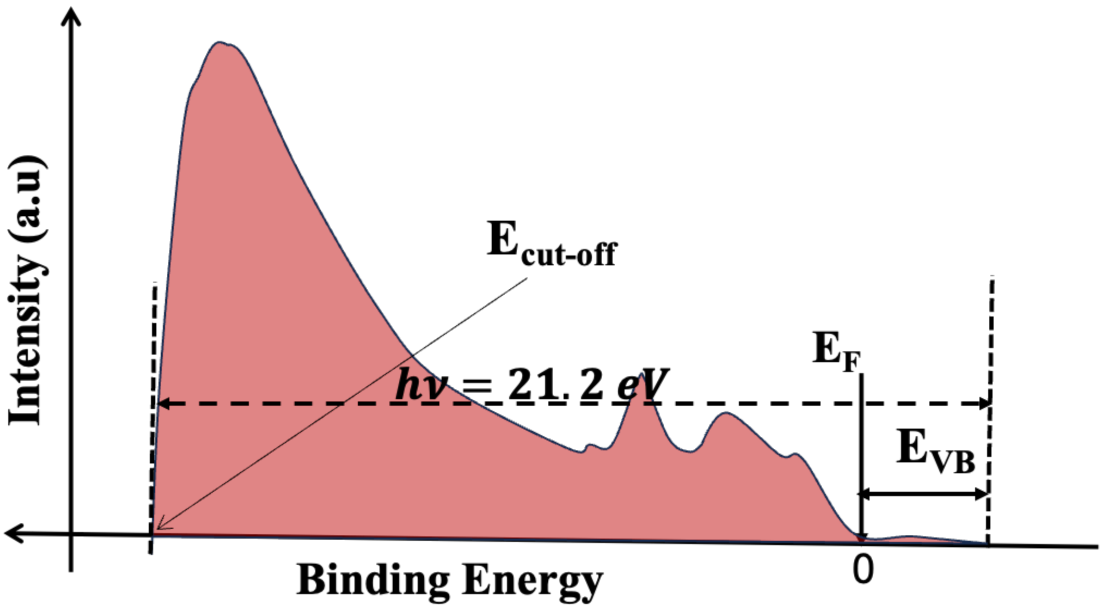

Figure 3.16: Schematic diagram of work function measurement using photoelectron spectroscopy

3.2.4.3 X-ray diffraction

X-ray diffraction (XRD) is used in chemistry and solid state physics to study the structure of crystalline materials. It is based on the phenomenon of x-ray diffraction, in which x-rays are scattered by the periodic arrangement of atoms within a crystal lattice, resulting in the formation of a diffraction pattern (see **Figure** 3.17.**a**). By measuring the angles and intensities of the diffracted waves, the crystal structure, crystal size, orientation, and other important properties of the sample can be determined. The diffraction condition for planes of index hkl separated by a distance d_{hkl} is given by Bragg's relation:

$$2dsin\theta = n\lambda \tag{3.2.21}$$

where λ is the wavelength of the incident radiation.

We have investigated the structural properties of TCO films and transition metal oxides prepared using the XRD technique. Our measurements were performed on an Empyrean PANalytical diffractometer using a Cu-Kα source at 45 kV/40 mA/$\lambda = 1.540598$ Å with a minimum resolution as low as 0.01deg. XRD scans were performed in ω-2θ symmetry (see **Figure** 3.17.**b**), incidence angle ω and the angle of the detector is 2θ (goniometer 2 circles: ω, 2θ / radius = 240 mm). The x-ray source is kept stationary and the sample and detector are rotated by $\theta\,\text{deg.s}^{-1}$ and $2\theta\,\text{deg.s}^{-1}$, respectively, i.e. in the direction (00l) where the diffraction vector is perpendicular to the film surface. Only diffraction from crystal planes parallel to the sample surface is detected, since the Bragg condition can only be satisfied for these planes (see **Figure** 3.17.**c**). When the structure is more or less crystalline, the grain size D can be determined as a function of the full width at half maximum (FWHM) β of the main peaks and taking into account the instrumental broadening, the calculation being based on the Scherrer formula given by the following equation

$$D = \frac{K\lambda}{\beta cos\theta} \tag{3.2.22}$$

where β = width at half height of the line under consideration (hkl). K is the Scherrer constant, also known as the shape factor, it depends on how β is determined, the shape of the grains and their size distribution [212]. In most cases, it varies between 0.89 for spherical particles at $\omega = 2\theta$ and 0.94 for cubic particles. For unknown particle shapes, it is fixed at 0.90, and we will use this value.

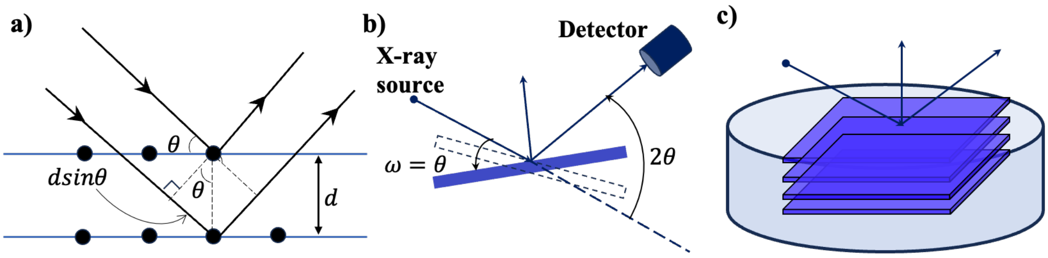

Figure 3.17: **a)** Diffraction of X-rays by a crystal lattice, **b)**and **c)** diffractometer beam path in $\omega = 2\theta$ mode

3.2.5 Surface morphology by AFM

The morphology of the different layers was determined by atomic force microscopy (AFM) in tapping or intermittent contact mode. A probe attached to a cantilever equipped with a piezoelectric oscillator interacts with the surface of the sample by coulombic attraction or repulsion. These interactions cause fluctuations in the amplitude of the oscillations and induce deflections of a laser beam directed at the cantilever; the reflection of this laser beam is detected by a synchronised photodetector. Based on this deflection, the instrument can create an atomic-scale topographic image of the sample surface at the atomic scale. By measuring the distance between the tip and the surface at each scanned point, the AFM can create a three-dimensional map of the sample topography.

3.2.6 Metal-Oxide-Semiconductor (MOS) capacitor analyses

3.2.6.1 Theory

The MOS or MIS (metal-insulator-semiconductor) capacitor is generally the basic building block of many semiconductor devices. A MOS structure can be simply defined as a capacitor whose value is a function of gate voltage. It is useful for the study of semiconductor surfaces. In a MOS structure, the oxide (insulator) must be of sufficient quality and thickness to minimise the leakage current between the metal and the semiconductor. This is especially true for SiO_2, which is obtained by thermal growth on clean Si surfaces. Thermal oxide have very few defects (mobile charges, fixed charges, etc.) and induce very low densities of interface states (Dits) with the semiconductor (Si). In the case of high defect densities, and if necessary, N_2H_2 annealing (425 °C, 30 minutes) can passivate the interfacial traps to density limits of $\sim 10^{10}\text{cm}^{-2}$. The reduction of Dits prevents pinning of the Fermi level [213] and allows a more accurate determination of the work function of the metal (gate). This section will describes the principle of determining the work function using simple MOS structures.

3.2.6.2 Ideal MOS structure

An ideal MOS (see **Figure** 3.18.**a**) is a theoretical model in which, under all bias conditions, no leakage current between the metal and the semiconductor (the insulator resistivity is infinite) and no charge is stored in the insulator. The only charges present in the structure are those in the semiconductor and those of opposite sign, but equal magnitude, at the metal-insulator interface, i.e., there are no interface traps or oxide charges of any kind. In practice,the real MOS is not perfectly ideal, but the ideal MOS serves as a theoretical reference for analysis. The total capacitance at a given gate voltage is expressed by the following relation:

$$C = \frac{C_s C_{OX}}{C_s + C_{OX}} \tag{3.2.23}$$

Where $C_{OX} = \varepsilon_{OX}/t_{OX}$ is the oxide capacitance and corresponds to C_{max} in accumulation regime, and C_s is the semiconductor capacitance and depends on the applied gate voltage, The relation between V_g and C_s is expressed by the following equation[214, 215]:

$$\begin{cases} C_s = -\dfrac{dQ_s}{d\psi_s} \\ Vg = \phi_m - \phi_s + \psi_s - \frac{Q_s}{C_{OX}} \end{cases} \tag{3.2.24}$$

Q_s is the solution of Poisson's equation whose analytical expression is easily found in the Boltzmann approximation, but in the degeneracy regime this approximation is no longer valid[214]. Nevertheless, a numerical solution that takes quantum effects into account can be found by numerically solving the Poisson-Schrodinger equation.
In the absence of an applied voltage and when the work function of the metal and the semiconductor are equal, the flat-band condition (see **Figure** 3.18.**b**) is given by the following relation:

$$\phi_m - (\frac{E_g}{e} - \phi_p) = 0 \tag{3.2.25}$$

For different work functions of the metal and the semiconductor, there is a certain value of the gate voltage, called the flat-band voltage V_{fb}, for which the flat-band condition is achieved, $\psi_s = 0$. The net charge is zero at the surface of the substrate.
The substrate capacitance is by:

$$C_{sfb} = \frac{\varepsilon_s}{L_d} \tag{3.2.26}$$

where L_d is the Debye length and is given by $L_d = \sqrt{\frac{\varepsilon_s kT}{e^2 n_N}}$ and ε_s the semiconductor permittivity.
In the presence of polarisation, three cases can occur at the surface of the semiconductor:

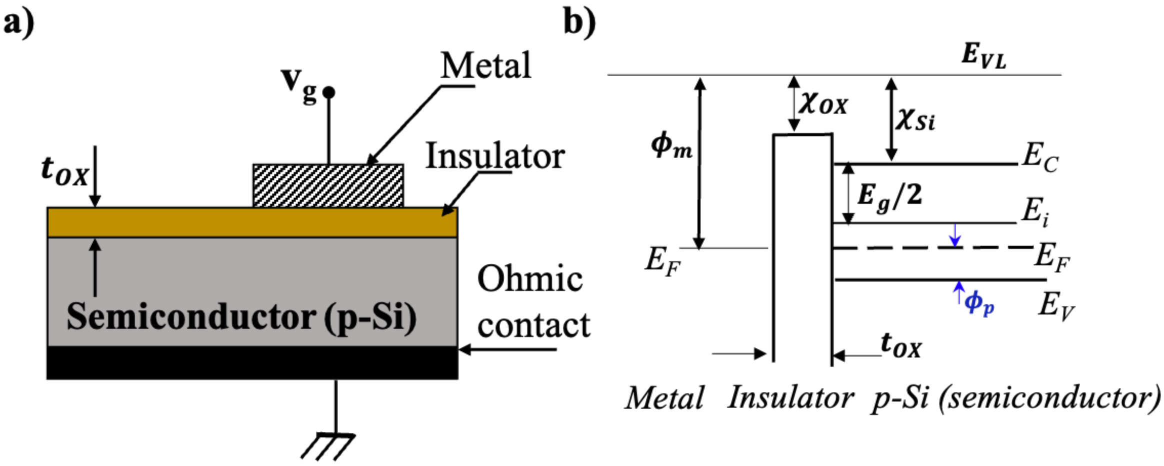

Figure 3.18: **a)** Ideal metal-insulator-semiconductor capacitor structure, **b)** energy-band diagrams of ideal p-type MOS capacitors at equilibrium V = 0.

At negative bias (**Figure** 3.19.**a**) and $V_g \ll V_{fb}$, near the semiconductor surface, the band edges bend upward and approach the Fermi level, leading to a strong accumulation of majority carriers (holes) and total capacitance $C \sim C_{OX}$.

When the polarisation is such that $V_g > V_{fb}$ (see textbfFigure 3.19.**b**), the band edges bend downward and the majority carriers are depleted a depth W in silicon substrate, this is the depletion regime. The semiconductor capacitance is defined as:

$$C_s = \frac{\varepsilon_s}{W} \tag{3.2.27}$$

Finally, when the gate voltage is very high compared to the flat band voltage, $V_g \gg V_{fb}$ (**Figure** 3.19.**c**), the band edges are bent down significantly and an n-type region is formed on the surface of the semiconductor due to the accumulation of minority carriers, this is the inversion regime, The total capacitance $C \sim C_{OX}$.

Experimentally, the inversion is observed only at low frequencies; at high frequencies, the minority carriers do not have enough time to respond to the potential variations, and the lifetime of the minority carriers is less than the period of the 1/f signal AC (where f is the frequency of the electrical excitation). The C(V) curve in **Figure** 3.20 illustrates the different operating regimes of the capacitor as described above.

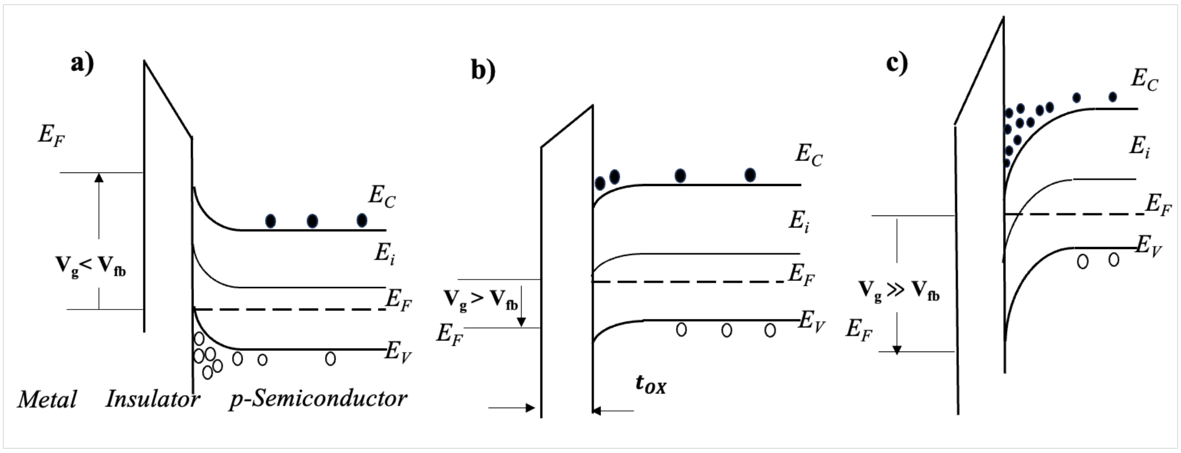

Figure 3.19: Energy-band diagrams for ideal p-type MOS capacitors under different bias, for **a)** accumulation, **b)** depletion, and **c)** inversion regimes.

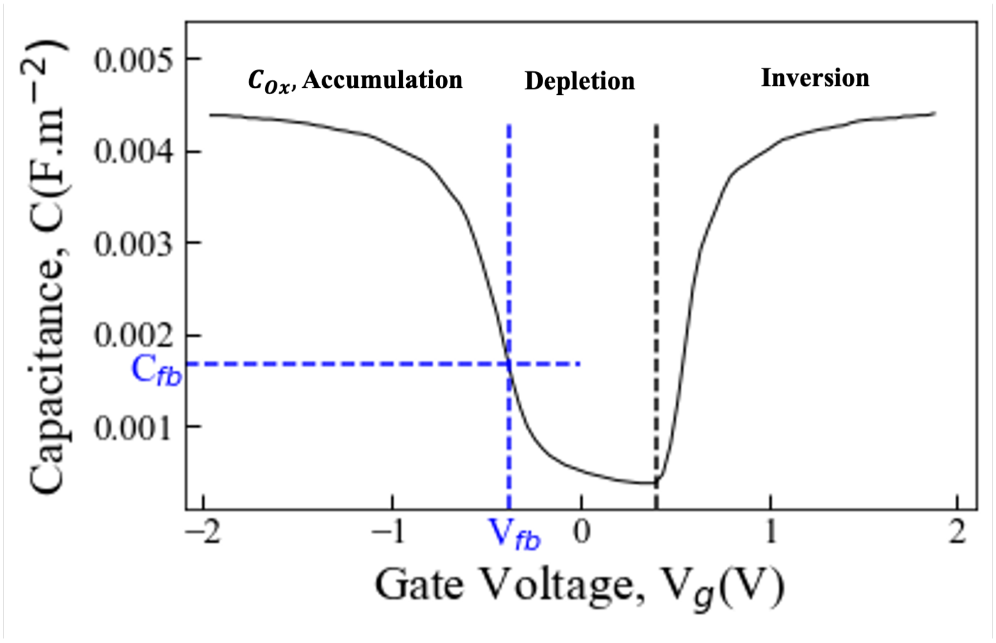

Figure 3.20: Ideal p-type MOS C-V curve obtained from one dimensional Poisson-Schrodinger simulations[216], with Na = 10^{15}cm^{-3}, t$_{OX}$ = 7.2 nm, and A = 3.72×10^{-8}cm^2

3.2.6.3 Gate work function

The energy band diagram of a MOS structure for a voltage $V_g = V_{fb}$ such that the flat band condition is achieved is shown in **Figure** 3.21. By comparing the measured C(V) curves with the theoretical model, it is possible to determine the various parameters useful for determining the work function and calculating the Dits. One important parameter is the equivalent oxide thickness (EOT), i.e., the thickness of a SiO_2 layer with the same electrical properties as a layer of high-k dielectric. It can be easily determined from the capacitance $C_{max} = C_{OX}$. However, this formula does not take into account the residual capacitance C_s of the semiconductor in the accumulation region and other effects that may be due to quantum confinement at the dielectric/semiconductor interface, so the error in determining the EOT can be considerable, especially for very ultra-thin dielectric layers, comparable to the de Broglie wavelength of the charge carriers.
To reliably extract the various parameters, we used solutions of the one-dimensional Poisson-Schrodinger equation that take into account the dependencies of the charge Q_s and the capacitance C_s on the potential at the semiconductor surface for different doping levels of the substrate[216]. The important parameters were determined by fitting our C(V) measurements to these data using a simple Python script (see Appendices). The substrate doping is determined directly by the simulation. Within the Boltzmann approximation, the substrate doping can also be determined from the C_{smin} by the expression :

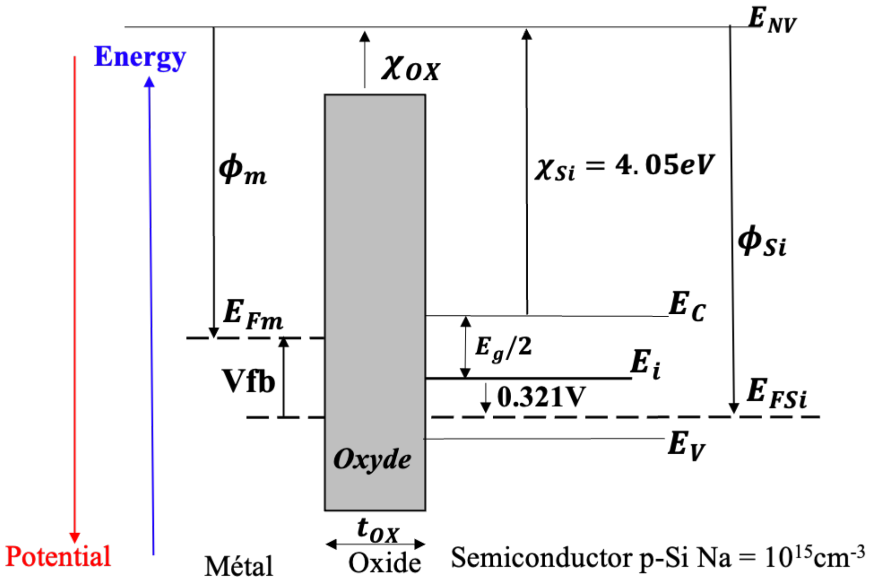

Figure 3.21: Energy band diagram of a p-type MOS capacitor in flat-band conditions, Na = 10^{15}cm^{-3}.

$$Cmin = \frac{\varepsilon_s}{W_{max}} \tag{3.2.28}$$

where is the depletion depth limit and is given by the following relation[214]:

$$W_{max} = \sqrt{\frac{2\varepsilon_s}{eN_a}\left(2.10(ln\frac{N_a}{n_i}) + 2.08\right)} \tag{3.2.29}$$

The flat band capacity C_{fb} can be calculated from the relation 3.2.23 by replacing C_s by C_{sfb}, the value of the gate potential corresponding to the C_{fb} can be read directly from the C-V curve, this value is nothing other than the V_{fb}:

$$V_{fb} = \phi_m - \phi_s = \phi_m - \phi_{Si} \tag{3.2.30}$$

The V_{fb} defined above depends on the oxidation temperature, the crystalline orientation of the substrate, the density of traps at the interface Dits, the annealing at low temperature, etc. The real expression of the V_{fb} is given by the following relation[199]

$$V_{fb} = \phi_m - \phi_{Si} - \frac{Q_{tot}}{\varepsilon_{OX}} EOT \tag{3.2.31}$$

Where Q_{tot} is the sum of all oxide and interface charges and ε_{OX} the oxide permittivity.
Thus, knowing the Si work function does not allow us to determine the actual gate work function. To determine the ideal V_{fb} accurately, we need to eliminate all the effects associated with the oxides and interface charges.
The methodology adopted consists of using different thicknesses of oxide (SiO_2), an even more appropriate method is the use of oxide bevelsLachaume, as it allows you to work on the same substrate and oxide with different thicknesses. A plot of V_{fb} as a function of EOT will then give a straight line with slope $Q_{tot} / \varepsilon_{SiO_2}$, while the y-intercept (EOT = 0) will give the flat band voltage $\phi_m - \phi_{Si}$.

3.2.6.4 Interface trapped charge densities extraction

There are several methods for extracting Dits, here we will use the simple method proposed by Castagné *et al* [217]. The density of interfacial states Dits is estimated from the difference between a measurement C(V) at high frequency C_{hf}), which should not include the contribution of the interfacial trap states, and another measurement at low frequency $C_{lf)}$, which should include all the contribution of the interfacial trap states :

$$Dits = \frac{1}{e}\left(\frac{C_{OX}C_{lf}}{C_{OX} - C_{lf}} - \frac{C_{OX}C_{hf}}{C_{OX} - C_{hf}}\right) \tag{3.2.32}$$

3.2.6.5 Application: p-Si/SiO_2/Al (reference)

Metal oxide semiconductor structures (MOS) for capacitance-voltage measurements and analysis were fabricated as follows. We used boron-doped p-Si C_z (100) substrates with resistivity values ranging from 0.8 to 4 Ω.cm. The surfaces of the substrates were first chemically cleaned by Caro + Dip HF 20s 1% +RCA and then thermally oxidised in an O_2+HCl atmosphere (HCl is used to limit metal contamination) at 900 °C. Growth times were defined for SiO_2 layers with thicknesses of 10 nm, 20 nm and 30 nm.

The oxide thicknesses were verified by ellipsometry (NANOMETRICS ATLAS II). The oxidised substrates were then annealed in a N_2H_2 gas environment at 425 °C for 30 minutes (FGA) to obtain a Si/SiO_2 interface with a low interface state density (Dit) of the order of 10^{10} $cm^{-2}eV^{-1}$ (verified by Hg drop measurements on CVmap). The 150 nm thick aluminium contacts were deposited on the different oxide thicknesses by thermal evaporation through a metal mask to define the surface of the capacities. An optical microscope image of the different devices is shown in **Figure** 3.22. After Al deposition, some devices were treated with a second FGA to restore the Si/SiO_2 interface.

3.2.6.6 Application to MOS capacitor with an ITO-H gate

Measurements on the MOS devices were made using an Agilent 4284A C(V) capacitance meter. The C(V) analyser applies an AC signal (frequency between 100 Hz and 1 MHz) V_g(t), which is superimposed on a main DC signal, on the gate contact (high terminal). The induced current

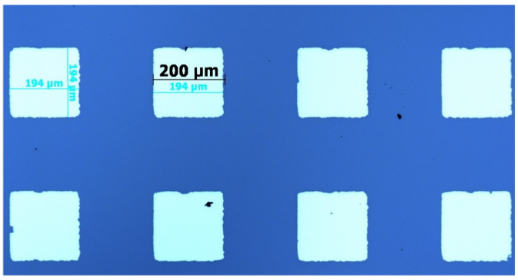

Figure 3.22: Optical microscope image of fabricated MOS structures, with corrected area of $\sim 3.72 \times 10^{-8}$ cm^2

is measured through the substrate via another probe (chuck), which is connected to earth (low terminal), and the capacitance is then calculated. The value of the gate work function was estimated from the C(V) curves obtained as follows. The values of V_{fb} and EOT were determined by fitting the experimental curves to the theoretical model. A comparison between the C(V) curves (t_{OX}= 10 nm) and simulation before and after FGA are shown in **Figure** 3.23 **a** and **b**. There is a significant reduction in Dits after FGA, comparing the high-frequency (500 kHz) and low-frequency (500 Hz) C(V) curves.

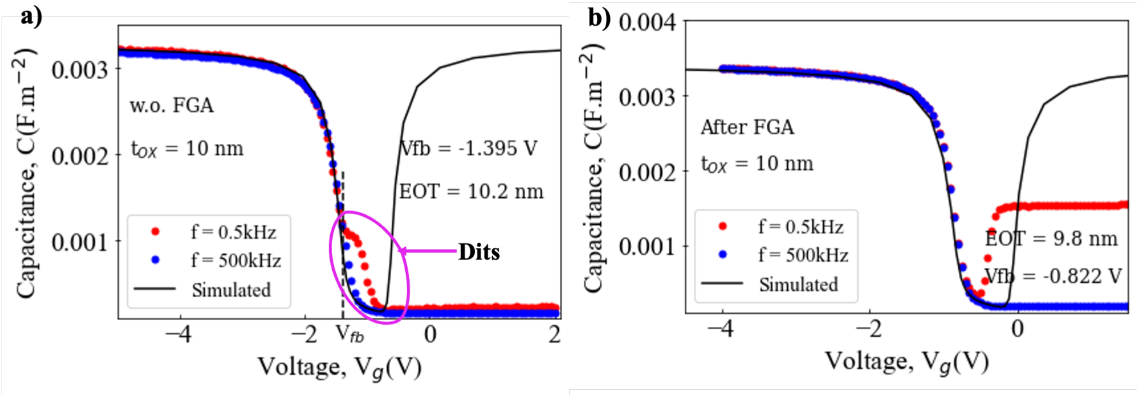

Figure 3.23: Fitting of C(V) measurements of Al//SiO$_2$//p-Si structures for t_{OX} = 10 nm of SiO$_2$ at high and low frequency, **a)** without FGA, **b)** after FGA

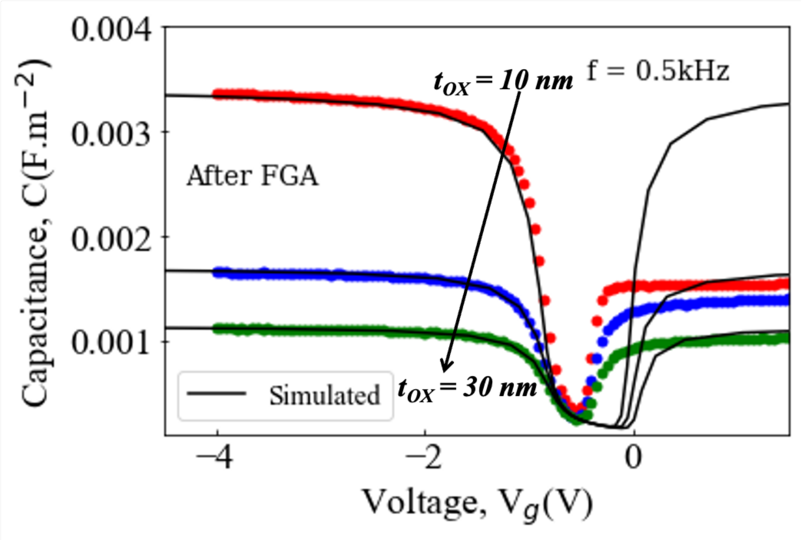

Figure 3.24: Fitting of C(V) measurements of Al/SiO_2/p-Si structures for different SiO_2 thicknesses after FGA. The measurements were carried out at low frequency (quasi-static mode)

The flat band potential and EOTs are extracted for different oxide thicknesses (3.24). The relationship between flat band voltage (V_{fb}) as well as Dits and SiO2 thickness (t_{OX}) or EOT for experimental samples was plotted.

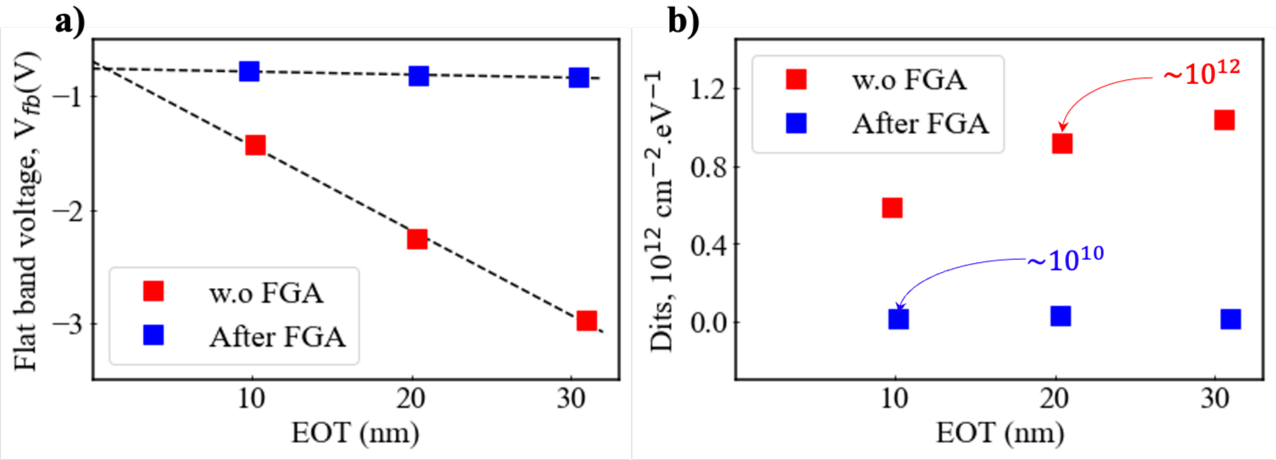

Figure 3.25: **a)** Relation between flat-band voltage V_{fb} and EOT, Interface defect density Dits for different SiO_2 thicknesses t_{OX} without and after FGA.

	V_{fb}(V)	WF_{Si}(eV)	WF_{Al} (eV)	Dits ($cm^{-2}eV^{-1}$)
w.o. FGA	**-0.66±0.07**	**5.02**	**4.28±0.07**	$\sim 10^{12}$
After FGA	**-0.765±0.004**	**5.02**	**4.185±0.004**	$\sim 10^{10}$

Table 3.3: Al work function extracted using the C(V) technique

The **Table** 3.3 summarises the various parameters extracted using the C(V) technique. The work function of Al (∼ 4.2 eV) is effectively obtained in both cases. We also note that after FGA, the flat-band potential no longer varies independently of the thickness of the oxide, reflecting global a reduction of charge in oxyde or at interface. Meanwhile, the Dits are drastically reduced (from,10^{12} to 10^{10} $cm^{-2}.eV^{-1}$). This gate will be used as a reference for all future work function extraction studies using the C(V) method.

Chapter 4

Transparent electrode based Sn-doped In_2O_3 and In_2O_3 and the effect of hydrogen doping

4.1 Introduction

In_2O_3-based transparent conductive films are one of the best TCO because they have optical and electrical properties superior to those of all other TCO. They are widely used as transparent electrodes in solar cells, display technologies (screens), LEDs, photodiodes, and many other optoelectronic applications. They are extremely stable, compatible with many types of substrates (rigid, flexible, polymer, etc.), and can be deposited using a variety of techniques (physical and chemical). These materials are also suitable for industrial etching [218]. As pointed out in the previous sections, the electrical and optical properties of TCO in general, and of In_2O_3-based TCO in particular, strongly depend on the oxygen concentration (or oxygen vacancies). In fact, the oxygen concentration of TCO determines the density of free carriers and strongly affects the mobility of these free carriers. In the case of ITO ($In_2O_3 : Sn$), intentional Sn doping also affects the density of free carriers and the properties of the deposited films. In the Kroger-Vink notation, the phenomena of doping by $V_O^{\bullet\bullet}$ oxygen vacancies (two-electron donors) and substitution of In atoms (In^{3+} cation) by Sn atoms (Sn^{4+} cation) are described by the following relations [219]:

$$O_O^{\times} \longrightarrow \frac{1}{2}O_2(g) + V_O^{\bullet\bullet} + 2e' \tag{4.1.1}$$

and

$$(2Sn_{In}^{\bullet}O_i'')^{\times} \longrightarrow \frac{1}{2}O_2(g) + 2Sn_{In}^{\bullet} + 2e' \tag{4.1.2}$$

Oxygen concentration can be precisely controlled during deposition by adjusting deposition parameters such as oxygen concentration in deposition atmosphere is $O_2(\%) = \dfrac{100 \times O_2}{O_2 + Ar}$, total deposition pressure, or substrate temperature.The doping reaction by neutral defects $(2Sn_{In}^{\bullet}O'')^{\times}$ (**Equation**7.0.1 and 7.0.2) depends not only on the Sn concentration, but also on the temperature (thermally activation mechanism), therefore, the growth of ITO films with optimal electrical and optical properties is generally achieved at temperatures between 150 - 400°C [109, 220, 221]. In this study, the material (especially PbS QDs) on which the transparent contacts are made does not allow the use of such thermal budgets. Therefore, close control of the oxygen partial pressure and the total deposition pressure is required to obtain high quality thin films at room temperature. On the deposition tool (**Figure** 3.5), we use an Ar+3%H_2 gas feed line that allows us to grow H-doped films such as hydrogen-doped indium oxide (In_2O_3:H or IOH) or hydrogen-doped indium tin oxide (H-ITO). The successful use of hydrogen as a dopant in TCO during sputtering process has already been demonstrated for ITO[222] or ZnO[223]. IOH is known to be a promising candidate for applications requiring high conductivity while maintaining good IR transparency. Its low preparation temperatures make it a suitable candidate for low-temperature applications, such as deposition on temperature-sensitive materials or in applications requiring deposition on plastic or polymer substrates [224, 225, 226]. Theoretical studies on hydrogen configuration in In_2O_3-based TCO have shown that interstitial or substitutional hydrogen on an oxygen site behaved as a shallow donor [227]. In addition, hydrogen incorporated at grain boundaries is considered as passivation of defects to reduce electron transport barriers (carrier mobility enhancement) [228, 229, 230, 231]. The free electron density of IOH is generally a factor of two lower than that of ITO, which can be explained by hydrogen passivation of defects at grain boundaries without the effect of active doping [232], and thus improved mobility.

In the following sections, we present the electrical performance and effects of hydrogen doping, optical properties, and structural aspects of tin-doped indium oxide films deposited by PVD at room temperature. We show the results of measuring the work function of the film with the best electrical and optical properties, and discuss the plasma damage effects related to the sputtering phenomenon. We will then compare the optimum electrical and optical properties of different In_2O_3-based oxides with different Sn concentrations as well as samples with and without hydrogen doping. Finally, we will conclude on the choice of a transparent electrode for optoelectronic devices in the IR range.

4.2 Sn-doped In_2O_3 films by RF sputtering and the effect of hydrogen doping

4.2.1 Experimental

Diffrent layers of IOH (hydrogen doped indium oxide), H-ITO (hydrogen doped indium tin oxide) and ITO (indium tin oxide) were deposited by RF magnetron sputtering on an Alliance Concept Cluster Tool machine (AC CT200) using commercial targets of In_2O_3, In_2O_3-doped Sn 1% and Sn 10% with purity 99.99% and density greater than 95%, with diameter of 101 mm in diameter and 6 mm thickness, supplied by *Kurt J. Lesker Company Ltd* (section **3.1.3**). Oxygen and Ar were used as process gases. For IOH and H-ITO deposits, Ar is replaced by an $Ar+3\%H_2$ mixture. As is mentioned earlier, the resistivity of indium oxides is improved with deposition temperature, but in our study the H-ITO electrode will be deposited on a material (PbS QDs) that is highly temperature-sensitive. Therefore, the deposition parameters were carefully tuned to ensure the growth of high-quality indium oxide-based TCO films at room temperature. To achieve this, an optimum oxygen partial pressure and sputtering pressure were determined.
The deposition rate of H-ITO (Sn 1%) as a function of oxygen partial pressure for a power of 50 watts and a sputtering pressure of 0.001 mbar is shown in **Figure** 4.1. The deposition rate decreases with increasing oxygen pressure. An increase in oxygen flow leads to a decrease in the concentration of the sputtering species (Ar^+), resulting in a decrease in sputtering yield and thus a decrease in deposition rate.

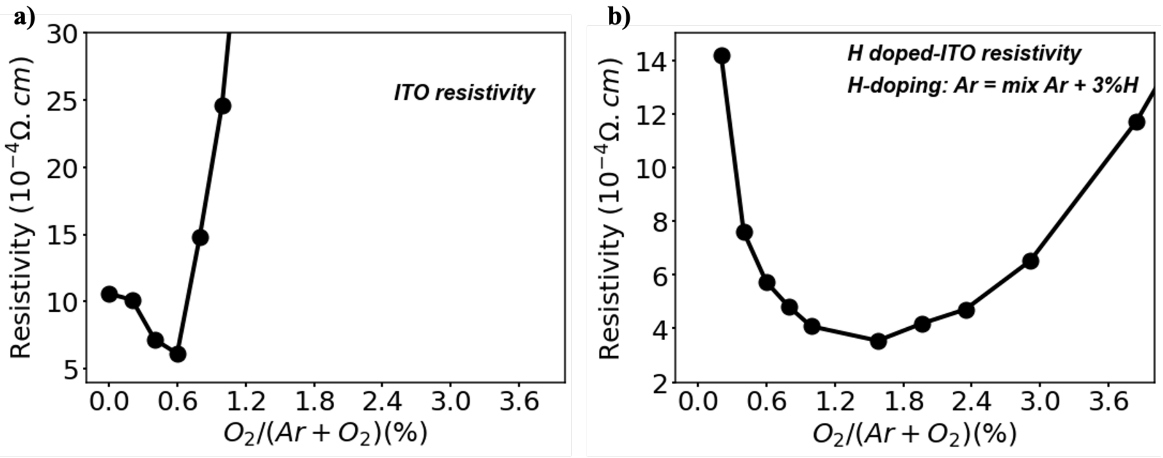

H

Figure 4.2: Resistivity of ITO and H-ITO (Sn 1%) as a function of oxygen concentration for $\sim$ 50 - 60 nm deposited on SiO$_2$ (500 nm) at room temperature and at a total pressure of 0.001 mbar, **a)** without hydrogen doping (ITO) and **b)** with hydrogen doping (H-ITO).

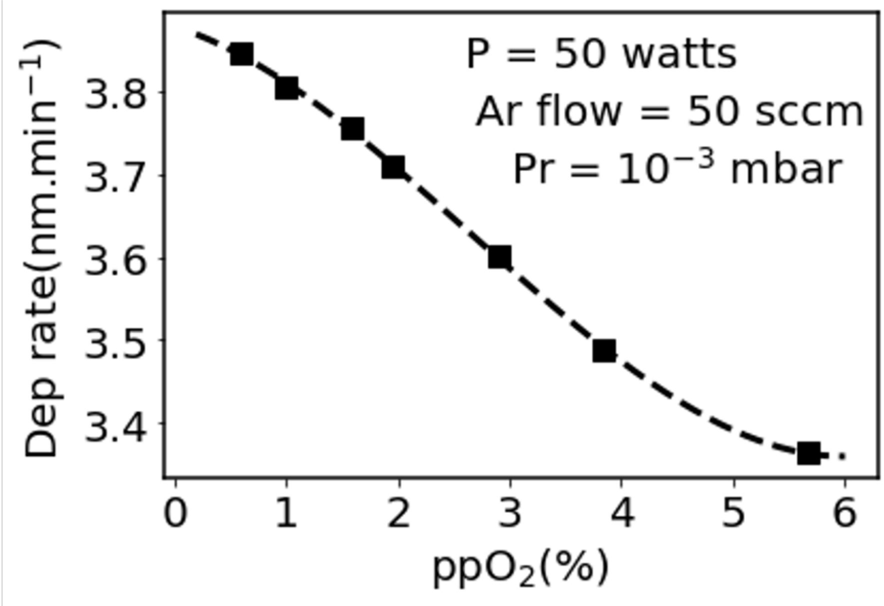

Figure 4.1: Deposition rate as a function of oxygen partial pressure for hydrogen-doped ITO (Sn 1%) at a sputtering power of 50 watts.

4.2.2 Electrical properties

The electrical resistivities measured by the van der Pauw four-probes technique for samples with thickness $\sim$ 50 nm , without and with hydrogen doping are shown in **Figures** 4.2**a** and 4.2**b** respectively. We found an optimum oxygen concentration of $\sim$ 0.6% for the non-hydrogen-doped samples (**Figure** 4.2**a**), corresponding to a resistivity of 6.12×10^{-4} Ω.cm, while the optimum for the hydrogen-doped films was 1.6%, corresponding to a resistivity of 3.73×10^{-4} Ω.cm. The resistivity of the hydrogen-doped films is comparable to that of ITO films deposited at high temperature [221, 233]. We also achieved very good uniformity with a standard deviation of less than 2% for sheet resistance measurements of 49 points on 200 mm substrate for the optimal recipes (**Figure** 4.3).

In the following, the properties of H-ITO samples (Sn 1%) at three different oxygen partial pressures (at the optimum oxygen concentration of 1.6%, the lowest and the highest oxygen

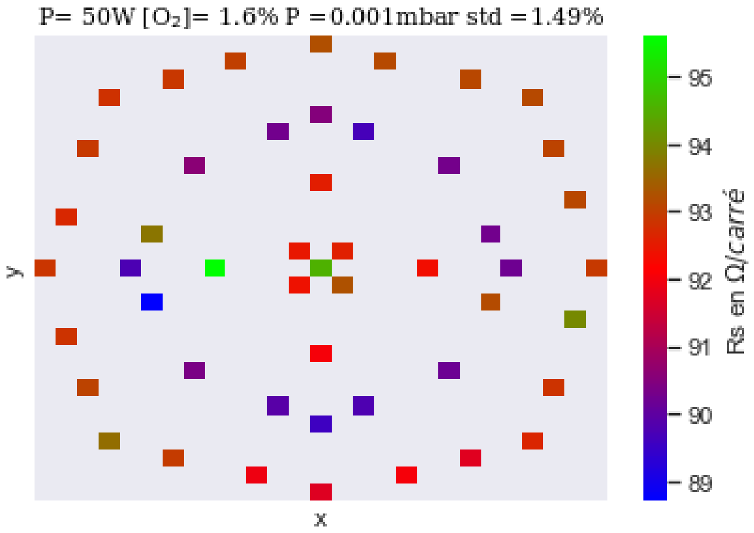

Figure 4.3: Film uniformity for ∼ 50 nm H-ITO, resistivity measurements of 49 points on 200 mm SiO$_2$ substrates for optimum oxygen concentration (1.6%).

concentration of 0.2% and 5.7%, respectively) are discussed.

Measurements of charge carrier mobility and density (**Figure** 4.4) show that as oxygen pressure increases, the density of oxygen vacancies incorporated into the film decreases, resulting in a decrease in the density of free charge carriers. The density value determined for the best recipe (ppO$_2$ = 1.6%) is 5.56×10^{20}cm^{-3}. Although it should be noted that the charge carrier density of ITO deposited at higher temperatures can reach 1×10^{21} cm^{-3} (highly degenerated semiconductor). Highly degenerated TCO films are not suitable for applications in the IR region, because the high charge carrier density leads to an increase in plasma frequency ω_p, resulting in stronger electron-photon interaction and lower optical transmission in the IR region. On the other hand, high degeneracy leads to an increase in the optical gap (Moss-Burnstein shift), making films with very high charge densities suitable for applications in the visible range.
The mobility increases as the free charge carrier density decreases. Mobility depends mainly on the density of ionised impurities, especially oxygen vacancies and Sn^{4+} ions, which in turn are related to the number of free charge carriers. In analogy to the evolution of the density of free charge carriers with the oxygen partial pressure, the mobility increases as the oxygen pressure increases. Hall measurements show that careful control of oxygen partial pressure allows the best compromise between mobility and free carrier density, which corresponds to the lowest electrical resistivity.

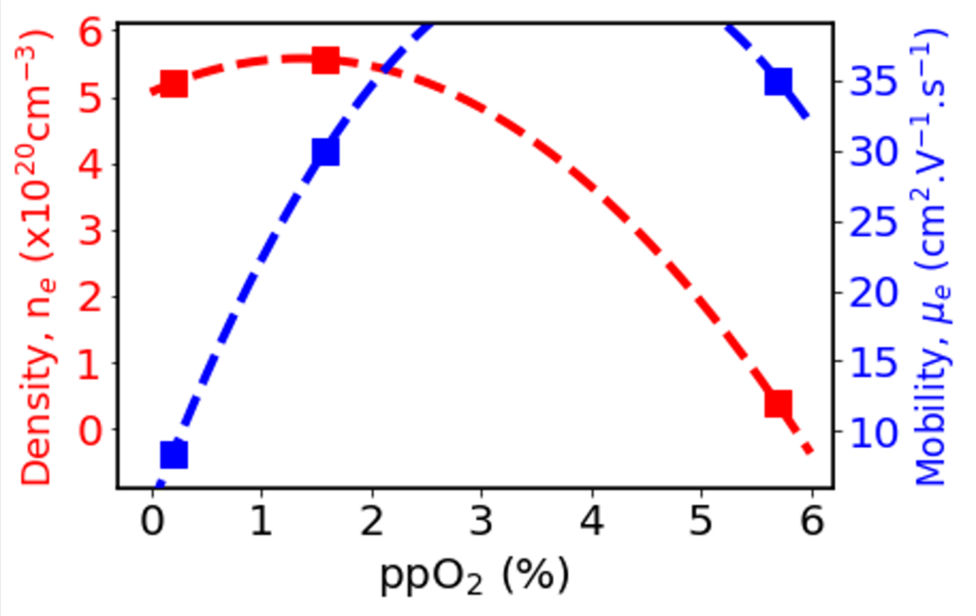

Figure 4.4: Free carrier density and Hall mobility versus oxygen deposition pressure H-ITO (Sn 1%)

4.2.3 Optical properties

Optical transmission and reflectance measurements for 50 nm H-ITO films of different oxygen concentration deposited on glass substrates (Corning Glass) are shown in **Figure** 4.5.**a** The best recipe (oxygen concentration = 1.6%) demonstrated an optical transmission of over 80% in the 600-1800 nm region. As the oxygen concentration increases, the concentration of free carriers decreases and reduces the absorption of light in the IR region, and therefore improving the optical transmission.

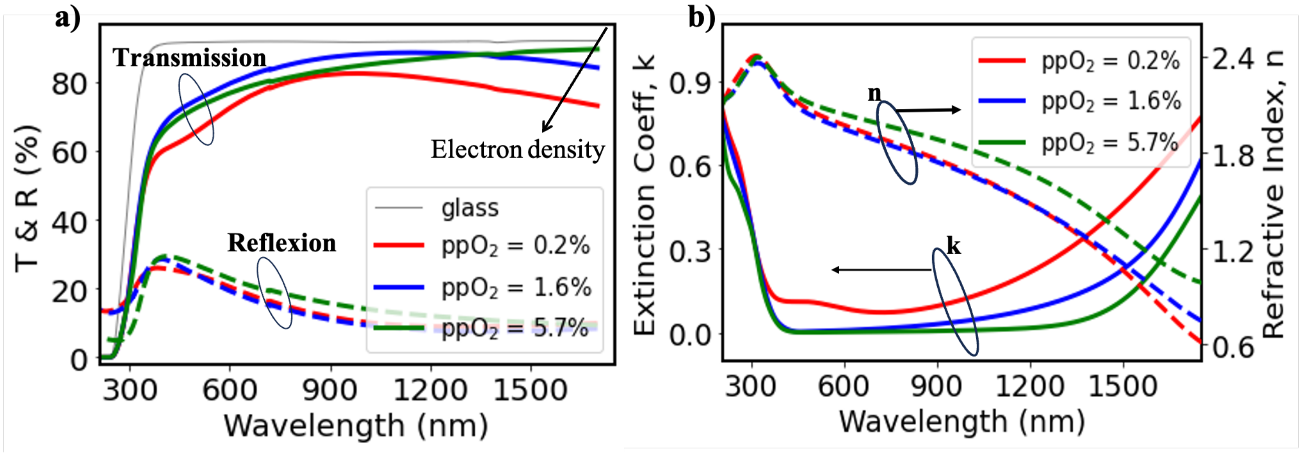

Figure 4.5: **a)** Optical transmission T and reflexion R , **b)** extinction coefficient k and refractive index n, of 50 nm H-ITO (Sn 1%) films deposited at different oxygen pressures

Figure 4.5.**b** shows the refractive index **n** and extinction coefficient **k** of ITO films deposited on Si substrates under different oxygen pressures and measured by spectral ellipsometry. With increasing oxygen pressure, the refractive index n of the H-ITO film increases and the extinction coefficient decreases in the Vis and IR regions. An increase in oxygen concentration leads to a decrease in oxygen vacancies and consequently to a decrease in carrier concentration, resulting in

lower optical losses in H-ITO thin films. These results are consistent with optical transmission and Hall effect measurements.
The extinction coefficients of H-ITO for different oxygen concentrations at some wavelengths of interest are listed in **Table** 4.1. The optical band gap E_{gopt} is calculated from the extrapolation of

Oxygen concentration (%)	k @633 nm	k @940 nm	k @1360 nm
0.2	0.079	0.105	0.327
1.6	0.009	0.035	0.141
5.7	0.002	0.006	0.042

Table 4.1: H-ITO (Sn 1%) extinction coefficients for different oxygen concentrations at several relevant wavelengths.

α^2 (where α is the absorption determined from the reflection coefficient) as a function of photon energy hν (Tauc-plot), as described in section **2.3.2.3**. **Figure** 4.6 shows the extrapolation of the absorptivity for three 50 nm H-ITO films at different oxygen pressures. The intercept of the x-axis corresponding to the optical gap decreases at higher oxygen pressure due to the difference in charge carrier density.

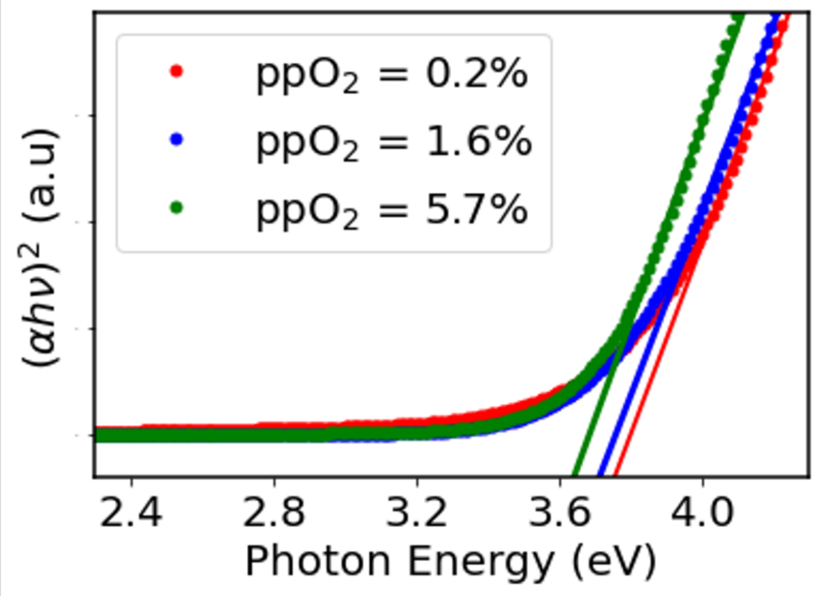

Figure 4.6: Optical band gap extraction images (Tauc-plot) of H-ITO (Sn 1%) thin films with different oxygen partial pressures.

According to the Moss-Burnstein relation, the optical gap should increase with carrier concentration as a function of $\mathbf{n}^{2/3}$. We also find that the optical gap is larger than 3.6 eV, and this large gap width explains the high transmission of In_2O_3-based TCO. Knowing the density and the optical gap and assuming that the band gap is changed only by the Moss-Burnstein effect, it is possible to estimate the fundamental gap E_{g0} and the reduced effective mass m∗. In this case, the fundamental gap and the effective mass correspond to the y-axis intercept and slope of the curve $E_{gopt} = f(n^{2/3})$, respectively. In reality, however, this measurement is complex because there is a band-gap narrowing effect that is the opposite of the Moss-Burnstein effect, known as the Hamberg and Granvqist effect, which is due to the electron-electron and electron-impurities scattering [100]. This phenomenon of band-gap narrowing is well known for Si with significant doping[234].

4.2.4 Surface morphology

In **Figure** 7.10 and **Figure** 4.8, we show the 2D and 3D morphologies of H-ITO (Sn 1%) and H-ITO (Sn 10%) thin films for different oxygen pressures deposited on Si substrates (1×1 μm scan). All thin films exhibit a smooth surface morphology, as expected due for the low deposition power (50 watts) and low deposition pressure (0.001 mbar). The grain size is larger with the Sn doping of 10 wt%. The roughness (RMS) is less than 1 nm in both cases (**Figure** 4.9). The roughness also decreased with decreasing oxygen pressures.

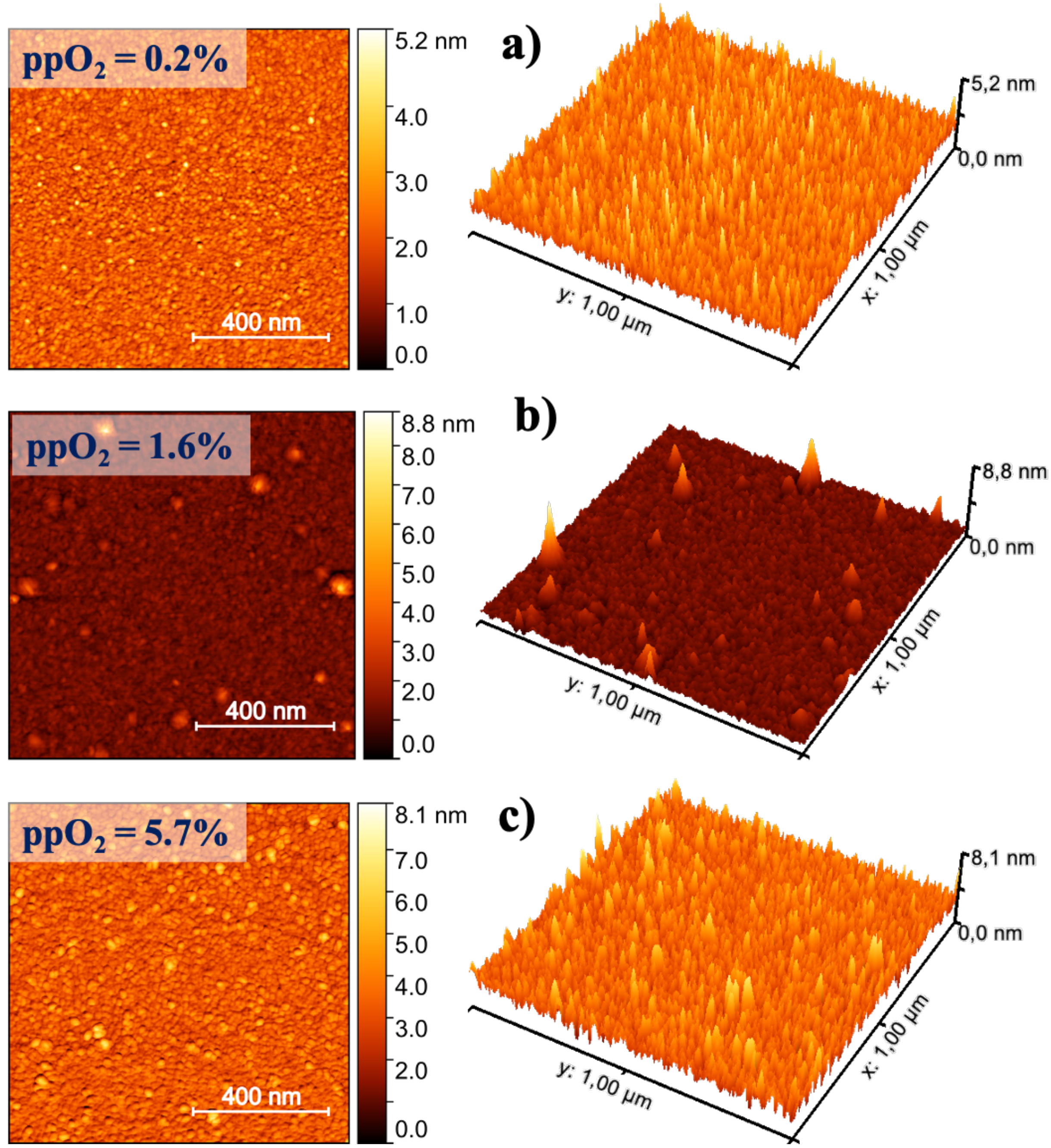

Figure 4.7: 2D and 3D Atomic force microscopy (AFM) micrographs showing the surface of H-ITO (Sn 1 %) films deposited on Si substrates with different oxygen partial pressures

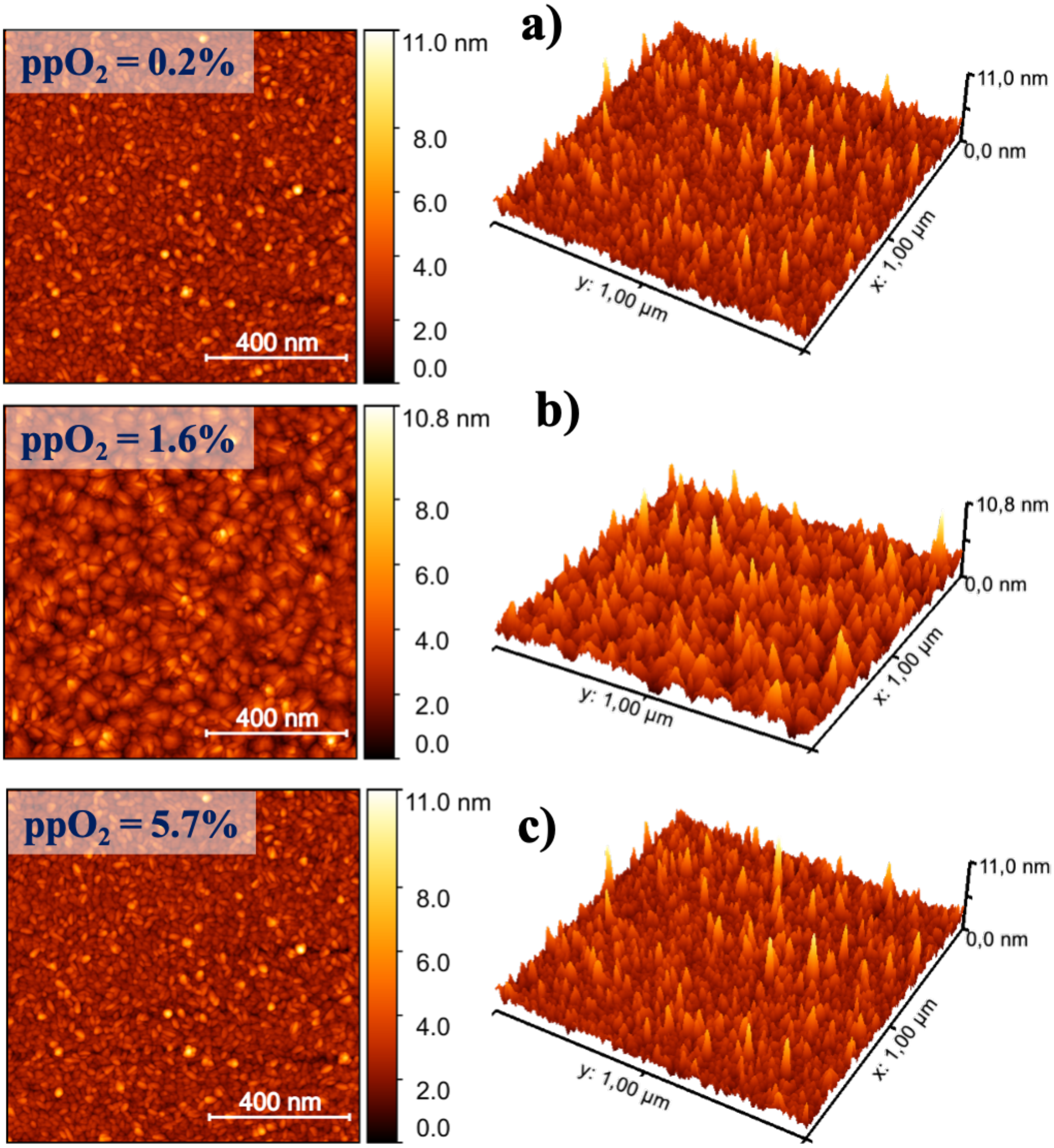

Figure 4.8: 2D and 3D Atomic force microscopy (AFM) micrographs showing the surface of H-ITO (Sn 10 %) films deposited on Si substrates with different oxygen partial pressures

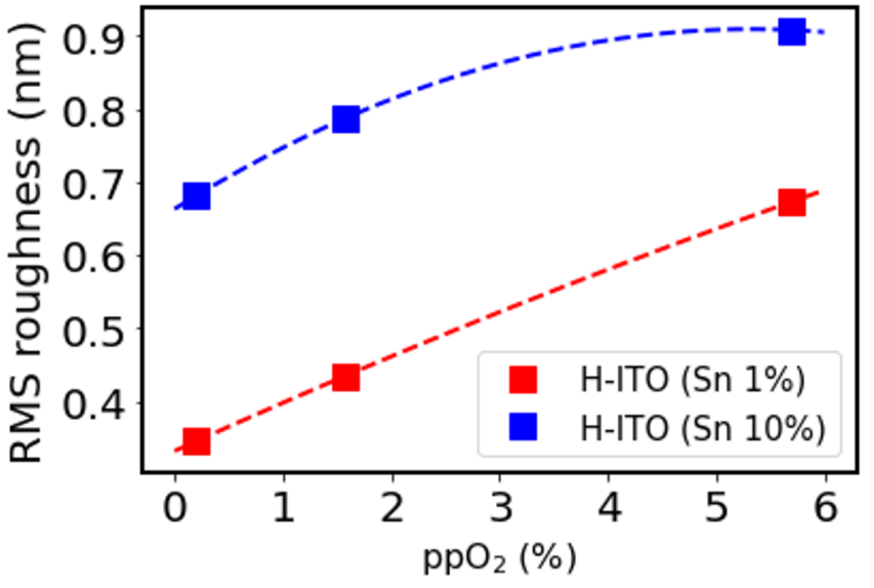

Figure 4.9: Surface roughness (RMS) versus oxygen partial pressure

4.2.5 Structural properties

Figure 7.11.**a** and 7.11.**b** show the structural properties of the H-ITO thin film as a function of oxygen pressure for 1% and 10% of Sn concentrations. Almost all films have a polycrystalline structure with diffraction peaks with (222) and (211) diffraction peaks for certain oxygen pressures, indicating a bixbyite-type cubic structure. Peak intensity generally increased with increasing O_2 concentration. The (440) peak is due to the increase in oxygen concentration (oxygen pressure), and the higher oxygen concentrations induce the formation of In-O bond networks and favour the growth in the direction perpendicular to the (222) plane[235].

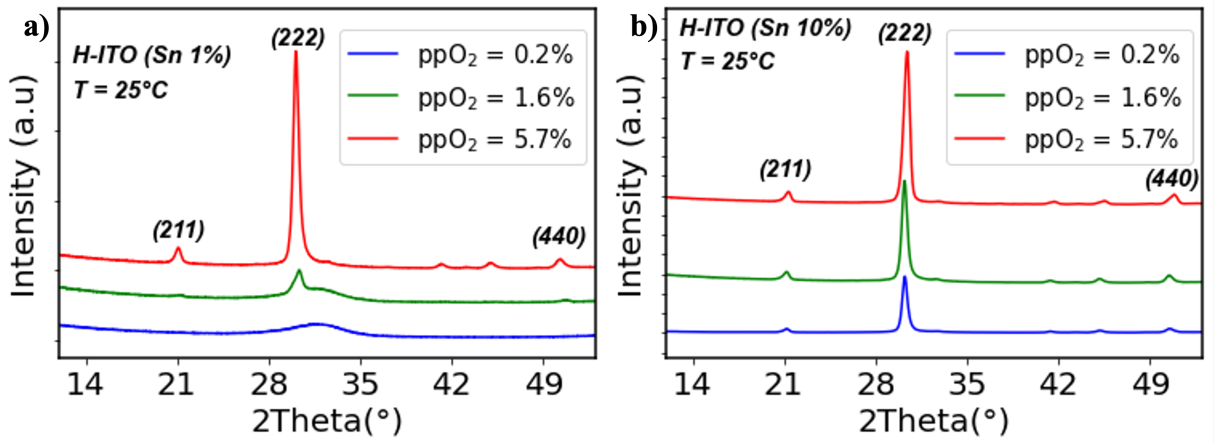

Figure 4.10: X-ray diffraction spectra of H-ITO (thickness of ≈ 60 nm) films grown at room temperature with different oxygen concentration for **a)** Sn 1 % and **b)** Sn 10 % .

It can also be observed that the films doped with 1% Sn are more amorphous than the films doped with 10% Sn, which is consistent with the AFM measurements. The grain size D estimated from the total half-width of the main peak (222), the Bragg diffraction angle and the X-ray wavelength was calculated using the Scherrer formula, D $\sim$ 20 nm for polycrystalline films. Despite the fact that all films have some degree of crystallinity, the structural properties do not provide a straightforward explanation for the electrical properties.

4.2.6 ITO-H (Sn 1%) work function by MOS capacitor analyses

The work function is one of the most important properties of an electrode because it defines the height of the energy barrier at the interfaces with other materials, affects the charge transport mechanisms in the devices, and can have a strong impact on their performance. In this work, the value of the H-ITO work function (Sn 1%) at the H-ITO/SiO$_2$ interface and the impact of process-induced damage during TCO deposition were extracted by C-V measurements and analysed using the method described in section **3.2.5**. For this purpose, devices with H-ITO(60 nm)/SiO$_2$/Si MOS structure and devices with Al(150 nm)/SiO$_2$/Si structure (reference) were fabricated. The effects induced by the H-ITO sputtering process were estimated as Dits and Vfb shifts at the SiO$_2$/Si interface and indium diffusion in SiO$_2$. Post-treatment of the devices, was performed to remove damage at SiO$_2$/Si interface. Their effects on the work function at the interface and Dits are also discussed. As Hall effect measurements have shown, H-ITO has a free carrier density of $n_e > 10^{20}$ cm^{-3}, and a rather low electrical resistivity $\rho \approx 10^{-4}$ Ω.cm, H-ITO behaves well as a semi-metallic material, therefore it is well validated for use as a metallic gate on MOS structures.

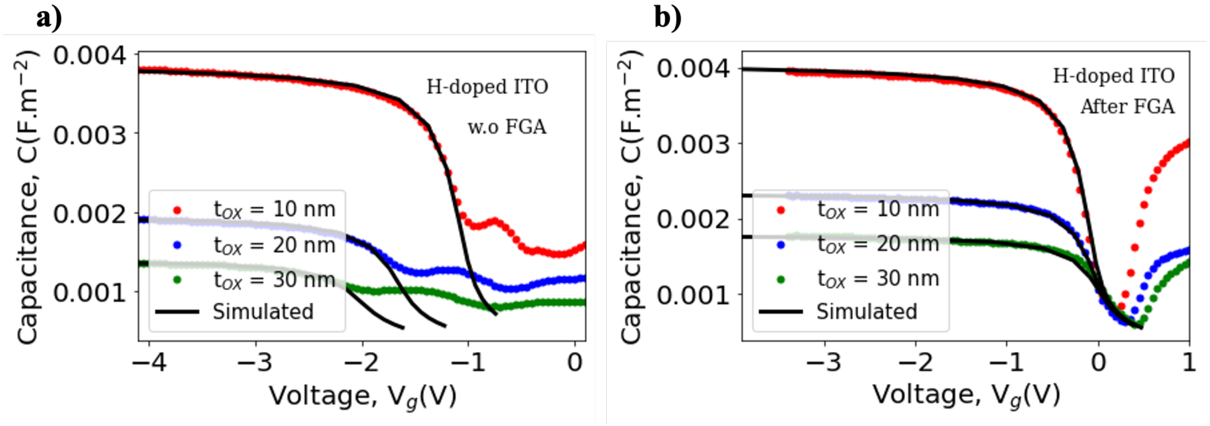

Figure 4.11: C-V curves measured and simulated for H-ITO/SiO$_2$/Si stacks for different SiO$_2$ thicknesses t_{OX} at frequency f = 0.5 kHz, **a)** before FGA and **b)** after FGA.

The experimental and simulated C-V curves of H-ITO(60 nm)/SiO$_2$/Si stacks for different SiO$_2$ thicknesses (10, 20, 30 nm) measured at a frequency of 0.5 kHz before and after FGA are shown in **Figure** 7.12.**a** and 7.12.**b** respectively. It can be seen that the C-V curves before FGA show anomalies in the depletion region, indicating damage caused by the deposition process. The C-V curves before FGA also shift to negative polarizations with increasing t_{OX}.

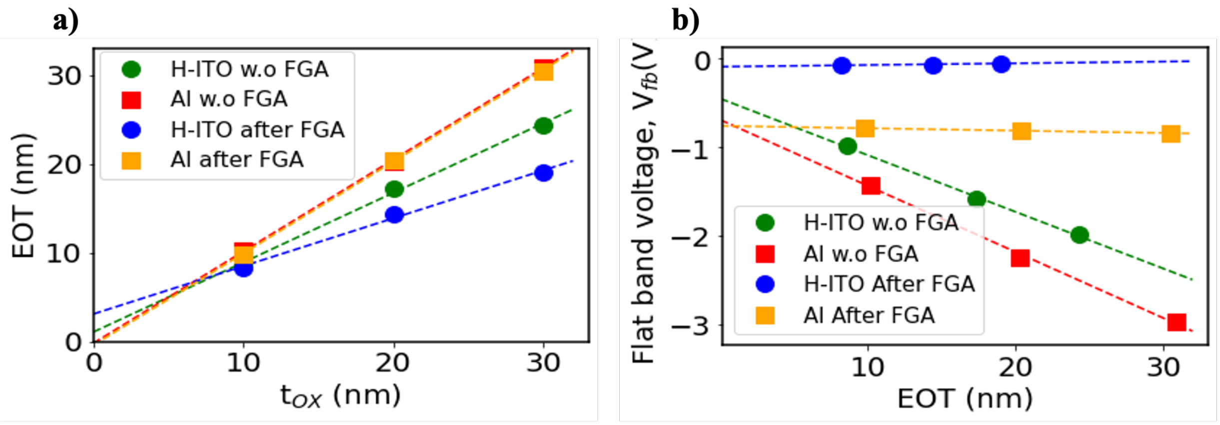

Figure 4.12: **a)** Equivalent oxide thickness (EOT) versus oxide thickness t$_{OX}$ and **b)** relation between flat-band voltage V$_{fb}$ and SiO$_2$ at f = 0.5 kHz, of H-ITO/SiO$_2$/Si stacks compared to Al/SiO$_2$/Si reference stacks before and after FGA.

This shift in V$_{fb}$ suggests that the silicon surface potential varies as a function of fixed charges in the insulator and/or Si/SiO$_2$ interface charges. After FGA, these different effects are no longer observed and the V$_{fb}$ is almost constant with the oxide thickness. **Figure** 7.13.**a** shows the evolution of the EOT values as a function of t$_{OX}$. EOT or equivalent oxide thickness, is given by the following equation:

$$EOT = \frac{\varepsilon_{SiO_2}}{\varepsilon_{OX}} t_{OX} \tag{4.2.1}$$

where ε_{SiO_2} and ε_{OX} are the dielectric constant of the SiO$_2$ and that of the oxide as in the device, respectively. Its value must be equal to t$_{OX}$ if the oxide is SiO$_2$. It can be seen that in the case of H-ITO/SiO$_2$/Si devices, the EOT values do not correspond to the t$_{OX}$ values; this decrease of EOT values compared to the Al/SiO$_2$/Si reference devices reveals a damage of the oxide induced by the H-ITO sputtering process. We will discuss this problem later.
The work function was calculated using the relationship between V$_{fb}$ and EOT. The plot of V$_{fb}$ against EOT can be fitted with linear approximation lines7.13.**b**. The value of V$_{fb}$ extrapolated to EOT = 0 corresponds to the difference $\phi_{H-ITO} - \phi_{Si}$ (see section 2.5.3). The work function values are summarised in Table 4.2. ϕ_{Al} = 4.28 eV and 4.18 eV before and after FGA respectively and correspond to the expected value for the Al reference gate.

	Flat Band Voltage, V$_{fb}$ (V)	**Work Function, ϕ (eV)**
Al w.o. FGA	-0.660±0.07	4.280±0.070
Al After FGA	-0.765±0.004	4.185±0.004
H-ITO w.o. FGA	-0.522±0.016	4.428±0.016
H-ITO After FGA	-0.203±0.001	4.747±0.001

Table 4.2: Work function of H-ITO (Sn 1%) and Al reference extracted by C(V) technique on SiO$_2$/Si substrate, with Si substrate doping N$_a$ = 2×10^{15} cm^{-3} corresponding to the work function ϕ_{Si} = 4.951 eV.

Although the EOT for the H-ITO gate are lower than expected, the relationship between them and the flat band voltage V$_{fb}$ remains quasi-linear and allows an accurate determination of the work function of the gate material. The work function before annealing is ϕ_{H-ITO} = 4.42 eV and after annealing ϕ_{H-ITO} = 4.74 eV. These values are in good agreement with the literature[236, 237, 238]. The difference between the measurement before and after FGA can be simply attributed to the change in the gate material due to the passivation annealing of the

SiO_2/Si interface. The value of the work function considered in the following is the one obtained without annealing, since the TCO in photodiode devices is not subjected to any treatment after deposition.

4.2.7 Interface defect and damage induced by ITO-H sputtering process

The density of interface defects near the middle gap at the Si/SiO_2 interface (Dits) was calculated using the **Equation** 3.2.32. The Dits value determined is shown in **Figure** 4.13 for samples with different t_{OX}. The maximum Dits value is about 2.4×10^{12} $cm^{-2}.eV^{-1}$ for samples with H-ITO gate without FGA, while the maximum value for Al reference gate is about 1.04×10^{12} $cm^{-2}.eV^{-1}$. The lower Dits values for Al indicate that Al evaporation process causes less damage to SiO_2 and the SiO_2/Si interface.

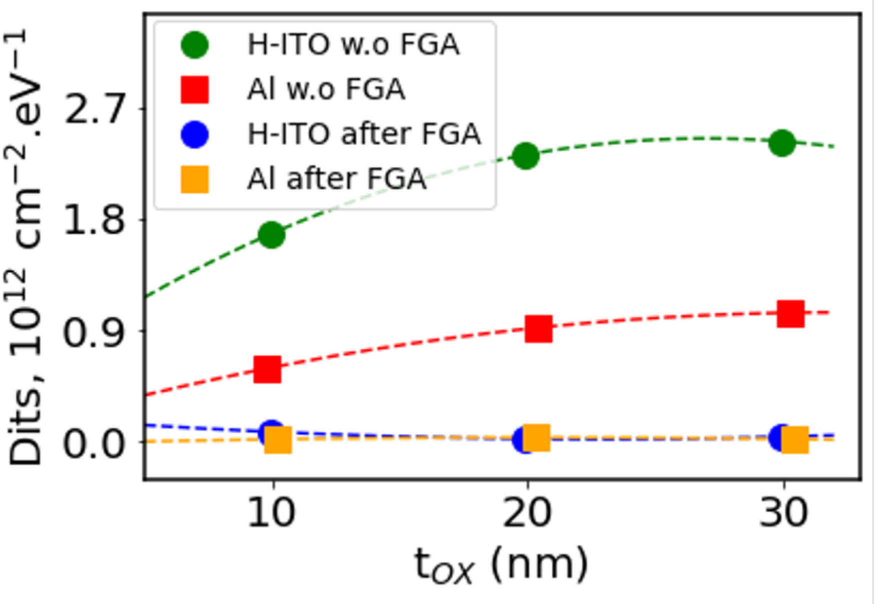

Figure 4.13: Interface defect density Dits near the mid-gap in Si as a function of SiO_2 thickness t_{OX} for Al and H-ITO gate before and after FGA.

After FGA, the Dits are significantly reduced, reaching 1.7×10^{10} - 7.6×10^{10} $cm^{-2}.eV^{-1}$. It should be noted that the method used here tends to overestimate the Dits, a more accurate technique such as conductance methods could be useful to accurately assess the energy signature of these defects [237].

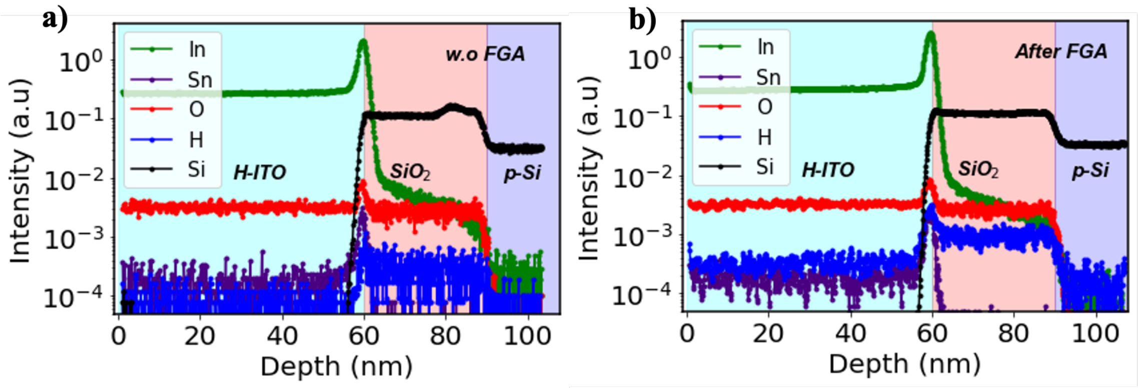

Figure 4.14: ToF-SIMS depth profiles intensity **a)** before FGA, and **b)** after FGA of H-ITO/SiO_2/Si stack.

In addition to important D_{its}, the results in **Figure** 7.13.**a** have shown an unexpected decrease in EOT for the H-ITO/SiO_2/Si stacks. To understand this decrease in EOT observed in the H-ITO lattice capacitors, ToF-SIMS measurements were performed on the H-ITO/SiO_2(30 nm)/Si structure before and after FGA (**Figure** 4.14.**a** and **Figure** 4.14.**b** respectively). They show a diffusion effect of the In species throughout the 30 nm of SiO_2. **Figure** 4.15.**a** is the schematic of the penetration of indium in SiO_2. Moreover, there is no difference between the results before and after FGA(**Figure** 4.15.**b**), suggesting that this diffusion occurs only during the H-ITO sputtering process. Kamioka et al. also observed similar indium diffusion effects at the ITO/MoO_x interface[239]. For rigorous optimization and good understanding of devices with transparent electrodes based on In_2O_3 deposited by sputtering, a thorough investigation of these diffusion phenomena at the interfaces could be useful.

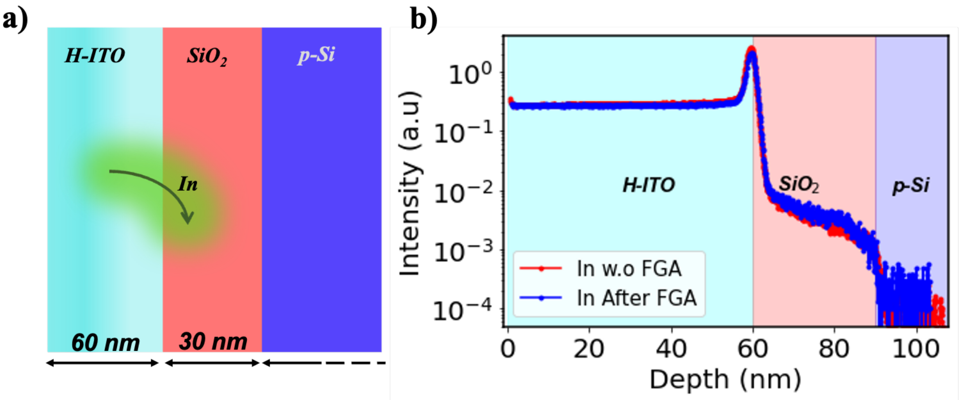

Figure 4.15: **a)** Schematic of the penetration of In atoms from the ITO into SiO_2, **b)** Depth profile of In concentration in the SiO_2 layer for H-ITO/SiO_2/Si samples measured by ToF-SIMS before and after FGA

The physical origin of the damage caused by the H-ITO (ITO) sputtering process is not yet very well understood. The decrease in the EOT of H-ITO lattice capacitors can be attributed to this phenomenon. The scattering of metallic elements such as indium atoms into SiO_2 can increase its dielectric constant, leading to a decrease in EOT. A simple model assuming the In scattering only over a certain thickness of SiO_2, i.e. assuming a boundary layer with a dielectric constant different from that of SiO_2, was unable to explain this phenomenon. Moreover, the linearity of the relationship between EOT and t_{OX} may indicate that In scattering impacts uniformly the entire thickness of SiO_2. The EOT reduction is then a consequence of the variation in the dielectric constant. UV photons with an energy of $\sim$ 8.8 eV present in the Ar plasma used for deposition can also induce positive charges in SiO_2 [240], leading to the change of SiO_2 permittivity, which may also explain the decrease in EOT.

4.2.8 Transparent electrodes for IR applications

We have investigated many properties of indium oxide based TCO thin films. We studied the case with different Sn doping and the effects of introducing hydrogen during deposition. **Figure** 4.16.**a** summarise the optimal electrical properties of various In_2O_3-based TCO films prepared at room temperature. They show that the films exhibit higher electrical resistivity with increasing Sn concentration. Impurities such as Sn^{4+} ions contribute to the creation of higher electron densities (one-electron donors), but also behave as electron scattering centres, leading to lower mobilities. We find that hydrogen doping leads to an improvement in mobility (impurities passivation), so that for two films with the same Sn concentration, further addition of hydrogen leads to an improvement in electrical properties. **Figure** 4.16.**b** shows the extinction coefficients k for the different TCO with different Sn compositions and the effects of hydrogen doping. Since the

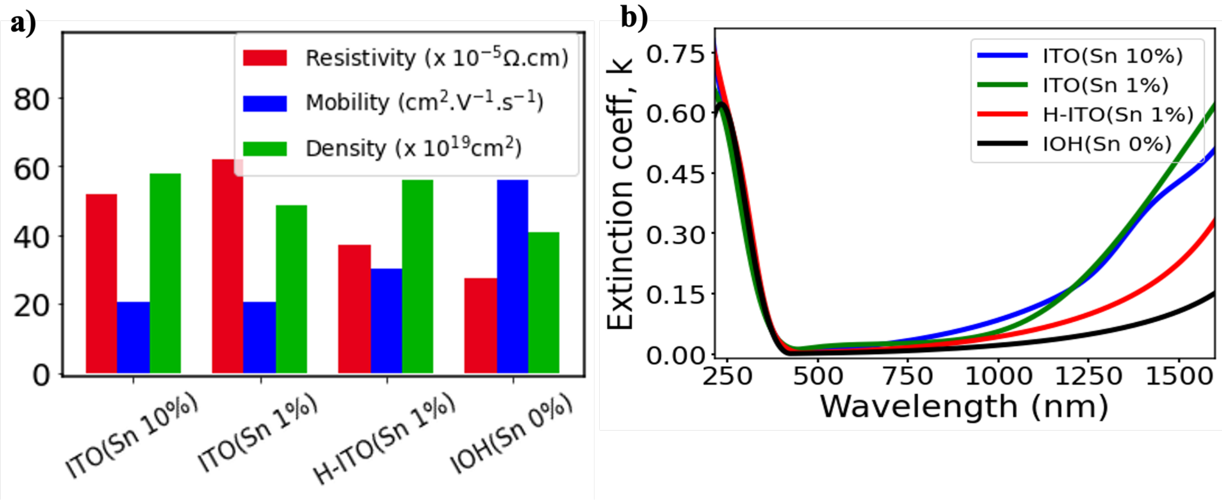

Figure 4.16: Comparison of electrical and optical properties between different In$_2$O$_3$-based TCO, **a)** comparison of electrical resistivity, mobility and free charge density, **b)** comparison of optical properties (extinction coefficient k).

extinction coefficient is directly related to absorption, it can be seen that the optical properties do not really change in the visible region, but that the extinction coefficient and thus absorption increase in the IR region. This increase is due to a higher electron density in films with a high Sn doping and reflects a stronger electron-photon interaction due to an increase in plasma frequency ω_p.

Thus, considering only the transmittance (or absorption) and resistivity (or conductivity) of the films as the key figures under the conditions of fabrication of In$_2$O$_3$-based TCO at ambient temperature, the films without Sn doping but doped with hydrogen are the most suitable TCO for applications in the IR region, mentioning the case of IOH (Sn 0%), which has a resistivity $\rho < 3\times10^{-4}\Omega$.cm and the lowest extinction coefficient in the IR range, i.e. the highest optical transmission.

4.3 Conclusion

The main challenge of this section was to optimise a TCO compatible with IR applications, such as photodiodes, at room temperature. To this end, thin In$_2$O$_3$-based TCO films were deposited by RF sputtering at room temperature and various characterizations were performed. We have shown that the electrical and optical properties of these TCO are mainly determined by the process parameters, of which oxygen concentration is the most important. This determines the charge carrier density of the TCO. Sn doping also leads to an increase in charge carrier density. Hydrogen doping and oxygen pressure control showed that the resistivity decreases with Sn concentration. Resistivities of $\rho < 4\times 10^{-4}\Omega$.cm for H-ITO (Sn 1%) and $\rho < 3 \times 10^{-4}\Omega$.cm for IOH were obtained, as well as an optical transmission T > 80% (50 nm thickness) in both cases. Although crystallisation temperatures of In$_2$O$_3$-based oxides are generally well above room temperature, some degree of crystallinity with extremely low roughness (RMS < 1 nm) was observed for all oxides prepared at room temperature. We also evaluated the work function for H-ITO (Sn 1%) using the C-V technique. The work functions obtained before and after the FGA $\phi_{H-ITO} = 4.43$ eV and $\phi_{H-ITO} = 4.74$ eV respectively, are in agreement with the literature. The difference between the work function value before and after FGA may be related to the change in H-ITO properties due to thermal annealing. The most useful measurement for the following study is that of H-ITO without FGA, as it corresponds to that of the material as used in photodiodes. There was also an unexpected decrease in EOT on the H-ITO gate, which could be attributed to damage from the gate deposition process (sputtering). ToF-SIMS measurements showed diffusion of indium into the SiO_2, which could explain the decrease in EOT. The damage caused by the H-ITO deposition process was also evaluated in terms of Dits. After FGA, the Dits decrease from 10^{12} $cm^{-2}.eV^{-1}$ to the limit of 10^{10} $cm^{-2}.eV^{-1}$, which allows a easier extraction of the flat band voltage V_{fb}, as well as an accurate determination of the gate work function.

Chapter 5

Hole extraction layers made transition metal oxides, NiO_x and MoO_x

5.1 MoO_x thin films

5.1.1 Introduction

MoO_x is a n-type material with tunable properties due to the different states of the O ligand and the multivalence of the Mo cation. It has a high work function of up to 7 eV in the case of MoO_3. Due to its electronic structure, optical and electrical properties, MoO_x is one of the promising materials, widely studied and used as a material for electron injection or hole extraction in various types of optoelectronic devices such as organic and inorganic solar cells, OLEDs or photodiodes. Most studies have shown that the ability of MoO_x to selectively transport holes is related to its high work function. In addition to the work function, the presence of gap states in MoO_x may also play a positive role in trap-assisted tunnelling transport of holes[241]. In this section, we will investigate the properties of MoO_x thin films deposited by reactive DC sputtering from a molybdenum (Mo) metal target. We use the XPS technique to evaluate the composition of films of different stoichiometries. We will present the electrical and optical properties as well as the structural properties and morphology of the films as a function of stoichiometry. Finally, we will determine the work function as a function of stoichiometry. In the literature, the work function of MoO_x is usually determined using the UPS technique. It is known that UPS technique is very sensitive to the surface, sample preparation and measurement conditions, which could explain the large variability in work function values among literature[142, 242, 243, 244, 245] In this work, the work function of MoO_x (x = 2.2 - 3) will also be determined using capacitance-voltage analyses of $Al/MoO_x/SiO_2/Si$ devices.

5.1.2 Experimental

MoO_x thin films were deposited on various substrate types using the reactive DC sputtering technique (in an O_2:Ar mixture) from Mo targets (99.9 % purity) supplied by Kurt J. Lesker Company Ltd. The films were deposited at different oxygen concentrations. The chamber was evacuated to a base pressure of less than 1×10^{-7} mbar, the deposition pressure was set at 0.0025 mbar. The Ar flow rate and deposition power were 50 sccm and 100 watts respectively, and the O_2 flow rate varied between 3 and 8 sccm, corresponding to a variation in the of oxygen concentration of between 5.66% and 13.8%. The rotation of the substrate was set to 20 rpm to improve the uniformity of the film. The deposition rate as a function ppO_2 is shown in **Figure** 5.1. The deposition rate is less than 2 Å.s^{-1} and decreases with increasing ppO_2. This decrease indicates the oxidation of the Mo target and/or a decrease in Ar^+ concentration in the sputtering chamber, which leads to a decrease in sputtering yield. The drop in the slope at ∼12 % could be related to a trend towards complete oxidation of the surface of the Mo target. The Al/MoOx/SiO_2/Si MOS structures were prepared following the steps described in **Section 3.2.7**.

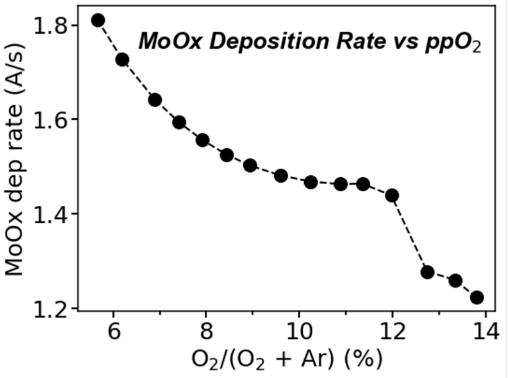

Figure 5.1: Room temperature MoOx thin films deposition rate change as a function of ppO$_2$ in %. Ar flow rate = 50 sccm, working pressure = 0.0025 mbar, DC power = 100 watts.

The various results are obtained using the characterization methods described in **Sections 3.2.1** to **3.2.6**.

5.1.3 Results and discussions

5.1.3.1 XPS analysis and the control of MoO$_x$ stoichiometry

XPS measurements were carried out (with a PHI500 VersaProbe II) to analyse the core level spectra, the oxidation states and the composition of the MoO$_x$ films. The excitation source was a monochromatic Al K$_\alpha$ X-ray with an energy of 1486.6 eV. The samples were stored in air for less than 30 minutes before being loaded into the spectrometer. There was no Ar preclean (known as GCIB) before XPS measurements to avoid any change in chemical states of the surface of MoO$_x$ samples. **Figure** 5.2 shows the XPS spectra of the Mo 3d state of MoO$_x$ films in the binding energy range of 239-225 eV at different oxygen concentrations in the narrow scan range. MoO$_x$ films deposited at low ppO$_2$ values between 5.66 and 8.42 % show a peak around 228-229 eV (**Figure** 5.2**a** and 5.2**b**), or a broadening or shift of the Mo 3d peak at lower binding energies up to 228 eV (**Figure** 5.2**c** to 5.2**e**), indicating a strong reduction of Mo of the presence of an high oxygen vacancies (presence of the Mo^{4+} oxidation state). The separation between the Mo 3d$_{5/2}$ and Mo 3d$_{3/2}$ doublets is not clear, the MoO$_x$ films are close to MoO$_2$ semi-metallic structures type. MoO$_x$ films deposited with a relatively high oxygen partial pressure exhibit spectra of the Mo 3d level showing two peaks associated to the Mo 3d$_{5/2}$ and Mo 3d$_{3/2}$ levels and clearly separated by the spin-orbit coupling energy (3.15 eV). These peaks are antisymmetric for films with a ppO$_2$ between 8.93 % and 11.97 % (**Figure** 5.2**f** to 5.2**h**), indicating a significant contribution of Mo^{5+} and/or Mo^{4+} oxidation states (Mo 4d^1 and/or Mo 4d^2), indicating the presence of oxygen vacancies or the formation of Mo cations with lower electronegativity (weaker coordination around the Mo atoms). At higher oxygen concentrations (**Figure** 5.2**k** to 5.2**i**), the two peaks are symmetric with Gaussian or Lorentzian shape, and the binding energy of the Mo 3d$_{5/2}$ level is much higher (∼232.5 eV), suggesting that the films are almost stoichiometric (close to MoO$_3$ with Mo 4d^0 band). There is also a residual presence of Mo^{5+} in the films, which we consider to be almost stoichiometric, and this residual concentration may be related to the entropy [246].

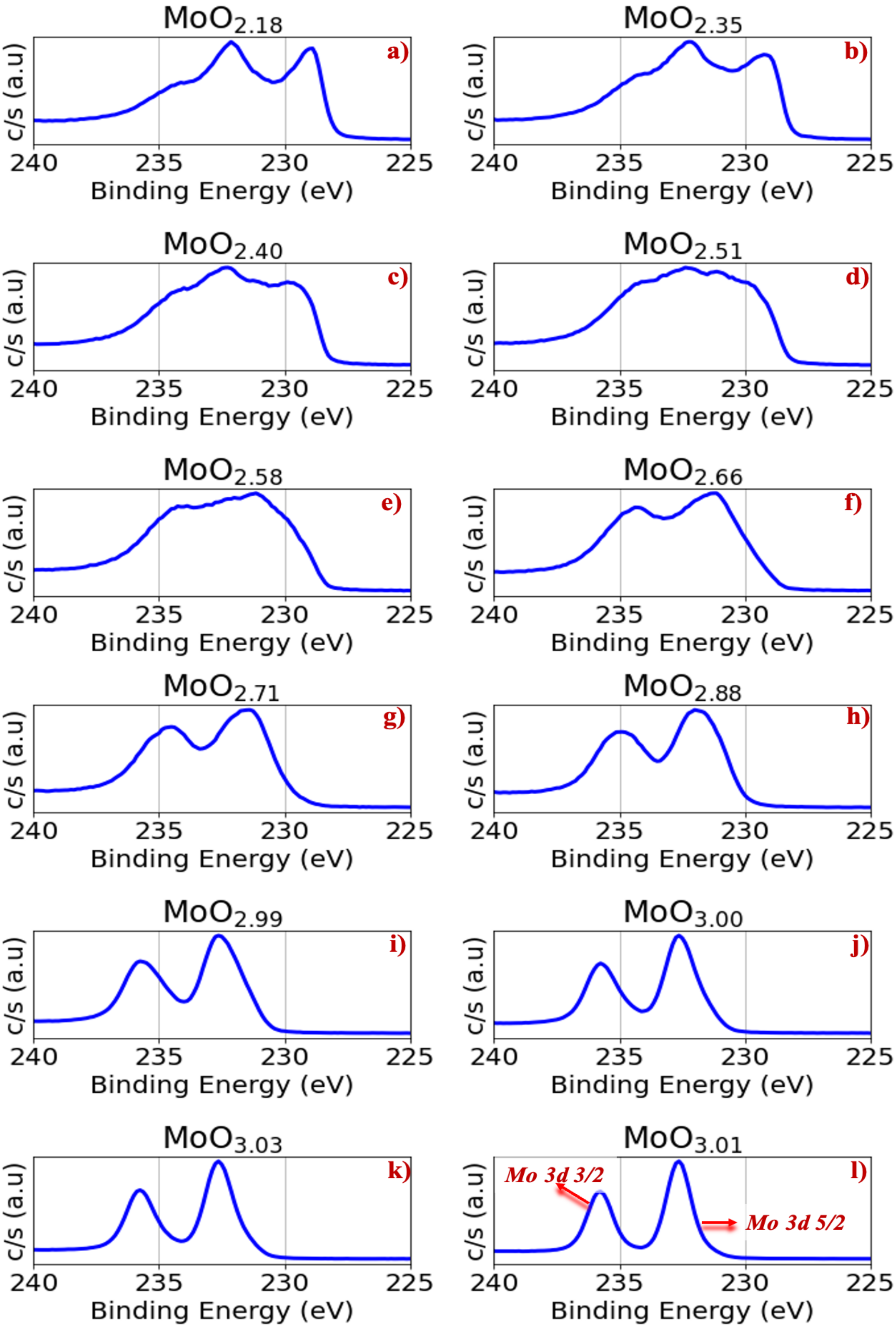

Figure 5.2: High-resolution XPS spectra at the Mo 3d core of MoO$_x$ films deposited at different oxygen flow rates, **a)** to **l)** correspond to 3.0, 3.7, 4.3, 4.6, 4.9, 5.3, 5.7, 6.1, 6.4, 6.8, 7.7, 8.0 sccm or O$_2$ partial pressures (ppO$_2$) of 5.66, 6.89, 7.92, 8.42, 8.93, 9.58, 10.23, 10.87, 11.35, 11.97, 13.34, 13.79% respectively (MoO$_x$ stoichiometries above the figures correspond to the extractions that are presented later in this section).

Table 5.1: Summary of the fitting parameters for the Mo $3d_{5/2}$ peaks at different ppO_2, the area indicated in the table corresponds to the relative area of each component with respect to the total area of the Mo 3d peak, the parameters corresponding to the Mo $3d_{3/2}$ peaks can be derived from those of the Mo $3d_{5/2}$ peak on the basis of the dependency relations between these two peaks (spin-orbit coupling, intensity ratio, and equal fwhm).

ppO_2 (%)	Mo $3d_{5/2}$ (6+)			Mo $3d_{5/2}$ (5+)			Mo $3d_{5/2}$ (4+)		
	Position	FWHM	Area	Position	FWHM	Area	Position	FWHM	Area
5.66	232.33	2.5	0.15	230.61	2	0.25	229.02	1.25	0.28
6.19	232.49	2.5	0.12	230.72	2	0.24	229.09	1.31	0.24
6.89	232.77	2	0.09	230.91	2	0.27	229.2	1.37	0.24
7.41	232.46	3.5	0.13	230.75	2.45	0.31	229.22	1.29	0.17
7.92	232.91	2	0.09	231.07	2	0.3	229.4	1.45	0.21
8.42	232.75	2	0.1	231.02	2	0.33	229.44	1.43	0.17
8.93	232.89	1.9	0.09	231.21	2	0.36	229.64	1.55	0.15
9.58	232.55	2	0.15	231.18	1.9	0.38	229.74	1.43	0.08
10.23	232.41	1.8	0.23	231.18	1.74	0.36	229.61	1.06	0.01
10.87	232.35	1.76	0.3	231.33	1.67	0.3	229.17	0.29	0
11.35	232.55	1.68	0.54	231.39	1	0.06			
11.97	232.6	1.42	0.54	231.42	1.05	0.06			
12.74	232.63	1.25	0.55	231.47	1.11	0.05			
13.34	232.62	1.32	0.55	231.43	1.03	0.05			
13.79	232.64	1.2	0.57	231.38	0.95	0.03			

For an in-depth analysis and to determine the composition of the different MoO_x films, i.e. the relative concentrations of the different oxidation states, a deconvolution of the peaks was performed with the *CasaXPS* software using Lorentz and Gaussian or mixed Lorentz-Gaussian functions. **Table** 5.1 summarises the binding energies, relative areas and fwhm of the Mo $3d_{5/2}$ peaks as a function of ppO_2. The Mo $3d_{5/2}$ and Mo $3d_{3/2}$ doublets are each separated by spin-orbit coupling 3.15 eV and an area ratio of $A_{Mo3d_{5/2}}$:$A_{Mo3d_{3/2}}$, corresponding to the ratio of the degeneracies of Mo $3d_{5/2}$ and Mo $3d_{3/2}$, $A_{Mo3d_{5/2}}:A_{Mo3d_{3/2}} = (2j_{+}+1):(2j_{-}+1) = (2\times\frac{5}{2}+1):(2\times\frac{3}{2}+1) = 3:2$ (with $j_{\pm} = |l \pm s|$), and we kept the fwhm between the two peaks equal in our fits. In films deposited at low oxygen concentrations (**Figure** 5.3**a** to 5.3**c**), the Mo 3d spectra show three doublets Mo $3d_{5/2}$ and Mo $3d_{3/2}$, each separated by spin-orbit coupling ernergy and with an intensity ratio of 3:2. As ppO_2 increases, the Mo^{4+} content decreases, disappearing at very high ppO_2 values (**Figure** 5.3**e** and 5.3**f**). The Mo^{5+} concentration initially increases with the ppO_2 value and then decreases above a certain ppO_2 value. We also note a shift in binding energy towards higher values (**Table** 5.1), which is due to an increase in the electronegativity of Mo as a result of the increase in oxygen content in the films. We also note that in addition to the symmetry of the nearly stoichiometric films, a decrease in fwhm is observed with increasing oxygen content. To observe the reduction in fwhm, keep in mind that we have modified the scale between the **Figure** 5.3**a** and **Figure** 5.3**f**.

The O 2p valence band spectra of MoO_xfilms for different oxygen partial pressures are shown in **Figure** 5.4. These spectra show two distinct peaks. The first peak near the Fermi level (binding energy = 0 eV) is directly related to the oxygen vacancies in the octahedral lattice, i.e. it is associated with the Mo $4d^n$ electrons, which remain weakly bound to the Mo atoms, and the second corresponds to the actual valence band. The intensity of the first peak decreases significantly with the oxygen partial pressure. The current literature assumes that these defects which are associated with oxygen vacancies, lead to the formation of a shallow donor state (close to the conduction band) into the band gap of MoO_x, hence the n-type nature of MoO_x[139].

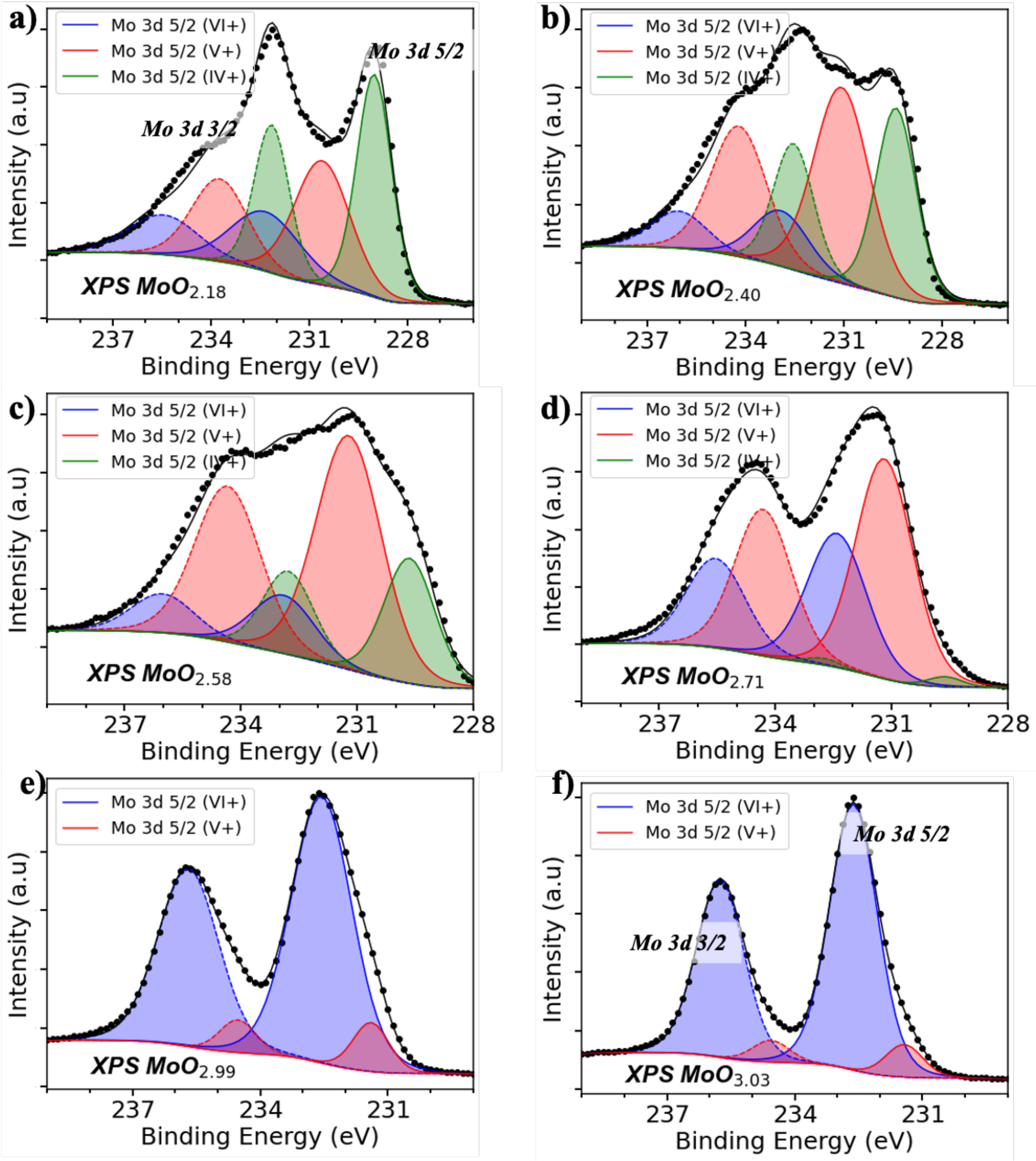

Figure 5.3: High-resolution Mo 3d XPS spectra fitting with components from Mo^{6+}, Mo^{5+}, Mo^{4+}.

At low oxygen concentrations (stoichiometry x < 2.8), this peak overlaps with the Fermi level, indicating a semi-metallic nature, since MoO$_2$ is known to be semi-metallic and exhibits a metallic Fermi-Dirac edge at zero energy[247]. The role of this peak is still controversial, as it probably plays an important role for band levels alignment and the charge (holes) transport in optoelectronic devices[115].

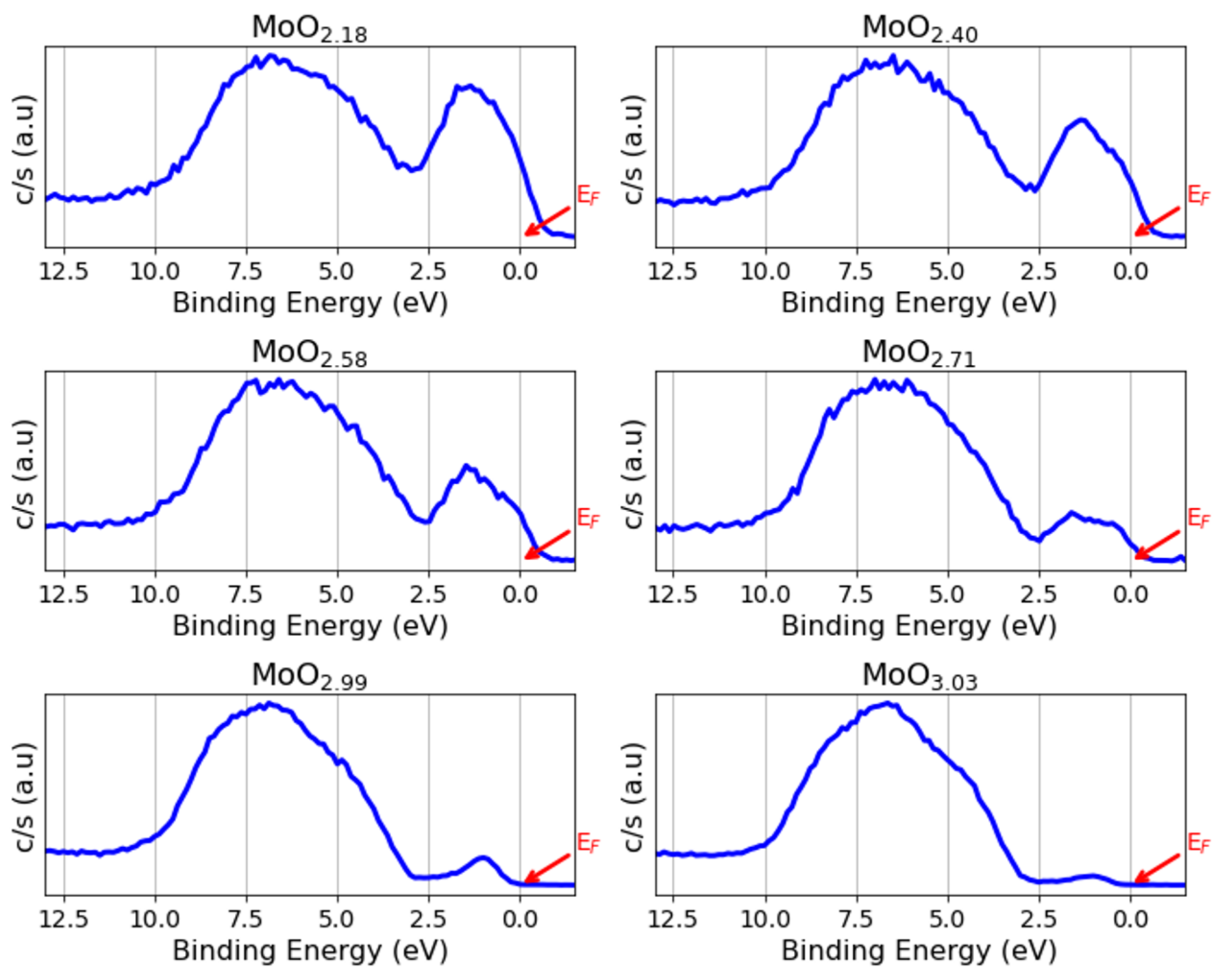

Figure 5.4: High-resolution XPS spectra of the O 2p valence band of MoOx films deposited at different oxygen partial pressures.

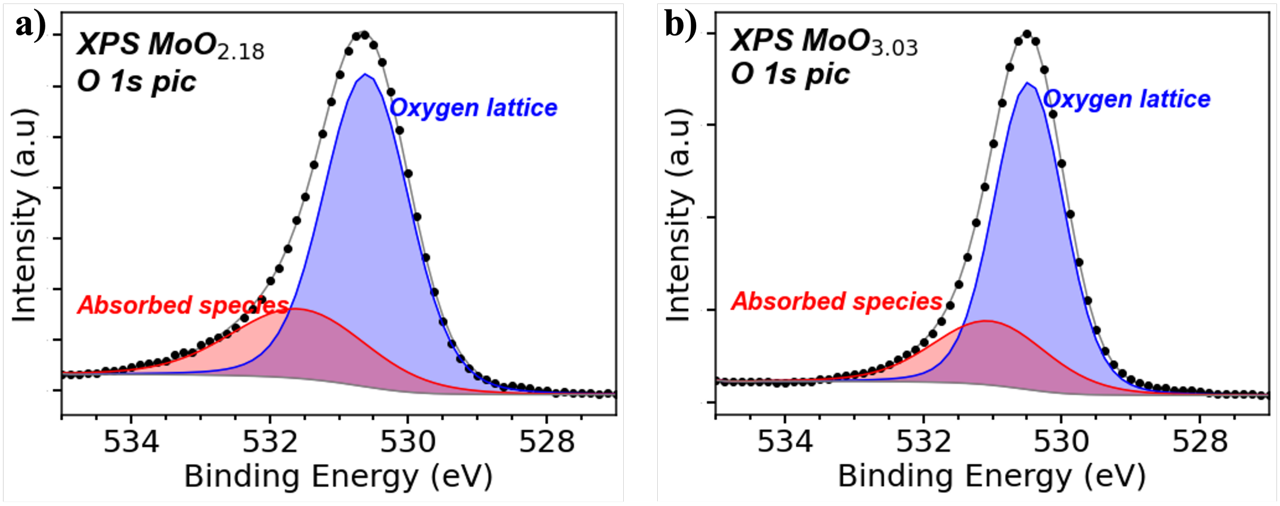

Figure 5.5: High-resolution XPS spectra of the central level of O 1s for the lowest **a)**, and highest **b)**oxygen partial pressure, showing the deconvolution into two peaks of the fitted curves corresponding to oxygen atoms in their lattice site (blue) and to oxygen vacancies or surface adsorbed oxygen (red).

The O 1s spectra for the film with the lowest oxygen concentration ($MoO_{2.18}$) and the highest oxygen concentration ($MoO_{3.03}$) are shown in **Figure** 5.5**a** and 5.5**b**. They are composed of two different peaks, one with a lower binding energy corresponding to the atoms in their lattice and the second corresponding to the oxygen vacancies and/or adsorbed oxygen.

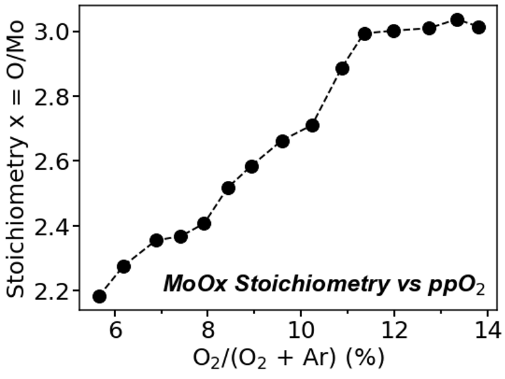

Figure 5.6: Evolution of MoO_x stoichiometry as a function of oxygen partial pressure, computed from XPS Mo 3d and O 1s spectra normalised with corresponding component effective RSF, x = O/Mo ratio.

The stoichiometry of the MoO_x films is determined by calculating the O/Mo atomic ratio after correcting the intensities (areas under the peaks) of the Mo 3d and O 1s core level peaks by their atomic relative sensitivity factor (RSF). **Figure** 5.6 shows the evolution of stoichiometry as a function of oxygen partial pressure. A linear increase in stoichiometry and saturation can be seen above a certain ppO_2, meaning that the films are almost completely oxidised (nearly stoichiometric structure). These study show that the formation of defect bands and reduced oxidation states (Mo^{4+}, Mo^{5+}) as well as the stoichiometry are directly related to the oxygen vacancies in MoO_x films, and they can be carefully controlled by the selection of deposition parameters, particularly the oxygen flow rate for room temperature experiments.

5.1.3.2 MoO_x electrical properties

The electrical resistivity, density and carrier mobility of MoOx at room temperature at different oxygen partial pressures (or stoichiometries) were determined from sheet resistance measurements using the van der Pauw four-probes method and Hall effect measurements on films with a thickness of ≈100 nm (**Figure** 5.7**a** and 5.7**b**). As shown in **Figure** 5.7**a**, the electrical resistivity of MoO_x films depends on the oxygen partial pressure used during deposition process, the resistivity of MoO_x increases between 2.15×10^{-3} Ω.cm and 1.20×10^{5} Ω.cm with an increase in stoichiometry between x = 2.18 and x = 3.03 or in oxygen partial pressure between 5.66 % and 13.34 % . We observe a variation in resistivity over more than 8 decades. At low oxygen partial pressures $ppO_2 < 8\%$ or stoichiometries $x < 2.5$, the films are semi-metallic-like, the resistivity is in the order of 10^{-3}Ω.cm and increases slowly with increasing ppO_2, the films have a charge carrier density in the order of 10^{23} cm^{-3} and very low electron mobilities in the order of 10^{-2} - 10^{-1} $cm^2.V^{-1}.s^{-1}$ (**Figure** 5.7**b**). The low mobility is related to the high concentration of ionised impurities (oxygen vacancies), which act as scattering centres and limit the mean free path of the charge carriers. The charge carrier density decreases with increasing oxygen partial pressure, as it is the case with all n-type semiconductor oxides. This decrease is due to the lower concentration of oxygen vacancies, which act as electron donors. The mobilities remain relatively low $\mu < 2$ $cm^2.V^{-1}.s^{-1}$. At high oxygen partial pressures ($ppO_2 < 11\%$) or at larger stoichiometries ($x > 2.8$), the MoO_x films are highly resistive (resistivity in the order of 10^{-3} Ω.cm), and density and mobility measurements are no longer possible due to instrumental limitations.

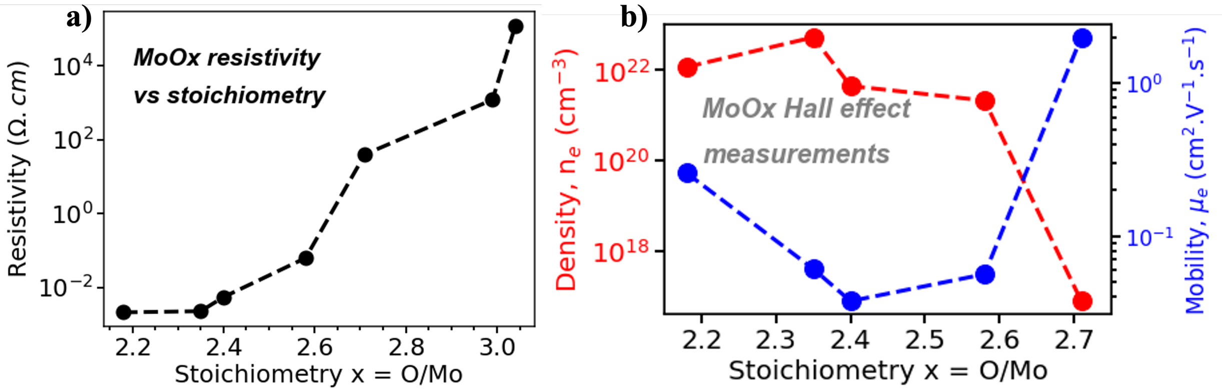

Figure 5.7: Electrical properties of MoOx with different ppO$_2$(stoichiometry), **a)** electrical resistivity, **b)** Free carrier density and electrons mobility as a function of MoOx stoichiometry.

We also carried out in-situ measurements of resistivity as a function of temperature. The results of the in-situ measurements of resistivity as a function of temperature in an N_2 and O_2 atmosphere (in proportions of approximately 20% O_2 and 80% N_2) show a decrease of the resistivity between 25°C and 320 - 350°C (**Figure** 5.8**a**). This decrease of the resistivity as a function of temperature reveals the semiconducting nature of all MoO_x films, and is well illustrated by the thermal activation phenomenon, characterised by the linear relationship between the logarithm of the sheet resistance R_s and measurement' temperature (**Figure** 5.8**b**). MoOx films with stoichiometry $x < 2.7$ are indeed semiconductors, but they are less sensitive to thermal activation (low slope of log(Rs) vs. T-curves). With these stoichiometries, we have an electrical behaviour at the boundary between semiconductors and metals, which can be explained by a high density of free charge carriers (see **Figure** 5.7**b**).

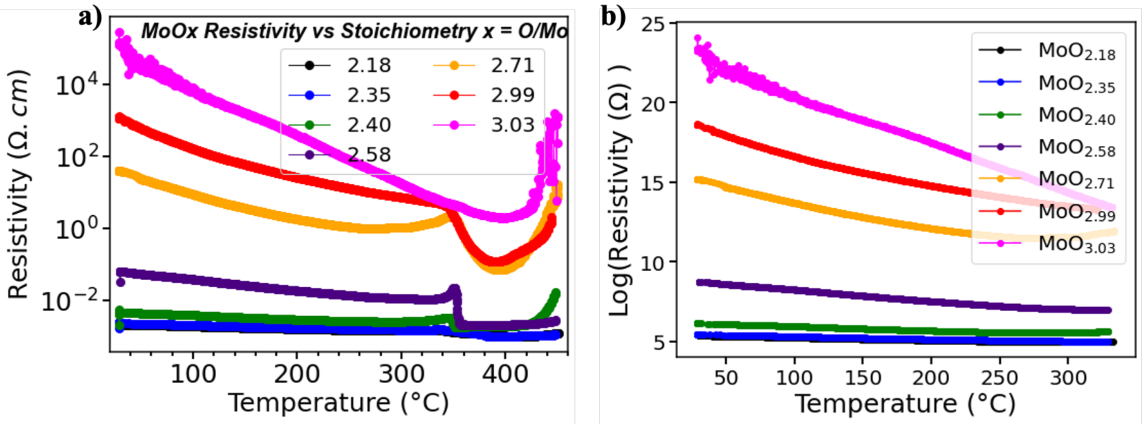

Figure 5.8: **a)** In situ electrical resistivity as a function of temperature of MoOx films with various stoichiometry in N_2+O_2 ambient, **b)** Plot of the logarithm of MoO_x sheet resistance as function of temperature (log(R_s) vs temperature.)

Above 390 - 400°C, an initial increase in electrical resistivity was observed in all MoO_x layers. This increase could be related to the onset of oxidation. However, this increase is less significant for films with low stoichiometry ($x < 2.7$). A reversibility of the resistivity measurement as a function of temperature is also observed, the resistivity recovering the initial values when returning to the initial temperature (**Figure** 5.9**a**). In this case, we are in the presence of a hysteresis phenomenon rather than an oxidation of MoO_x film. On the other hand, the temperature measurement is irreversible at higher oxygen concentrations (stoichiometry $x > 2.7$). The final resistivity values are identical for all stoichiometries, but are significantly higher than the initial values, more than 4 decades higher (see **Figure** 5.9**b**). As will be shown by the XPS measurements below, there is a complete and non-reversible oxidation of the MoO$_x$ (**Figure** 5.10) films.

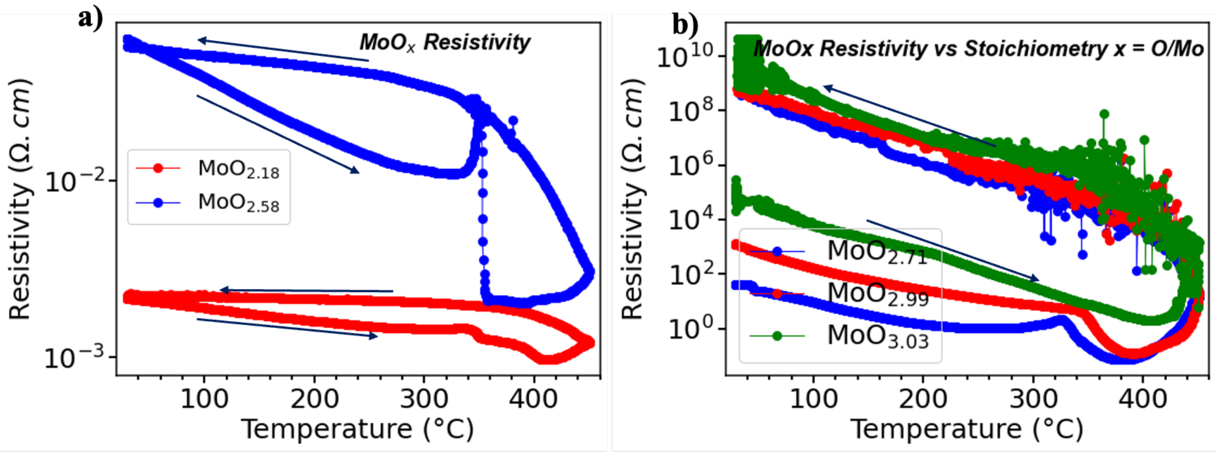

Figure 5.9: In situ electrical resistivity as a function of temperature, forward and reverse measurement for higher oxygen concentrations or stoichiometry x < 2.7 (**a** and for higher oxygen concentrations or stoichiometry x > 2.7 (**b**).

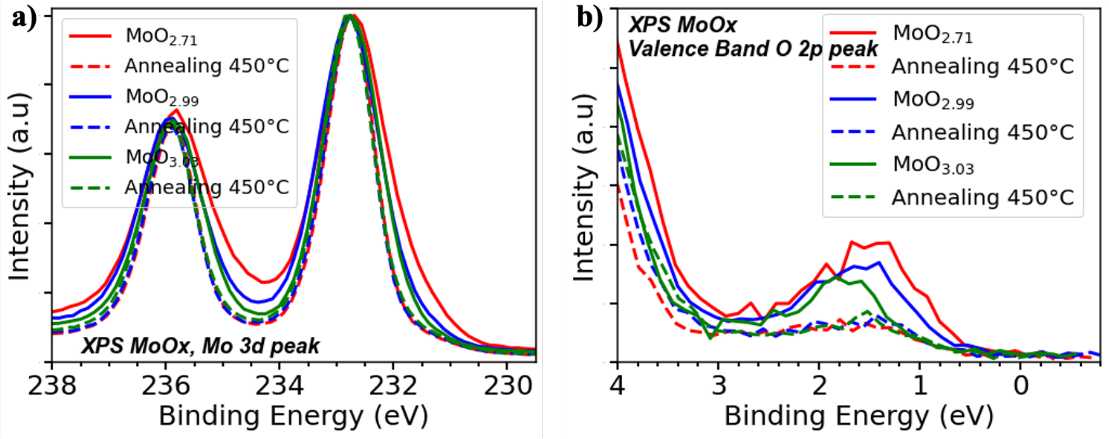

Figure 5.10: XPS Mo 3d (**a**) valence band O 2p (**b**) spectra of MoO$_x$ with different stoichiometry after annealing at 450°C, showing complete oxidation of different films

The XPS measurements after the in-situ electrical resistivity measurements as a function of temperature 25°C → 450°C → 25°C (**Figure** 5.10**a**) show that the samples with the stoichiometry x > 2.7 are completely oxidised. The subsequent Mo 3d spectra are identical, completely symmetrical and the fmhw are reduced (recall that the broadening of the Mo 3d peak is usually associated with the presence of the weakly oxidised Mo^{4+} or Mo^{5+} states). The valence band spectrum (**Figure** 5.10**b**) also shows the vanishing of gap states near the Fermi level (binding energy = 0 eV) after the in-situ resistivity measurements. It is known that annealing of MoO$_x$ (x ∼ 3) in an inert atmosphere or in the absence of oxygen and plasma annealing lead to the opposite phenomenon, i.e. a reduction towards layers with lower stoichiometry (lower resistivity). Numerous studies suggest a transition from MoO$_3$ to MoO$_2$ around 700K (∼ 430°C) [248, 249]. To summarise, MoOx films with low stoichiometry (2 < x < 2.7) can be considered as materials at the boundary between semiconductors and metals, since they have a relatively high free carrier density n$_e$ $> 10^{21}$ cm^{-3}, and show a relatively low thermal activation effect (very low slope of log(Rs) vs. T curves). The oxidation kinetics or mechanisms of MoO$_x$ films depend not only on the annealing conditions but also on the initial stoichiometry of these films. A similar and more in-depth study could be useful to understand the oxidation and reduction mechanisms of MoO$_x$ as well as the oxidation and reduction kinetics depending on the initial stoichiometry of MoO$_x$.

5.1.3.3 MoO$_x$ optical properties

Figure 5.11**a** shows the optical transmission spectra of MoO$_x$ at different oxygen partial pressures (stoichiometry) as a function of wavelength for 15 nm thick layers. The optical transmission of MoO$_x$ depends on its stoichiometry. Nearly stoichiometric films ($x > 2.7$) have excellent optical transmission (over 80%) in the Vis-IR range. The optical transmission decreases significantly with stoichiometry, and films with lower stoichiometry ($x < 2.5$) have an optical transmission of less than 60 % in the Vis-IR range. This drastic reduction of the optical transmission is associated with low oxidation states of the Mo cation and therefore high electron density, which is consistent with electrical measurements and XPS analyses.

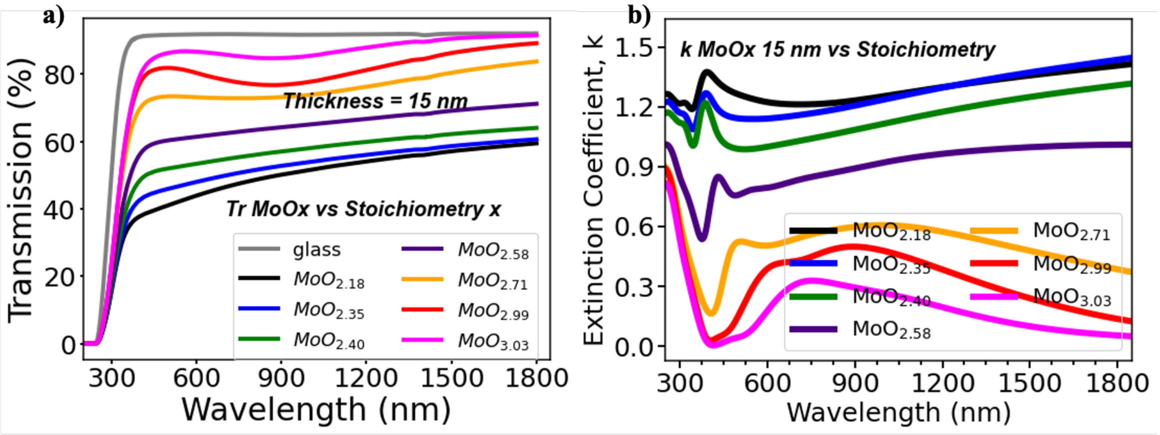

Figure 5.11: MoO$_x$ optical properties as function of the films stoichiometry (oxygen partial pressure), **a)** Optical transmittance spectra by transmission measurements, **b)** Extinction coefficient ***k*** by ellipsometry measurements.

The extinction coefficients of films of different stoichiometries derived from the ellipsometry measurement are shown in **Figure** 5.11**b**. The extinction coefficient measures the absorption of the material, which depends on the gap and the electron density of the material. The extinction coefficient of MoO$_x$ decreases with increasing stoichiometry, reflecting a decrease in optical absorption. These results are consistent with the optical transmission measurements.
To determine the different optical gaps, the Tauc digrams (**Figure** 5.12**a**) were obtained from the extinction coefficients by calculating the absorption coefficient using the relationship $\alpha = \dfrac{4\pi k}{\lambda}$, taking into account direct transitions. Films with low stoichiometry show two absorption bands, the first band before 2.5 eV can be attributed to gap states associated with oxygen defects, and the second absorption corresponds to the transitions between the valence band and the conduction band. The optical gap increases with stoichiometry (**Figure** 5.12**b**). At higher ppO$_2$ the optical gap becomes constant. The Tauc plots are consistent with previous analyses and suggest that the optical properties of MoO$_x$ are easily tunable and are correlate strongly with the electrical properties. For stoichiometry $x < 2.8$, subgap optical absorption is observed. It is suggested that this sub-gap absorption in metal oxides is mainly due to the presence of oxygen defects[250]. This property is problematic for the transparency of MoO$_x$ films, but interesting

in terms of electrical properties, as the sub-gap states cause an increase in the concentration of carriers, as well as an increase in the conductivity of the film.

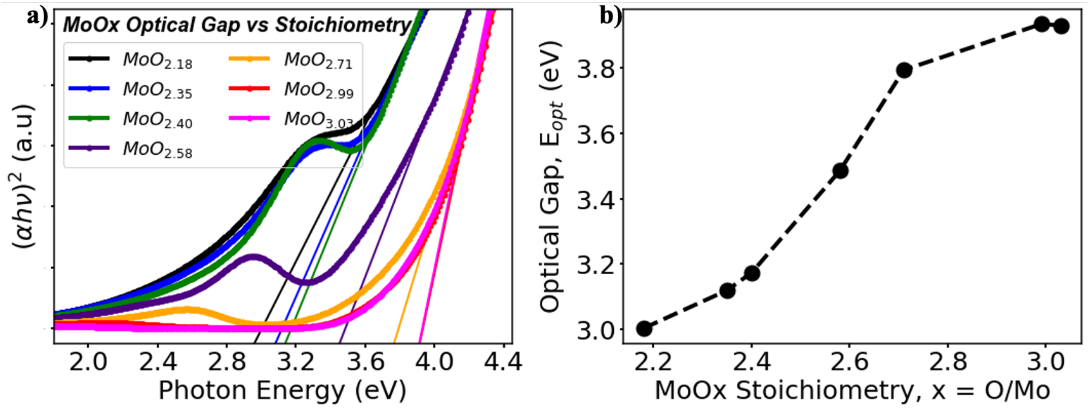

Figure 5.12: **a)** Tauc plot of MoOx with different stoichiometry, **b)** Evolution of the MoOx optical band gap as function of the stoichiometry.

In summary, there is therefore a balance between the optical and electrical properties, i.e. conductivity improves at the expense of optical transmission and vice versa.

5.1.3.4 Structural properties and surface morphology

Figure 5.13 shows the x-ray diffraction measurements of the films with higher and lower stoichiometry. No obvious peaks were detected, indicating that the MoO_x film is not crystallised. The amorphous properties of the films can be attributed to the low growth temperature. During the MoO_x sputtering process, the films did not have enough energy to form a nanocrystalline or polycrystalline structure, even with a relatively high power density used for this study (125 W.cm^2) .

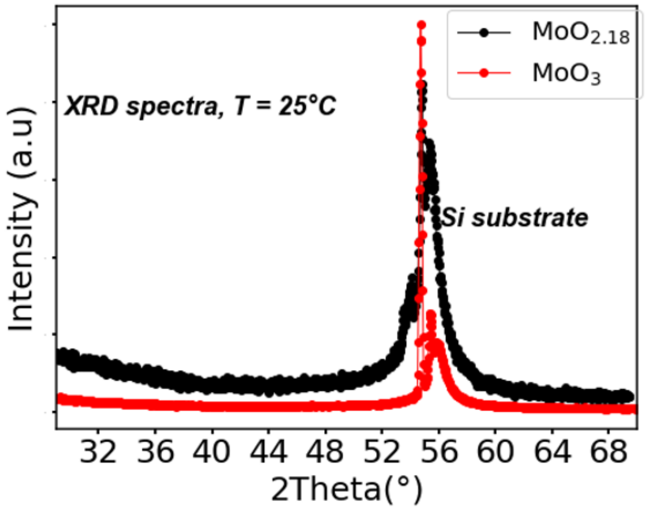

Figure 5.13: X-ray diffraction pattern of the MoOX film with the lowest and highest stoichiometry

The surface topography of the MoO_x films was also investigated using AFM. **Figure** 5.14**a-f** shows two-dimensional (2D) AFM diagrams of MoO_x thin films deposited at different oxygen partial pressures (ppO_2). These AFM images show that all the MoO_x films exhibit a remarkably smooth surface morphology. No grain or particle-like structures are observed, the films are very flat with a peak-to-valley height of less than 3 nm in all cases. The surface roughness of the films with root mean square (RMS) as a function of stoichiometry is shown in **Figure** 5.15 . The films are flat and almost smooth with a roughness (RMS) of less than 0.5 nm.

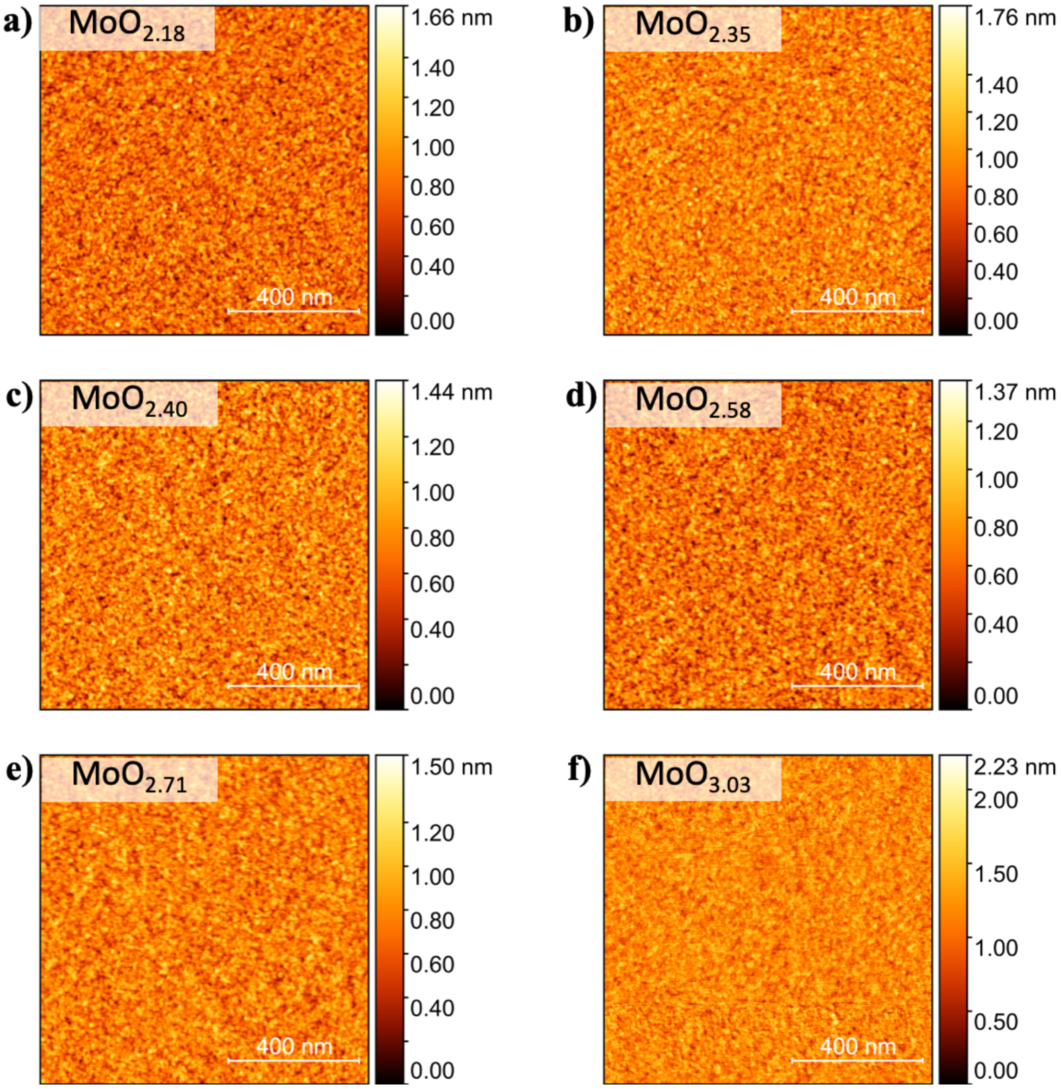

Figure 5.14: 2D AFM images of MoOx with various stoichiometry

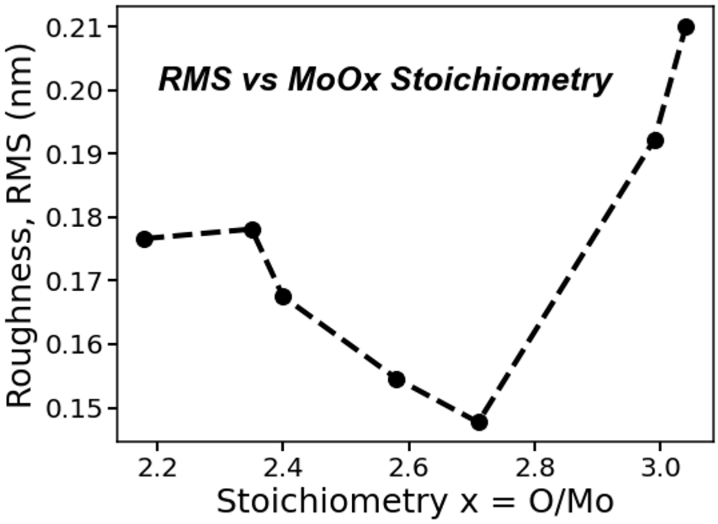

Figure 5.15: Evolution of roughness (RMS) as a function of MoO$_x$ stoichiometry

5.1.3.5 MoOx work function using UPS measurement and MOS capacitor C-V analyses

One of the most desired properties of hole extraction films is their high work function. In a simplified case, the energy barrier for the transport of holes at the interface between a given semiconductor and the hole extraction layer can be considered as the difference between the ionisation energy of said semiconductor and the work function of the extraction layer, where a high value of the work function is required to minimise this energy barrier. In this section, we will evaluate the work function of MoO$_x$ using two different techniques, the UPS measurement and the C-V measurement and analysis of Al/MoO$_x$/SiO$_2$/Si capacitance.

MoO$_x$ work function using ultraviolet photoelectron spectroscopy (UPS) measurements

We performed work function measurements on MoO$_x$ films with stoichiometries x = 2.18, 2.58, 2.71 and 3.03. The UPS measurements were performed on a **XPEEM ScientaOmicron NanoESCA Mkl** spectrometer microscope equipped with a He(I) source with energy $h\nu$= 21.22 eV. Prior to the measurements, the spectrometer chamber loaded with samples was exposed to an ultra-high vacuum with a pressure of about 10^{-10} mbar.

To avoid possible chemical changes associated with surface preparation, we initially chose to perform the measurements without etching; we simply limited the exposure times of the samples in the ambient atmosphere as much as possible. The UPS spectra of MoOx samples of 4 different stoichiometries are shown in **Figure** 5.16.

	$MoO_{2.18}$	$MoO_{2.58}$	$MoO_{2.71}$	$MoO_{3.03}$
ϕ_{MoOx} **(eV)**	4.3±0.05	5.4±0.05	4.8±0.05	4.5±0.05

Table 5.2: MoO$_x$ work function values obtained without surface preparation.

The work function is determined by measuring the photoemission threshold of the secondary electron spectrum and the Fermi energy level (Section on XPS and UPS measurement techniques). The values of the work function are summarised in **Table** 5.2. The values obtained at low stoichiometries (x = 2.18, 2.58) are in agreement with the literature, but the work values obtained for $MoO_{2.71}$ and $MoO_{3.03}$ are very low compared to the literature values. In fact, an increase in work function is expected with increasing stoichiometry[133]. Due to the difficulties

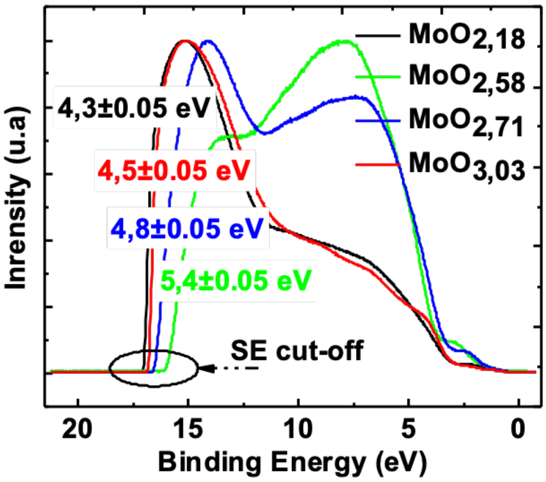

Figure 5.16: **a)** UPS spectra of MoOx with various stoichiometry

encountered with the samples with higher stoichiometry ($MoO_{2.71}$ and $MoO_{3.03}$), we performed the measurements after surface preparation. We used a low damage ion beam etching (gun cluster ion beam or GCIB) with Ar clusters (Ar^+_{2500} with an energy of 5 keV at 5 nA, i.e. 2eV/atom) on a 2×2 mm^2 surface for 90 seconds on the **PHI 5000 VersaProbe II** spectrometer. The survey spectrum (**Figure** 5.17 **a**) shows the disappearance of the C 1s peak after GCIB, indicating effective decontamination of the surface with GCIB. A sample transfer was then performed between the **PHI 5000 VersaProbe II** and the **XPEEM ScientaOmicron** using a capsule in a neutral atmosphere (nitrogen), with all samples on the same support. The UPS spectra of MoOx samples of 4 different stoichiometries are shown in **Figure** 5.17 **b**, where significant differences were observed between the different measured surfaces. The work function is determined from the measurement of the photoemission threshold of the secondary electron spectrum and the position of the Fermi level. The values after GCIB are summarised in **Table** 5.3. There is an overall increase in the work function after GCIB. As before, the values of the work function for MoO_x (x = 2.18, 2.58) are close to the expected values. $\phi_{MoO_{2.58}} \simeq 6$ eV is in agreement with the literature[251] and corresponds to the order of magnitude of the work function expected for MoO_x films with high stoichiometry. The work function values obtained for $MoO_{2.71}$ and $MoO_{3.03}$ remain very low compared to the literature values. This anomaly is therefore not due to surface contamination. The most likely hypothesis for the origin of these low work function values for higher stoichiometry is the limitation of the spectrometer we used for the work function measurements. Charge effects can occur when photoelectrons are emitted from material surfaces with high electrical resistivity. Indeed, the photoemission from resistive films leads to an accumulation of positive charges on the surface (the emitted electrons are replaced at a very low rate due to the low conductivity), which leads to the reduction of the photoelectrons kinetic energy, hence the low values of work function compared to those expected.

	$MoO_{2.18}$	$MoO_{2.58}$	$MoO_{2.71}$	$MoO_{3.03}$
ϕ_{MoOx} **(eV)**	4.65±0.05	5.95±0.05	4.70±0.05	4.80±0.05

Table 5.3: MoO_x work function measured after surface preparation by Ar clusters etching (GCIB)

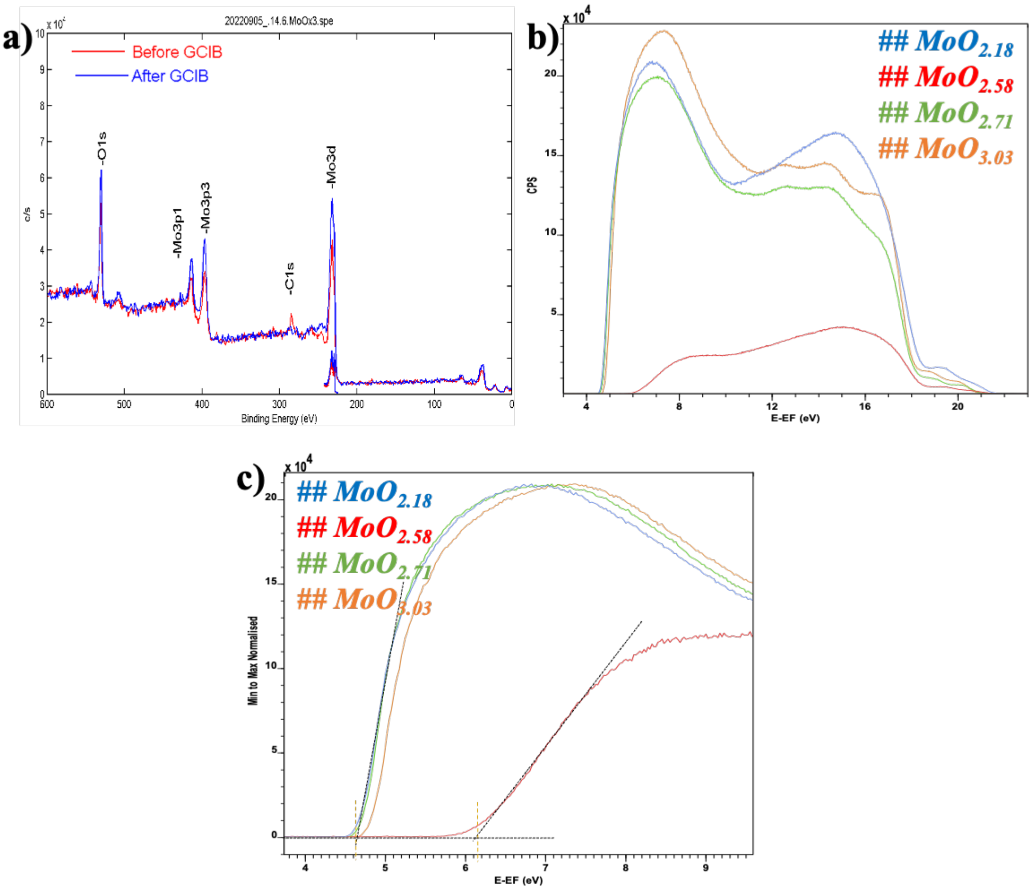

Figure 5.17: **a)** XPS analysis for surface preparation prior to UPS measurement, with a gun cluster ion beam (GCIB) consisting of low-energy Ar$^+$ clusters, 5 keV at 5 nA, etching during 90 seconds **b)** UPS spectra of MoO$_x$ with various stoichiometry after surface preparation (GCIB), **c)** Expanded view of the secondary electrons threshold (secondary cut-off for determining the work function).

In conclusion, the work function measurements by UPS are consistent for MoO$_x$ films with resistivity $\rho < 1$ Ω.cm. Above this value, we are limited by the capabilities of the measurement tool.

MoOx work function using MOS capacitor C-V analyses

In this section, we will determine the work function of MoO$_x$ based on the C-V measurements. For this purpose, we have fabricated Al/MoOx/SiO$_2$/Si MOS structures. SiO$_2$/Si substrates with different SiO$_2$ thicknesses were prepared according to the procedure described in section on Metal-Oxide-Semiconductor (MOS) capacitor analyses. MoO$_x$ with thicknesses of 15 nm with oxygen partial pressures corresponding to the stoichiometry x = 2.18, 2.35, 2.58, 2.71, 3.03 were deposited by DC reactive sputtering on the SiO$_2$/Si substrates (p-type) through a physical mask (S = 200×200 μm^2). The deposition of MoO$_x$was immediately followed by the deposition of a 100 nm thick aluminium layer by thermal evaporation in order to obtain better electrical contacts. Some devices underwent FGA in order to evaluate the effects of annealing on the MoOx work function. The C-V curves of the MOS structures were measured at signal frequencies in the range of 100 Hz to 100 kHz.

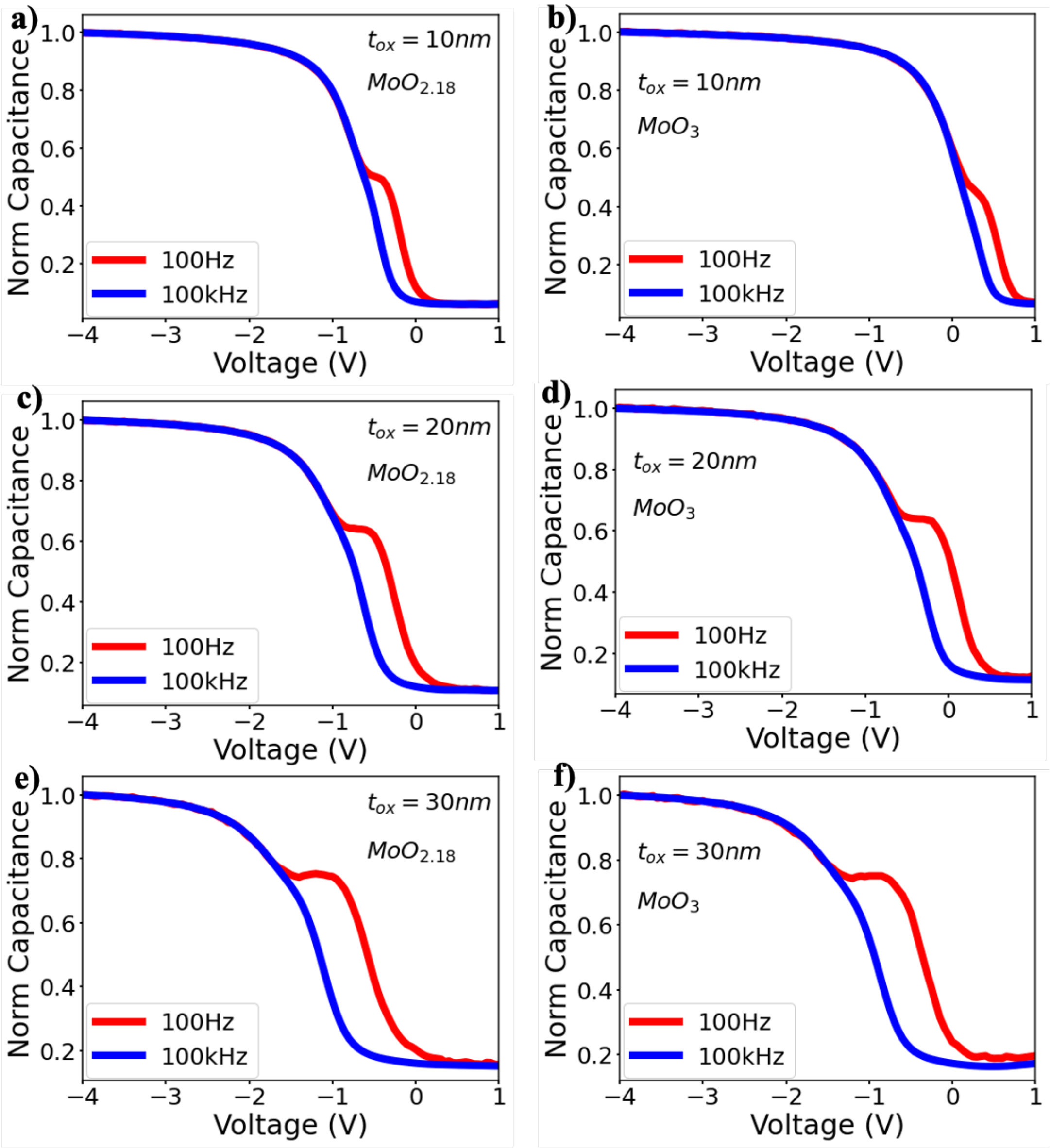

Figure 5.18: C-V curves for Al/MoOx/SiO2/Si stack , $t_{OX} = 10$ nm (**a** and **b**), $t_{OX} = 20$ nm (**c** and **d**), $t_{OX} = 30$ nm (**e** and **f**) with Al and MoOx as-growth; the measurement frequencies are 100 Hz, and 100 kHz and the capacitance is normalized by the maximum capacitance.

The C-V curves at the lowest stoichiometry ($x = 2.18$) and at the highest stoichiometry ($x = 3.03$) are shown in **Figure** 5.18**a** and 5.18**b** for $t_{OX} = 10$ nm, 5.18**c** and 5.18**d** for tox = 20 nm, 5.18**e** and 5.18**f** for $t_{OX} = 30$ nm, at the highest and lowest frequencies (100 Hz and 100 kHz). The curves shift towards negative voltages as a SiO_2 thickness increases, indicating the presence of oxide and interface charges. For the same oxide thickness, but with different stoichiometries, the curves shift towards positive voltages as the MoO_x stoichiometry increases, this shift could be related to the change of the MoO_x work function. We also noted that there is a hump in the inversion region of the C-V curve at low frequency (100 Hz), indicating the damage (Dits) caused by the MoO_x sputtering process at the SiO_2/Si interface.

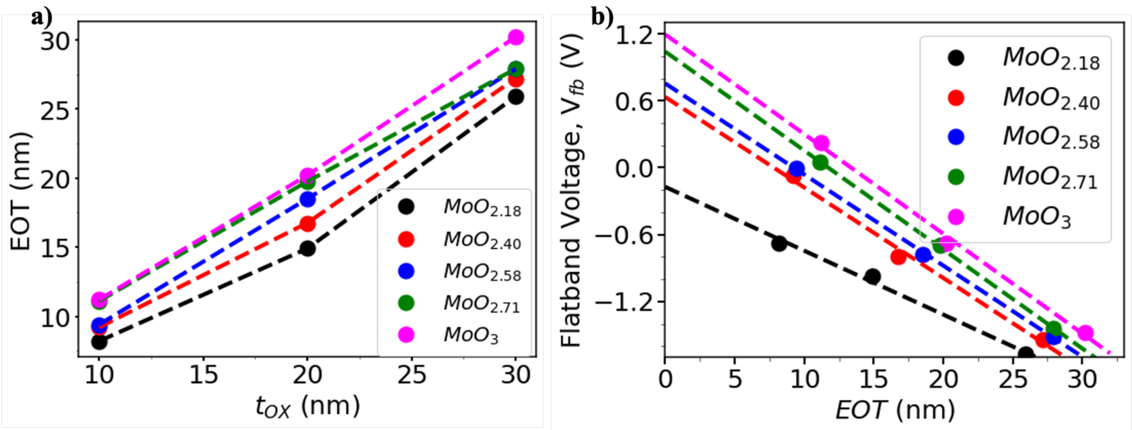

Figure 5.19: **a)** Relation between the equivalent oxide thickness EOT and and the oxide t$_{OX}$ for 100 Hz C-V curves. **b)** Relation between the flat band voltage V$_{fb}$ and the EOTf or MoOx with various stoichiometry, the linear lines are fitted by linear regression method.

Figure 5.19**a** shows the equivalent oxide thickness EOT extracted from the maximum capacitance value in the accumulation region as function of the oxide thickness t$_{OX}$(ellipsometry values). We observe that the various MoOx films behave like metal gate (electrical conductors). In fact, a slight increase in EOT is observed as the stoichiometry of the MoO$_x$ films increases. However, this increase is almost negligible and cannot be attributed to the dielectric nature of the MoOx films. On the other hand, this slight increase in EOT can be related to the effects of the sputtering process on the SiO2. For example, when the oxygen concentration in the deposition atmosphere is increased, there is a decrease in the sputtering species(Ar$^+$), which may have more or less effect on the SiO2 substrate. The flatband potentials Vfb as a function of EOT extracted from the C-V analyses are shown in **Figure** 5.19**b**. A simple linear regression is used to extract the flat-band potential V$_{fb0}$ at EOT = 0, which is then independent of oxide charges and Dits and directly related to MoO$_x$ gate work function.

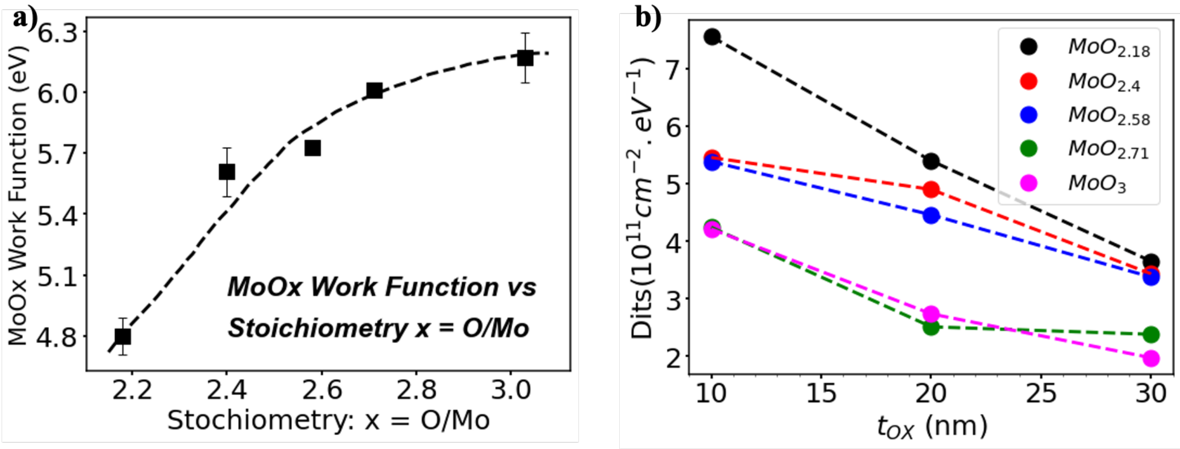

Figure 5.20: **a)** MoOx work function as function of the stoichiometry, **b)** Dits as a function of t$_{OX}$ for different MoOx stoichiometry.

The work function of MoOx is calculated from Vfb0 using the following relationship:

$$V_{fb0} = \phi_{MoOx} - \phi_{Si} \qquad (5.1.1)$$

The evolution of the work function as a function of the MoO$_x$ stoichiometry is shown in **Figure** 5.20**a**. There is an increase of the work function with stoichiometry and for nearly stoichiometric films the work function $\phi_{MoOx} > 6$ eV. These results are consistent with those from the literature (UPS measurements) [133]. As the MoO$_x$ stoichiometry increases, the low-valence Mo states associated with the donor states (oxygen vacancies) in the MoO$_x$ band gap gradually decrease. However, these variations in gap states density do not provide a direct explanation for the large variations in work function (Work function difference of more than 1 eV between MoO$_2$ and MoO$_3$) as a function of stoichiometry. The increase in work function could be related to a general change in the electronic structure of MoO$_x$, in particular an increase in ionisation energy or electronic affinity with increasing stoichiometry (ionisation of MoO$_3$ is more difficult than that of MoO$_2$).

The damage caused by the MoO$_x$ gate deposition process was evaluated in terms of Dits. The Dits as a function of oxide thickness for different MoO$_x$ stoichiometries are shown in the **Figure** 5.20**b**. An increase of Dits is observed with decreasing MoO$_x$ stoichiometry and SiO$_2$ thickness

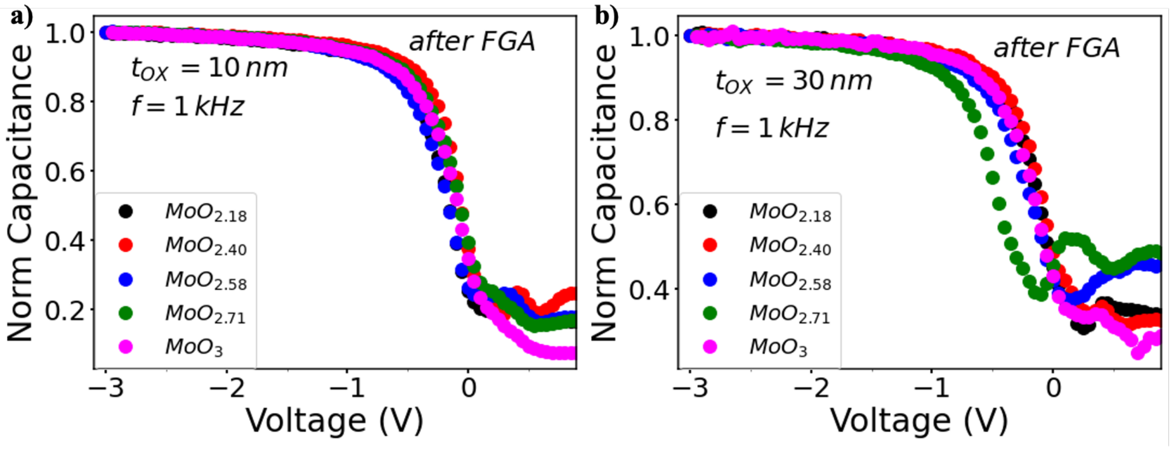

Figure 5.21: Normalized C-V curves at 1 kHz for Al/MoO$_x$/SiO$_2$/Si stack with different MoO$_x$ stoichiometry after annealing at 425°C during 30 minutes in N$_2$ + H$_2$ ambient (FGA), **a)** t$_{OX}$ = 10 nm, and **b)** t$_{OX}$ = 30 nm

On the one hand, the increase of Dits with decreasing SiO$_2$ thickness can be explained by the fact that the SiO$_2$/Si interface is less protected by a lower SiO$_2$ thickness during the MoO$_x$ sputtering process, which leads to a stronger degradation of the interface. As for the increase in Dits with decreasing stoichiometry, the origin and explanation is more difficult, but one could be that the energies of the chemical species in the plasma decrease with increasing oxygen partial pressure, leading to relatively less degradation of the SiO$_2$/Si interfaces at higher stoichiometries, as MoO$_x$ layers with higher stoichiometry are deposited with higher oxygen partial pressure.
We have also performed C-V measurements on Al/MoO$_x$(15nm)/SiO$_2$/Si structures after FGA (annealing in N$_2$H$_2$ atmosphere at 425°C during 30 minutes). The normalised C-V curves with different MoO$_x$ stoichiometry after FGA for t$_{OX}$ = 10 nm **Figure** 5.21**a** and, t$_{OX}$ = 30 nm **Figure** 5.21**b** are shown.

After the FGA, there is a significant reduction of Dits (absence of the hump near the inversion region as observe in the C-V curves of structures without FGA). There is no further effect of charge and Dits, and the flat band potential V$_{fb}$ is almost identical, regardless of the stoichiometry of the MoO$_x$ or the thickness of the SiO$_2$ (no variation of V$_{fb}$ with EOT). The work function of MoO$_x$, ϕ_{MoOx} = 4.9±0.1 eV after FGA is identical for all stoichiometries. The value of the work function obtained is close to that of MoO$_{2.18}$. These observations may indicate that that the FGA process led to a reduction of all MoO$_x$ films to metalic-like MoO$_{2.18}$. Several literature references indicate a reduction of MoO$_{3-x}$ to MoO$_2$ at temperatures close to 700K when annealed in an inert atmosphere or in the absence of oxygen [252].

5.2 NiO$_x$ thin films

5.2.1 Introduction

Nickel oxide (NiO$_x$), often mistaken as a Mott-Hubbard insulator, is actually a charge transfer insulator[137], with a rhombohedral or cubic structure, the cubic structure being the most notable. NiO$_x$ in stoichiometric form (x = 1) has a high resistivity of the order of 10^{13} Ω.cm at room temperature[253], this resistivity can be reduced by more than 10 orders of magnitude by controlling the oxidation states of the transition metal Ni such as Ni^{2+} and Ni^{3+}. The meteoric advance of perovskite-based solar cells and organic semiconductors has put NiO$_x$ at the centre of innovations in photovoltaic and many other optoelectronic applications such as photodetectors (photodiodes). This metal oxide is known for its exceptional electronic properties that favour the extraction of holes. It has achieved remarkable conversion efficiencies (PCE) of over 22% and excellent stability on single junction perovskite solar cells[254]. p-type NiO$_x$ is a wide bandgap semiconductor that offers a combination of electrical and optical properties, and an optimal electronic band structure that can be tuned according to the deposition conditions. The electrical and optical properties of NiO$_x$ can be tuned by changing the concentration of Ni^{3+} ions, either by the introduction of monovalent atoms or by the formation of nickel vacancies and/or interstitial oxygen in the NiO$_x$ lattice[255]. For example, a high oxygen partial pressure can cause significant changes in the chemical composition of NiO$_x$ thin films (The excess oxygen should lead to an increase in Ni^{3+} defects), which strongly influence the electrical resistivity. In addition to its potential for hole extraction, NiO$_x$ also has electron-blocking properties and is very compatible with low temperature processing. These properties make it a promising material for band alignment engineering or HTL on IR photodiodes based on QDs such as PbS or perovskite QDs. The possibility of large-area deposition (by PVD or PLD) also makes them suitable for industrial-scale applications. This section focuses on the room temperature preparation and characterization of NiO$_x$ thin films as hole transport layers in PbS QDs and perovskites based photodiodes.

5.2.2 Experimental

The NiO$_x$ thin films were deposited at room temperature (without intentional heating of the substrate) by RF magnetron sputtering (AC CT200), on different types of substrates (Corning glass, Si and SiO$_2$ substrates depending on the intended final characterizations to be preformed), from a NiO target (supplied by Praxair Technology Inc), with 103 mm in diameter and 3 mm thick bonded on a copper plate by indium paste. The target was of 3N purity, Ni and O composition in a 1:1 ratio. Prior to any deposition, the target was pre-sputtered during 30 minutes to decontaminate and de-oxidise the target surface, the chamber base pressure was reduced to $\simeq 10^{-7}$ mbar. The distance between the target and the substrates was maintained at about 22 cm and the substrate was rotated at 45 rpm to achieve uniform thickness on 200 mm substrate. The total sputtering power was maintained at 100 W, with the deposition pressure varying between 0.002 and 0.004 mbar. The Ar flow rate was set at 50 sccm and the oxygen flow was varied between 0 and 15 sccm corresponding to an oxygen concentration varying between 0 and 23.08%.
Films thickness were monitored by adjusting the deposition time and using XRR measurements. For a total deposition pressure of 0.002 mbar, the deposition rate and volume density of the films as a function of oxygen concentration are shown in **Figure** 5.22. There is a decrease in deposition rate due to oxidation of the target with the addition of oxygen and a reduction in sputtering efficiency. There are also extremely low deposition rates, of the order of 0.1 Å.s^{-1}. Intuitively, a decrease of the film density is expected with increasing oxygen concentration in the deposition atmosphere, since the atomic mass of oxygen is lower than that of nickel, so that an

increase in the O/Ni ratio in NiO$_x$ films should lead to the decrease of the film density. The observed increase of the density indicates that the films become less porous as the oxygen partial pressure increases, and this decrease of the porosity dominates over the increase of the O/Ni ratio (see **Figure** 5.23, fitting data are shown in appendix).

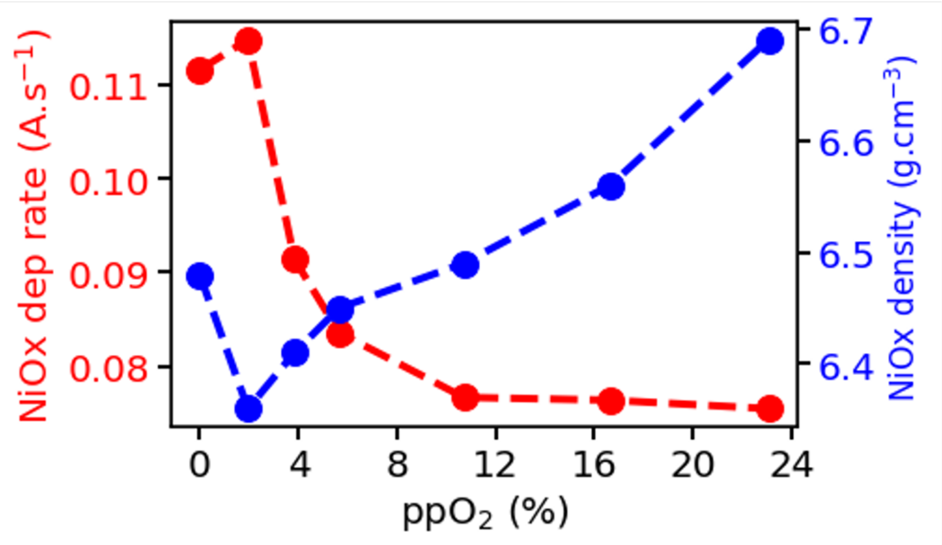

Figure 5.22: In red, the change in deposition rate of NiOx thin films at room temperature as a function of ppO$_2$ in %, Ar flow rate = 50 sccm, working pressure = 0.002 mbar, RF power = 100 watts. In blue, NiOx volume density in g.cm^{-3} as a function of oxygen partial pressure (O$_2$ flow rate varies between 0 sccm and 15 sccm).

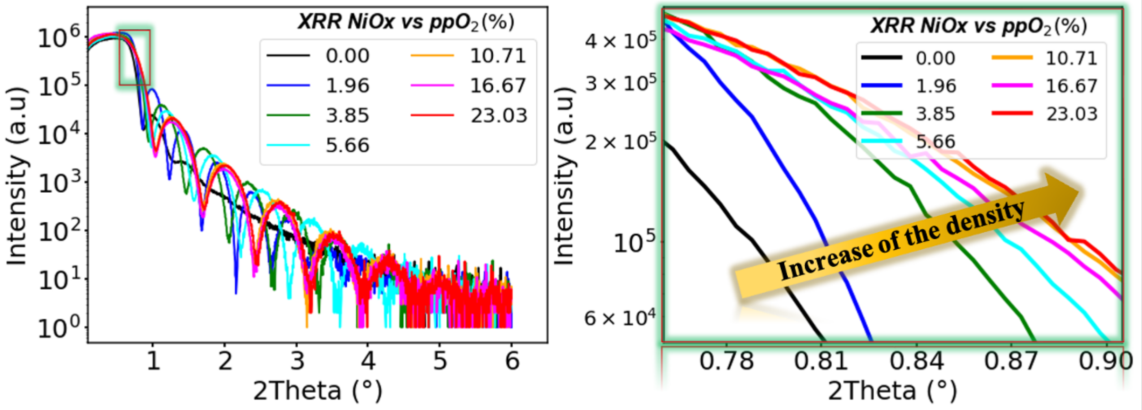

Figure 5.23: NiO$_x$ X-ray reflectometry measurements as a function of oxygen concentration, the image on the right shows the highlight of the region θ = 0.6-0.9°, the shift to the right corresponds to an increase in the density of the NiO$_x$ films.

5.2.3 Results and discussions

Different types of characterization were performed and we present and discuss their results in the following sections. Since the properties of NiO$_x$ films are expected to change depending on the oxygen concentration, we will first examine the chemical composition of NiO$_x$. Secondly, we will present some properties of NiO$_x$ films prepared at different oxygen concentrations (oxygen flow rate).

5.2.3.1 XPS analyses and NiO$_x$ composition

We have used XPS to identify the Ni oxydisation states and to study the composition of NiO$_x$ thin films as a function of ppO$_2$. The spectra of Ni 2p, Ni 3s and O 1s are shown in **Figures** 5.24**a**, 5.24**b** and 5.24**c**, respectively. The magnification of the highlighted region of the O 1s peak (**Figure** 5.24**d**) at about 531 eV shows an increase of the intensity with increasing oxygen partial pressure. In contrast, the Ni 2p and Ni 3s spectra show no sensitivity to the change of the oxygen pressure. Therefore, the most suitable peak for assessing the composition of the different NiO$_x$ films is that of the O 1s core level.

Figure 5.25**a-d** shows the O 1s peak, which was carefully de-convoluted using Gaussian functions centered at 529.3 eV, 531.1 eV, and 532.1 eV corresponding to NiO lattice oxygen (or Ni^{2+}), Ni vacancies or interstitial oxygen (Ni$_2$O$_3$ or Ni^{3+}), or substitutions of Ni^{2+} ions by Ni^{3+} ions and hydroxide groups or absorbed water (NiOOH), respectively. Even though the NiO$_x$ was prepared in a vacuum system without water in the deposition atmosphere, hydroxylation was observed in all our NiO$_x$ films. This hydroxylation is related to the exposure of the films to ambient air. This effect persists even if the air exposure time is extremely shortened, as the phenomenon of hydroxylation is almost ubiquitous in metal oxides. The increase in oxygen concentration leads to the evolution of NiO$_x$ (x $\approx$ 1) to Ni$_2$O$_3$, i.e. an increase in Ni^{3+} and a decrease in Ni^{2+}.

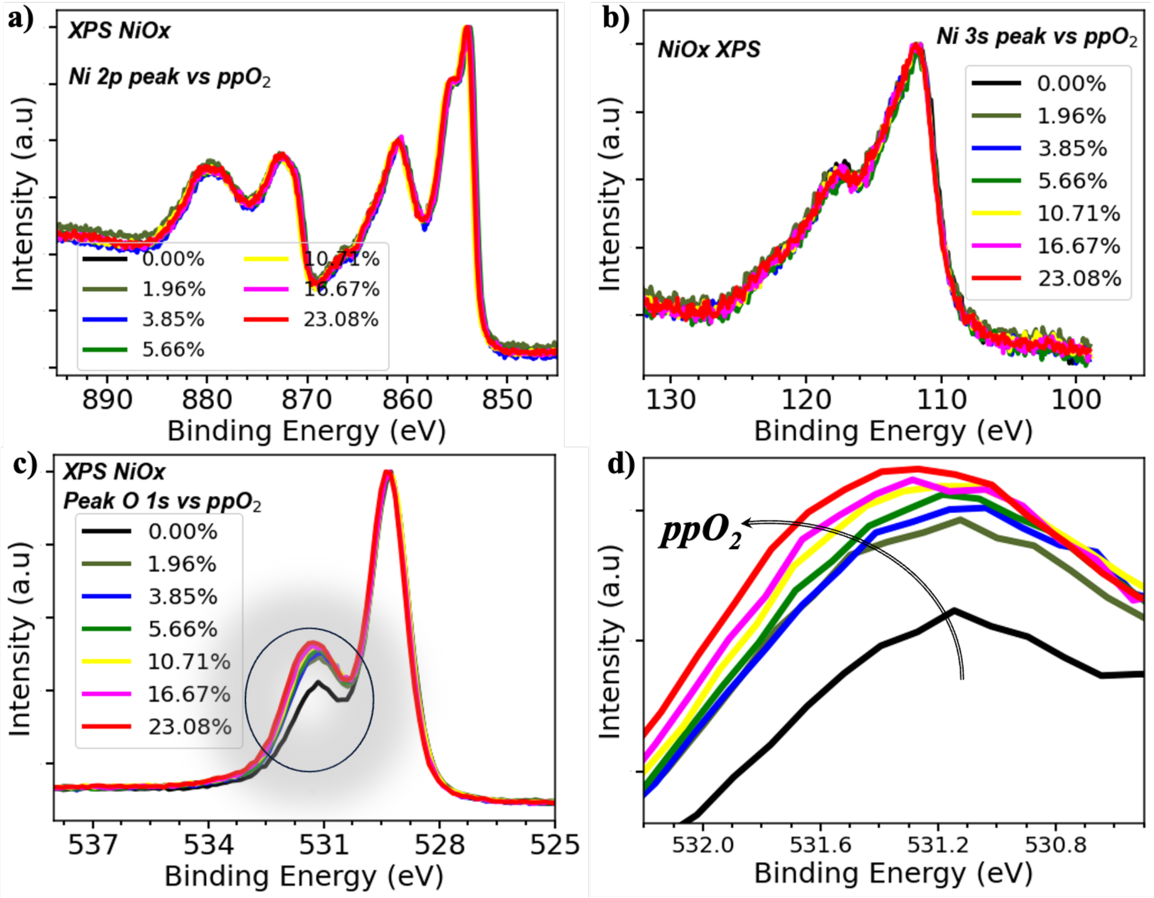

Figure 5.24: XPS spectra of NiO$_X$ films deposited under the different oxygen partial pressures, **a)** Ni 2p, **b)** Ni 3s, **c** O1s, **d)** Expanded view of the second peak of O 1s core level showing the relative increase of the intensity with oxygen partial pressure.

The composition of the films in proportions (in %) NiO:Ni$_2$O$_3$:NiOOH or Ni^{2+}:Ni^{3+}:NiOOH ranged from 68.85:25.21:5.95 for NiO$_x$ (ppO$_2$ = 0.0%) to 56.26:36.18:7.56 for NiO$_x$ (ppO$_2$ = 23.08%). The NiO$_x$ film deposited at the highest oxygen partial pressure has the highest Ni^{3+}

concentration, which is associated with significant oxygen and nickel defects generation described in Kroger-Vink notation by the following relation[256]:

$$2Ni_{Ni}^{\times} + \frac{1}{2}O_2(g) \rightarrow 2Ni_{Ni}^{\bullet} + O_O^x + V_{Ni}'' \tag{5.2.1}$$

More clearly, the above relationship corresponds to the doping mechanism of NiO$_x$ films by interstitial oxygen atoms or Ni vacancies (the formation of an ionized nickel vacancy leads to the release of two holes in the material):

$$\frac{1}{2}O_2(g) \rightarrow O_O^x + V_{Ni}'' + 2h \tag{5.2.2}$$

$Ni_{Ni}^{\times}$, $Ni_{Ni}^{\bullet}$, V_{Ni}'' and O_O^x represent lattice Ni^{2+}, Ni^{3+}, ionized nickel vacancies and lattice oxygen O^{2-} respectively. Ni^{3+} ions thus act as acceptors, and we will observe their effects on the electrical and optical properties of NiO$_x$ films. The **Figure** 5.26 summarizes the chemical composition measurements and shows an increase in the Ni_2O_3/NiO ratio with increasing oxygen partial pressure. The concentration of Ni_2O_3 groups increases significantly in the 0 - 5% partial pressure range, while the increase is slower in the 5 - 23% range.

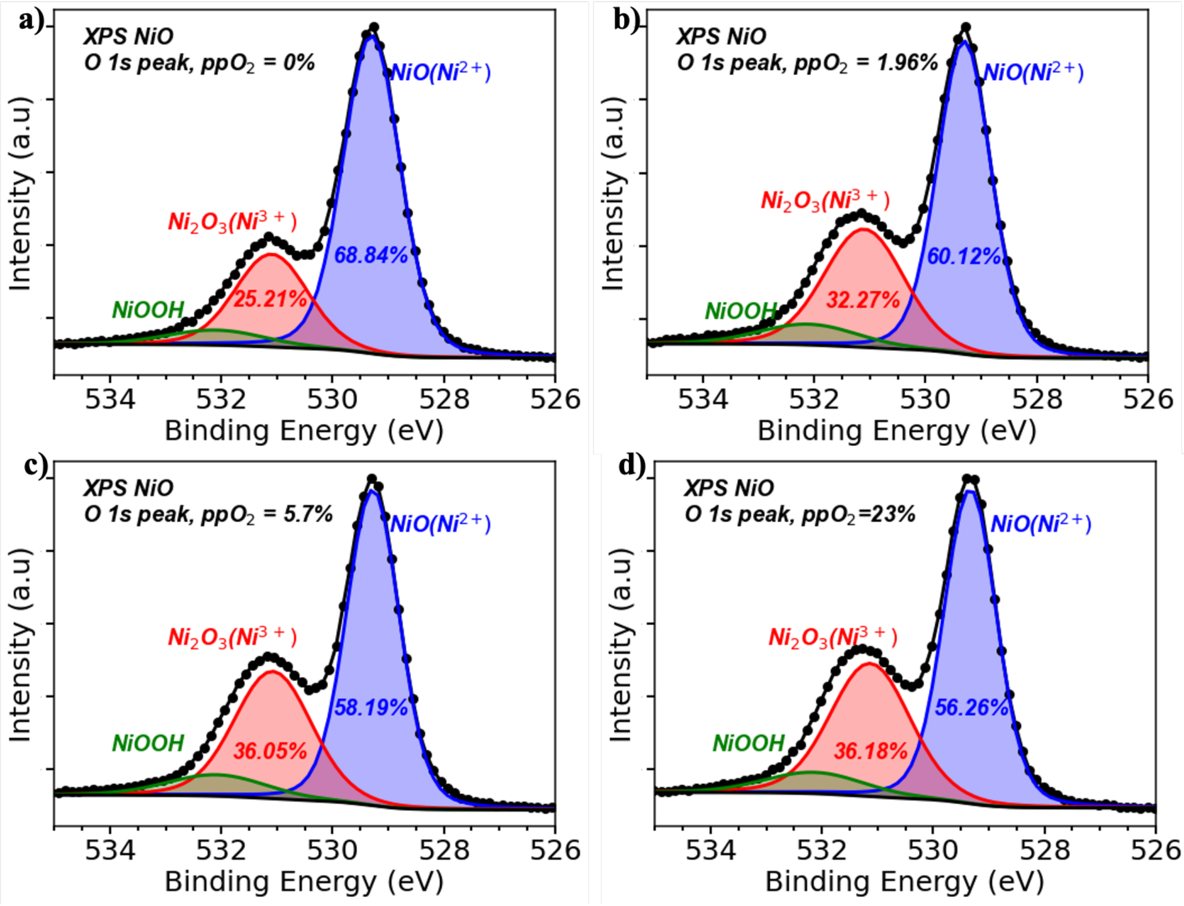

Figure 5.25: Composition of NiO$_x$ by O 1s XPS spectra fitted into lattice oxygen NiO (Ni^{2+}), interstitial oxygen or oxygen defect Ni_2O_3 (Ni^{3+}), and loosely bound hydroxide related group NiOOH concentrations.

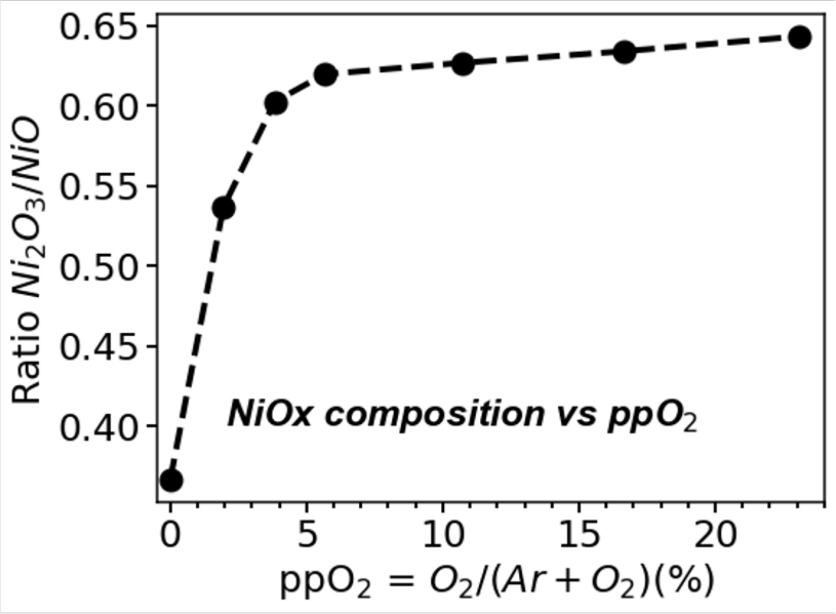

Figure 5.26: Evolution of the NiO$_x$ composition (Ni$_2$O$_3$/NiO ratio) as function of the oxygen partial pressure.

5.2.3.2 NiO$_x$ electrical properties

Electrical resistivity measurements are shown in **Figure** 5.27. Electrical resistivity decreases between 25.68 Ω.cm to 0.71 Ω.cm when the oxygen concentration varies between 0 and 23.08%. The decrease in electrical resistivity over more than a decade is related to the increase in Ni^{3+} concentration. Due to the relatively high electrical resistivities, accurate Hall effect measurements were only possible on NiOx samples prepared with a high oxygen concentration, with hole densities of $\approx 10^{17}$ cm^{-3} and an electrical mobility in the order $\approx 1 - 10^2$ cm^2.V^{-1}.s^{-1}. These Hall effect measurements also prove that sup-stoichiometric NiO$_x$ films (x > 1) are p-type semiconductors and confirm the fact that the formation of (interstitial) oxygen defects or Ni vacancies (or the substitution of Ni^{2+} cations by Ni^{3+}) leads to the formation of acceptor states in the material, described by **Equation**: 5.2.1.

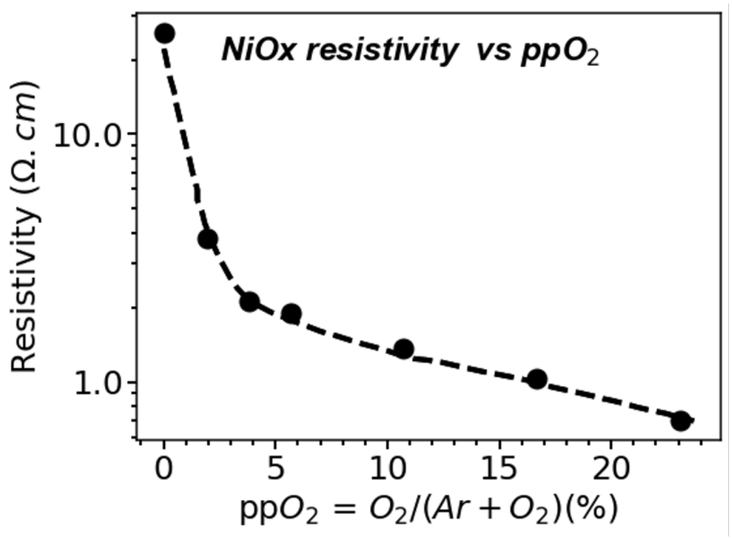

Figure 5.27: NiO$_x$ electrical resistivity as function of oxygen partial pressure.

We have also performed in-situ measurements of the electrical resistivity of NiO$_x$ in an

O_2+N_2 atmosphere between 25°C and 450°C. The measurements were performed at different time points on different samples prepared from identical samples (a substrate with a 30 nm NiO_x deposited on SiO_2, then cleaved into different samples). The **Figure** 5.28**a** show that NiO_x behaves like a semiconductor, with an overall decrease in resistivity as a function of temperature. This can be explained by thermal activation in the material or the ionisation of neutral defects (Ni vacancies or interstitial O). Resistivity measurements at different time intervals on different but almost identical samples (with the only difference being the duration of exposure to the ambient atmosphere before measurement) have shown that NiO_x, like almost all other transition metal oxides, is unstable in air. This instability is reflected in a continuous increase in electrical resistivity at room temperature (resistivity value at 25°C) of about one decade after one month's exposure to the ambient atmosphere (**Figure** 5.28**b**). In addition to the increase in electrical resistivity, at $\simeq$ 200°C a hump of unknown origin appears and increases progressively as the time of exposure to ambient air increases. The observed instability of NiO_x films (increases resistivity) can be attributed to the absorption of H_2O or moisture by the NiO_x films (increased concentration of NiOOH complexes). Complementary XPS measurements could provide a better understanding of this degradation phenomenon.

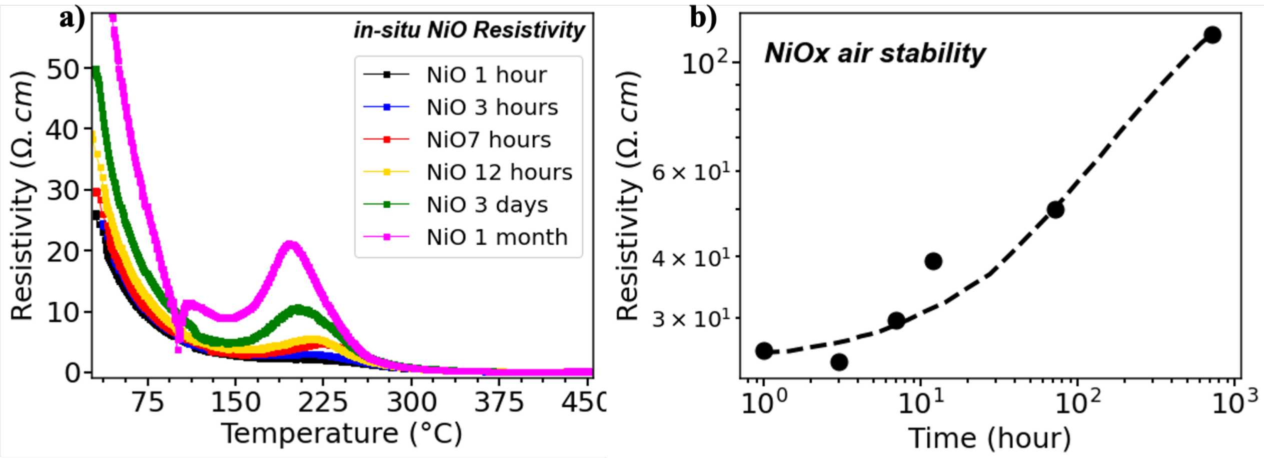

Figure 5.28: **a)** NiO_x (ppO_2 = 0.0%) in-situ electrical resistivity as a function of temperature and, **b)** NiOx air stability, changes in electrical resistivity over time (resistivity measured at room temperature T = 25°C.)

5.2.3.3 NiO_x optical properties

The optical transmission measurements for NiO_x at different oxygen partial pressures are shown in **Figure** 5.29**a**. For films with a thickness of 30 nm, the transmission values in the lower IR range are between 60 % and 85 %. The variation as a function of oxygen concentration is not significant. However, there is a difference between the optical transmission of the NiOx films deposited without additional oxygen (ppO2 = 0 %) and the films deposited with added oxygen. The transmission value at 940 nm, one of the wavelengths of interest, is about 75 % for NiOx (ppO2 = 0 %) and about 65 % for the other oxygen concentrations. The slight decrease in optical transmission between the film deposited without added oxygen and the films deposited with $ppO_2 > 0\%$ can be attributed to the high concentration of Ni^{3+} cations, as Ni^{3+} ions act as F color centers and lead to darkening of the NiO_x films. This effect is well known and is associated with the electrochromic properties of NiO_x.[257, 258]. The relatively low optical transmission of NiO_x films with a thickness of 30 nm (lower than 80% in Vis-NIR) could be a problem for their use in devices such as photodiodes, as the films would absorb a significant portion of the light signal at such thicknesses. Fortunately, the optimal thickness are between 5-10 nm, as we will see in the section on QD-based photodiodes using NiO_x as HTL. **Figure** 5.29**b** shows the evolution of the optical NiOx transmission ($ppO_2 = 0\%$) as a function of films thickness, with transmission values greater than 80% in the Vis-NIR range for layer thickness less than 10 nm.

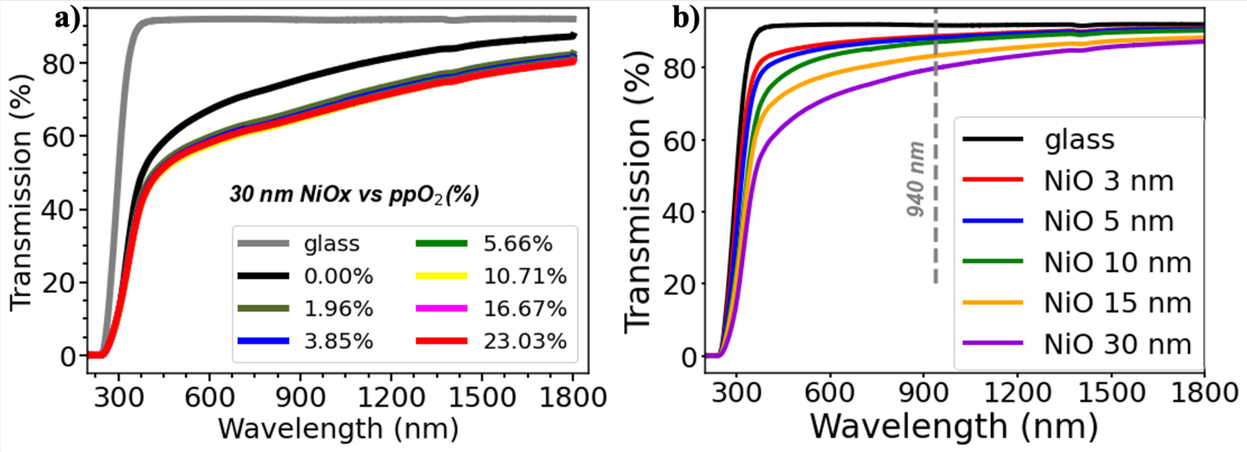

Figure 5.29: **a)** Optical transmission spectra of the NiO$_x$ thin films with different oxygen concentration (thickness = 30 nm), **b)** Optical transmission spectra on NiO$_x$ ($ppO_2 = 0.0\%$) for different thicknesses.

The extinction coefficients k obtained from ellipsometric measurements (**Figure** 5.30**a**) show that the NiO$_x$ film deposited without oxygen has the lowest extinction coefficient values between 600 - 1800 nm, i.e. the lowest optical absorption ($\alpha = \dfrac{4\pi k}{\lambda}$). There is very good agreement between the optical transmission measurements and the ellipsometry measurements. As with the optical transmission, the films deposited with oxygen also show only a very insignificant increase in the extinction coefficient with increasing oxygen concentration. Measurements of the optical gap using Tauc diagrams (**Figure** 5.30**b**) give $E_{gopt} = 3.37$ eV for NiO$_x$ ($ppO_2 = 0\%$), this optical gap decreases only very slightly with increasing oxygen concentration.

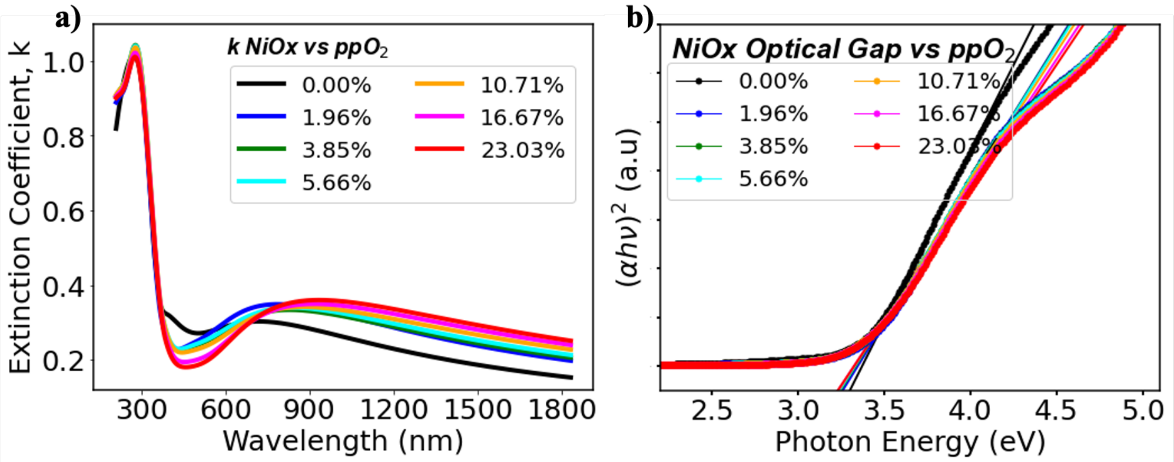

Figure 5.30: **a)** NiO$_x$ extinction coefficient and, **b)** NiO$_x$ Tauc-plot (optical band-gap) as function of oxygen partial pressure.

5.2.3.4 NiO$_x$ structural properties and surface morphology

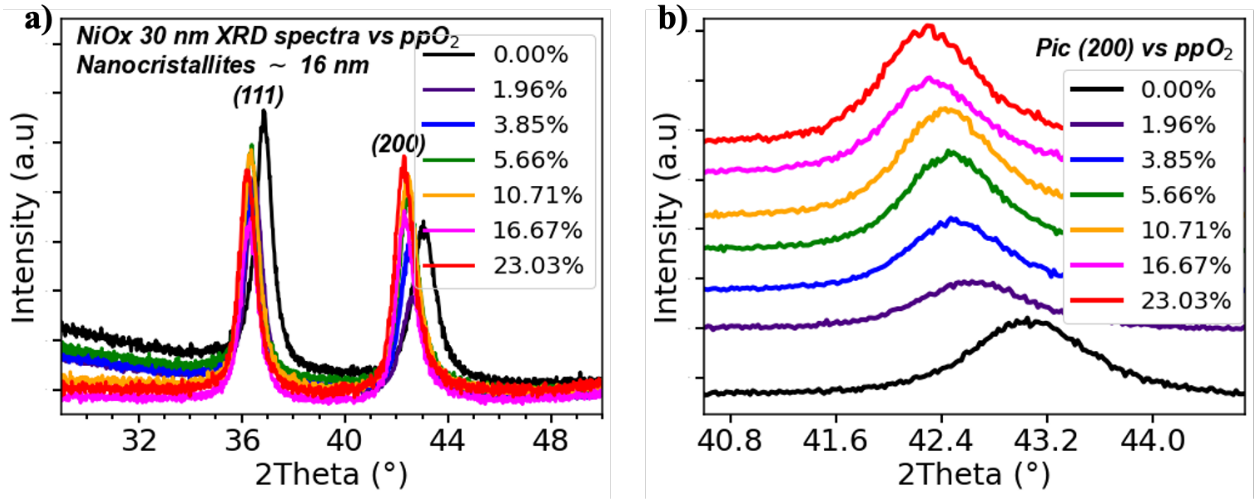

Figure 5.31: **a)** Grazing incidence angle x-rays diffraction patterns of NiO$_x$ as function of oxygen partial pressure, features are labelled with the corresponding (hkl) reflections of NiO$_x$ cubic-phase, **b)** Expanded view of (200) pic showing the shift towards low Bragg angles.

Figure 5.31**a** shows grazing incidence X-ray diffraction spectra of 30 nm thick NiO$_x$ films measured at room temperature as a function of oxygen partial pressure. All films were nanocrystalline with preferred orientations in the (111) and (200) planes, with peaks occurring around $2\theta =$ 36-37° and 42-43°, respectively, indicating the cubic rock salt structure. The intensity of the peak (111), which corresponds to the main plane of the NiO crystal (rock salt with face-centred cubic structure), decreases with decreasing oxygen concentration. This decrease indicates a decrease in crystallinity, which can be attributed to the increase in defects (Ni vacancies or interstitial oxygen atoms) in the NiO$_x$ structures as the oxygen concentration increases. The grain size D estimated by the Scherrer formula $D = \dfrac{0.9\lambda}{Bcos\theta}$ was about 16 nm for the oxygen-free film and lower values (8-11 nm) for the films prepared with oxygen. With increasing ppO$_2$, we observe a shift of peaks (111) and (200) to lower Bragg angles,$2\theta = 36.85 \rightharpoonup 36.45 \rightharpoonup 36.35 \rightharpoonup 36.3 \rightharpoonup 36.37 \rightharpoonup 36.35 \rightharpoonup 36.17$ and $43.05 \rightharpoonup 42.63 \rightharpoonup 42.47 \rightharpoonup 42.45 \rightharpoonup 42.43 \rightharpoonup 42.43 \rightharpoonup 42.31 \rightharpoonup 42.29$, respectively for (111) and (200) peaks, as ppO$_2$ increases between $0 \rightharpoonup 23\%$ (**Figure** 5.31**b**). In the literature, this shift is generally attributed to the existence of strains in NiO$_x$ films[259, 260]. Interstitial oxygen atoms can induce tensile strains in NiO$_x$ films. These measurements can be correlated with the XRR measurements, the increase in film density with increasing oxygen concentration observed may be related to the insertion of additional oxygen atoms resulting in strains in the NiO lattice.

2D AFM images show the surface topography of NiO$_x$ films deposited with different oxygen partial pressures. The film deposited without oxygen (**Figure** 5.32**a**) has the highest peak-to-valley value ($\approx$ 10.0 nm) and a RMS surface roughness greater than 1 nm. A grain-like or nanocrystalline structure is also observed, confirming the grain size value obtained in GIXRD. As ppO$_2$ increases, the overall surface roughness decreases and the crystalline signature is less and less visible on the AFM images (**Figure** 5.32**b** - 5.32**f**). The evolution of roughness as a function of ppO$_2$ is shown in **Figure** 5.33.

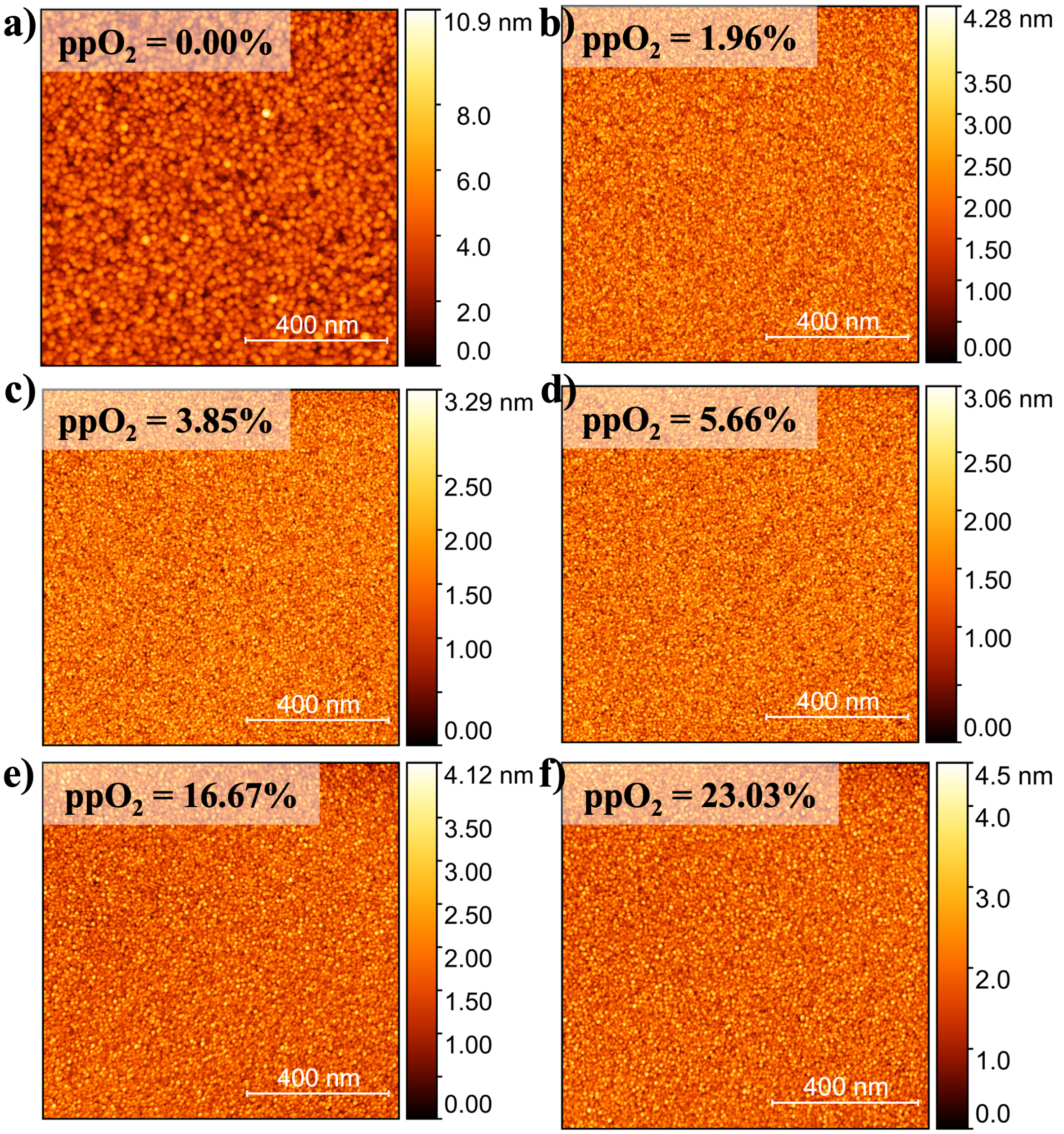

Figure 5.32: 2D AFM images of NiO$_x$ with different oxygen partial pressure

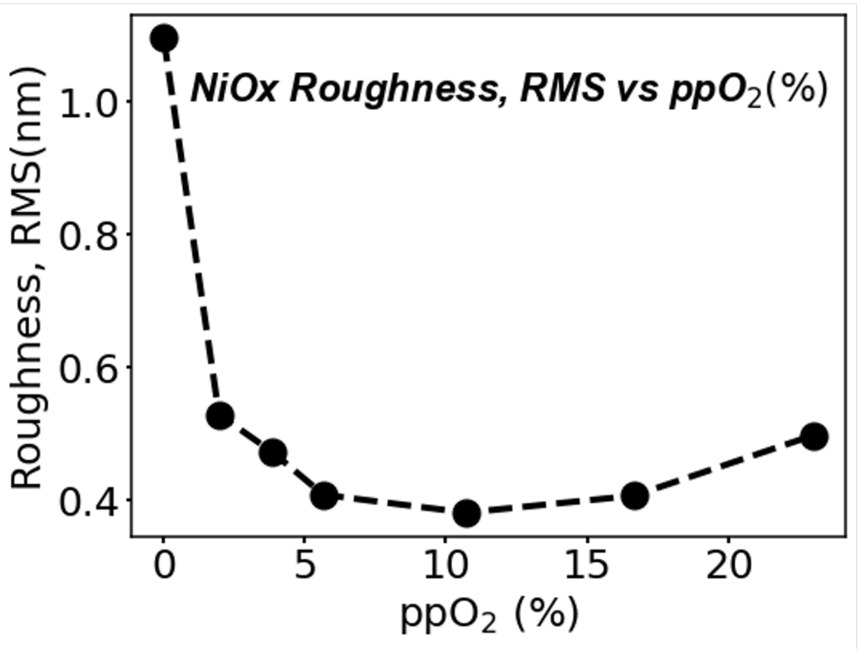

Figure 5.33: Evolution of NiO$_x$roughness (RMS) obtained from AFM measurements, as a function oxygen partial pressure ppO$_2$ (%).

5.2.3.5 NiO$_x$ work function by UPS measurements

Measurements of the work function of NiO$_x$ deposited at different working pressures and without oxygen addition (ppO$_2$ =0%) were performed with UPS. To decontaminate the sample surface, we used a 120 second low damage etching ion beam or GCIB. The procedure is almost identical to that described in the section on measuring the MoO$_x$ work function after surface preparation. The XPS measurement (survey spectrum) in **Figure** 5.34**a** shows the disappearance of the C 1s peak (≈ 284 eV) associated with surface contamination, indicating that we have a clean surface. We also note an increase in signal intensity after GCIB. The UPS spectra recorded after GCIB are shown in **Figure** 5.34**b**. All three samples show almost identical spectra, indicating minor variations in the work function of the NiOx films with total deposition pressure. **Figure** 5.34**c** and 5.34**c** correspond to the expanded view on the secondary electron cut-off (SEC) and the valence band regions. The secondary cut-off region (17.1-17.4 eV) show only slightly changes. The structure of the valence band shows that there are almost no gap states for NiO$_x$ (ppO$_2$ = 0.0%) as observed in MoO$_x$, and that the Fermi level is located at ≈ 1 eV above the NiO$_x$ valence band maximum. This considerable energy difference (≈ 1 eV) between the position of the Fermi level and the top of the valence band may be somewhat perplexing. Considering the case of p-type Si with doping levels similar to those in NiO$_x$ films (10^{16} - 10^{17} cm^{-3}), the Fermi level is found to be about 0.18-0.12 eV above the valence band, i.e. a variation of about 60 meV per decade on the acceptor density. However, several other authors have reported similar results[261, 262]. We will retain the value of E_F - E_V ≈ 1 eV where necessary in the following.

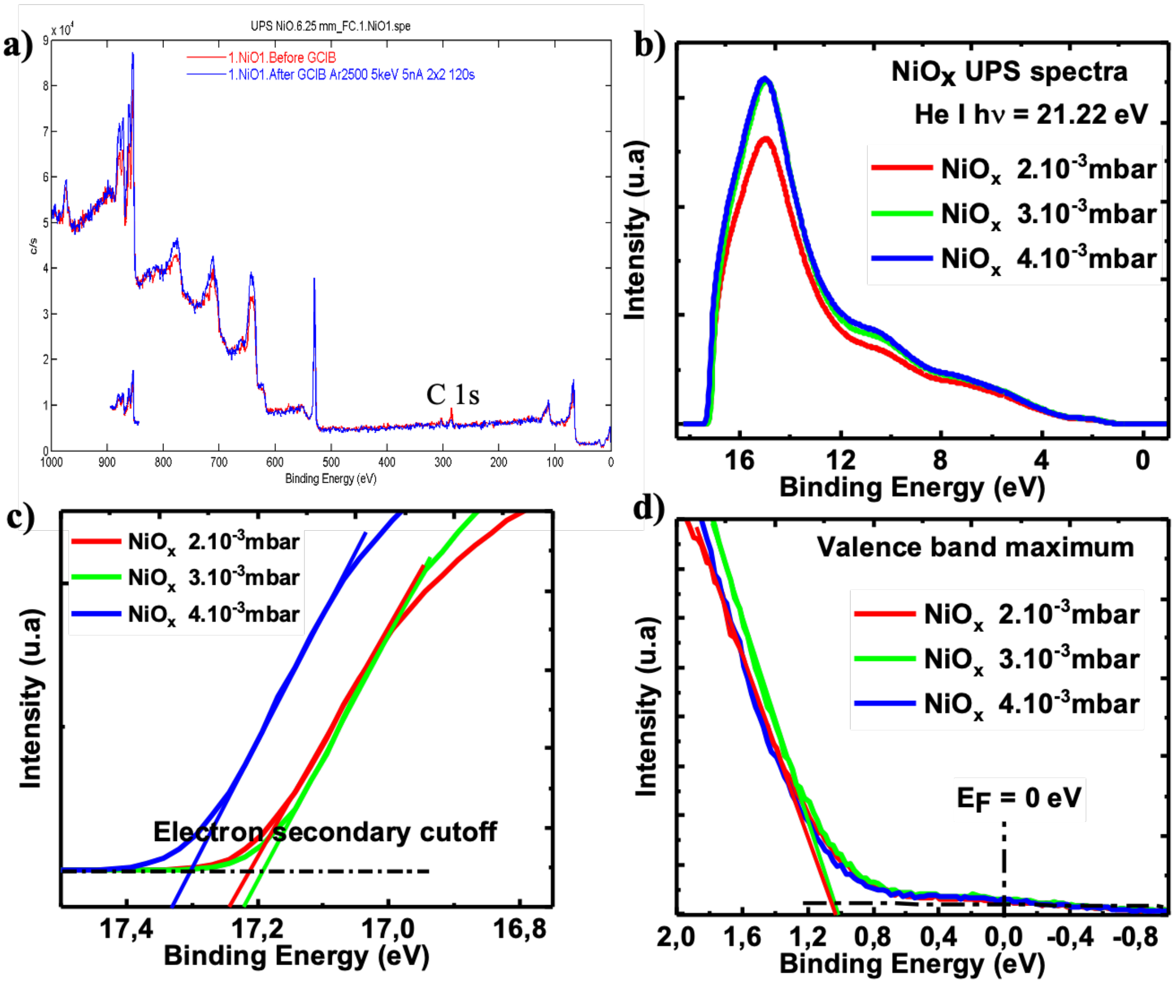

Figure 5.34: **a)** XPS analysis for surface preparation prior to UPS measurement, with a gun cluster ion beam (GCIB) consisting of low-energy Ar$^+$ clusters, 5 keV at 5 nA, etching during 120 s **b)** UPS spectra of the NiOx films at different deposition pressures (0.002, 0.003 and 0.004 mbar), **c)** secondary electrons cut-off for determining the work function, **d)** binding energy range valence band spectra

Working pressure (mbar)	0.002	0.003	0.004
ϕ_{NiOx} **(eV)**	3.92±0.05	4.01±0.05	4.03±0.05

Table 5.4: NiO$_x$ work function values after surface preparation for various total deposition pressures.

The work function is determined by measuring the photoemission threshold on the secondary electron spectrum and the position of the Fermi level. The values of the work function are summarized in **Table** 5.4. The work function is between 3.92 - 4.03) eV. These values are about 0.4-1.9 eV below the expected values and the literature [263, 264, 265]. Due to the electrical properties of NiO$_x$ (resistivity in the order of 10 Ω.cm, hole density of about 10^{16} cm^{-3}), we believe that we encounter the same difficulties as when measuring the work function of highly stoichiometric MoO$_x$ films (with high electrical resistivity).

5.3 Conclusion

In this section, we have investigated the properties of MoO$_x$ and NiO$_x$ prepared by DC/RF sputtering as potential hole extraction materials on PbS-based perovskite QDs. We have shown that the properties of these materials are strongly dependent on their oxygen concentration and can be easily tuned by the choice of deposition conditions.

Investigations on MoO$_x$ have shown that the stoichiometry can be easily controlled during deposition by the oxygen partial pressure. At a partial pressure between 5.67% and 19.35%, we obtained a stoichiometry or O/Mo ratio between x = 2.18-3, with oxidation almost complete at ppO$_2$ = 12%. We have shown that the electrical resistivity of MoO$_x$ varies from 10^{-3} Ω.cm to 10^5 Ω.cm when the stoichiometry x varies between x= 2.18-3, i.e. by more than 8 orders of magnitude. MoO$_x$ films with stoichiometry $x < 2.5$ are semi-metallic-like with charge carrier densities of 10^{21}-10^{23} cm^{-3} and mobilities of about 10^{-2} cm^{2}V^{-1}s^{-1}, while films with $x > 2.7$ are highly resistive and the mobility and density of the free charge carriers are no longer easily measurable. There is a trade-off between the electrical and optical properties of MoO$_x$, with increasing stoichiometry, there is a deterioration of the electrical properties and an improvement of the optical properties, in particular an increase in the optical gap and thus the optical transmission. All MoO$_x$ films deposited at room temperature were completely amorphous, and exhibited very low surface roughness (RMS $<$ 0.5 nm). The work function was determined using two different techniques. UPS measurement showed limitations on highly resistive materials (there would be a charging effect leading to lower values than expected). Consistent values of the work function were obtained by UPS measurements on MoO$_x$ films with lower stoichiometry (low electrical resistivities), while the values of films with a stoichiometry $x > 2.7$ were too low compared to literature. The C-V method enabled us to measure values for the work function that were close to the expected values and in very good agreement with those from the literature (increasing work function with stoichiometry and $\phi > 6$eV for nearly stoichiometric films). These C-V measurements and analysis have also shown that, regardless of the stoichiometry, the MoO$_x$ films behave like metallic gate and not like dielectrics, as one might expect, especially for films with a stoichiometry $x \approx 3$. The EOT values are all close to the prepared SiO$_2$ thickness.

Concerning NiO$_x$ material, depositions and characterizations showed that NiO$_x$ ($x > 1$) is a p-type semiconductor in contrast of n-type MoO$_x$. NiO$_x$ electrical and optical properties change in the opposite direction to MoO$_x$ with increasing oxygen concentration. The determination of NiO$_x$ stoichiometry by XPS is not straightforward due to the complex nature of the Ni 2p and Ni 1s peaks, but quantification of the different chemical states around Ni was achieved with the O 1s core level peak. An increase in Ni$_2$O$_3$ or Ni^{3+} concentration was observed simultaneously with a decrease in NiO (Ni^{2+}) concentration with increasing oxygen partial pressure. Both phenomena correspond to an increase in the concentration of Ni vacancies or interstitial oxygen atoms. These defects act as acceptors and generate a greater density of holes, leading to a decrease in resistivity and optical transmission with increasing oxygen partial pressure. All NiO$_x$ films deposited from a NiO target at room temperature were nanocrystalline with grain sizes of 8 - 16 nm and low surface roughnesses, RMS of 0.4 - 1.1 nm. The high concentration of oxygen relative to Ni led to tensile strains in the NiO$_x$ films and made them less dense. Moreover, like most metal oxides, NiO$_x$ is very unstable in the ambient atmosphere (resistivity increases with respect to the air exposition time). NiO$_X$ work function measurements by UPS were unsuccessful due to their relatively low conductivity.

In the next section, we present results for photodiode devices incorporating NiO$_x$, MoO$_x$ as a hole extraction layer and hydrogen-doped ITO as a transparent electrode.

Chapter 6

Photodiodes based on PbS QDs and perovskites

6.1 PbS QDs based IR p-i-n photodiodes

6.1.1 Introduction

Infrared detectors with high efficiency are necessary for numerous applications such as spectroscopy, night and computer vision, medical imaging, consumer electronics, and astronomy[266]. Over the last decade, significant progress has been made in the development of detectors based on colloidal quantum dots to replace traditional III-V semiconductor-based detectors (InGaAs, InP, GaN), which involve expensive manufacturing processes and poor performance[267]. Colloidal quantum dot technology offers many advantages, including low cost and easy fabrication, high performance, direct integration with silicon electronics for imaging systems, the possibility of dimension reduction, and compatibility with flexible substrates[40]. Significant efforts have been made in the synthesis and deposition of a light-harvesting layer (PbS QDs) with high stability, good electrical and optical properties[55]. Efforts have also been made to achieve contacts allowing proper transport of electrons and holes at each electrode in a p-i-n photodiode architecture[1]. Different classes of materials are used as hole extraction layers, with the primary ones consisting of transition metal oxides and organic semiconductors. Traditionally, n-type MoO_x has been the most frequently used material, but it requires a precisely defined choice of MoO_x stoichiometry and the additional use of a p-type PbS layer for good performance[9, 10]. This section will focus specifically on the study of hole extraction layers and the transparent electrode based-In_2O_3 TCO. We will show the comparison between different hole extraction layer materials and demonstrate the interest of NiO_x ultra-thin film as extraction layers.

6.1.2 Experimental

6.1.2.1 Device fabrication and electrical measurements set-up

The structure of the photodiode is shown in **Figure** 6.1 . The anode (top electrode) consists of a transparent conductive hydrogen-doped indium oxide electrode (H-ITO). H-ITO films with different properties are deposited by RF magnetron sputtering in an $Ar:O_2:H_2$ atmosphere at different oxygen concentrations and deposition powers with a fixed sputtering pressure of 0.001 mbar (section on the investigation of the properties of In_2O_3-based TCO), starting from an In_2O_3-Sn target (Sn 10 wt%, purity 6N, 4 inch diameter, by Kurt J. Lesker), The electrical resistivity ρ of the ITO-H films vary between 420 $\mu\Omega$.cm and 820 $\mu\Omega$.cm, with an optical transmission of more than 80% at 940 nm for thicknesses between 22 and 100 nm.

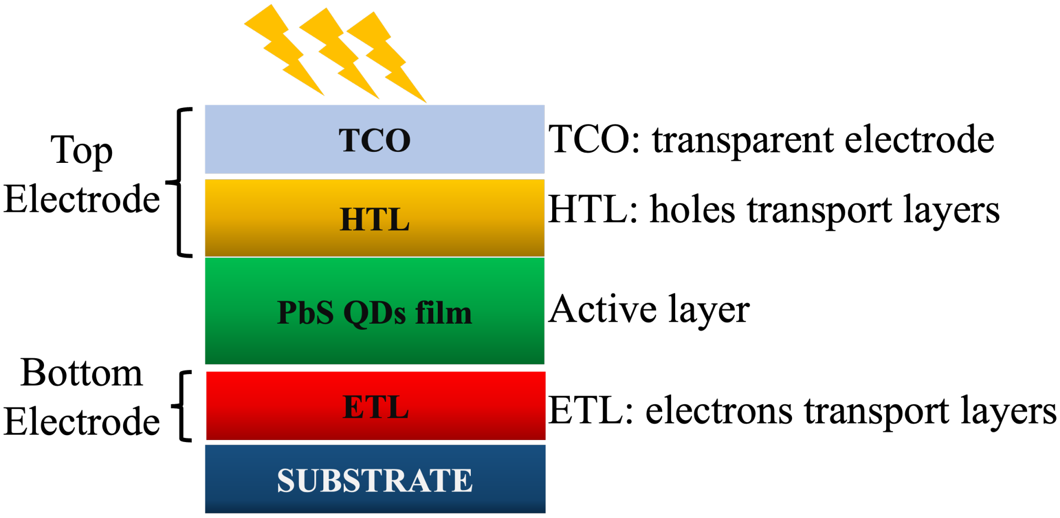

Figure 6.1: Device architecture of PbS QDs film based photodiodes.

NiO_x and MoO_x holes extraction layers were deposited at room temperature respectively by RF sputtering from a 4.0 inch diameter NiO target with a purity of 3N supplied by Praxair (with a sputtering pressure of 0.002 mbar and an RF power of 50 W), and by reactive DC sputtering from a metallic Mo target supplied by Kurt J. Lesker with a purity of 99.99% (with a sputtering pressure of 0.0025 mbar, a DC power of 100 W and a different oxygen concentration of O_2). The properties of these materials are described in the section on metal oxide (NiO_x and MoO_x) hole extraction layers. We will present photodiodes with holes extraction layers based on Mo-doped NiOx. Holes extraction layers based on Mo-doped NiO_x will be prepared by co-sputtering between NiO and Mo targets. The Mo concentration in these films was defined by adjusting the powers on the Mo and NiO targets. Investigations on NiO_x extraction layers deposited from a NiO target by reactive RF sputtering were performed after the difficulties faced when using NiO_x films deposited from a Ni metal target (Ni target supplied by Kurt J. Lesker). The deposition of the transparent H-ITO electrode and the different HTL materials was performed on the PbS QDs layer at a very low deposition rate of less than 1 $nm.min^{-1}$ in order to limit damage caused on the PbS QDs film by the plasma sputtering process.

The PbS QD layer absorbing at 940 nm (see absorption spectrum in **Figure** 6.2) deposited on an optimised TiN/ZnO electron transport layer is supplied by STMicroelectronics. The exciton peak at 940 nm is directly associated to the material band gap or the PbS QDs and corresponds to the detection wavelength of the photodiode or the operating wavelength of the photodetector. The current-voltage (J-V) characteristics in the dark and under illumination were carried out in a black box on photodiodes with an area of 1 mm^2 using an Agilent 4256 sourcemeter. The J-V characteristics under illumination were performed with monochromatic light (940 nm) from a Xe source using a Czerny-Turner monochromator (to select a specific wavelength), and the power of the light beam used was $\approx 0.6\mu W.cm^2$. The anode of the photodiode is connected to the negative terminal of the voltage source, and the cathode of the diode is connected to the positive terminal of the voltage source. The electric field, generated by a negative voltage applied to the anode, drives the holes toward the MoO_x or NiO_x hole extraction layers. The most important characteristics of photodiode are obtained or derived from the J-V characteristics at reverse biasing of the photodiode.

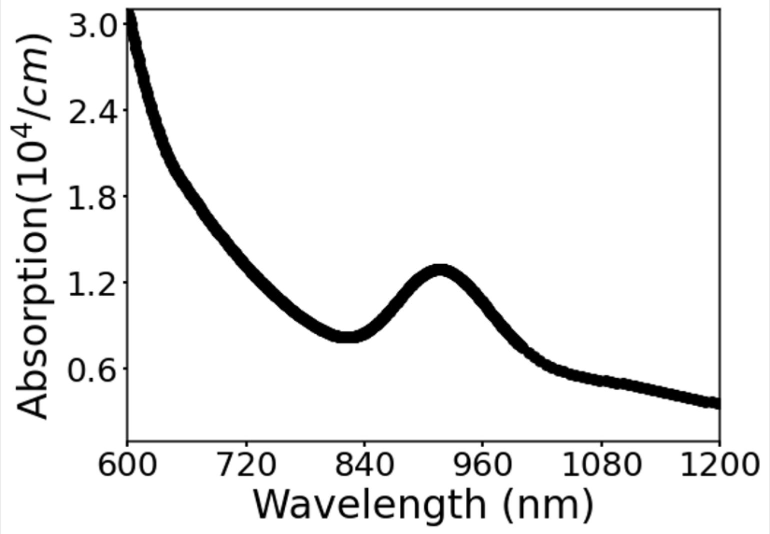

Figure 6.2: PbS QDs absorption with the first exciton peak located at ∼ 940 nm.

6.1.2.2 Validation of the simplified fabrication process route for photodiode devices

To avoid the complexity of etching and wet or cleaning processes, we used a highly simplified method to fabricate photodiodes. Full-plate deposition of the Si/Ta/TiN/ZnO/PbS QDs/MoO_x (15 nm)/ITO (100 nm) stack were performed. The devices with different surfaces were defined using a diamond saw (see **Figures** 6.3**a**, 6.3**b**, 6.3**c**, and 6.3**d**). To validate the fabrication method, the J-V characteristic under dark and under illumination were compared with a reference device corresponding to a complete stack of Si/Ta/TiN/ZnO/PbS QDs/MoO_x (15 nm)/ITO entirely made with classical clean-room processes by STMicroelectronics Crolles (simplified process and reference). **Figures** 6.4**a** and 6.4**b** show that we obtain for both devices almost identical current levels under illumination (at 940 nm) and in the dark depending with respect to the applied voltage, i.e. the same external quantum efficiency (EQE ≈ 33%). This results validates the fabricating process used. In the following sections, all photodiodes based on PbS QDs will be fabricated using this technique.

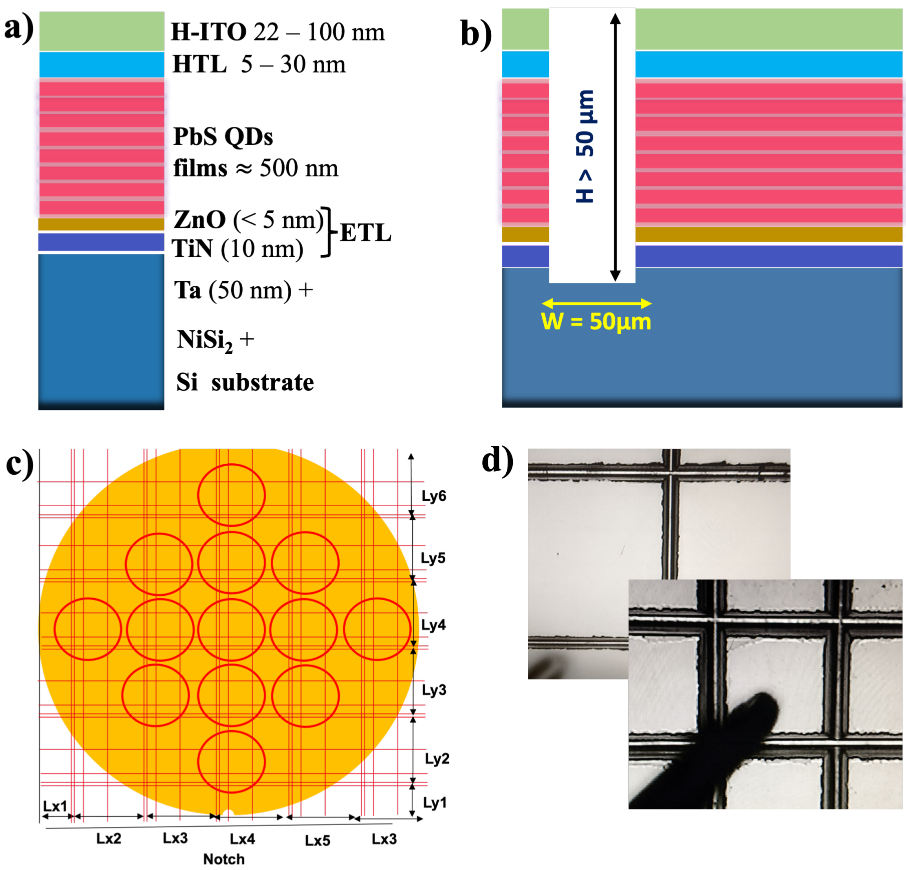

Figure 6.3: **a)** Photodiode architecture, the electron-hole pair light collecting material (PbS QDs) is sandwiched between a hole extraction electrode (HTL) and an electron extraction electrode (ETL), the ETL is deposited on Ta (diffusion barrier), which in turn is deposited on a silicided silicon substrate (the silicidation enables ohmic contact between Ta and the substrate), **b)** Representation of an isolation line with a diamond saw (50 micrometre depth and width), **c)** Repetition of the isolation lines in vertical and horizontal direction to obtain numerous patterns, **d)** Optical microscope image of the isolation lines obtained.

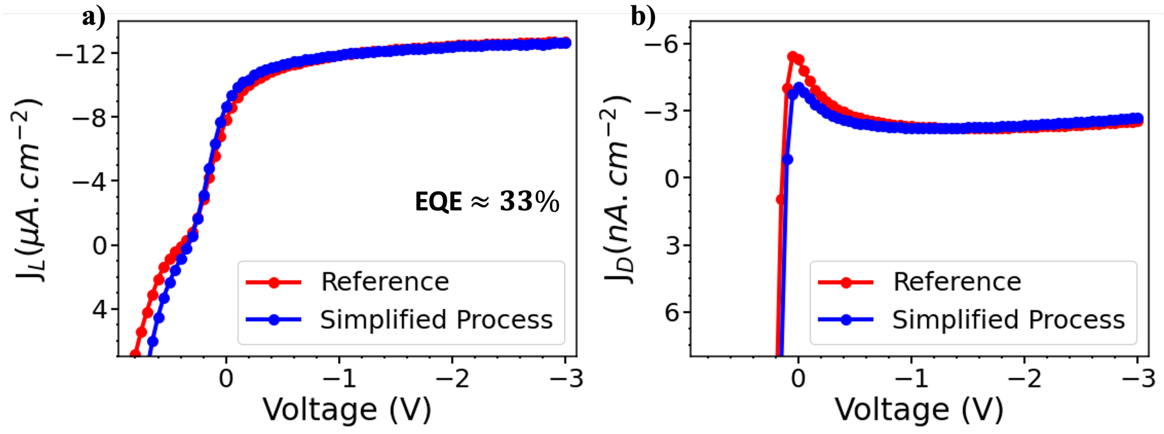

Figure 6.4: Comparison between the reference photodiode and a device fabricated using the simplified diamond saw chip isolation process, **a)** Current-voltage characteristic under illumination at 940 mm and, **b)** Current-voltage characteristic under dark on a surface area of 1 mm^2.

6.1.3 Results and discussion

6.1.3.1 Investigation of the properties of the transparent ITO electrode on the performance of the photodiodes

We have investigated the properties of the transparent H-ITO electrode on the performance of Si/Ta/TiN/ZnO/QDs PbS/MoO$_x$ (15 nm)/H-ITO photodiodes. The different H-ITO coatings (using an AC CT200 sputtering tool) were performed on a Si/Ta/TiN/ZnO/QDs PbS/MoO$_x$ (15 nm) stack supplied by STMicroelectronics Crolles. Although a reduction in optical transmission as a function of thickness was observed at 940 nm, **Figure** 6.5**a**, **Figure** 6.5**b** and 6.5**c** show that this reduction in thickness had no major effect on the performance (EQE) of the photodiodes, and no significant change was observed in the evolution of current density (under dark and illumination) as a function of the applied voltage.

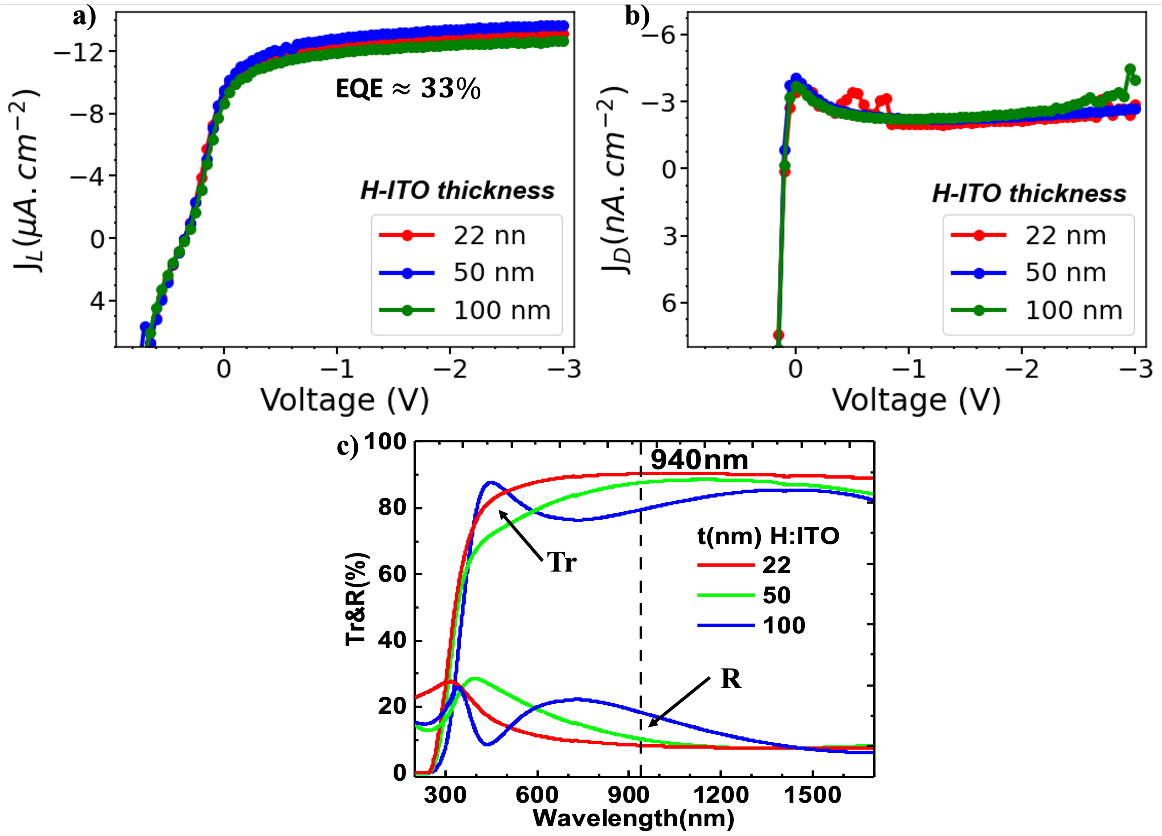

Figure 6.5: Investigation of the influence of H-ITO thickness on photodiode performance, **a)** current-voltage characteristic under illumination at 940 mm and, **b)** Current-voltage characteristic under dark, **c)** Optical transmission for different H-ITO thicknesses.

We have also investigated the effects of changing the resistivity of the transparent electrical contact on the performance of the photodiode. For this purpose, we chose 50 nm H-ITO films with resistivity between 420 $\mu\Omega$.cm and 820 $\mu\Omega$.cm (**Figure** 6.6**a**). We find that changing the resistivity of the transparent electrical contact has no real effect on the resistivity of H-ITO and the EQE remains the same, about 33% at -2 V. Possible effects of H-ITO sputtering were also investigated by varying the deposition power (RF generator power) between 25 and 150 W, and no significant effects were observed (**Figure** 6.6**b**).

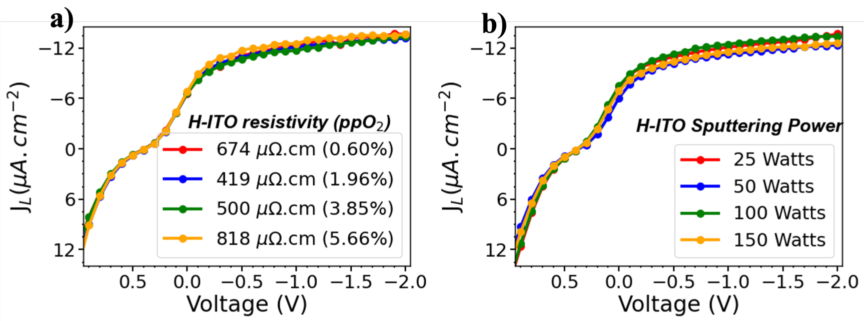

Figure 6.6: Investigation of the influence of H-ITO resistivity (**a**) and deposition power (**b**) on photodiode performances.

6.1.3.2 p-i-n photodiode based on MoO_x and NiO_x HTL prepared by reactive sputtering from metallic targets (Mo and Ni)

Figure 6.7**a** and 6.7**b** show the current-voltage characteristics of the Si/Ta/TiN/ZnO/QDs PbS/MoO_x (15 nm)/H-ITO (50 nm) devices under illumination and dark with different MoO_x coating conditions. We have selected the H-ITO film with the optimal properties (optimised as described in the section on In_2O_3-based transparent conductors) for the fabrication of our devices. The chosen film is the one with the best figure of merit of $\frac{T^{10}}{Rs} = 3.32\times10^{-2}\ \Omega^{-1}$ (ρ = 419 $\mu\Omega$.cm) with a Sn concentration of 10 %wt and the thickness of 50 nm (T is the optical transmission at 940 nm and Rs is the sheet resistance). The 15 nm MoO_x and 50 nm H-ITO films were sequentially deposited (on AC CT200). The photodiode structures with different surfaces were then defined by diamond saw isolation.

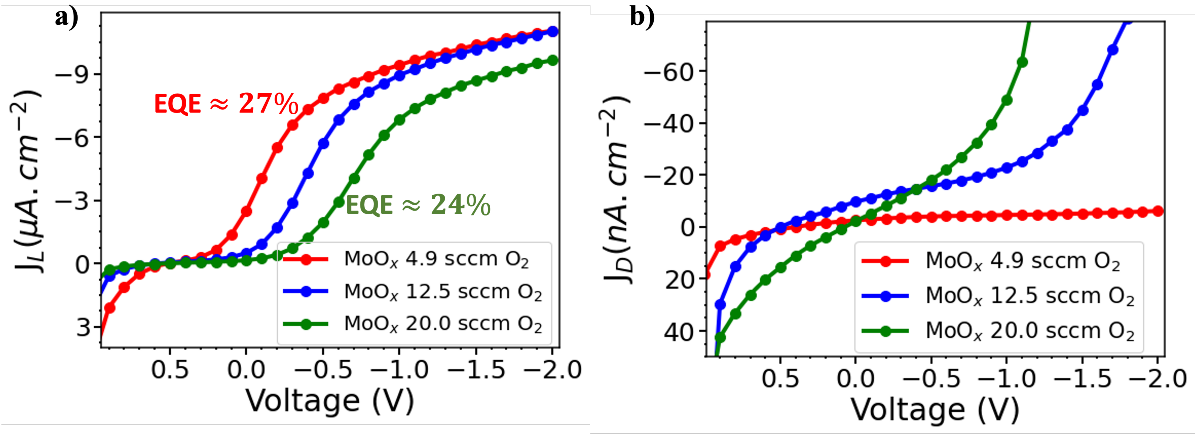

Figure 6.7: Investigation of MoO_x-based extraction layers deposited from a metal target with different oxygen flow rates (in sccm) or O_2:Ar ratio = 4.9:50, 12.5:50, 20:50 **a)** Current-voltage characteristic under illumination at 940 mm and, **b)** Current-voltage characteristic under dark.

The current-voltage characteristics show a decrease in EQE at -2 V, there is a reduction from ≈ 33% to 24 - 27%, we also have the 'S'-shaped curves and the deterioration of the dark current. The degradation of the photodiode performances (quantum efficiency and dark current) is even greater when the oxygen flow rate used to prepare the MoO_x layer increases, the 'S'-shaped curves are also more pronounced. The 'S'-shape of the J-V curves is known as a signature of charge extraction issues in the device[268, 269, 270]. The observed deterioration in the performance of the photodiodes may be related to the several factors:

First, the properties of MoO_x layers may not be optimised for efficient hole extraction. The work function of MoO_x and the density of defect states induced in the MoO_x gap by oxygen vacancies are generally considered to be the properties that define the potential of MoO_x as a HTL. These properties (work function and defect levels in the band gap) as well as the electrical and optical properties of MoO_x are strongly dependent on the oxygen concentration (MoO_x stoichiometry). As they play an important role in the alignment of the bands with the PbS QD films and the mechanism of hole extraction[124, 144], they need to be better optimised by adjusting the oxygen flow rate used for their deposition. The oxygen flow rate enables the control of the stoichiometry and therefore the band structure (width of the band gap, density of the defect states, work function) of MoO_x.
Second, the PbS CDs film are known to be sensitive to oxygen and moisture, and this sensitivity is even more pronounced if the surface of the QDs is not sufficiently passivated[8]. The XPS Pb 4f core level of PbS measured on the Si/Ta/TiN/ZnO/PbS QDs stack on which the MoO_x/H-ITO layers were deposited shows the formation of PbO_x and sulphates ($Pb(OH)_2$), indicating oxidation of the PbS film surface (**Figure**6.8). The increase in degradation observed in the J-V curves under illumination and in the dark when the oxygen gas flow rate is increased, when the oxygen concentration in the deposition atmosphere increases. It could also be explained by the fact that the oxygen introduced directly on top the PbS-QDs layer during the MoO_x deposition can contributes to the degradation (oxidation) of the PbS-QDs layer.

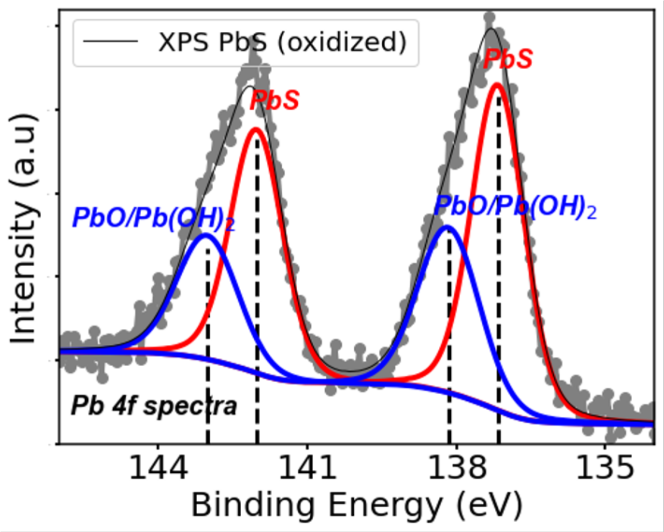

Figure 6.8: XPS spectra of Pb $4f_{7/2}$ and Pb $4f_{5/2}$ peaks in oxydized PbS QDs film , $PbO_x/Pb(OH)_2$ and PbS doublets are fitted with a 4:3 intensity ratio and 4.86 eV splitting energy.

We have also studied NiO_x hole extraction layers obtained from a metal target (reactive sputtering in an argon-oxygen atmosphere). In the previous Si/Ta/TiN/ZnO/QDs PbS/MoO_x (15 nm)/H-ITO structures, the MoO_x was replaced by NiO_x films (15 nm) deposited with different oxygen flow rates (**Figure** 6.9**a** and 6.9**b**). As we increase the oxygen flow rate, similar degradation of the EQE was observed on the Si/Ta/TiN/ZnO/QDs PbS/NiO_x (15 nm)/H-ITO devices (EQE $<$ 27% at -2V). However, the dark currents are not degraded and are comparable to those of the reference devices ($\approx$ 5 $nA.cm^{-2}$ at -2 V). This result is interesting because it indicates that NiOx can effectively act as a barrier for minority carriers or electrons.

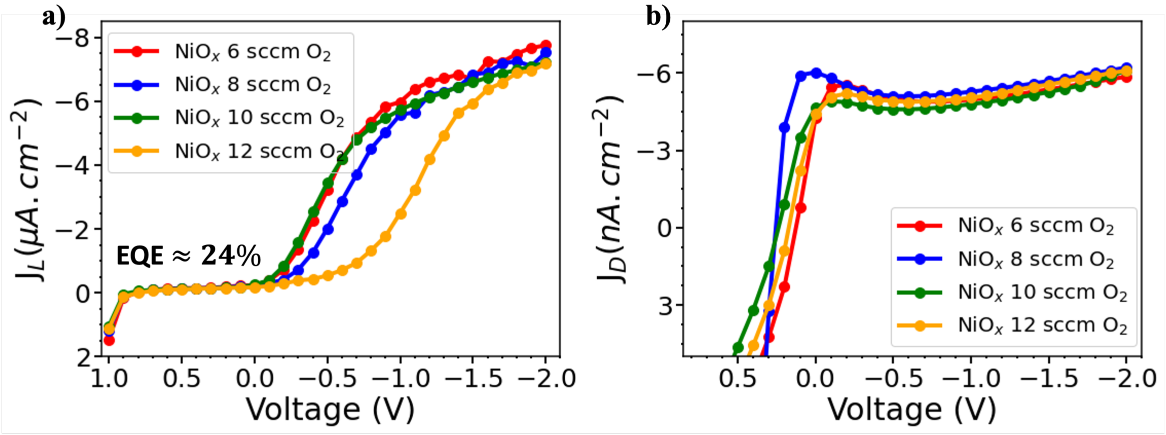

Figure 6.9: Investigation of NiO_x-based extraction layers deposited from a metal target with different oxygen flow rates (in sccm) or O_2:Ar ratio = 6:50, 8:50, 10:50 10:50 **a)** Current-voltage characteristic under illumination at 940 mm and, **b)** Current-voltage characteristic under dark.

These results show that the properties of the transparent electrode (TCO) have a very limited influence on the performance of the photodiode. There is no change in EQE, and the shapes of the J-V characteristics are not modified when the properties of the H-ITO film are changed. However, the performance of the photodiodes depends on the conditions under which the HTL is deposited in MoOx. The main challenges in optimising the photodiodes mainly concern the PbS/HTL-QDs interface and the stability of the PbS-QDs film (protection against oxidation or moisture).

6.1.3.3 p-i-n photodiode based on NiO_x HTL deposited from non-metallic NiO target

Due to the difficulties highlighted in the previous sections, we have opted for a non-metallic target. Precautions were also taken to ensure the quality of the PbS layers prior to HTL and transparent contact. In this study, we limited the exposure time of the PbS QDs film (Si/Ta/TiN/ZnO/PbS QDs) to avoid degradation of the PbS QDs film. The decomposition of the Pb 4f peak shows that the $PbO_x/Pb(OH)_2$ subpeak is not present (**Figure** 6.10), demonstrating the good surface quality of the PbS QDs film. In this section, we investigate NiOx HTLs deposited from a NiO oxide target. This approach will allows us to limit potential degradation of the PbS QDs film caused by the use of oxygen during HTL deposition. **Figure** 6.11**a** and 6.11**b** show the J-V characteristics of the photodiodes, under illumination and under dark, respectively, as the thickness of the NiO_x layer is increased. There is a general decrease in saturation current with increasing NiO_x thickness (**Figure** 6.11**a**), which can be attributed to increase of the optical absorption by the NiO_x film according to the Beer-Lambert law. It is also important to notice that the use of NiO_x leads to an increase in EQE from ≈33 % (a value that can be compared to the 33% EQE obtained on our MoO_x reference device) to 43% at -2 V.

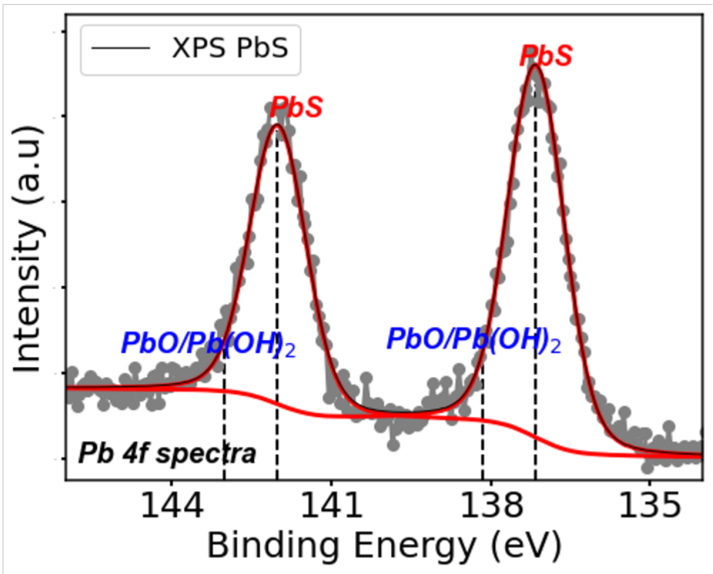

Figure 6.10: XPS spectra of Pb $4f_{7/2}$ and Pb $4f_{5/2}$ peaks of a clean surface PbS QDs film , PbS doublet is fitted with a 4:3 intensity ratio and 4.86 eV splitting energy.

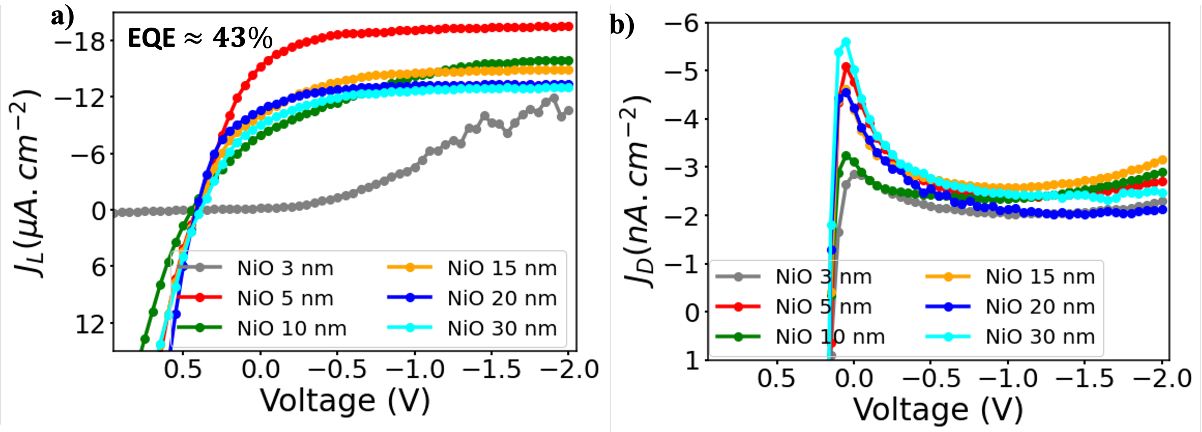

Figure 6.11: **a)** Current-voltage characteristics under light, and **b** Dark current of the photodiodes as a function of NiOx thickness.

Another important parameter for photodiodes is the operating bias, which is defined here as the voltage at which the current is 95 % of the saturation current. For the optimal NiO_x thickness, this value is around -0.4 V which is significantly lower compared to the MoO_x HTL (greater than -1 V). In addition, we observe an improvement in the short-circuit current (current density at zero bias) and the absence of an "S"-shape in the J-V characteristic, indicating highly efficient hole extraction by the NiO_x HTL (5 nm), or confirming the better band levels alignment between NiO_x film (5 nm thick) and the PbS QDs film. With optimised PbS QD film, we have achieved an extremely low dark current level $_D \approx 3$ nA.cm^{-2}, where the thickness of the extraction layer has no significant influence on the dark current (**Figure** 6.9**b**).

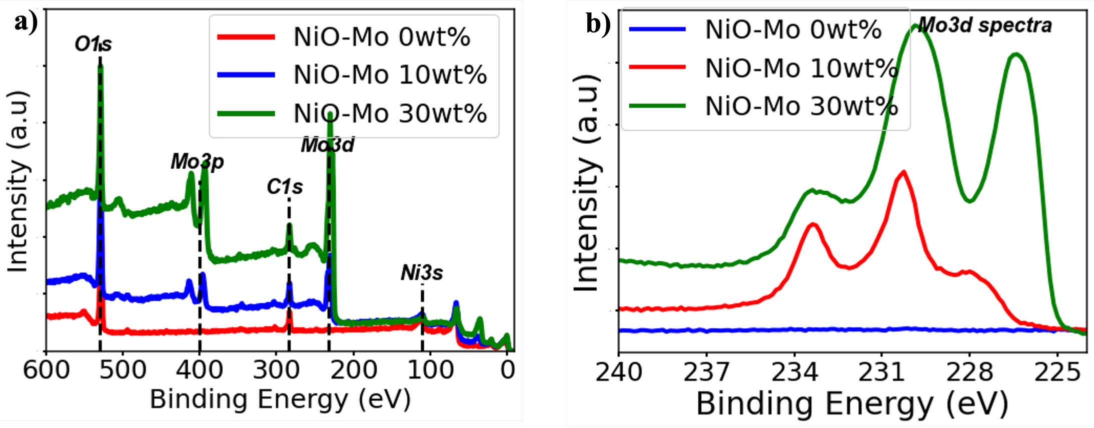

Figure 6.12: a) XPS survey spectra of NiO-doped Mo, and b) High-resolution XPS spectra of Mo 3d core level in NiO-doped Mo.

We also used HTL based on Mo-doped NiOx (0 %, 10 %, 30 %). The XPS transmission spectrum and the high-resolution Mo 3d peak (**Figure** 6.12**a** and 6.12**b**) illustrate the Mo doping of NiO$_x$. The aim of Mo doping is to modified the electrical properties of NiO$_x$, such as a reduction of the electrical resistivity or the modification of the band structure and to observe the effects on the performance of the photodiode.

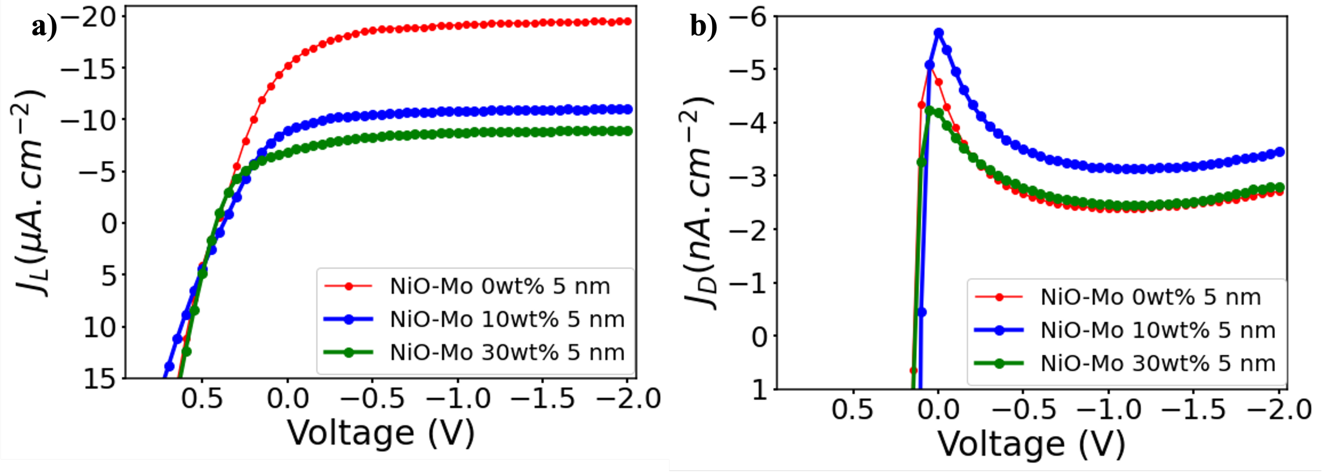

Figure 6.13: **a)** Current-voltage characteristics under light , and **b** Dark current of the photodiodes for NiO-doped Mo with different Mo concentrations.

Figure 6.13**a** and 6.13**b** show the J-V characteristics under illumination and in the dark for different Mo concentrations. There is neither an improvement of the EQE compared to NiO$_x$ HTL nor a significant change in dark current, the decrease of the EQE is well correlated with the decrease in optical transmission due to high Mo metal doping (**Figure** 6.14). On the other hand, compared to NiO$_x$(Mo 0 wt%) the operating bias decreases with increasing Mo concentration, i.e. the saturation current is reached at a lower voltage, for NiO$_x$(Mo 30 wt%), the operating bias is obtained ≈ - 0.3V. Nevertheless, these materials could be useful in a configuration where the PbS QDs film is deposited on the HTL and does not interfere with the illumination of the device.

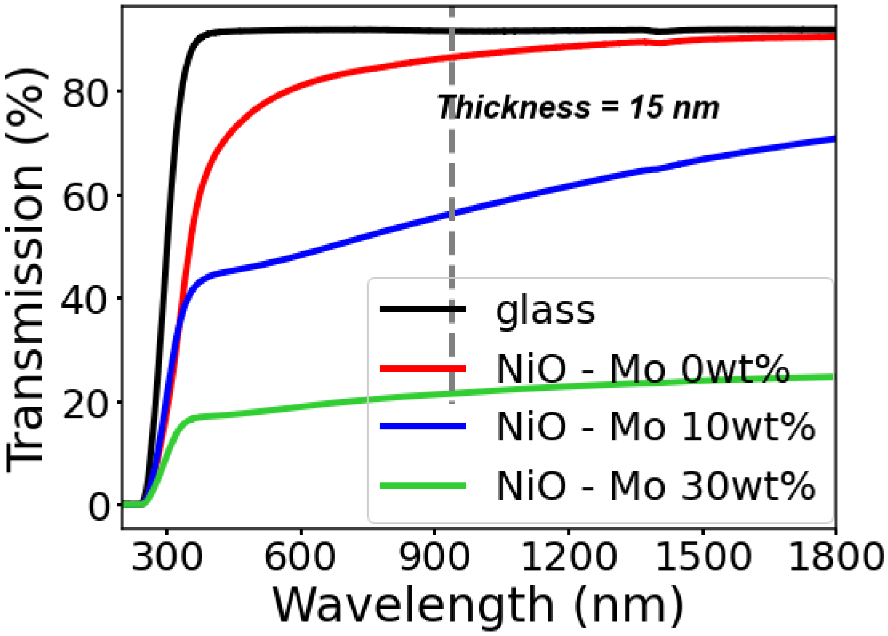

Figure 6.14: NiO doped Mo optical transmission (15 nm thickness).

To find out which material has the best hole extraction and electron blocking potential, we need to compare the investigated p-type hole extraction layers with the n-type hole extraction layers. In the following sections, we will compare NiO_x HTL with MoO_x films. For better understanding, we will also sketch and discuss the band alignment diagrams at the top electrode of the device.

6.1.3.4 Comparison between NiO_x and MoO_x HTL

In order to perform a good comparative study, we remade Si/Ta/TiN/ZnO/PbS/MoO_x (15 nm)/H-ITO photodiodes. The MoO_x films are still prepared from a metallic target, and we compare it with the optimum obtained with NiO_x (5 nm thickness). Nevertheless, the quality of the PbS QDs film is better controlled than in previous studies with MoOx, with a surface that is not oxidised or only briefly exposed to the ambient atmosphere and therefore not oxidised (see the XPS measurement in **Figure** 6.10). The thickness chosen for the MoO_x is ≈ 5 nm. For devices with MoO_x HTL, the EQE value obtained at -2 V is ≈ 31%, which is significantly lower than the 43% obtained with the NiO_x film of the same thickness. The EQE value at -2 V varies slightly between the two MoO_x stoichiometries (**Figure** 6.15**a** and 6.15**b**), and the value of short-circuit current (at voltage = 0 V) is lower for MoO_3. Although the improvement in performance compared with the oxidised Pbs QDs films in the previous studies with MoO_x(Figure 6.7), the "S" shapes of the J-V characteristics are still present. This effect is more pronounced for MoO_3, i.e. the MoO_x film prepared with a higher oxygen flow rate (compared with $MoO_{2.4}$). These "S" shape of the J-V characteristics is the signature of holes extraction issues and strengthen the idea of alteration of the PbS QDs film by reactive oxygen sputtering process. Compared with NiO_x (5 nm), the operating voltage with MoO_x is greater than -0.9 V. There is also a degradation of the dark current, which tends to be greater for MoO_3, which may indicate PbS QDs film quality also has an impact on the dark current. The dark current curves show an overshoot around 0 V. There is no real explanation for this effect; it could simply a measurement artefact.
To summarise, NiO_x has a very good potential for hole extraction, and compared to MoO_x, the NiO_x-HTL led to an overall improvement in the performance of the photodiode. MoO_x films with a very high stoichiometry (x ≈ 3) have a low hole extraction potential. The use of MoO_x requires an appropriate choice of target stoichiometry (use of non-metallic targets), as the Mo

oxidation process on top of the PbS QDs film may contribute to the surface degradation, leading to a degradation of the photodiode performances. The necessity of using a MoO_x target with a specific stoichiometry poses a technological or experimental issue, as the optimal stoichiometry for efficient charge extraction is not known in advance.

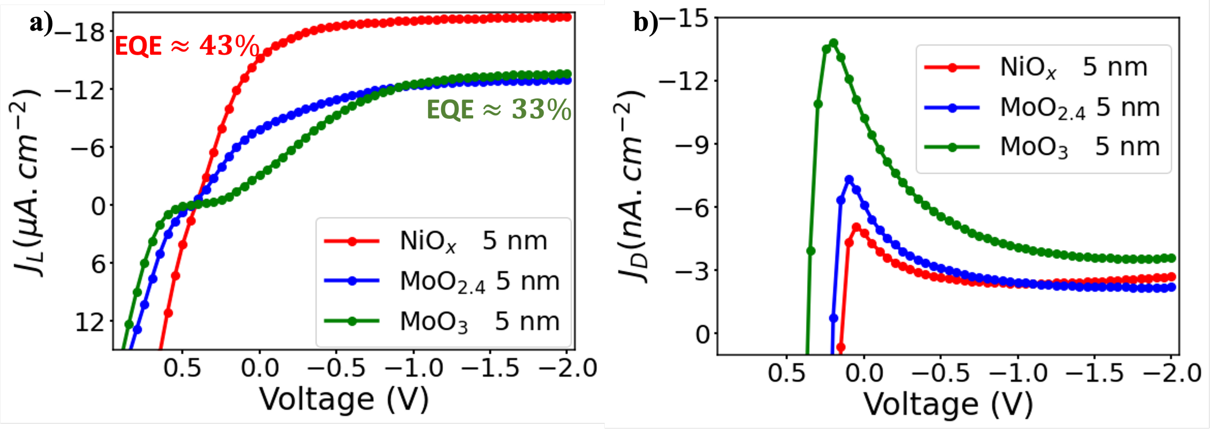

Figure 6.15: Comparison between NiOx and MoOx HTL, **a)** Current-voltage characteristics under light, and **b** Dark current.

6.1.3.5 Hole extraction efficiency and alignment of the energy band levels alignment

The construction of the band diagram (**Figure** 6.16) can provide an explanation for the mechanism of hole transport through a defined hole extraction layers. On the basis of the properties of different materials obtained in the previous sections, and assuming that, at equilibrium, the Fermi levels of the different layers of the stack are aligned, we propose a band alignment diagram for hole transport and a discussion. The hypothesis that the Fermi levels are aligned is based on the fact that the various electrode materials in the device are electrically conductive according to previous electrical studies.

It should be noted that this study is based on a simple hypothesis and may not reflect the actual reality of the devices, as the parameters used to build the diagram come from different sources. Despite the difficulties reported with the UPS measurement, we will use the value obtained to build the energy diagram, since the configuration of the bands would not change significantly if we had obtained a work function of ≈ 5 eV for NiO_x.

The ideal energy band configuration is shown in **Figure** 6.16**a**. When the photodiode is in operation, the hole extraction (HTL) and electron extraction layers (ETL) should facilitate the separation of excitons (electron-hole pairs) generated by the absorption of photons by the PbS QDs. In addition to the alignment of the energy bands, the extraction electrodes must have electrical properties that facilitate the rapid transfer of charges in order to limit their potential recombination. For example, good electrical mobility can facilitate charge transport and limit their accumulation or recombination at the interfaces. The energy reference is taken as the vacuum level of the TCO (H-ITO). The positions of the band edges of the other layers are aligned with respect to the vacuum level of the H-ITO under the assumption that the Fermi levels are aligned. The work function of H-ITO $\phi = 4.4$ eV is obtained from C-V measurements and analyses (before annealing). We have selected $MoO_{2.71}$ whose work function $\phi = 6.01$ eV is derived from MOS C-V measurements and analyses (without annealing), the defect band due to oxygen vacancies in MoO_x is ≈ 0.3 - 0. 4 eV below the Fermi level and the position of the conduction band minimum is 0.5 eV above the Fermi level, values which were reported in the work of Kanai [271], Meyer [154] and Kröger[131]. As the difference between the MoO_x and H-ITO work function is very large, the alignment of the Fermi levels between the two materials implies the existence of a significant interfacial dipole.

The band gap of the PbS QD is 1.32 eV (absorption wavelength = 940 nm) according to the optical absorption spectrum of the PbS QDs film and that of $MoO_{2.71}$ is 3.8 eV according to the optical gap measurements. The work function of the PbS QDs is between 4.3 - 5.0 eV according to the literature[11]. The NiO$_x$ work function $\phi = 4.0$ eV and the position of the Fermi level with respect to the valence band are derived from UPS measurements, the Fermi level of NiO$_x$ is ≈1 eV above its BV. The NiO$_x$ band gap width $E_g = 3.37$ eV is determined from optical gap measurements(Tauc plot).

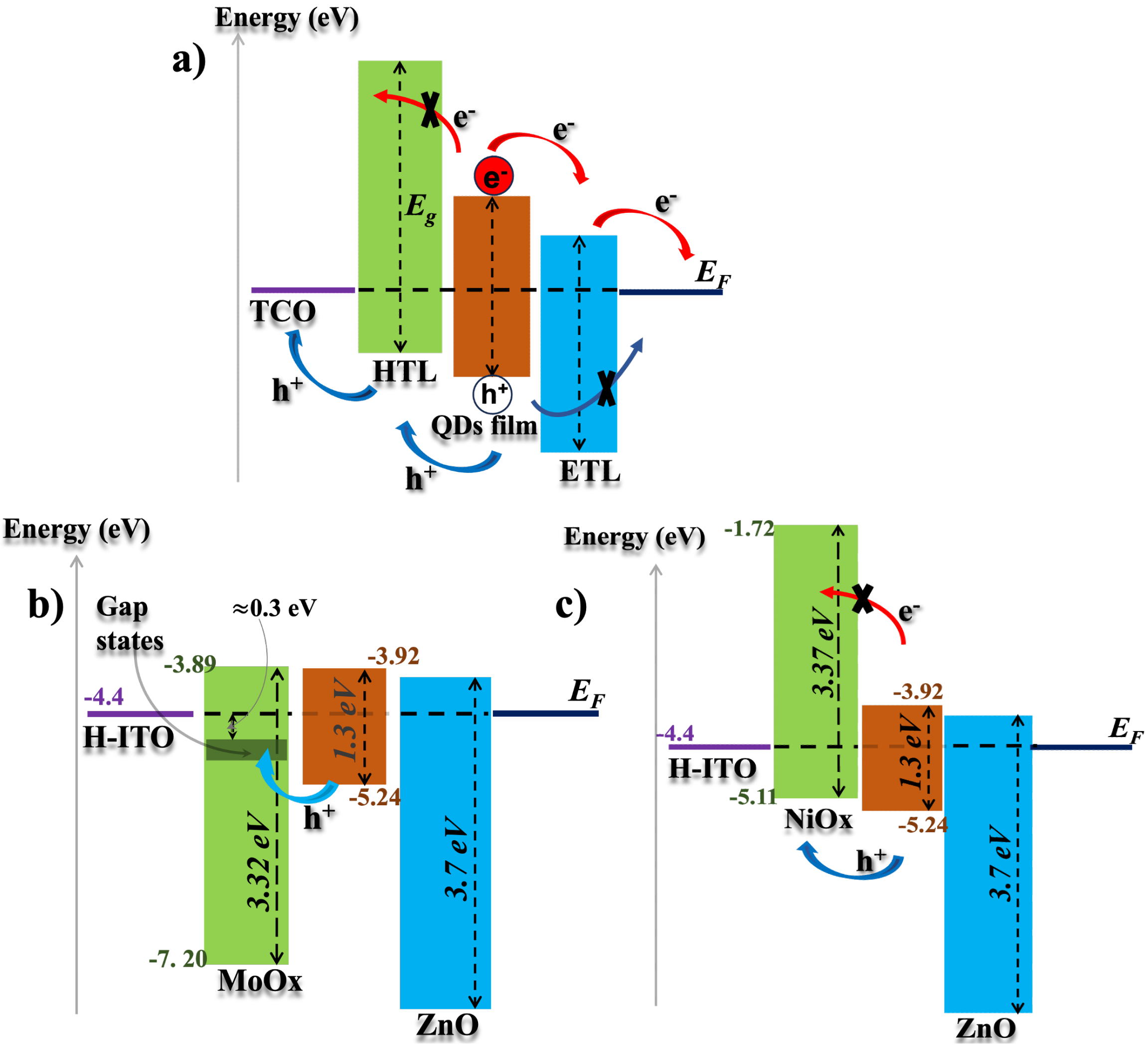

Figure 6.16: Schematic band levels alignment diagram of the ETL/PbS QDs/HTL/TCO **a)** Ideal or desired energy levels configuration. **b)** Schematic energy diagram of the PbS/MoO$_x$(x = 2.71)/H-ITO interfaces. **c)** Schematic energy diagram of the PbS/NiO$_x$/H-ITO interfaces.

Figure 6.16**b** and 6.16**c** show respectively the band alignment diagrams of photodiodes based on MoO$_x$ and NiO$_x$extraction layers (intermediate case of $MoO_{2.71}$). **Figure** 6.16**b** shows that the VB of the MoO$_x$ HTL is well below the VB of the PbS QDs layer because MoO$_x$ is of n-type and has a very wide band gap with $E_g = 3.8$ eV. The energy diagram obtained from our hypotheses with MoOx is similar to those in the literature(see **Figure** 6.17) [11].

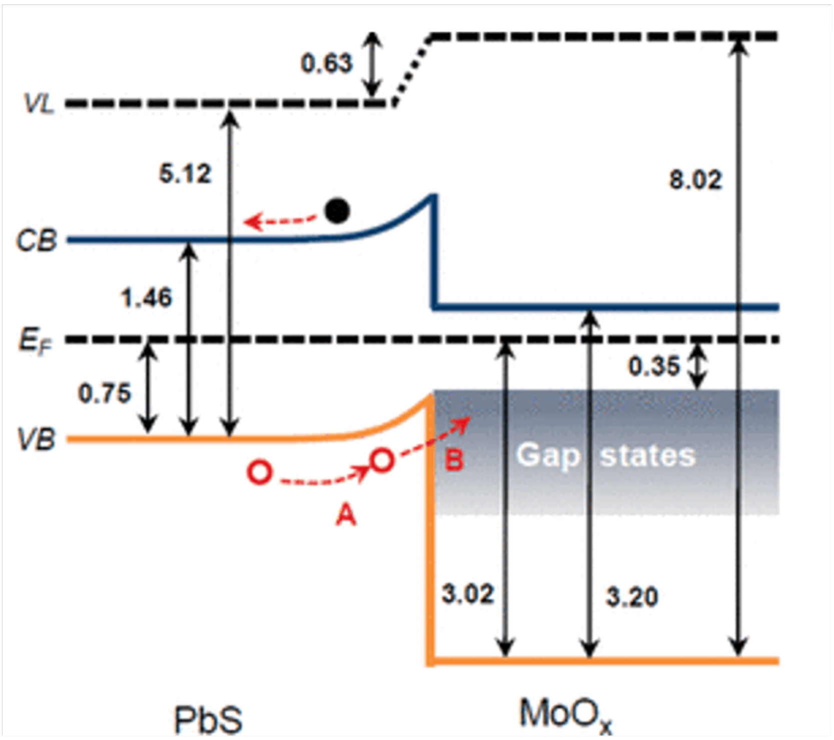

Figure 6.17: Schematic energy diagram of interfacial layers PbS/MoOx based on UPS measurements[11]

.

Such a configuration should lead to a large hole injection barrier at the MoO_x/PbS interface, resulting in poor device performance rather than increasing EQE or decreasing the operating potential of the photodiodes. It is hypothesised that the relative efficiency of hole extraction by MoO_x is mainly related to the existence of gap states (oxygen gaps) in the band gap. These gap states (electron donors) are supposed to create hole transport states by injecting electrons into the PbS QDs structure. This could explain why $MoO_{2.4}$ leads to better performance compared to MoO_3 (lower operating voltage and less pronounced "S" shape). We also note that the positioning of the conduction bands of MoO_x and PbS QDs can facilitate the transport of electrons from PbS to MoO_x, which can lead to a degradation of device performance. The band diagram with NiO_x provides a more favourable situation for the transport of holes and blocking of electrons between the PbS QD film and NiO_x. The p-type nature and wide band gap $E_g = 3.37$ eV as well as the position of the Fermi level of NiO_x relative to its valence band (about 1 eV above the BV) lead to band-to-band charge transport (holes), which could explain the excellent performance with NiO_x.

In summary, we have proposed an equilibrium band diagram for the MoO_x/PbS QDs and NiO_x/PbS QDs interfaces based on the assumption of Fermi-level alignment. We have confirm that the transport of holes through MoO_x occurs mainly via gap states in the MoO_x gap (gap-state assisted transport), while in the case of NiO_x, direct band-to-band transport occurs between the NiO_x and PbS QDs films. Finally, it should be noted that the electrical mobility of the charge carriers in the extraction layer can also facilitate the removal of charges by preventing recombination at the interfaces. The higher mobility of NiO_x, of the order of 20 $cm^2.V^{-1}.s^{-1}$ compared to MoO_x 0.03 - 2 $cm^2.V^{-1}.s^{-1}$, could also explain the high potential for hole extraction by NiO_x. The proposed band diagrams are based on the sole assumption that the Fermi levels are aligned. The actual situation may be more complex. Furthermore, if we take into account that all our materials, PbS QDs, NiO_x and MoO_x , are sensitive to oxygen or ambient atmosphere and that our measurements of work function are mainly performed by UPS after a certain time of air exposure, then the proposed diagrams may not reflect exactly the reality of our devices.

6.2 Visible range perovskites based photodiodes

This study deals with the fabrication of transparent electrodes on perovskite photodiodes.This study is not at the core of this thesis work, but it is part of the same project and is conducted within the collaboration with Cea-Liten. Since the same materials (metal oxide extraction electrodes, transparent electrical contact) are involved the fabrication of perovskite-based photodiodes and similar optimizations as for the PbS-QDs-based photodiodes have to be made. Perovskites, generally hybrid organometallic and/or lead halides compounds, are crystalline materials with interesting properties for optoelectronic applications. Because of their high optical absorption in the Vis-IR range, they are one of the most promising materials for the fabrication of image sensors. They can be easily synthesised in solution. They also have remarkable charge transport properties, i.e. high electrical mobility compared to conventional organic semiconductors or PbS QDs. They have a tunable band gap, i.e. they can be tailored to absorb light in a specific wavelength range by adjusting their chemical composition. Perovskite materials are an alternative to PbS QDs as light harvesting material in Vis-IR photodiodes, and tremendous research efforts are being made to extend their absorption to a wider radiation range as well as to improve the durability or reliability of perovskite-based devices. Perovskite devices are typically manufactured in such a way as to limit the degradation of the perovskite material, which is known to be sensitive to the effects of sputtering. This is usually done by a glass→TCO→HTL→perovskite→ETL→metal or glass→TCO→ETL→perovskite→HTL→metal integration, where the metal is deposited by a soft process such as thermal evaporation.

In this section, we have fabricated bifacial glass→ITO(bottom)→HTL→perovskite→ETL→H-ITO(top) photodiodes and a glass→ITO(bottom)→HTL→perovskite-ETL→metal(Cu, top) reference on a glass substrate.

The aim of the study is to demonstrate the fabrication of a transparent top electrode on perovskite, which enables perovskite-based photodiodes to be integrated directly into a CMOS readout circuit(for image sensor devices).

6.2.1 Experimental

Figure 6.18**a** shows the structure of the stack or perovskite layer $Cs_{0.17}FA_{0.83}PbI_3$ layer with a thickness of 470 nm, which was prepared in solution and deposited by spin-coating and absorbs in the Vis range (400-800 nm). The perovskite layer is sandwiched between a PTAA (poly(triaryl amine), $[C_6H_4N(C_6H_2(CH_3)_3)C_6H_4]_n$)-hole extraction electrode and a C_{60}/BCP (bathocuproine, $C_{26}H_{20}N_2$) electron extraction electrode. The ITO (bottom) is a commercial ITO layer with a thickness of 100 nm, a resistivity of about 1×10^{-4} Ω.cm and an electrical density of $n_e > 10^{21}$ cm^{-3}, while the H-ITO layers (top) were prepared by sputtering on an AC-CT200. All structures were encapsulated with a polymer to protect them from oxidation and moisture. **Figure** 6.18**b** shows a schematic of the fabricated photodiode structures, with the bottom ITO electrode shown in green and the top electrode in red. The black discs represent the photodiodes with a surface area of S ≈ 3.14 mm^2.

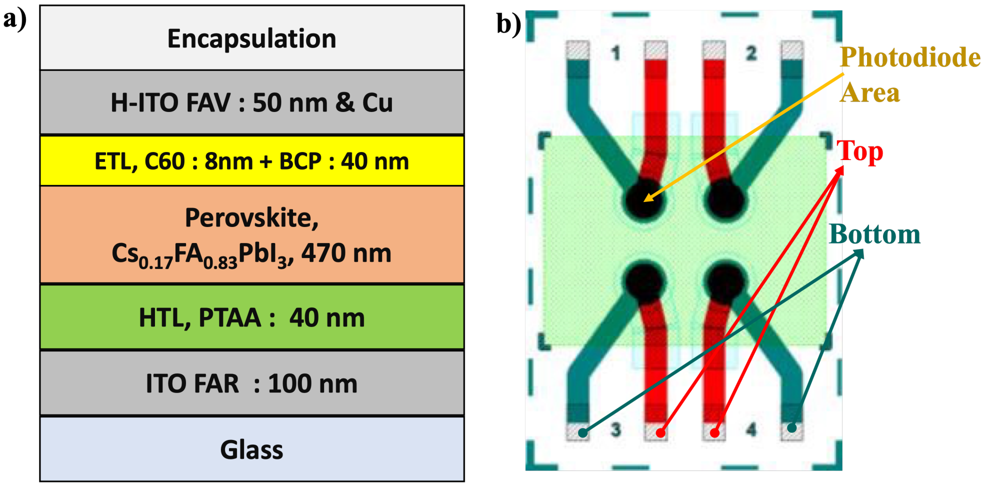

Figure 6.18: **a)** Photodiode architecture based on a perovskite absorbing in Vis , **b)** Schematic structure of the devices fabricated (four photodiodes in each substrate).

6.2.2 Results and discussion

The deposition parameters and electrical properties of these different H-ITO layers are summarised in **Table** 6.1. The resistivities range from 372-750 Ω.cm, and the extremely low deposition rates of 0.15-1.2 $Å.s^{-1}$ were chosen to avoid degradation of the C_{60}, BCP and perovskite films by the H-ITO sputtering process. **Figure** 6.19**a** shows the optical transmittances between the different ITO and H-ITO layers that we have used below and above the perovskite. The high transmission of the commercial ITO film (bottom) in the Vis range is related to a degeneracy of the BC (Moss-Burstein shift) due to the high density of free electrons. The strong reduction of the optical transmission in the IR, the plasmon-photon interaction, has the same cause as the increase of the optical transmission in the visible ($n_e > 10^{21}$ cm^{-3}). Measuring the optical gaps by plotting Tauc diagrams (**Figure** 6.19**b**) shows that the gap of commercial ITO is larger than that of our different H-ITO layers, confirming the Moss-Burstein shift.

Table 6.1: H-ITO Split on ETL/Perovskite Process Conditions

Process conditions: p = 0.001 mbar, T = 25°C, O_2 : Ar = 0.5 sccm : 50 sccm		
Sputtering Power	**ρ in $\mu\Omega$.cm**	**dep rate(nm.s^{-1})**
RF 25W	480 ± 3%	0.015
RF 50W	372 ± 2%	0.037
DC 50W	750 ± 5%	0.120
DC 25W	570 ± 3%	0.063
DC 10W	468 ± 3%	0.024
Reference, Cu electrode, by thermal evaporation		

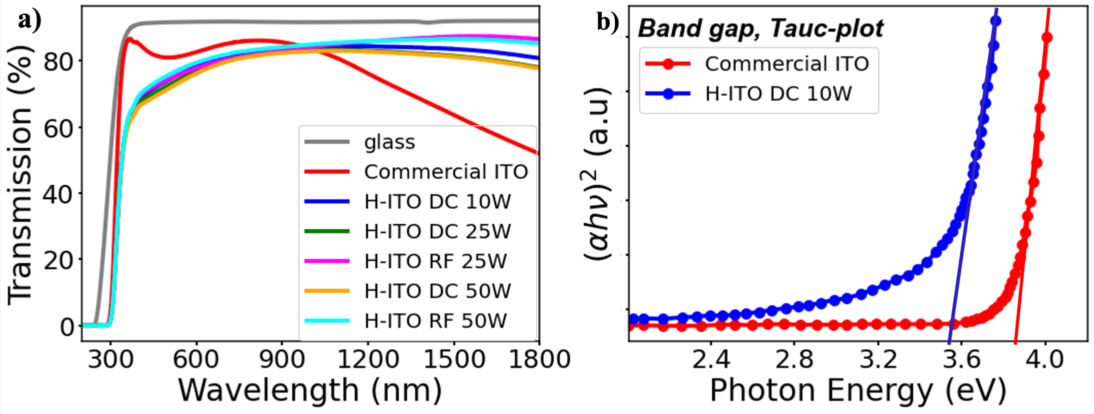

Figure 6.19: **a)** Optical transmission of the different films deposited as transparent electrodes on the top and bottom face of the bifacial photodiodes, **b)** Change of the optical gap between ITO (bottom contact) and H-ITO of the top contact due to different free charge carrier densities.

The characteristic J-V measurements were performed in the dark and under illumination at 560 nm with a light power of 0.86 W.m^{-2}. **Figure** 6.20**a** and 6.20**b** show a comparison of J-V characteristics between the Cu reference electrode and the transparent H-ITO electrode (P = 10 W DC), measured under illumination and in the dark respectively. Compared to the Cu reference electrode, the photodiodes with H-ITO top electrode have better properties, the saturation current under illumination is reached at lower voltage, and no leakage current is observed at relatively high voltage. Similarly, the current of the Cu reference is completely degraded above -0.5 V (increase of J_D by several decades, 10^{-8} to 10^{-5} mA.cm^{-2}).

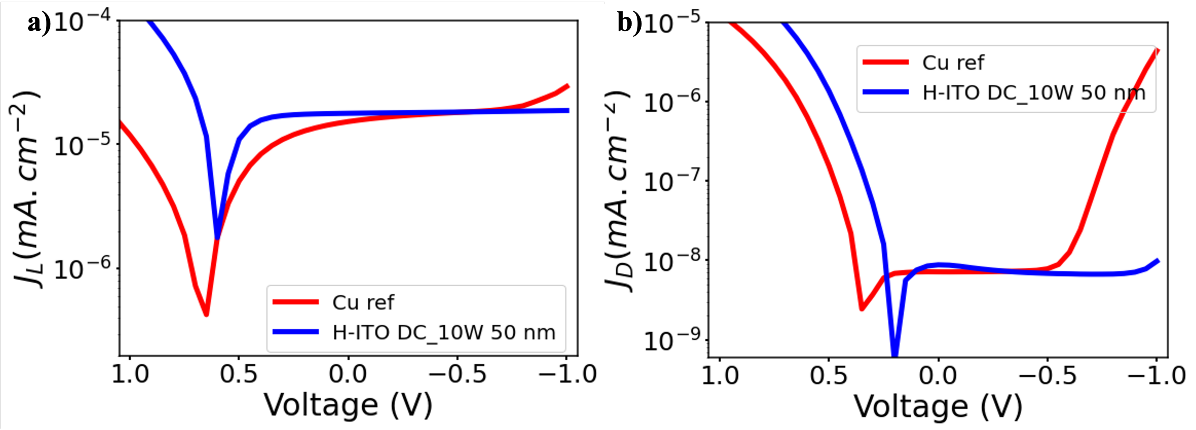

Figure 6.20: Comparison between the Cu electrode (top contact) and the H-ITO contact deposited by DC sputtering with a power P = 10 W, **a)**Current-voltage characteristics under light, and **b** Dark current of the perovskite photodiodes.

The H-ITO electrodes also exhibit a lower hysteresis at 10 W DC (**Figure** 6.21**a** and 6.21**b**). The hysteresis effects observed with the Cu reference are complex. There are several explanations in the literature. Some authors suggest that perovskites may undergo structural reorganisation in response to an electrical bias (electric field), leading to a change in device properties [272]. This can also be attributed to ion migration, trapping and dettraping mechanism in the bulk perovskite material, leading to a redistribution of charge in the photodiode[273] .

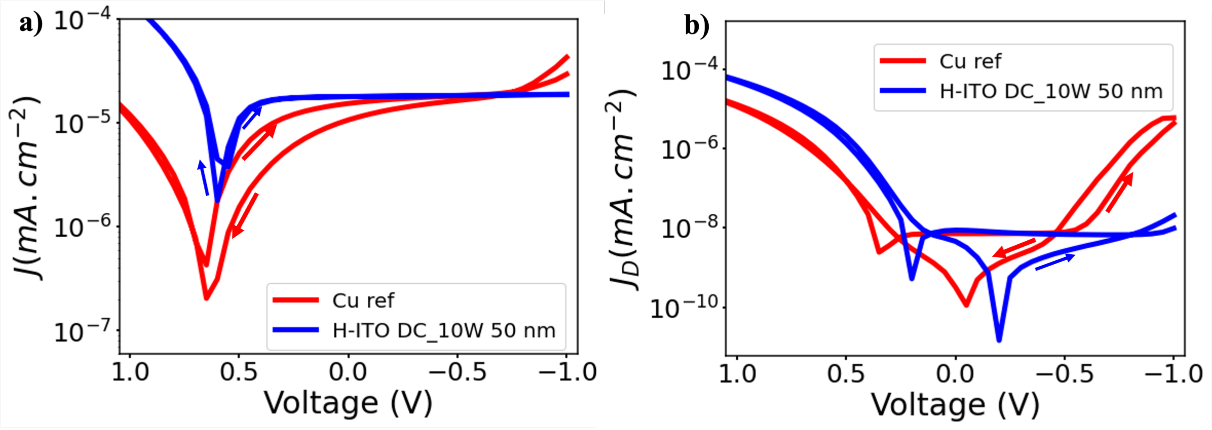

Figure 6.21: Current-voltage curve hysteresis in perovskite photodiodes, **a)**Current-voltage characteristics under light, and **b** Dark current

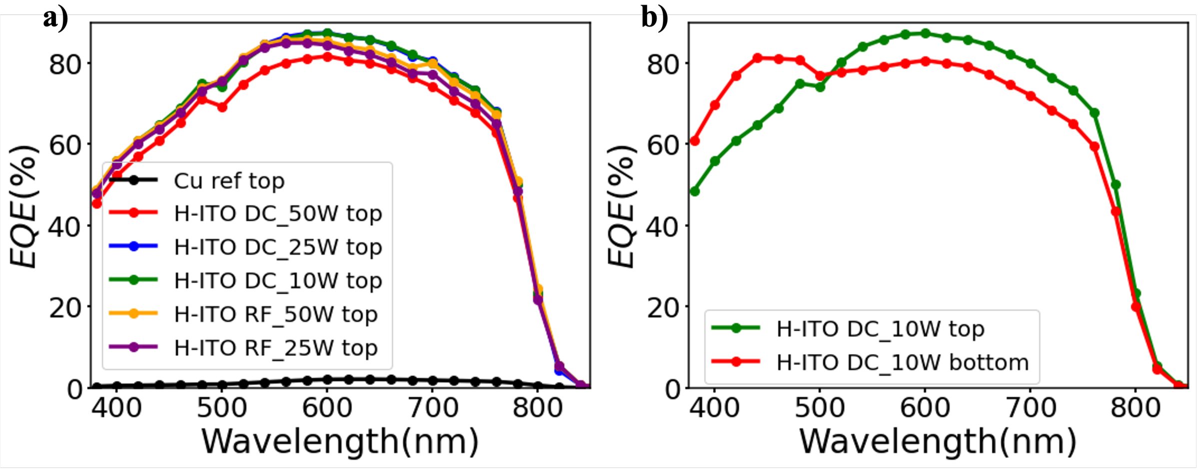

Figure 6.22: **a)** Evolution of the external quantum efficiency (EQE) between different deposition processes of the H-ITO and Cu reference (top electrode) in the visible range, **b)** spectrum range, **b)**EQE comparison between the top and bottom contact.

Figure 6.22**a** shows the evolution of external quantum efficiency (EQE) as a function of wavelength for different H-ITO electrode. The EQE quantum efficiency is EQE $>$ 70% between 400 - 750 nm, with no notable change observed with the change in the properties of the top transparent electrode. There is a difference in quantum efficiency between the front-side (top) and the backside(bottom) , see **Figure** 6.22**b**. The optical and electrical properties of the ITO film on the bottom and the H-ITO films on the front do not provide any direct explanation for this difference.

6.3 Conclusion

In this section, we have integrated transparent electrodes based on In_2O_3 and charge extraction layers based on transition metal oxides. We first demonstrated the efficiency of a simplified fabrication process for photodiodes. We then investigated the effects of the properties of the transparent electrode and the extraction layers on the performance of the photodiodes. It was found that changing the properties of the transparent H-ITO electrode had no significant direct effect on the performance of the devices. The H-ITO/MoO_x or H-ITO/NiO_x interface is less critical, but great efforts must be made to optimise the HTL/PbS QDs interface. It has been shown that prolonged exposure of the PbS QDs film with the ambient atmosphere can lead to oxidation of the surface and thus to degradation device performances. For MoOx HTL fabricated from a Mo metal target, the quantum yield is limited to ≈ 33 %, and the operating voltage is relatively high due to the J-V characteristics. In contrast, with NiO$_x$ HTL we were able to achieve EQE ≈43 %, demonstrate more efficient hole extraction and a very low operating voltage of ≈ -0.4 V. Based on the hypothesis that the Fermi levels are aligned between the different materials composing the photodiode, we have shown that the transport of holes between the PbS QDs films occurs from band to band, while in the case of MoO$_x$ the gaps play an important role. Finally, we have fabricated a transparent H-ITO electrode on perovskite-based photodiodes ($Cs_{0.17}FA_{0.83}PbI_3$), demonstrating the possibility of integrating these photodiodes directly into CMOS readout circuits.

Chapter 7

Conclusion and Perspectives

7.1 Conclusion

The aim of this work was to optimise a top electrode in the IR range of the light spectrum for photodetector devices based on PbS QDs or on perovskite, in a polarisation configuration where it has to collect holes and block electrons while being as transparent as possible. Below is a summary of the various studies we have conducted. First, we thoroughly investigated In_2O_3-based TCO deposited by sputtering at room temperature. We focused on the deposition conditions, the composition of the target (Sn concentration) and hydrogen doping to maximise light transmission while maintaining excellent electrical properties. In this study, we were able to explore the fundamental mechanisms that determine the conductivity and transparency of In_2O_3-based TCO while seeking to maximise its performance for specific applications, especially for IR photodiodes. The results obtained show that hydrogen-doped ITO (H-ITO) films are a promising solution, with a remarkably low electrical resistivity at room temperature $\rho < 350\times10^{-4}$ Ω.cm and a high optical transmission in the IR range, T > 80%. The introduction of hydrogen improves the electrical conductivity by a relative increase in the mobility of the charge carriers and not by an increase of the density **n** of the free charge carriers, which in turn improves the optical transmission in the IR range. This is because the plasmon-photon interaction (plasmonic absorption) is weaker when the density of free carriers is low, the plasma pulsation given by **Equation** 7.1.1, show that, a low density of free carriers leads to a lower plasma pulsation, i.e. a larger wavelength.

$$\omega_p \propto \sqrt{\frac{ne^2}{m^*\varepsilon_0\varepsilon_r}} \tag{7.1.1}$$

We have also shown that the effects of hydrogen doping become less significant with increasing Sn concentration, as the effect of the high charge carrier density generated by Sn doping becomes dominant. Regardless of the Sn concentration, with or without hydrogen doping, the film with the optimal perfomance is always obtained with the addition of oxygen during deposition, which allows the best compromise between mobility and carrier density. The TCO films obtained were all polycrystalline and exhibited very low surface roughness. The work function measured on the H-ITO film (Sn 10 %) using MOS capacitors was $\phi \approx 4.4$ eV without gas-forming annealing, while a value of $\phi \approx 4.7$ eV was obtained after annealing. Based on the MOS capacitance analyses, we found that the deposition of ITO layers can lead to degradation effects on the substrates on which they were deposited. In particular, for the stacks of H-ITO/SiO_2/Si structures, we observed a decrease in EOT, which can be explained by the change in permittivity of part or all of the SiO_2 thickness due to the diffusion of In. These H-ITO films will later be integrated within photodiode structures based on PbS QDs or on perovskites.

Second, we investigated hole extraction layers based on molybdenum oxide (MoO_x) and nickel oxide (NiO_x).

MoO_x is an n-type semiconductor whose properties strongly depend on the oxygen concentration (stoichiometry). MoO_x films of various stoichiometry were prepared by DC sputtering at room temperature. It has been shown that the properties of MoO_x can be precisely controlled by adjusting the oxygen concentration during deposition. The MoO_x composition can be also modified by post-deposition treatments such as thermal annealing. Using XPS analyses, we were able to determine the evolution of stoichiometry as a function of the oxygen flow rate used during deposition. Using the van der Pauw's four-probe technique, we demonstrated that the resistivity of MoO_x strongly depends on the oxygen vacancy concentration and varies by more than 7 orders of magnitude between $MoO_{2.18}$ and MoO_3. MoO_x films with low stoichiometry are inherently semi-metallic in nature with a free carrier density of up to 10^{21} cm^{-3} for $MoO_{2,18}$. The electrical mobilities, only measurable for stoichiometry $x < 2.8$ are very low and vary between 3×10^{-2} - 2 $cm^2.V^{-1}.s^{-1}$ for $2.18 < x < 3$. For 15 nm thick films with a stoichiometry $x < 2.8$, the optical transmission in the IR is less than 80 %. This low stoichiometry is associated with a relatively high density of free charge carriers (due to oxygen vacancies). In contrast, the optical transmission of MoO_x with stoichiometry $x > 2.8$ eV is over 80 %. The optical gap measured using the Tauc plot increases between 2.9 - 3.8 eV when the stoichiometry x changes between 2.18 and 3. The MoO_x films prepared at room temperature are completely amorphous, with an effective roughness rms < 1 nm. Work function measurement using UPS is limited to films with relatively low resistivity, for nearly stoichiometric films, the work function measurement becomes difficult due to charge effects. This difficulty is primarily due to the limitations of the spectrometer available to us. On the other hand, measurements of the work function by CV analysis have shown surprisingly interesting results: we have observed an increase of the work function with increasing stoichiometry and, a work function $\phi > 6$ eV is obtained for almost stoichiometric films, which is in very good agreement with the literature (UPS measurements).

Similar studies have been carried out on NiO_x. In contrast to MoO_x, NiO_x is generally a p-type semiconductor with a wide band gap ($E_g = 3.2$ eV). We prepared NiO_x films from a non-metallic NiO target at room temperature with different oxygen concentrations. XPS characterization allowed us to analyse the composition of these different films. When the oxygen concentration is increased, an increase in the Ni^{3+}/Ni^{2+} ratio is observed, which is reflected by an increase in Ni^{3+} defects (mainly due to Ni^{2+} substitution) and the occupation of interstitial sites by oxygen atoms (oxygen defects). These defects play the role of electron acceptors, and Hall measurements have shown, as far as possible, an increase in the density of free carriers (holes) between 10^{16} - 10^{17} cm^{-3} and a decrease in mobility with the increase in oxygen concentration (increase in Ni^{3+}/Ni^{2+} ratio). Using four probes van der Pauw method, a decrease in resistivity between 25.7 - 0.7 Ω.cm was observed when the gas flow rate ratio of Ar and O_2, Ar:O_2 (in sccm) varied between 0:50 and 15:50. The NiO_x films deposited at room temperature are polycrystalline and have a grain size of about 11 nm (XRD and AFM). The concentration of oxygen atoms in the interstitial sites increases with increasing oxygen concentration, which leads to tensile stresses in the NiO_x films. These interstitial sites also lead to an increase in the volume density of the films. The films exhibit very low roughness, rms < 1.1 nm. As with most transition metal oxides, we found that NiO_x is unstable and its resistivity increases with the duration of exposure to the ambient atmosphere. Precise measurements of the work function done by UPS were not possible due to the relatively high resistivity of the NiO_x layers, similar effect was observed with nearly stoichiometric MoO_x films. These materials were then used as a hole extraction layer on PbS QDs-based photodiodes.

Third, we integrated In_2O_3-based TCO as well as MoO_x and NiO_x HTL in the order to fabricate photodiode structures. For the PbS QDs-based photodiodes, we adopted a simplified device fabrication process. It was found that the properties of the H-ITO films have only a limited effect on the performance of the devices. No significant changes in external quantum efficiency (EQE) were observed by changing the optical transmission, the electrical resistivity of the films or the power of the plasma generator used for H-ITO sputtering (deposition power). The studies have shown that the major optimisation effort must be directed not only on the HEL/PbS QDs interface, but also on the stability or the surface quality of the PbS QDs film. Indeed, the preservation of the surface of the PbS QDs film was one of the major challenges during this work. It is also important to prioritise non-metallic targets, since deposition in a reactive atmosphere can also lead to degradation of the PbS QDs film. With PbS QDs films whose surface is oxidised, we obtained photodiodes with poor performance, such as lower EQE compared to the reference, we also obtained "S"-shaped J-V characteristics with operating voltages well above -0.5 V, and in some cases, we observed the degradation of the dark current with MoO_x HTL. The use of NiO_x HTL deposited from a NiO target allowed us to obtain photodiodes with very interesting properties: an EQE $\approx$ 43 % for the optimal NiO_x film thickness, an operating voltage of $\approx$ -0.4 V and a ultra-low dark current of 3 nA.cm^{-2}. Considering the alignment of the Fermi levels at equilibrium, the band diagrams show that, with NiO_x HTL, there is a band-to-band transport, while with MoO_x the defect levels in the MoO_x gap play an important role in the holes extraction mechanism. Finally, we have fabricated transparent top electrodes on photodiodes (bifacial), validating the possibility of their direct integration into CMOS readout circuits for the fabrication of imaging devices.

7.2 Perspectives

The transparent metallic contacts studied here are In_2O_3-based TCO. It is the most expensive and rarest of the base metals making up n-type TCO (In, Zn, Sn). We could consider replacing ITO or H-ITO by ZnO-based TCO, e.g. Al-doped ZnO, which also has interesting electrical and optical properties. This would be more environmentally friendly and would reduce production costs and the price of the devices produced. Transition metal oxides can be obtained either by non-reactive sputtering (Ar plasma) from non-metallic targets with a given stoichiometry (MoO_x and NiO_x) or by reactive sputtering (Ar + O_2) from metallic targets (e.g. Mo and Ni). Since the properties of NiO_x or MoO_x and their hole-extraction efficiency are highly dependent on their stoichiometry (O:Mo or O:Ni), and to avoid possible degradation due to oxidation phenomena when these HTL are deposited on sensitive substrates (film of PbS QDs), co-sputtering between a metallic Mo or Ni target and a non-metallic NiO or MoO_3 target can enable the optimal stoichiometry (allowing the best hole extraction or performance devices to be obtained). MoO_x and NiO_x HTL could also be prepared using ultra-low damage techniques such as PLD, this would limit any degradation on the PbS QDs film caused by sputtering process. To avoid the difficulties associated with UPS measurements (case of highly resistive materials), the performance of MoO_x and NiO_x can also be evaluated using the Kelvin Probe Force Microscopy (KPFM) technique. Given the sensitivity of these oxides to the ambient atmosphere, in situ characterizations should be considered to obtain the properties of the materials as they exist in the devices. For simplicity (because small QDs are more stable than large ones), our studies on photodiodes were limited to PbS QDs absorbing in the NIR at 940 nm ($\approx$ 3.2 nm in size). This study could be extended to PbS QDs films that absorb at 1360 nm in the SWIR. To better characterise our devices, more in-depth studies such as as stress measurements and time-resolved measurements, EQE stability over time could be performed. Other inorganic hole extraction layers such as CuO_x could also be investigated. Finally, in perovskite-based photodiodes, the PTAA (holes) and C_{60}/BCP charge extraction layers can be replaced by more robust and stable materials. NiO_x could be used as HTL instead of NiO_x PTAA and SnO_2 could be used to replace organic electron extraction layer C_{60}/BCP.

Appendices

Simple python script for TCO optical properties simulation (classical model)

```
# -*- coding: utf-8 -*-
"""
Created on Mon Feb 13 12:15:48 2023

@author: Louis David MOHGOUK ZOUKNAK
"""
import numpy as np
import matplotlib.pyplot as plt
font = {'family': 'arial', 'color':  'black', 'weight': 'bold',
   'size': 20, 'fontstyle':'italic'}
c = 3.0e8 vitesse de la lumière
el = 1.602e-19  # charge élémentaire
epsr = 4.0
eps0 = 8.85e-12 # permittivité du vide
m = 0.4*9.1094e-31 # electron mass (ITO)
t = 100*1e-9  # TCO thickness

def k1(n,mu, wavelength):   # Coeff d'extinction
    tau = 1e-4*m*mu/(3*el)
    omega = 2*np.pi*c/wavelength
    wn = np.sqrt(n*el**2/(m*eps_0))
    eps1 = epsr - (wn**2*tau**2) / (1+omega**2*tau**2)
    eps2 = (wn**2*tau)/(omega*(1+omega**2*tau**2))
    return np.sqrt( 0.5*np.sqrt(eps1**2+eps2**2) - 0.5*eps1)
def N1(n, mu, wavelength):  # indice de refraction
    tau = 1e-4*m*mu/(3*el)
    omega = 2*np.pi*c/wavelength
    wn = np.sqrt(n*el**2/(m*eps_0))
    eps1 = eps_r - (wn**2*tau**2) / (1+omega**2*tau**2)
    eps2 = (wn**2*tau)/(omega*(1+omega**2*tau**2))
    return np.sqrt( 0.5*np.sqrt(eps1**2+eps2**2) + 0.5*eps_1)
def alpha1(n, mu, wavelength):   # Absorption
    tau = 1e-4*m*mu/(3*el)
    omega = 2*np.pi*c/wavelength
    wn = np.sqrt(n*el**2/(m*eps_0))
    eps1 = epsr - (wn**2*tau**2) / (1+omega**2*tau**2)
```

```
    eps2 = (wn**2*tau)/(omega*(1+omega**2*tau**2))
    return 4*np.pi*np.sqrt( 0.5*np.sqrt(eps1**2+eps2**2) - 0.5*eps1)/wavelength

wavelength = 1e-9*np.linspace(200,2500, 1000)#  en nm
alpha1 = alpha1(5e20*1e6, 50,  wavelength)
N1 = N1(5e20*1e6, 50, wavelength)
k1 = k1(5e20*1e6, 50, wavelength)
R1 = ((N1-1)**2+k1**2)/((N1+1)**2+k1**2)
T1 = (1-R1)*np.exp(-alpha1*t)
A1 = 1-R1-T1

plt.text(280, 30, 'Mobility (cm$^{2}$.V$^{-1}$.s$^{-1}$)', fontdict= font)
plt.plot(1e9*wavelength, 100*A1, label =r'50', color = 'k', lw = 4)
plt.show()
plt.text(250, 35, 'Density (cm$^{-3}$)', fontdict= font)
plt.plot(1e9*wavelength, 100*A1, label =r'$4.10^{20}$', color = 'k', lw = 4)
plt.show()

A1 = 1-R1-T1
plt.plot(1e9*wavelength, 100*R1,label =r'$4.10^{20}$', color = 'k', lw = 4)
plt.show()
plt.plot(1e9*wavelength, 100*T1,label =r'$4.10^{20}$', color = 'k', lw = 4)
plt.text(350, 55, 'Density n(cm$^{-3}$)', fontdict=font)
plt.xlim(280, 2500)
plt.show()

def wp(n): #Plasma frequency
    return 1e9*2*np.pi*c/np.sqrt(n*el**2/(m*epsr*eps0))
print([wp(1e6*1e20*n) for n in [4, 6, 8, 10]])
```

Frequency dependence of C-V capacitances for H-ITO and Al reference gates for a 10 nm oxide (SiO$_2$).

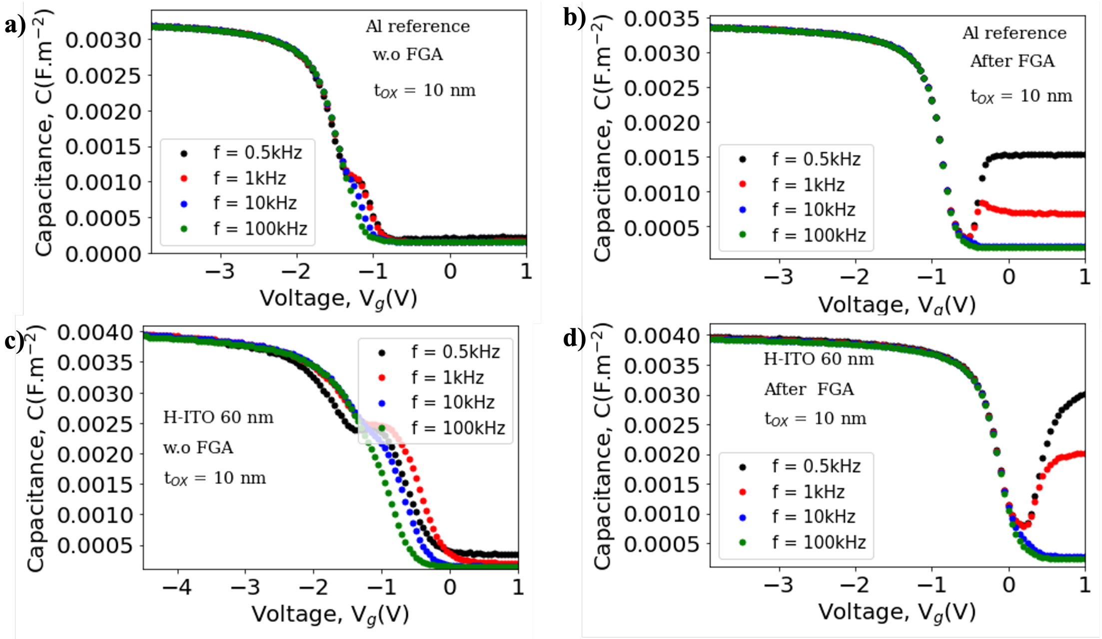

Figure 1: C-V curves at different frequencies: **a)** and **b)** correspond to measurements on Al/SIO2/Si before and after FGA respectively, **c)** and **d)** correspond to measurements on H-ITO/SiO$_2$/Si before and after FGA respectively.

Python Script for MOS capacitor simulation

```
# -*- coding: utf-8 -*-
"""
Created on Tue Feb 16 17:59:20 2021

@author: Louis David MOHGOUK ZOUKNAK
"""

import matplotlib.pyplot as plt
import numpy as np
import pandas as pd

T = 300.             # Température en °K
tox = 10.6e-7   # Epaisseur de l’oxyde en nm convertie en m
eox = 3.9            # Pemittivité relative de l’oxyde
S = 0.93*(200.*1e-4)**2
#S  = 5e-4

# Constantes physiques
e0 = 8.85e-14    # En F.m-1
q = 1.602e-19     # Charge élementaire en C
k = 1.38e-23    # Constante de Boltzmann en eV.K-1

# Paramètres du sustrat type p
es = 11.9        # Permittivité relative du Si, sans unité
chi_s = 4.05       # Affinité électronique du Si en eV
Nd = 1.e10         # Densité de donneurs en cm-3
Na  = 2.9E15     # Densité d’accepteurs en cm-3

Eg = 1.17- (4.73*1e-4*T**2)/(T+636.0)    # Bandgap du Si, formule de Vashirini
Nv = 2.5e19*(0.59*T/300.)**1.5  # Densité d’état effective de la bande de valence
Nc = 2.5e19*(1.06*T/300.)**1.5  # Densité d’état effective de la bande de conduction


# Positions des bandes

ni = (Nc*Nv)**0.5*np.exp(-q*Eg/(2*k*T))   # Densité intrinsèque de porteurs
Ec  = Eg          # Energie du min de la BC
Ev = 0.            # Energie du min de la BV
Ei = Ec + k*T*np.log(ni/Nc)/q      # Energie du niveau intrinsèque
```

```
phi_T = k*T      # Potentiel thermique

#Résolution de l'équation de l'électroneutralité: calcul du niveau de Fermi
def bissection(f,a,b):
    precision = 1e-10
    c = min(a,b)
    d = max(a,b)
    count = 0
    while (d-c)>precision :
        if f(c)*f(d)>0.:
            print("Pas de racine dans",c,"et",d)
        count = count + 1
        m = (c+d)/2.
        if f(m)*f(c)<0:
            d = m
        else:
            c= m
    return (c+d)/2.0

def f(Ef):
    return  Nv*np.exp(q*(Ev - Ef)/phi_T)- Nc*np.exp(q*(-Ec + Ef)/phi_T) +
    Nd - Na   # Equation de l'électroneutralité électronique

Ef  = bissection(f, Ev, Ec) # Calcul du niveau de Fermi
phi_Si = (Ec- Ef) + chi_s

n0 =  ni*np.exp(q*(-Ei + Ef)/phi_T)  # Densité d'électrons à l'équilibre
p0 =  ni*np.exp(q*(Ei - Ef)/phi_T)   # Densité de trous à l'équilibre

Ld1 = np.sqrt(e0*es*phi_T/(2*ni*q**2))  # Longuer de Debye

# Charge de surface

phi_B  = Ef - Ei     # Potentiel dans le bulk du SC
print("phi_B= ", phi_B, "phi_T = ", phi_T)
def Qs(psi_S):
    phi_S = psi_S + phi_B
    us = q*phi_S/phi_T
    ub = q*phi_B/phi_T
    f  = np.sqrt(2)*np.sqrt( (ub - us)*np.sinh(ub) - (np.cosh(ub)- np.cosh(us)))
    c1 = es*e0/Ld1
    return np.sign(ub-us)*c1*phi_T*f/q

def C(psi_S):
    phi_S = psi_S + phi_B
    us = q*phi_S/phi_T
    ub = q*phi_B/phi_T
    f  = np.sqrt(2.)*np.sqrt((ub - us)*np.sinh(ub)-(np.cosh(ub)- np.cosh(us)))
    c1   = es*e0/Ld1
    Cox = eox*e0/tox
    Cs = -np.sign(ub-us)*c1*(np.sinh(us)-np.sinh(ub))/f
```

```
    return S*Cs*Cox/(Cs+Cox)
nbx = 201

Vfb0 = -1.15
Q0  = 5.e10*q

df_ps = pd.read_csv(r'H:/MesuresAvril2021/syntheseessai2.txt',index_col
= 0, delimiter = '\t', header = None)
df_ps.to_csv (r'H:/MesuresAvril2021/syntheseessai2.csv', index=None)
df_ps = df_ps.reset_index()

# Importation de la base de données et indexation des tableaux
i = 0
count = 1
while i<575:
    a = 'Vgsc_' + str(count)
    b = 'Csc_' + str(count)
    c = 'Qsc_' + str(count)
    d = 'Y_' + str(count)
    e = 'col_' + str(count)
    df_ps = df_ps.rename(columns={df_ps.columns[i]: a})
    df_ps = df_ps.rename(columns={df_ps.columns[i+1]: b})
    df_ps = df_ps.rename(columns={df_ps.columns[i+2]: c})
    df_ps = df_ps.rename(columns={df_ps.columns[i+3]: d})
    df_ps = df_ps.rename(columns={df_ps.columns[i+4]: e})
    i = i+5
    count = count+1

phi_fs = phi_T*np.log(Na/ni)/q
tsub = 1.
beta = q/phi_T

dopage = 4

a = 'col_'+str(dopage)
b = 'Vgsc_'+str(dopage)
c = 'Qsc_'+str(dopage)
d = 'Csc_'+str(dopage)

Na = 1.e-6*df_ps[a][48]
Vgsc = df_ps[b]
Qsc = df_ps[c]
Csc = df_ps[d]
Vfbsub = sum(df_ps[a][-3:])

def f(Ef):
    return  Nv*np.exp(q*(Ev - Ef)/phi_T)- Nc*np.exp(q*(-Ec + Ef)/phi_T)
     + Nd - Na   # Equation de l'électroneutralité électronique
Ef  = bissection(f, Ev, Ec) # Calcul du niveau de Fermi

phi_Si = (Ec-Ef) + chi_s
```

```
Na1 = df_ps[a][48]*np.exp(-q*Ef/phi_T)
Nv = 2.5e19*(0.59*T/300.)**1.5
phi_fs = (1./beta)*(np.log(Na/Nv))+0.5*Eg

CV36_FGA_bis2 = pd.read_csv(r'H:MesuresAvril2022CV36_30nm
_MoOx14_Al_FGA_bis2.txt',index_col = 0,
skiprows = 2, delimiter = ';')
CV36_FGA_bis2.to_csv (r'H:/MesuresAvril2022/
CV36_30nm_MoOx14_Al_FGA_bis2.csv', index=None)
CV36_FGA_bis2 = CV36_FGA_bis2.reset_index()

Cox  = eox*e0/tox

df = CV36_FGA_bis2
Qf = 0.e15
Dvfb  = 0.28
Vfbs = -phi_fs + Vfbsub + Dvfb
print('Vbfs00 = ', Vfbs+0.239)
while Dvfb < 0.5:
    Vfbs = -phi_fs + Vfbsub + Dvfb-q*Qf/Cox
    Vsub = Vfbs + Vgsc -Qsc/Cox
    Csub = Cox*Csc/(Cox+Csc)
    plt.scatter(df['Vg'], df['C.5k']/S, color = 'violet', label = '100kHz',
    s = 10, marker = 'v')
    plt.show()
    Dvfb = Dvfb+0.01213
print("Dvfb =", Dvfb, "Vfb = ", Vfbs, "Na = ", Na, 'WF  = ', Vfbs+phi_Si, 'WFmidgap
= ', -phi_fs+phi_Si, 'phi_Si = ', phi_Si, 'phi_fs = ', phi_fs)
```

XRR spectra (measured and fitted) of NiOx with different oxygen partial pressure, ppO$_2$ (%)

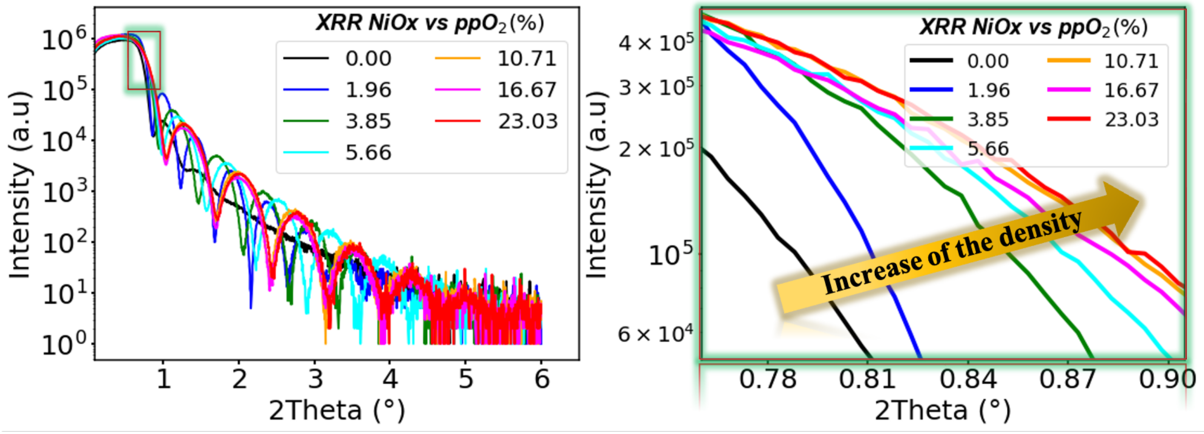

Figure 2: XRR measurements of NiOx films with different oxygen concentrations (**left**), change of the down set slope showing the evolution of film density as a function of oxygen concentration (**right**)

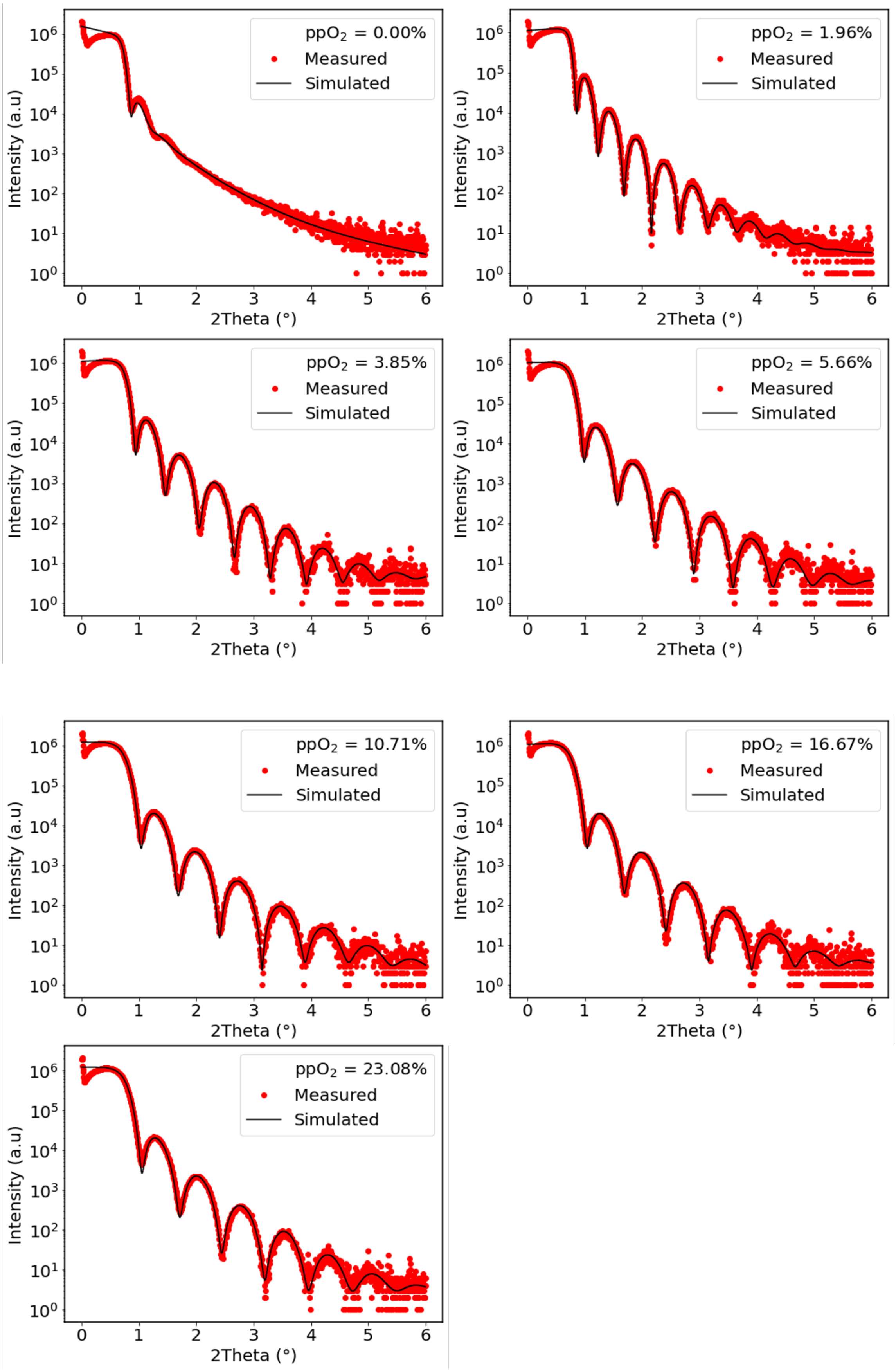

Figure 3: NiO$_x$ XRR curves and fitting curves data at different oxygen concentrations.

Evidence of hydrogen doping of In$_2$O$_3$-based TCO by SIMS (secondary-ion mass spectrometry) measurements

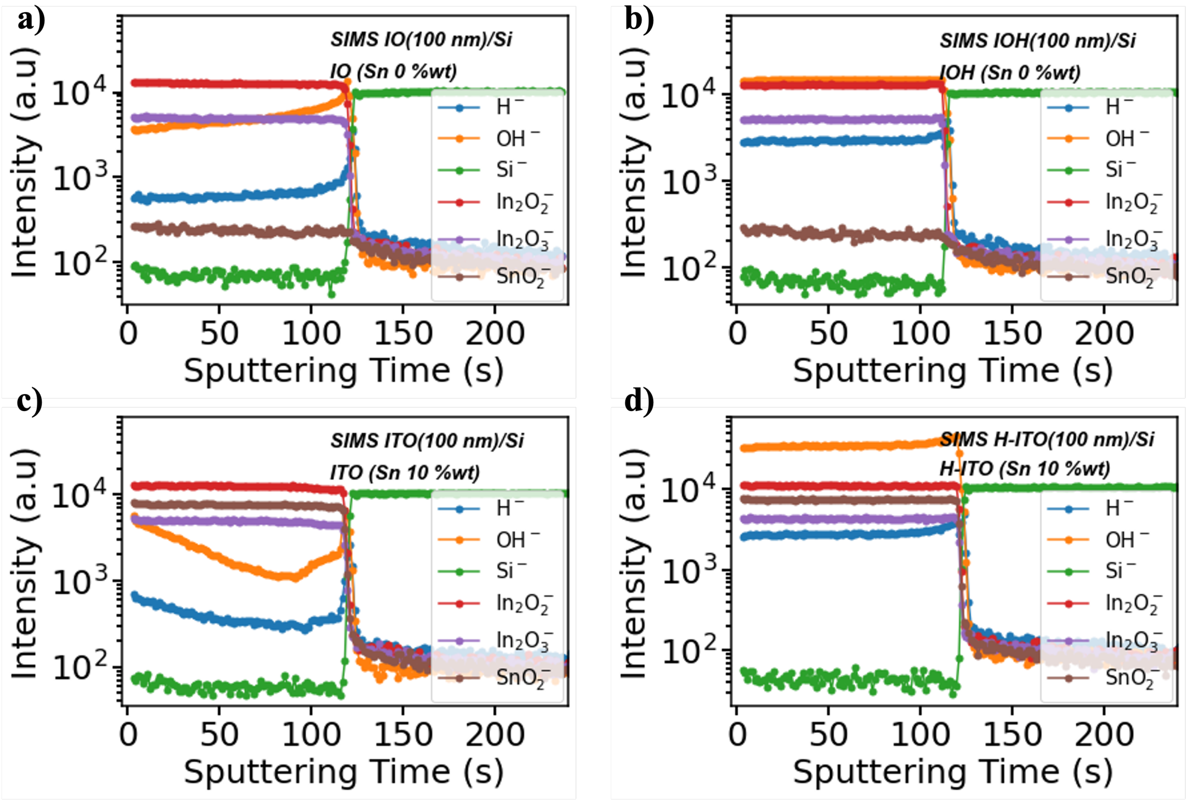

Figure 7.4: Hydrogen doping of In$_2$O$_3$-based TCO, secondary ion mass spectrometry (SIMS) measurements: **a)** 100 nm In$_2$O$_3$ from an In$_2$O$_3$ target on Si, **b)** 100 nm IOH (hydrogen doped In$_2$O$_3$) from an In$_2$O$_3$ target) on Si, **c)** 100 nm ITO (Sn doped In$_2$O$_3$) from an ITO target (Sn 10% wt) on Si **d)**100 nm H-ITO (hydrogen doped ITO) from an ITO target.

List of Figures

List of Tables

Abstract

7.0.1 Version française

Au cours des dernières décennies, le développement de matériaux à zéro dimension (0D) ou de points quantiques (QDs ou quantum dots) a connu une croissance significative. Parmi ceux-ci, les QDs de sulfure de plomb (PbS) ont fait l'objet d'une attention particulière en raison de leurs propriétés exceptionnelles, notamment l'absorption optique accordable de 600 à 2600 nm. Les QDs de PbS sont considérés comme l'un des matériaux les plus prometteurs pour la prochaine génération de capteurs infrarouges. Leur utilisation dans le domaine de l'industrie suscite donc un intérêt croissant. Lorsque ces matériaux sont intégrés dans des dispositifs optoélectroniques, ils nécessitent l'utilisation d'électrodes efficientes pour l'extraction de charges, ainsi qu'un contact électrique transparent dans l'IR pour l'obtention de meilleures performances. Dans ce travail de thèse, des études des propriétés des électrodes d'extraction de trous (HTL) à base d'oxydes des métaux de transition et du contact électrique transparent à base d'In_2O_3 (TCO ou oxyde transparent et conducteur) préparés par pulvérisation cathodique ont été réalisées. Ces études ont été menées dans un premier temps sur des couches individuelles. Les caractérisations des films TCO ont permis de montrer l'intérêt du dopage à l'hydrogène sur l'amélioration de leurs propriétés optiques dans le domaine infrarouge du spectre électromagnétique (domaine d'intérêt pour les applications visées). Dans un second temps, afin de fabriquer des structures photodiodes, elles ont été intégrées sur un film de QDs de PbS déposé sur une électrode optimisée pour l'extraction et le transport d'électrons. Les caractérisations appropriées ont permis de montrer que les films ultraminces de NiOx peuvent être de meilleures alternatives aux couches de MoOx traditionnellement utilisées comme matériaux d'extraction et de transport de trous sur les films de QDs de PbS.

7.0.2 English version

Over the last few decades, there has been significant growth in the development of zero-dimensional (0D) materials or quantum dots (QDs). Among these, lead sulphide (PbS) QDs have received particular attention because of their outstanding properties, including tunable optical absorption from 600 to 2600 nm. PbS QDs are considered to be one of the most promising materials for the next generation of infrared sensors. There is therefore growing interest in their use in industry. When these materials are integrated into optoelectronic devices, they require the use of efficient electrodes for charge extraction, as well as a transparent electrical contact in the IR for better performance. In this thesis work, studies of the properties of hole extraction electrodes (HTL) based on transition metal oxides and of the transparent electrical contact based on In_2O_3 (TCO or transparent and conductive oxide) prepared by sputtering were performed. These studies were initially carried out on individual layers. Characterisation of the TCO films showed that hydrogen doping improves their optical properties in the infrared region of the electromagnetic spectrum (the region of interest for the targeted applications). Secondly, in order to fabricate photodiode structures, they were integrated onto a film of PbS QDs deposited on an electrode optimised for electron extraction and transport. Appropriate characterisations have shown that ultra-thin NiOx films can be better alternatives to the MoOx layers traditionally used as hole

Scientific Communications

1. p-type NiOx ultrathin film as highly efficient hole extraction layer in n-type PbS quantum dots based NIR photodiode: **Louis David Mohgouk Zouknak**, Mickael Gros-Jean, Serge Blonkowski, Charles Leroux, Gerard Ghibaudo, December 2023, Solid-State Electronics 212(9):108836.
2. Buried Interfaces of IR Photodetector Devices Analyzed with Lab-Based XPS/HAXPES: Roman Charvier, M. Juhel, STMicroelectronics, France; O. Renault, Univ. Grenoble Alpes, CEA, Leti, France; A. Valery, D. Guiheux, **L. Mohgouk Zouknak**, STMicroelectronics, France; B. Domenichini, ICB UMR 6303 CNRS-Université de Bourgogne, France, AVS Quantum Science Workshop: Materials & Surface Science of Quantum Sensing, November 5, 2023(Oral presentation).
3. p-type NiOx ultrathin film as highly efficient hole extraction layer in n-type PbS quantum dots based NIR photodiode: **Louis David Mohgouk Zouknak**, Mickael Gros-Jean, Serge Blonkowski, Charles Leroux, Gerard Ghibaudo, Juin 2023, INFOS2023 Conference (Oral presentation).
4. Ultra-fast CV methods ($< 10\mu$s) for interface trap spectroscopy and BTI reliability characterization using MOS capacitors: T Mota Frutuoso, X Garros, J Lugo-Alvarez, RK Kammeugne, **LDM Zouknak**, A Viey, W Vandendeale, P Ferrari, F Gaillard, March 2022 IEEE International Reliability Physics Symposium (IRPS conference paper).

Extended summary in French (résumé de la thèse en français)

Les films conducteurs transparents à base d'In_2O_3 sont l'un des meilleurs TCO car ils ont des propriétés optiques et électriques supérieures à celles de tous les autres TCO. Ils sont largement utilisés comme électrodes transparentes dans les cellules solaires, les technologies d'affichage (écrans), les LED, les photodiodes et de nombreuses autres applications optoélectroniques. Ils sont extrêmement stables, compatibles avec de nombreux types de substrats (rigides, flexibles, polymères, etc.) et peuvent être déposés à l'aide de diverses techniques (physiques et chimiques). Ces matériaux conviennent également à la gravure industrielle. Comme indiqué dans les sections précédentes, les propriétés électriques et optiques du TCO en général, et du TCO à base d'In_2O_3 en particulier, dépendent fortement de la concentration d'oxygène (ou des vides d'oxygène). En fait, la concentration en oxygène du TCO détermine la densité des porteurs libres et affecte fortement la mobilité de ces porteurs libres. Dans le cas de l'ITO (In_2O_3 : Sn), le dopage intentionnel au Sn affecte également la densité des porteurs libres et les propriétés des films déposés. Dans la notation de Kroger-Vink, les phénomènes de dopage par des lacunes d'oxygène $V_O^{\bullet\bullet}$ (donneurs de deux électrons) et de substitution d'atomes In (cation In^{3+}) par des atomes Sn (cation Sn^{4+}) sont décrits par les relations suivantes

$$O_O^{\times} \longrightarrow \frac{1}{2}O_2(g) + V_O^{\bullet\bullet} + 2e' \tag{7.0.1}$$

et

$$(2Sn_{In}^{\bullet}O_i'')^{\times} \longrightarrow \frac{1}{2}O_2(g) + 2Sn_{In}^{\bullet} + 2e' \tag{7.0.2}$$

La concentration d'oxygène peut être contrôlée avec précision pendant le dépôt en ajustant les paramètres de dépôt tels que la concentration d'oxygène dans l'atmosphère de dépôt est $O_2(\%) = \frac{100 \times O_2}{O_2 + Ar}$, la pression totale de dépôt, ou la température du substrat. Les réactions de dopage par des défauts neutres $2Sn_{In}^{\bullet}O_i'')^{\times}$ données l'**Equation** 7.0.2 et l'**Equation** 7.0.1 dépendent non seulement de la concentration en Sn, mais aussi de la température (par des mécanismes d'activation thermique), c'est pourquoi la croissance de films ITO avec des propriétés électriques et optiques optimales est généralement réalisée à des températures comprises entre 150 et 400°C[109, 220, 221]. Dans cette étude, le matériau (en particulier les PbS QDs) sur lequel les contacts transparents sont réalisés ne permet pas l'utilisation de tels budgets thermiques. Par conséquent, les conditions adaptées telles que la composition des cibles les paramètres de dépôt ainsi que les gaz utilisés doivent être trouvées pour la réalisation à température ambiante des films minces de TCO à base d?InIn_2O_3 de haute qualité. Sur notre machine de dépôt (Alliance Concept Cluster Tool 200 ou AC CT200), nous disposons en plus de la ligne d'alimentation en Ar, une ligne composée d'un mélange Ar +3%H_2. Cette ligne d'alimentation en gaz Ar+3%H_2 qui nous permettra d'étudier des films dopés H tels que l'oxyde d'indium dopé à l'hydrogène (In_2O_3:H ou IOH) ou l'oxyde d'indium et d'étain dopé à l'hydrogène (H-ITO). L'utilisation réussie de l'hydrogène comme dopant dans le TCO pendant le processus de pulvérisation a déjà été démontrée pour l'In_2O_3[222]. L'IOH est connu pour être un candidat prometteur pour les

applications nécessitant un contact électrique ayant une conductivité élevée tout en conservant une bonne transparence IR. La possibilité de fabrication des films de TCO à base d'In_2O_3 à température ambiante en font des candidats idéals pour des applications dont l'utilisation d'un budget important est un paramètre critique, c'est le cas des dépôts sur des matériaux sensibles à la température ou des applications nécessitant un dépôt sur des substrats en plastique ou en polymère[224, 225, 226]. Des études théoriques sur la configuration de l'hydrogène dans le TCO à base d'In_2O_3 ont montré que l'hydrogène incorporé aux joints de grains est considéré comme une passivation des défauts pour réduire les barrières de transport des électrons (amélioration de la mobilité des porteurs) [228, 229, 230, 231]. Ainsi la densité d'électrons libres de l'IOH est généralement inférieure d'un facteur deux à celle de l'ITO, on a une amélioration de la conductivité qui se fait par une augmentation de la mobilité plutôt que par la densité [34].
Dans cette partie, nous étudions les effets du dopage à l'hydrogène sur les performances électriques, les propriétés optiques et les aspects structurels des films d'oxyde d'indium dopé à l'étain déposés par PVD à température ambiante. Nous montrons les résultats de la mesure de la fonction de travail du film présentant les meilleures propriétés électriques et optiques, et discutons des effets des dommages causés par le plasma lié au phénomène de pulvérisation. Nous comparerons ensuite les propriétés électriques et optiques optimales de différents oxydes à base d'In_2O_3 avec différentes concentrations de Sn ainsi que des échantillons avec et sans dopage à l'hydrogène. Enfin, nous conclurons sur le choix d'une électrode transparente pour les dispositifs optoélectroniques dans la gamme IR. Différentes couches d'IOH (oxyde d'indium dopé à l'hydrogène) de H-ITO (oxyde d'indium-étain dopé à l'hydrogène) et d'ITO (oxyde d'indium-étain) ont été déposées par pulvérisation magnétron RF en utilisant des cibles commerciales d'In_2O_3 dopé Sn 10 %wt, d'In_2O_3 dopé Sn 1 %wt, d'In_2O_3. L'oxygène et l'Ar ont été utilisés comme gaz de traitement. Pour les dépôts IOH et H-ITO, l'Ar est remplacé par un mélange l'Ar+3%H_2. Les paramètres de dépôt ont été soigneusement réglés pour garantir la croissance de films TCO à base d'oxyde d'indium de haute qualité à température ambiante. Pour ce faire, une pression partielle d'oxygène et une pression de pulvérisation optimales ont été déterminées.

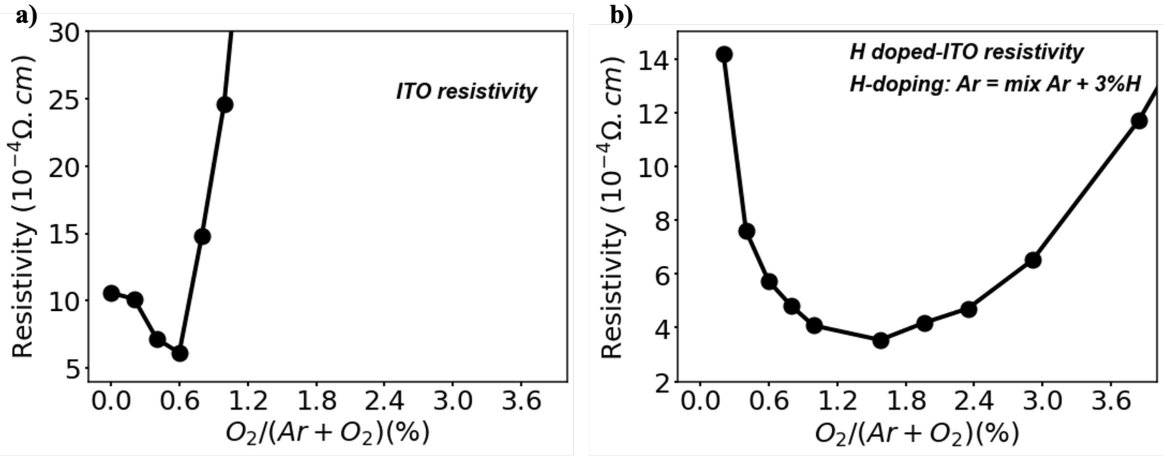

Figure 7.5: Résistivité de H-ITO (Sn 1%) en fonction de la pression de dépôt d'oxygène de ≈50 nm déposée sur SiO_2 (500 nm) à température ambiante et à une pression totale de 0.001 mbar, **a)** sans dopage à l'hydrogène et **b)** avec dopage à l'hydrogène.

Pour une cible ITO (Sn 1%wt), les résistivités électriques mesurées par la technique des quatre pour des échantillons d'une épaisseur ≈ 50 - 60 nm, sans et avec dopage à l'hydrogène, sont présentées dans les **Figure** 7.5**a** et 7.5**b** respectivement. Nous avons trouvé une concentration optimale d'oxygène de ≈ 0.6 % pour les échantillons non dopés à l'hydrogène correspondant à une résistivité de 6.12×10^{-4} Ω.cm, tandis que l'optimum pour les films dopés à l'hydrogène est de ≈1.6 %, correspondant à une résistivité de ≈3.73×10^{-4} Ω.cm. La résistivité des films dopés à l'hydrogène est comparable à celle des films d'ITO déposés à haute température [221, 234]. Nous avons également obtenu une très bonne uniformité avec une déviation standard de moins de 2% pour les mesures de résistance en 49 points des films de H-ITO (concentration d'oxygène = 1.6%) déposés sur des substrats de SiO_2 en 200 nm (**Figure** 7.6).

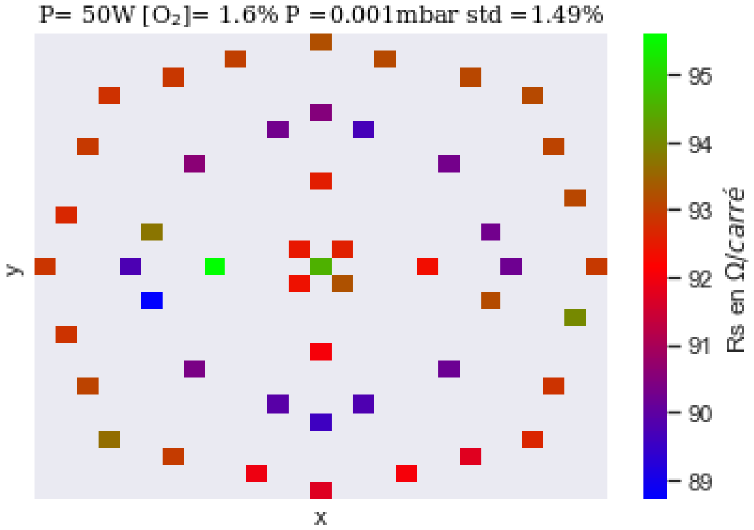

Figure 7.6: Uniformité du film pour ≈50 nm H-ITO, mesures de résistivité de 49 points sur des substrats SiO_2 de 200 mm pour une concentration optimale d'oxygène (≈1.6%).

Les mesures de la mobilité et de la densité des porteurs de charge (**Figure** 7.7) montrent que lorsque la pression d'oxygène augmente, la densité des lacunes d'oxygène incorporées dans le film diminue, ce qui entraîne une baisse de la densité des porteurs de charge libres. La valeur de la densité déterminée pour la meilleure recette (ppO_2 = 1.6%) est de $5.56\times10^{20}cm^{-3}$. Il convient toutefois de noter que la densité de porteurs de charge de l'ITO déposé à des températures plus élevées peut atteindre $1\times10^{21}cm^{-3}$ (semi-conducteur hautement dégénéré). Les films TCO hautement dégénérés ne conviennent pas aux applications dans la région IR, car la densité élevée de porteurs de charge entraîne une augmentation de la fréquence du plasma ω_p, ce qui se traduit par une interaction électron-photon plus forte et une transmission optique plus faible dans la région IR (forte absorption plasmonique). La mobilité augmente lorsque la densité des lacunes d'oxygène ou celle des porteurs de charges libres diminue. La mobilité dépend principalement de la densité des impuretés ionisées, en particulier des lacunes d'oxygène et des ions Sn^{4+}, qui à leur tour sont liés au nombre de porteurs de charges libres. Par analogie avec l'évolution de la densité des porteurs de charge libres en fonction de la pression partielle d'oxygène, la mobilité augmente à mesure que la pression d'oxygène s'accroît. Les mesures de Hall montrent qu'un contrôle minutieux de la pression partielle d'oxygène permet d'obtenir le meilleur compromis entre la mobilité et la densité de porteurs de charge libres, ce qui correspond à la résistivité électrique la plus faible.

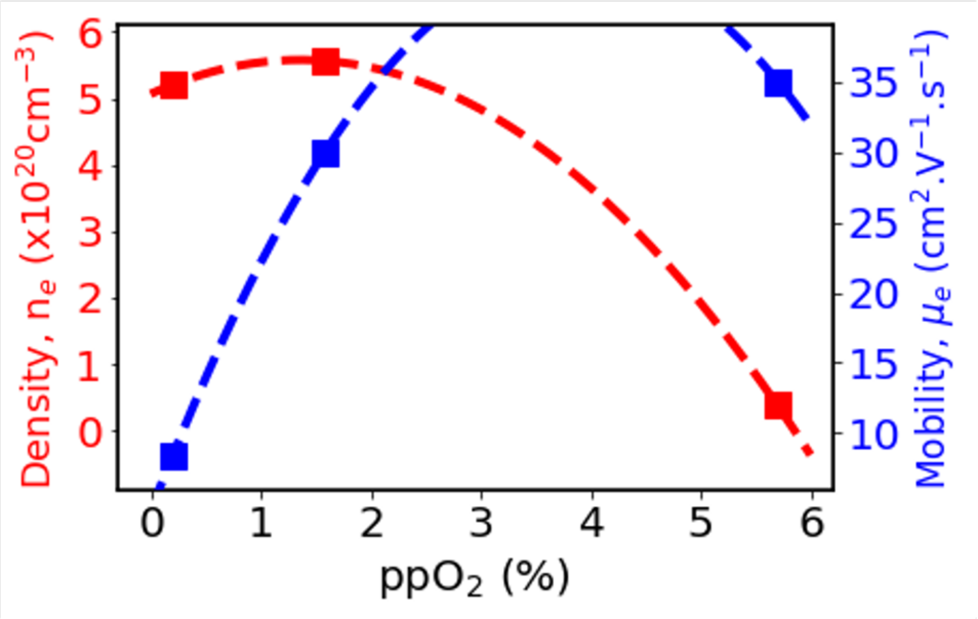

Figure 7.7: Densité de porteurs libres et mobilité de Hall en fonction de la pression de dépôt d'oxygène H-ITO (Sn 1%).

Les mesures de transmission et de réflexion optique pour des films H-ITO de 50 nm de différentes concentrations d'oxygène déposés sur des substrats en verre sont présentées dans la **Figure** 7.8.**a** Pour concentration d'oxygène 1.6% correspondant au fil ayant la meilleure résistivité électrique, on a une transmission optique T > 80 % dans la région 600 - 1800 nm. Lorsque la concentration en oxygène augmente, la concentration en porteurs libres diminue et réduit l'absorption de la lumière dans la région IR, améliorant ainsi la transmission optique (concentration d'O_2 = 5.7%). Les mesures d'éllipsométrie(**Figure** 7.8.**b**) montrent une diminution du coefficient d'extinction **k** des films de H-ITO dans les régions Vis et IR lorsque la concentration d'oxygène augmente, c'est-à-dire une diminution de l'absorption (diminution de l'interaction plasmon-photon). Ces résultats sont cohérents avec les mesures de transmission optique et celles d'effet Hall.

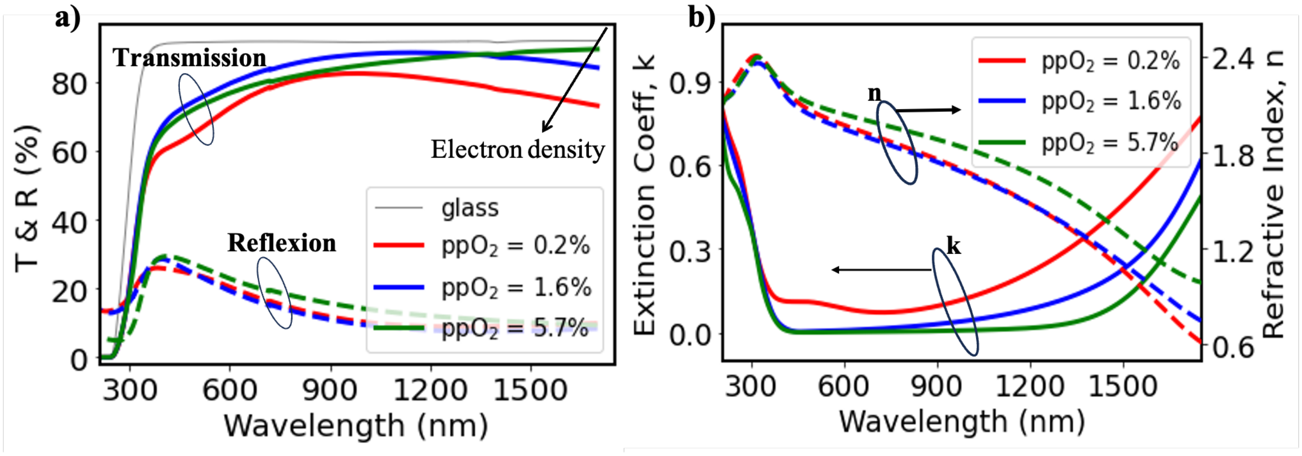

Figure 7.8: **a)** Transmission optique T et réflexion R, **b)**coefficient d'extinction k et indice de réfraction n, des films de ≈50 nm de H-ITO (Sn 1%) déposés à différentes pressions d'oxygène.

La bande interdite optique E_{gopt} est calculée à partir de l'extrapolation de α^2, où α est l'absorption déterminée à partir du coefficient de réflexion) en fonction de l'énergie photonique hν

(diagramme de Tauc, $\alpha^2 \propto$ (E_{gopt} - $\alpha h\nu$ (**Figure** 7.9). On a une légère augmentation de bande interdite optique diminue lorsque la concentration d'oxygène diminue. Cette augmentation peut s'expliquer par une différence de densité des porteurs de charge. En efffet, d'après la relation de Moss-Burnstein, la bande interdite optique devrait augmenter avec la concentration de porteurs en fonction de $n^{2/3}$. Nous constatons également que le gap optique est supérieur à 3.6 eV, et cette grande largeur de gap explique la transmission élevée du TCO à base d'In_2O_3. Connaissant la densité et le gap optique et en supposant que la bande interdite n'est modifiée que par l'effet Moss-Burnstein, il est possible d'estimer le gap fondamental E_{g0} et la masse effective réduite m^*. Dans ce cas, la lacune fondamentale et la masse effective correspondent à l'ordonnée à l'origine et à la pente de la courbe E_{gopt} = $f(n^{2/3})$, respectivement. En réalité, cette mesure est complexe car il existe un effet de rétrécissement de la bande interdite opposé à l'effet Moss-Burnstein, connu sous le nom d'effet Hamberg et Granvqist, qui est dû à la diffusion électron-électron et électron-impuretés [100].

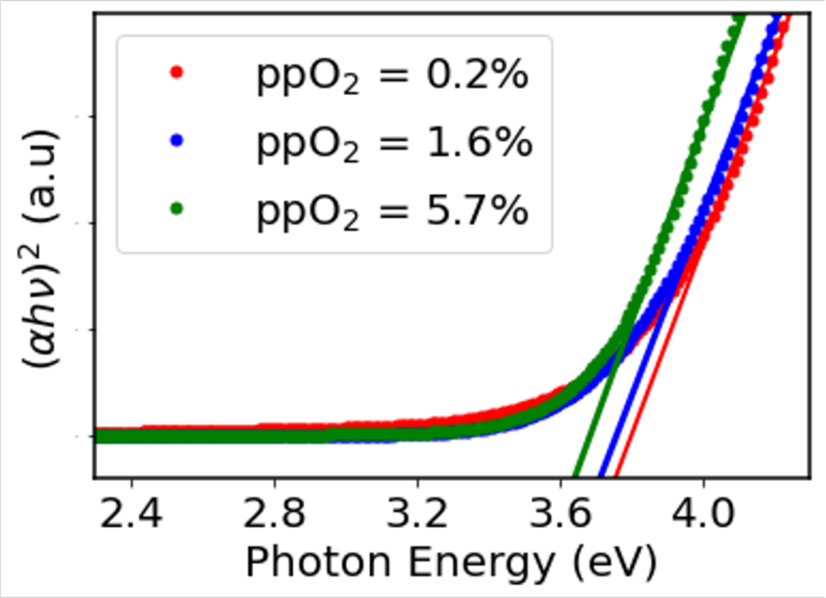

Figure 7.9: Images d'extraction de la bande interdite optique (diagramme de Tauc) de films minces de H-ITO (Sn 1%wt) à différentes pressions partielles d'oxygène.

Les **Figure** 7.10 **a**, **b** et **c** montrent les morphologies AFM 2D et 3D des films minces H-ITO (Sn 1%) déposés à différentes concentrations d'oxygène sur des substrats de Si. Ces images sont obtenues par des mesures AFM avec un balayage sur 1×1 μm^2. Tous les films minces présentent une morphologie de surface lisse et n'ont pas de structure en grain. En raison de la faible puissance de dépôt (50 watts) et de la faible pression de dépôt (0.001 mbar), on a de très faible rugosité rms < 1 nm. Avec une concentration de Sn 10%wt, on a obtenu des rugosités plus importantes et notamment une structure en forme de grain pour la concentration d'oxygène de 1.6%.

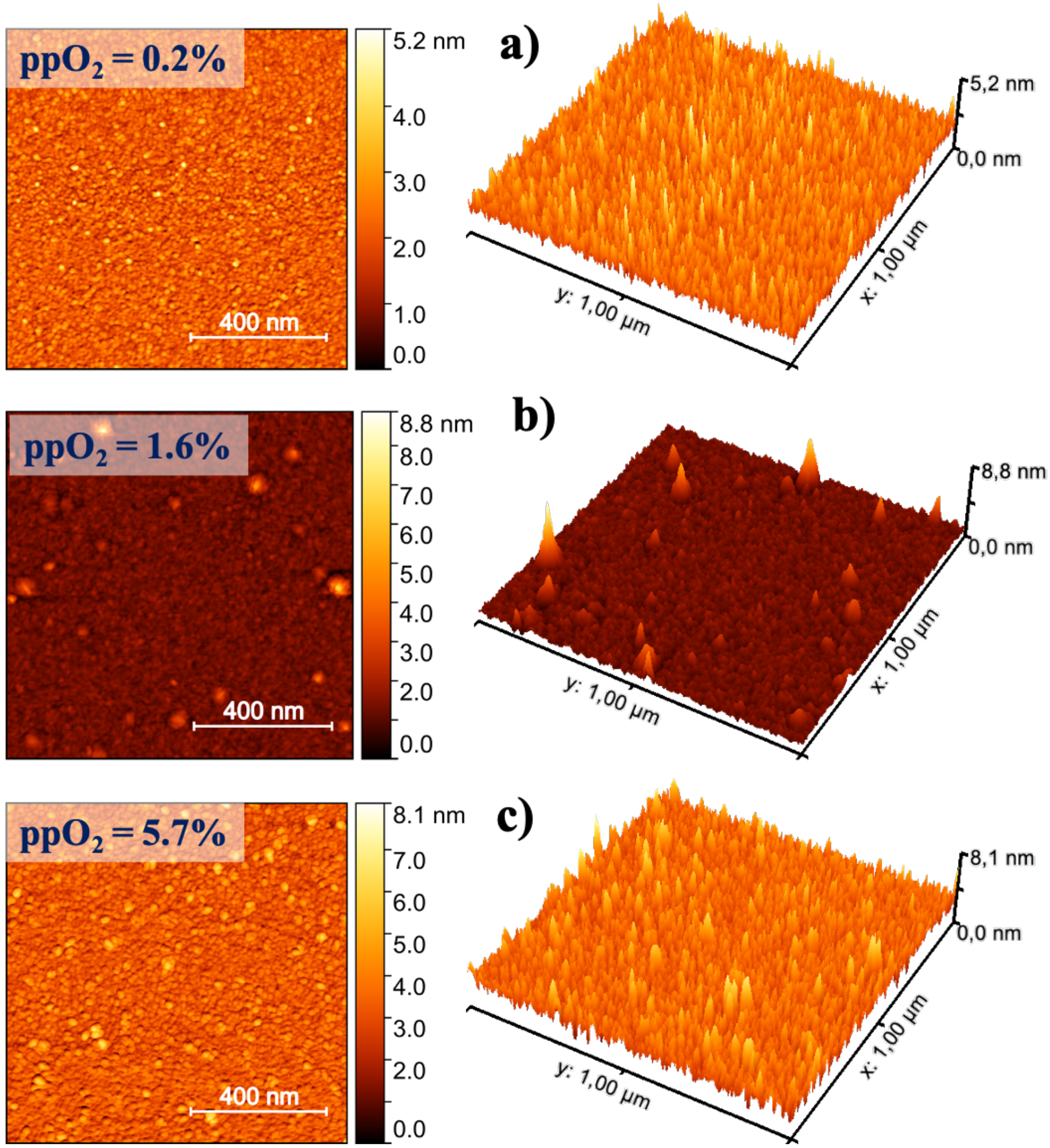

Figure 7.10: **a,b,c)** Images 2D et 3D par microscopie à force atomique (AFM) montrant la surface, c) Spectres de diffraction des rayons-X des films H-ITO (Sn 1 %) préparés à température ambiante avec différentes concentrations d'oxygène.

Les **Figure** 7.11.**a** and 7.11.**b** montrent les propriétés structurelles des films minces de H-ITO en fonction de la pression d'oxygène pour des concentrations de Sn de 1 % et 10 %. Tous les films de H-ITO ont une structure polycristalline avec des pics de diffraction (222) et (211) pour certaines pressions d'oxygène, indiquant une structure cubique de type bixbyite. L'intensité des pics augmente généralement avec l'augmentation de la concentration en O_2. Le pic (440) est dû à l'augmentation de la concentration en oxygène, qui induit la formation de réseaux de liaisons In-O et favorise la croissance dans la direction perpendiculaire au plan (222) [235]. Bien que tous les films présentent un certain degré de cristallinité, les propriétés structurelles ne permettent pas d'expliquer directement les propriétés électriques.

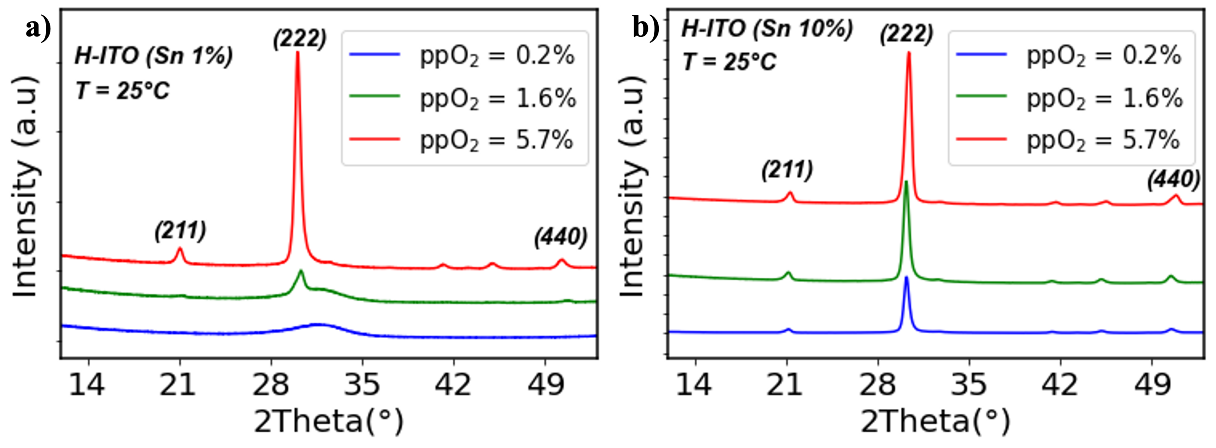

Figure 7.11: X-ray diffraction spectra of H-ITO films grown at room temperature with different oxygen concentration for **a)** Sn 1 % and **b)** Sn 10 % .

Le travail de sortie est l'une des propriétés les plus importantes d'une électrode car il définit la hauteur de la barrière énergétique aux interfaces avec d'autres matériaux, affecte les mécanismes de transport de charge dans les dispositifs et peut avoir un impact important sur leurs performances. Ainsi, nous avons déterminé le travail de sortie de l'ITO-H (Sn 1%) par les mesures et analyses des capacité (C-V) MOS. À cette fin, des structures MOS H-ITO (60 nm) /SiO_2/Si et des dispositifs de référence en Al (150 nm) /SiO_2/Si ont été fabriqués. Les effets induits par le processus de pulvérisation H-ITO ont été estimés comme des décalages Dits et Vfb à l'interface SiO_2/Si. Les résultats sont comparés avec ceux des dispositifs pairs ayant subi un post-traitement thermique (recuit N_2H_2, 425°C durant 30 minutes), permettant de passiver l'interface SiO_2/Si et de réduire les charges d'oxydes (SiO_2). Les courbes C-V expérimentales et simulées des empilements référence en Al/SiO_2/Si et de H-ITO (60 nm)/SiO_2/Si pour différentes épaisseurs de SiO_2 (10, 20, 30 nm), mesurées à une fréquence de 0,5 kHz avant et après recuit thermique sont présentées sur les **Figure** 7.12.**a** and 7.12.**b**. On observe des anomalies dans la région de déplétion des caractéristiques C-V avant recuit, indiquant des dommages causés par le processus de dépôt. Les courbes C-V avant recuit sont également décalées passent vers des tensions négatives lorsque l'épaisseur d'oxyde t_{OX} augmente. Ce décalage correspond au changement du potentiel des bandes plates V_{fb} , et met en évidence une variation du potentiel de surface du silicium en fonction des charges fixes dans l'isolant et/ou des charges de l'interface Si/SiO_2.

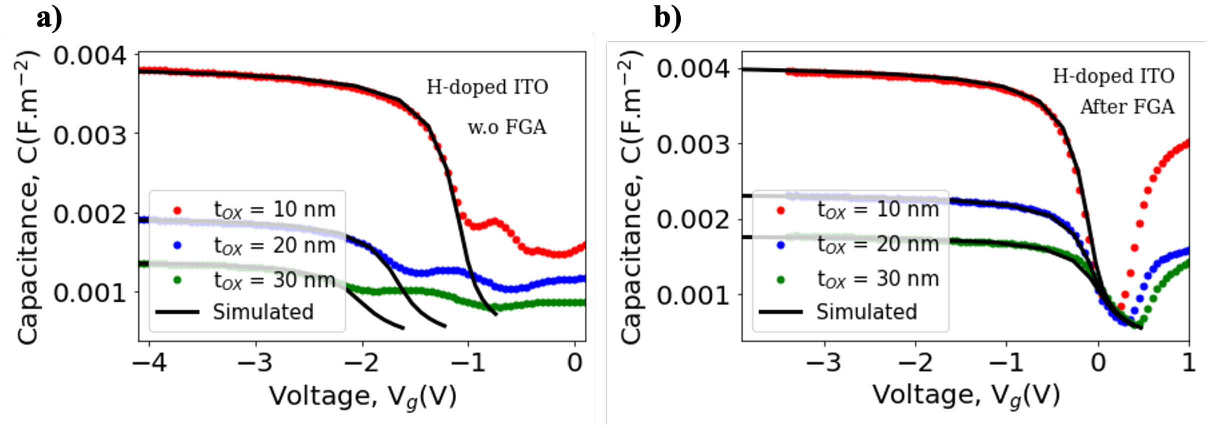

Figure 7.12: Courbes C-V mesurées et simulées pour les empilements H-ITO/SiO_2/Si pour différentes épaisseurs de SiO_2 t_{OX} à la fréquence f = 0,5 kHz, **a)** avant FGA et **b)** après FGA.

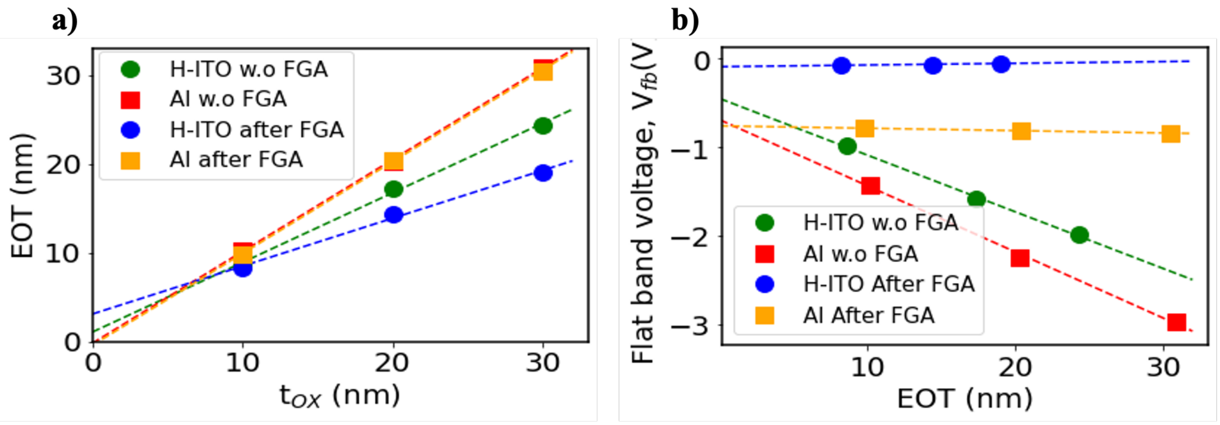

Figure 7.13: **a)** Evolution de l'épaisseur d'oxyde équivalente (EOT) en fonction de l'épaisseur d'oxyde t$_{OX}$ et **b)** Relation entre la tension de bande plate V$_{fb}$ et SiO$_2$ à f = 0,5 kHz, des empilements H-ITO/SiO$_2$/Si comparés aux empilements de référence Al/SiO$_2$/Si avant et après recuit.

Après recuit de passivation, ces différents effets ne sont plus observés et le V$_{fb}$ est presque constant avec l'épaisseur de l'oxyde. La **Figure** 7.13**.a** montre l'évolution des valeurs des épaisseurs équivalents d'oxydes (EOT) en fonction de t$_{OX}$, l'EOT. La relation entre ces deux grandeurs est rappelée par l'équation suivante :

$$EOT = \frac{\varepsilon_{SiO_2}}{\varepsilon_{OX}} t_{OX} \tag{7.0.3}$$

où ε_{SiO_2} et ε_{OX}sont respectivement la constante diélectrique du SiO$_2$ et celle de l'oxyde tel qu'il est dans le dispositif. Sa valeur doit être égale à t$_{OX}$ si l'oxyde est SiO$_2$. Les valeurs des EOT et du potentiel de bande plates sont extraites en superposant les C-V mesurées à un modèle théorique. Pour les dispositifs H-ITO/SiO$_2$/Si, les valeurs EOT ne correspondent pas aux valeurs t$_{OX}$; cette diminution des valeurs EOT par rapport aux dispositifs de référence Al/SiO$_2$/Si révèle un une dégradation de l'oxyde induite par le processus de pulvérisation H-ITO. Des mesures de ToF-SIMS ont montré que cette diminution de l'EOT pourrait être liée à la diffusion de l'In dans le SiO$_2$ entrainant une augmentation de sa permittivité diélectrique. Le travail de sortie a été calculée en utilisant la relation entre V$_{fb}$ et EOT. Le tracé de V$_{fb}$ en fonction de EOT peut être ajusté avec des d'approximation linéaires (**Figure ??.b**). La valeur de V$_{fb}$ extrapolée à EOT = 0 correspond à la différence $\phi_{H-ITO} - \phi_{Si}$. Les valeurs des travaux de sortie obtenus sont résumées dans le **Tableau** 7.1.

	Flat Band Voltage, V$_{fb}$ (V)	**Work Function, ϕ (eV)**
Al w.o. FGA	-0.660±0.07	4.280±0.070
Al After FGA	-0.765±0.004	4.185±0.004
H-ITO w.o. FGA	-0.522±0.016	4.428±0.016
H-ITO After FGA	-0.203±0.001	4.747±0.001

Table 7.1: Fonction de travail de H-ITO (Sn 1%) et de la référence en Al extraite par la technique C(V) with Si dopage N$_a$ = 2×10^{15} cm^{-3} et travail de sortie correspondant ϕ_{Si} = 4.951 eV.

Le travail de sortie de l'aluminium ϕ_{Al}= 4.28 eV et 4.18 eV avant et après FGA respectivement et correspondent à la valeur attendue pour la grille de référence en Al. Bien que les EOT pour la grille H-ITO soient plus faibles que prévu, la relation entre eux et V$_{fb}$ reste quasi-linéaire et permet une bonne détermination de la fonction de travail du matériau de la porte. Le travail de sortie avant recuit est ϕ_{H-ITO} = 4.42 eV alors qu'après recuit ϕ_{H-ITO} = 4.74 eV, ces valeurs sont bien en accord avec la littérature [237, 238]. La valeur maximale de Dits est d'environ 2.4×10^{12}

cm^{-2}.eV^{-1} pour les échantillons avec une grille H-ITO sans recuit, tandis que la valeur maximale pour la grille de référence en Al est d'environ 1.04×10^{12} cm^{-2}. Les valeurs Dits plus faibles pour l'Al indiquent que le processus d'évaporation de l'Al impacte moins l'interface SiO$_2$/Si. Après recuit, les Dits sont considérablement réduits, atteignant 1.7×10^{10} - 7.6×10^{10} cm^{-2}.eV^{-1}.

Nous avons ensuite étudié les couches d'extraction de trous à base d'oxyde de molybdène (MoO$_x$) et d'oxyde de nickel (NiO$_x$) individuelles.

Le MoO$_x$ est un semi-conducteur de type n dont les propriétés dépendent fortement de la concentration en oxygène (stœchiométrie). Des films de MoO$_x$ de différentes stœchiométries ont été préparés par pulvérisation cathodique à température ambiante. Il a été démontré que les propriétés du MoO$_x$ peuvent être contrôlées avec précision en ajustant la concentration d'oxygène pendant le dépôt. La **Figure** 7.14 montre l'évolution de stœchiométrie du MoO$_x$ en fonction du flux d'oxygène utilisé pour le dépôt. En utilisant des analyses XPS, nous avons pu déterminer l'évolution de la stœchiométrie en fonction du débit d'oxygène utilisé pendant le dépôt (**Figure** 7.15).

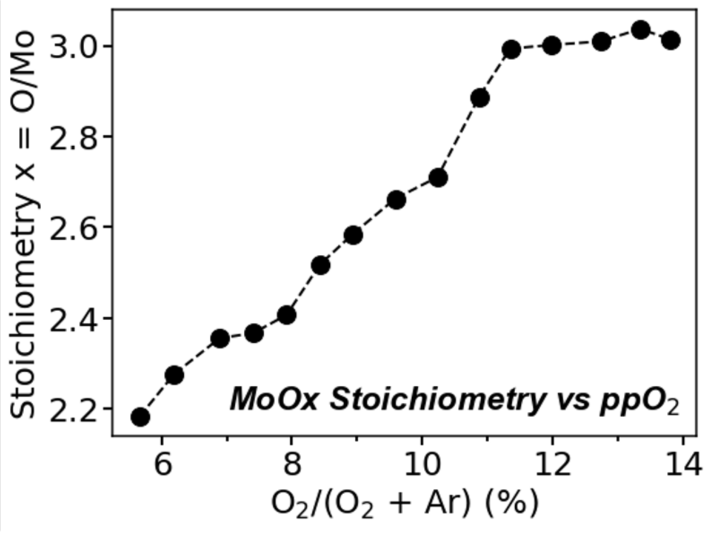

Figure 7.14: Évolution de la stœchiométrie du MoO$_x$ en fonction de la pression partielle d'oxygène, calculée à partir des spectres XPS Mo 3d et O 1s normalisés avec les composantes effectives correspondantes. RSF (facteurs de sensibilité relative), x = rapport O/Mo.

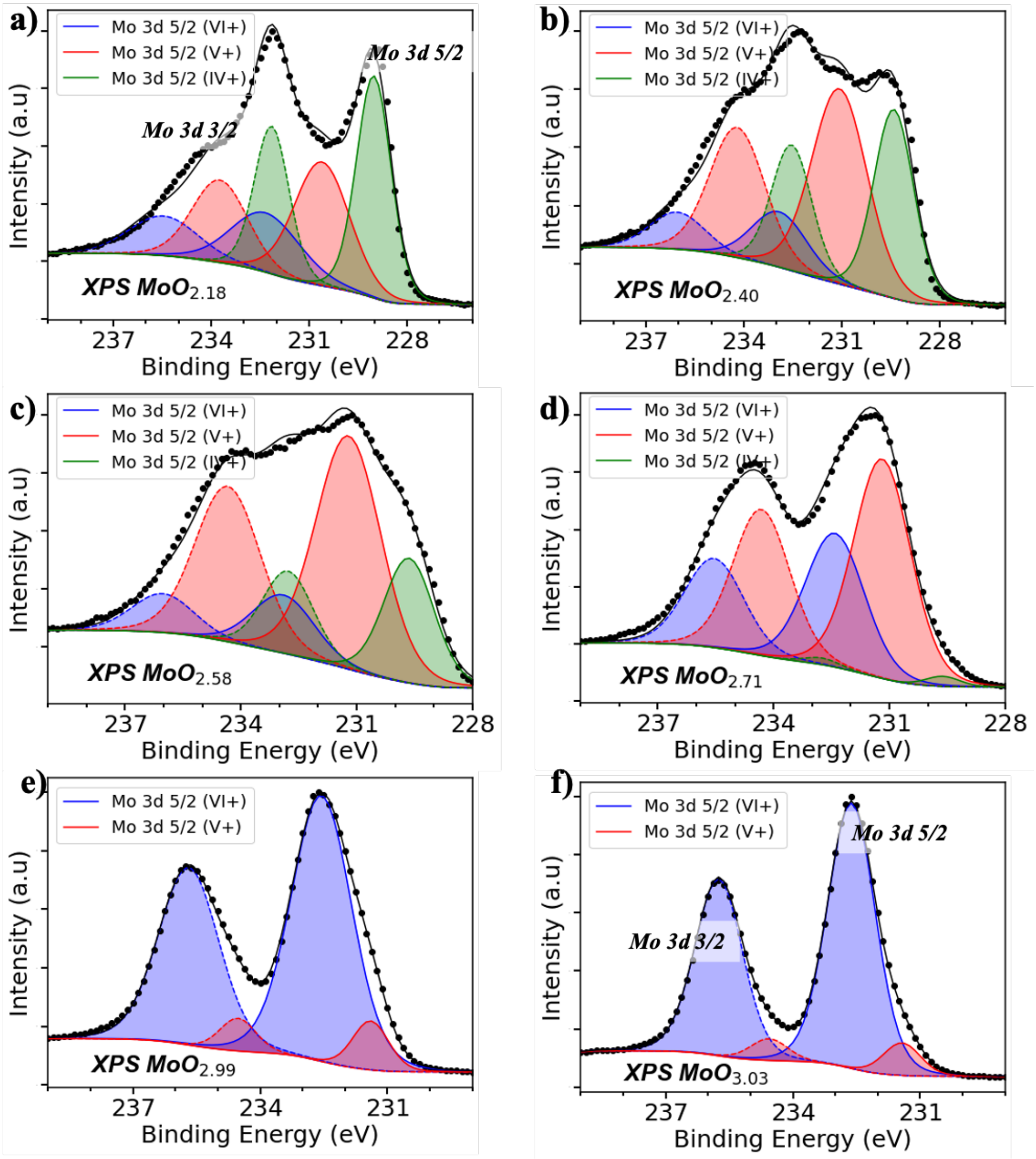

Figure 7.15: Spectre XPS haute résolution du Mo 3d à différentes concentrations d?oxygènes, ajusté avec les espèces chimiques de Mo^{6+}, Mo^{5+} and Mo^{4+}.

En utilisant la technique des quatre pointes de van der Pauw, nous avons montré que la résistivité du MoO_x dépend fortement de la concentration en vacance d'oxygène et varie de plus de 7 ordres de grandeur entre le $MoO_{2.18}$ et le MoO_3 (**Figure** 7.16**a**). Les films de MoO_x à faible stœchiométrie sont intrinsèquement semi-métalliques, avec une densité de porteurs libres pouvant atteindre 10^{21} cm^{-3}pour le $MoO_{2.18}$. Les mobilités électriques, mesurables uniquement pour une stœchiométrie $x < 2.8$, sont très faibles et varient entre 3×10^{-2} - 2 $cm^2.V^{-1}.s^{-1}$ pour $2.18 < x < 3$ (**Figure** 7.16**b**).

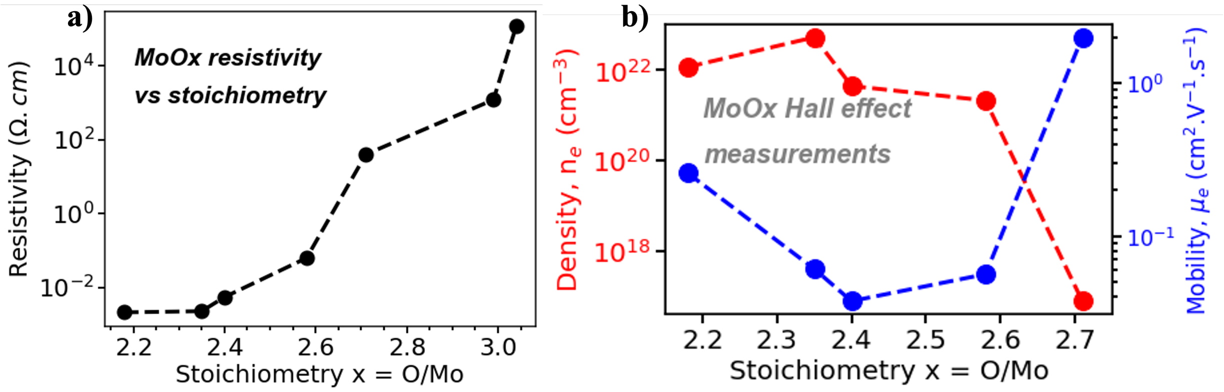

Figure 7.16: Propriétés électriques du MoO_x avec différentes ppO_2 (stœchiométrie), **a)** résistivité électrique, **b)** densité des porteurs libres et mobilité des électrons en fonction de la stœchiométrie du MoO_x.

Pour des films de 15 nm d'épaisseur avec une stœchiométrie $x < 2.8$, les mesures de transmission optique ont montré que la transmission du MoO_x dans l'IR est inférieure à 80 %. Cette faible stœchiométrie est associée à une densité relativement élevée de porteurs de charge libres (due aux lacunes d'oxygène). En revanche, pour les stœchiométries $x > 2.8$ eV est supérieure à 80 % (**Figure** 7.17**a**). Les mesures optiques ont également montré que la largeur de la bande interdite optique augmente lorsque la stœchiométrie x augmente (**Figure** 7.17**b**).

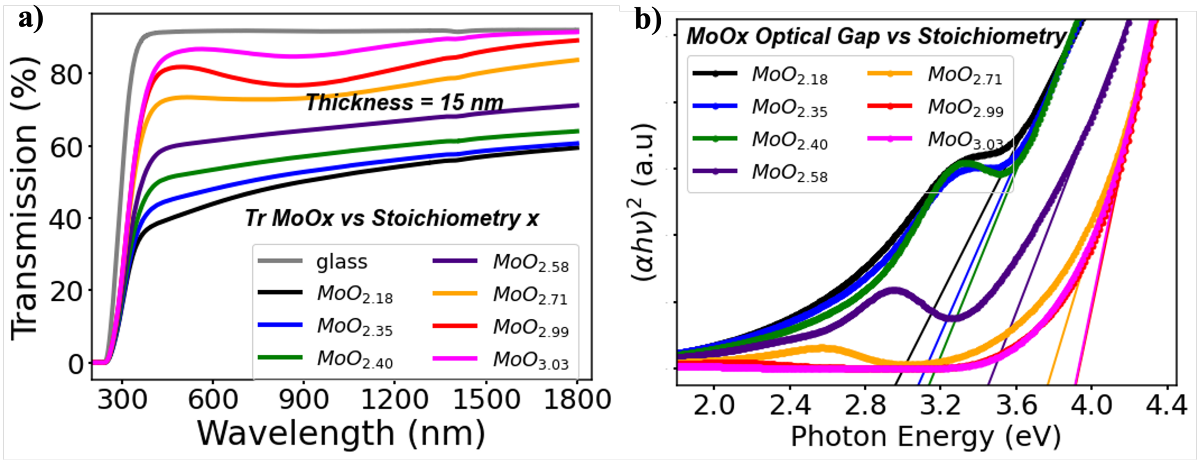

Figure 7.17: **a)** Spectre de transmission optique par mesures de transmission du MoO_x en fonction de la stœchiométrie des films (pression partielle d'oxygène), **b)**Tracé de Tauc montrant l'évolution de la largeur de la bande interdite optique du MoO_x en fonction de la stœchiométrie.

La mesure de la fonction de travail à l'aide de l'UPS est limitée aux films ayant une résistivité relativement faible, pour les films presque stœchiométriques, la mesure de la fonction de travail devient difficile en raison des effets de charge. Cette difficulté a été attribuée principalement aux limitations du spectromètre dont nous disposons. D'autre part, les mesures de la fonction de travail par analyse CV ont montré des résultats étonnamment intéressants. Les courbes C-V à la stœchiométrie la plus faible ($x = 2.18$) et à la stœchiométrie la plus élevée ($x = 3.03$) sont présentées sur les **Figure** 7.18**a** et 7.18**b** pour $t_{OX} = 10$ nm, aux fréquences les plus élevées et les plus basses (100 Hz et 100 kHz). La **Figure** 7.18**c** montre l'épaisseur d'oxyde équivalente EOT extraite de la valeur maximale de capacité dans la région d'accumulation en fonction de l'épaisseur d'oxyde t_{OX} (valeurs d'éllipsométrie). Nous observons que les différents films MoO_x se comportent comme des grilles métalliques (conducteurs électriques). En effet, une légère augmentation de l'EOT est observée lorsque la stœchiométrie des films de MoO_x augmente. Cependant, cette augmentation est presque négligeable et ne peut être attribuée à la nature diélectrique des films MoO_x. D'autre part, cette légère augmentation de l'EOT peut être liée aux effets du processus de pulvérisation sur le SiO_2. Par exemple, lorsque la concentration d'oxygène dans l'atmosphère de dépôt est augmentée, il y a une diminution de l'espèce de pulvérisation (Ar^+), qui peut avoir plus ou moins d'effet sur le substrat SiO_2. Les potentiels de bande plate V_{fb} en fonction de l'EOT extraits des analyses C-V sont présentés dans la **Figure** 7.18**c**. Une simple régression linéaire est utilisée pour extraire le potentiel de bande plate V_{fb0} à EOT = 0, qui est alors indépendant des charges d'oxyde et des Dits et directement lié à la fonction de travail de la grille MoO_x(**Figure** 7.18**d**).

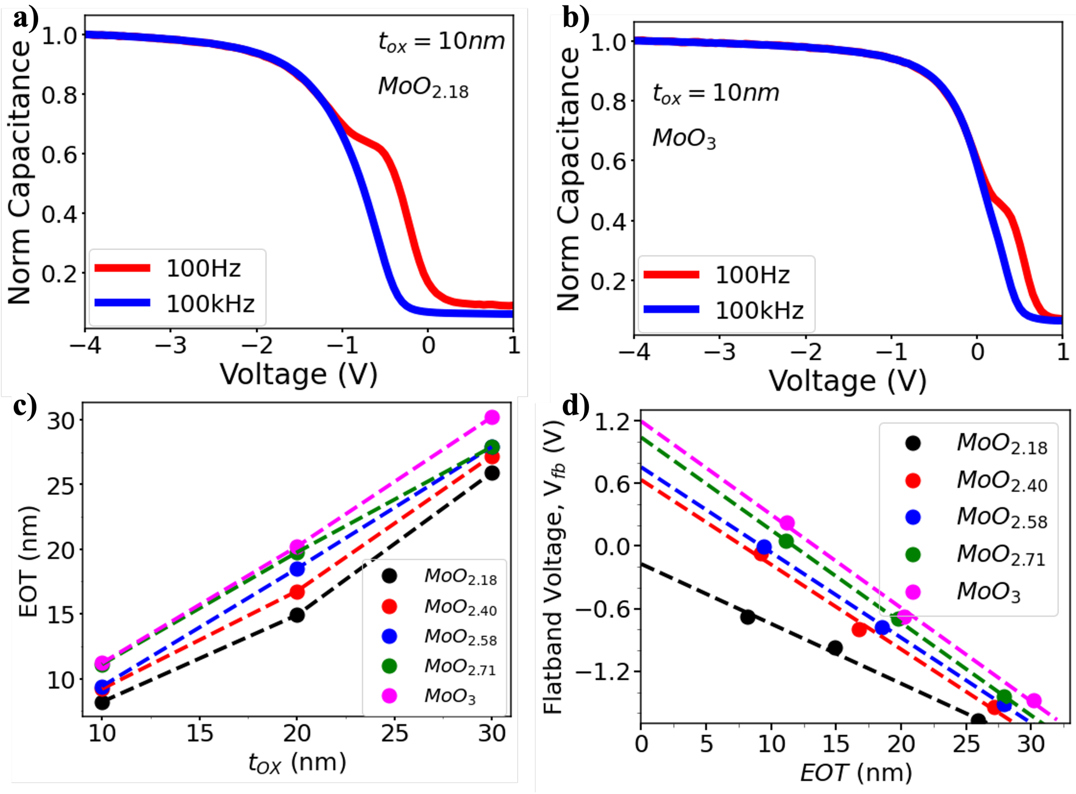

Figure 7.18: **a)-b)** Courbes C-V normalisée par la capacité maximale de l'empilement $Al/MoO_{2.18}/SiO_2/Si$ et $Al/MoO_3/SiO2/Si$, t_{OX} = 10 nm aux fréquences de mesure 100 Hz et 100 kHz, **c)** Relation entre l'épaisseur d'oxyde équivalente EOT et d'oxyde t_{OX} pour des mesures à C-V de 100 Hz. **d)** Relation entre le potentiel de bande plate V_{fb} et l'EOT pour les films de MoO_x avec différentes stœchiométries, les points sont ajustées par la méthode de régression linéaire.

On a observé une augmentation du travail de sortie avec l'augmentation de la stœchiométrie et, un travail de sortie $\phi > 6$ eV est obtenu pour des films presque stœchiométriques (**Figure** 7.19), résultat qui est en très bon accord avec la littérature (mesures UPS).

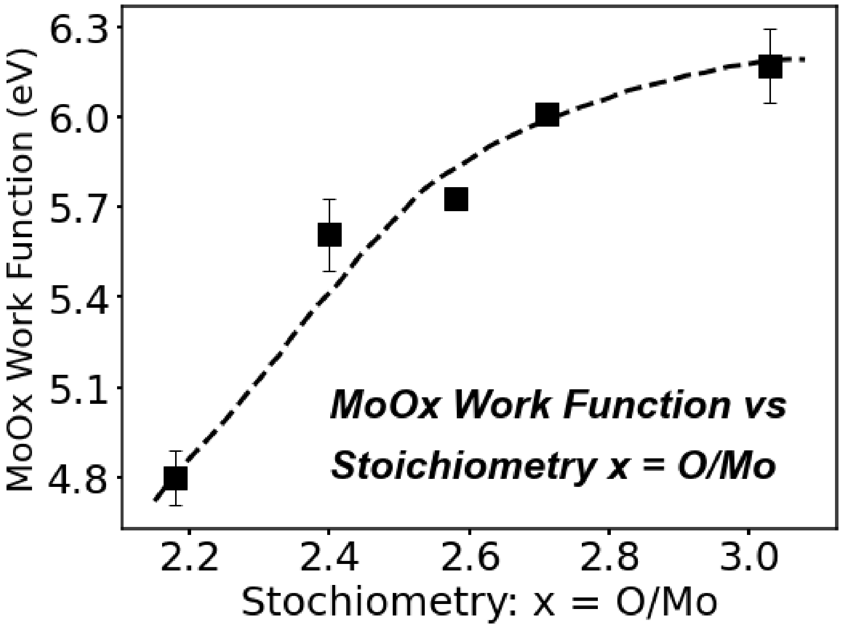

Figure 7.19: Evolution du travail de sortie du MoOx en fonction de la stœchiométrie.

Des études similaires à celles sur le MoO$_x$ ont été réalisées sur le NiO$_x$. Contrairement au MoO$_x$, le NiO$_x$ est généralement un semi-conducteur de type p avec une large bande interdite. Nous avons préparé des films de NiO$_x$ à partir d'une cible de NiO non métallique à température ambiante avec différentes concentrations d'oxygène. La caractérisation XPS nous a permis d'analyser la composition de ces différents films (**Figure** 7.20)

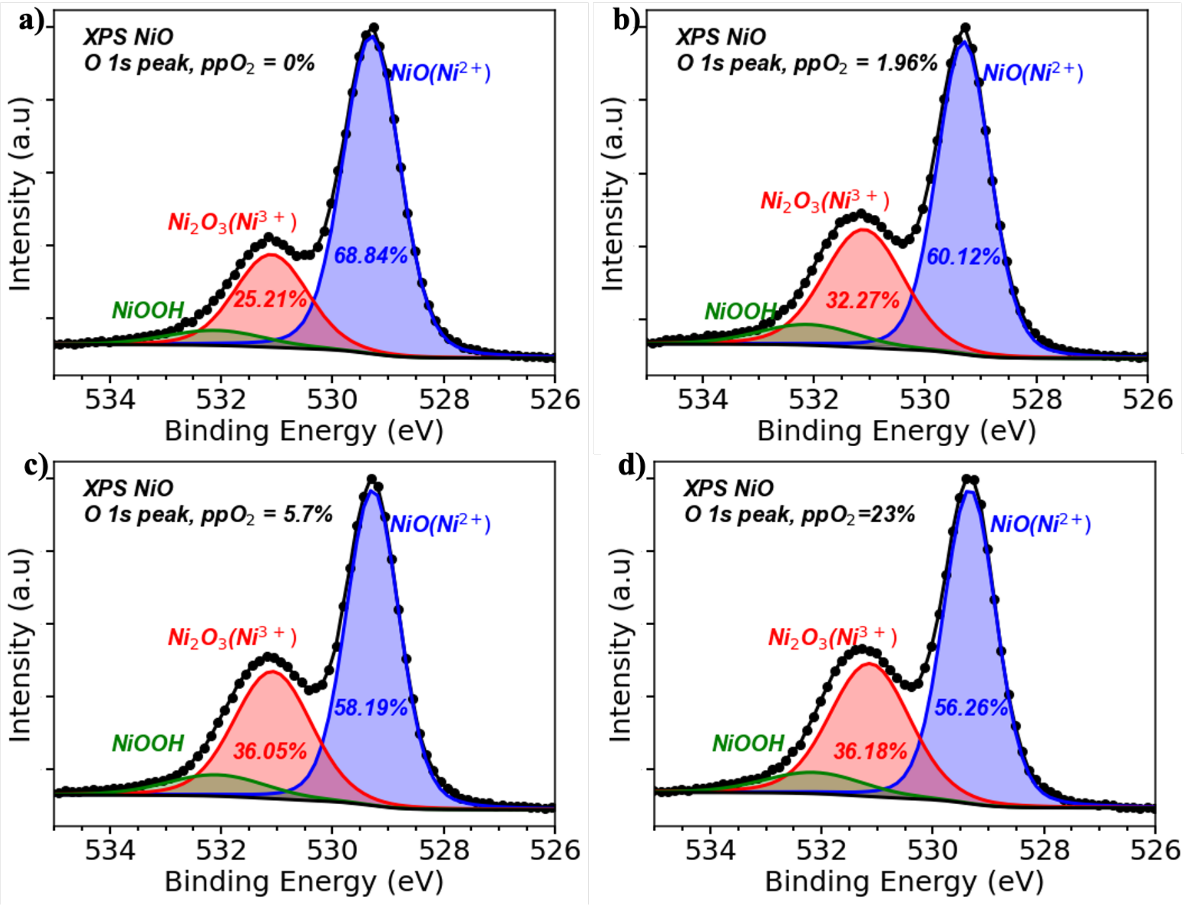

Figure 7.20: Analyse de la composition du NiO_x, spectres XPS O 1s ajustés en fonction de la composante NiO (Ni^{2+}), celle des oxygène interstitiels ou défauts d'oxygène Ni_2O_3 (Ni^{3+}), et concentrations de groupe lié à l'hydroxyde NiOOH faiblement lié.

Lorsque la concentration en oxygène augmente, une augmentation du rapport Ni^{3+}/Ni^{2+} est observée, ce qui se traduit par une augmentation des défauts Ni^{3+} et l'occupation des sites interstitiels par des atomes d'oxygène (défauts d'oxygène). Ces défauts sont supposés jouer le rôle d'accepteurs d'électrons. En effet, les mesures de Hall ont confirmé la nature de type-p des films de NiO_x, en raison des résistivités relativement élevées, les mesures d'effet Hall n'ont pas été réalisable pour toutes les concentrations d'oxygène. Pour les concentrations d'oxygène les plus élevées, on a obtenu une densité de porteurs libres (trous) de l'ordre de 10^{17} cm^{-3} et les mobilités électriques de l'ordre $1 - 10^2$ $cm^2.V^{-1}.s^{-1}$. En utilisant la méthode van der Pauw à quatre pointes, une diminution de la résistivité entre 25.7 - 0.7 Ω.cm a été observée lorsque le rapport des débits de gaz Ar et O_2, Ar:O_2 (en sccm) variait entre 0:50 et 15:50 (**Figure** 7.21**a**). Les mesures de résistivité électrique ont également monté que le NiO_x, comme d'autres oxydes des métaux de transitions est instable à l'atmosphère ambiante. On a observé une augmentation de la résistivité avec le temps d?exposition à l'air (**Figure** 7.21**b**).

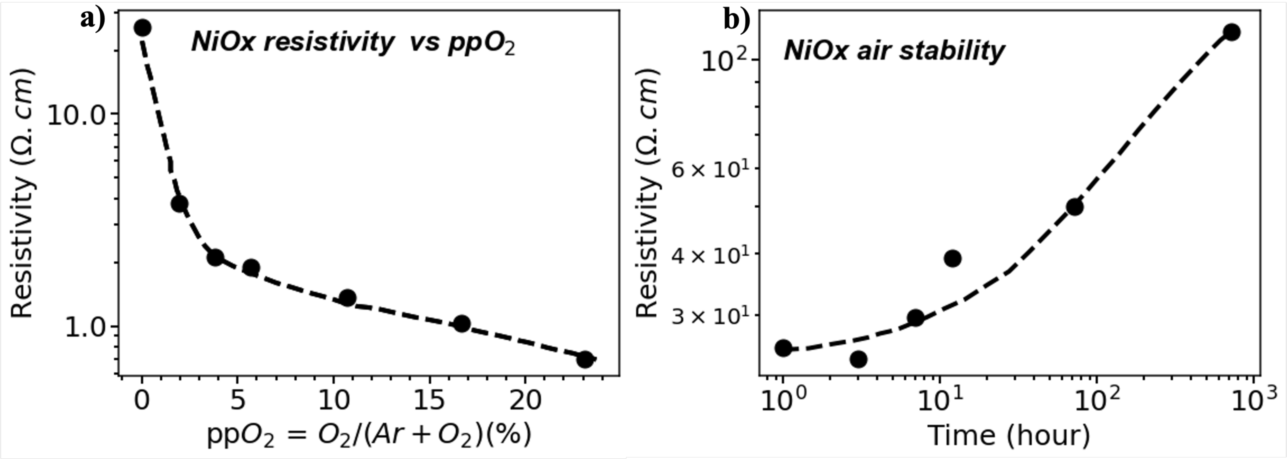

Figure 7.21: **a)**Résistivité électrique du NiO$_x$ en fonction de la pression partielle d'oxygène, **b)** Stabilité du NiOx dans l'air, évolution de la résistivité électrique dans le temps (résistivité mesurée à température ambiante T = 25°C.)

Les films de NiO$_x$ déposés à température ambiante sont polycristallins et ont une taille de grain d'environ 11 nm (**Figure** 7.22**a**). Les mesures de XRD ont montré que lorsque le nombre d'atomes d'oxygène dans les sites interstitiels augmente avec la concentration d'oxygène, ce qui conduit à des contraintes de traction dans les films de NiOx, décalage de la position du pic (200) avec la concentration d'oxygène (**Figure** 7.22**b**). Ces sites interstitiels entraînent également une augmentation de la densité volumique des films. Comme pour la plupart des oxydes de métaux de transition, nous avons constaté que le NiO$_x$ est instable et que sa résistivité augmente avec la durée d'exposition à l'atmosphère ambiante. Tout comme avec avec des films de MoO$_x$ presque stœchiométriques, mesures précises du travail de sortie effectuée par UPS n'ont pas été possibles en raison de la résistivité relativement élevée des couches de NiO$_x$.

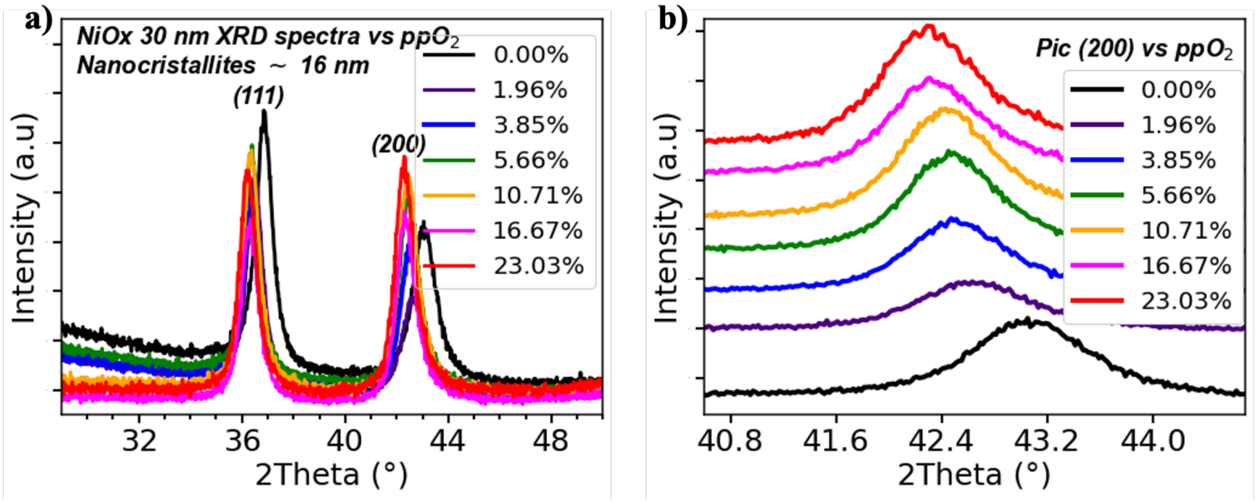

Figure 7.22: **a)** Diagrammes de diffraction de rayons -x à angle d'incidence rasant de NiO$_x$ en fonction de la pression partielle d'oxygène, les caractéristiques sont étiquetées avec les réflexions (hkl) correspondantes de la phase cubique de NiO$_x$, **b)** Vue élargie de la région du pic (200) montrant le déplacement vers des angles de Bragg plus faibles.

Ces matériaux (NiOx et MoOx) ont ensuite été utilisés comme couche d'extraction de trous sur des photodiodes à base de PbS QDs.
Nous avons enfin intégré des TCO à base d'In$_2$O$_3$ ainsi que des HTL MoOx et NiOx afin de

fabriquer des structures de photodiode. Pour les photodiodes à base de PbS QDs, nous avons adopté un processus de fabrication simplifié. Nous avons constaté que les propriétés des films H-ITO n'ont qu'un effet limité sur les performances des dispositifs. Aucun changement significatif de l'efficacité quantique externe (EQE) n'a été observé en modifiant la transmission optique, la résistivité électrique des films ou la puissance du générateur de plasma utilisé pour la pulvérisation de H-ITO (puissance de dépôt). Les études ont montré que les principaux efforts d'optimisation doivent porter non seulement sur l'interface HEL/PbS QDs, mais aussi sur la stabilité ou la qualité de la surface du film de PbS QDs. En effet, la préservation de la surface du film de QDs PbS a été l'un des principaux défis de ce travail. Il est également important de privilégier les cibles non métalliques, car le dépôt dans une atmosphère réactive et oxydante peut également entraîner une dégradation du film de PbS QDs. Avec des films de PbS QDs dont la surface est oxydée, nous avons obtenu des photodiodes aux performances médiocres, telles qu'une EQE plus faible par rapport à la référence, nous avons également obtenu des caractéristiques J-V en forme de "S", indiquant des difficultés d'extraction de charges (trous), avec des tensions de fonctionnement bien supérieures à -0,5 V. L'utilisation de NiOx HTL déposé à partir d'une cible de NiO nous a permis d'obtenir des photodiodes avec des propriétés très intéressantes.

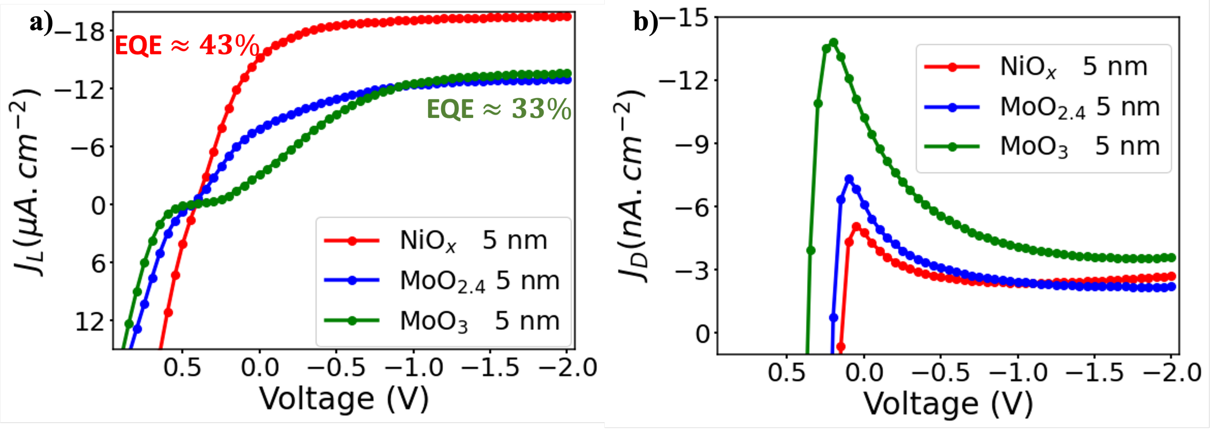

Figure 7.23: Comparaison entre les couches d'extraction de trous en NiOx et en MoOx , **a)** Caractéristiques courant-tension sous illumination, et **b** Courants d'obscurité.

La **Figure** 7.23 **a** et 7.23 **b** montrent les comparaisons entre le MoOx et l'optimum en NiOx. On note une très bonne valeur du rendement de conversion, EQE ≈ 43 % pour l'épaisseur optimale du film de NiOx (5 nm), une tension de fonctionnement de ≈ -0.4 V et un courant d'obscurité ultra-faible de 3 nA.cm^{-2}.

La construction des diagrammes de bandes d'énergies a montré qu'on était plus proche de la configuration de bande idéale avec l'HTL en NiOx que le MoOx. Avec les films de MoOx, les niveaux de défauts dans le gap du MoOx doivent jouer un rôle important dans le mécanisme d'extraction des trous.

Bibliography

[1] Xingtian Yin, Cong Zhang, Yuxiao Guo, Yawei Yang, Yonglei Xing, and Wenxiu Que. PbS QD-based photodetectors: future-oriented near-infrared detection technology. *Journal of Materials Chemistry C*, 9(2):417–438, 2021. ISSN 2050-7526, 2050-7534. doi: 10.1039/D0TC04612D. URL `http://xlink.rsc.org/?DOI=D0TC04612D`.

[2] Mark Hopkinson, Trevor Martin, and Peter Smowton. III–V semiconductor devices integrated with silicon. *Semiconductor Science and Technology*, 28(9):090301, September 2013. ISSN 0268-1242. doi: 10.1088/0268-1242/28/9/090301. URL `https://dx.doi.org/10.1088/0268-1242/28/9/090301`.

[3] Rinku Saran and Richard J. Curry. Lead sulphide nanocrystal photodetector technologies. *Nature Photonics*, 10(2):81–92, February 2016. ISSN 1749-4893. doi: 10.1038/nphoton.2015.280. URL `https://www.nature.com/articles/nphoton.2015.280`.

[4] Lorenzo Colace and Gaetano Assanto. Germanium on Silicon for Near-Infrared Light Sensing. *IEEE Photonics Journal*, 1(2):69–79, August 2009. ISSN 1943-0655. doi: 10.1109/JPHOT.2009.2025516. URL `https://ieeexplore.ieee.org/document/5075653`. Conference Name: IEEE Photonics Journal.

[5] Haiyan Wang, Yu Sun, Jin Chen, Fengchao Wang, Ruiyi Han, Canyun Zhang, Jinfang Kong, Lan Li, and Jing Yang. A Review of Perovskite-Based Photodetectors and Their Applications. *Nanomaterials*, 12(24):4390, December 2022. ISSN 2079-4991. doi: 10.3390/nano12244390. URL `https://www.ncbi.nlm.nih.gov/pmc/articles/PMC9784743/`.

[6] J. S. Steckel, E. Josse, A. G. Pattantyus-Abraham, M. Bidaud, B. Mortini, H. Bilgen, O. Arnaud, S. Allegret-Maret, F. Saguin, L. Mazet, S. Lhostis, T. Berger, K. Haxaire, L. L. Chapelon, L. Parmigiani, P. Gouraud, M. Brihoum, P. Bar, M. Guillermet, S. Favreau, R. Duru, J. Fantuz, S. Ricq, D. Ney, I. Hammad, D. Roy, A. Arnaud, B. Vianne, G. Nayak, N. Virollet, V. Farys, P. Malinge, A. Tournier, F. Lalanne, A. Crocherie, J. Galvier, S. Rabary, O. Noblanc, H. Wehbe-Alause, S. Acharya, A. Singh, J. Meitzner, D. Aher, H. Yang, J. Romero, B. Chen, C. Hsu, K. C. Cheng, Y. Chang, M. Sarmiento, C. Grange, E. Mazaleyrat, and K. Rochereau. $1.62\mu \mathrmm$ Global Shutter Quantum Dot Image Sensor Optimized for Near and Shortwave Infrared. In *2021 IEEE International Electron Devices Meeting (IEDM)*, pages 23.4.1–23.4.4, December 2021. doi: 10.1109/IEDM19574.2021.9720560. ISSN: 2156-017X.

[7] Jonathan S. Steckel, Andras G. Pattantyus-Abraham, Emmanuel Josse, Eric Mazaleyrat, and Krysten Rochereau. 66-1: High Resolution Quantum Dot Global Shutter Imagers. *SID Symposium Digest of Technical Papers*, 52(1):975–977, 2021. ISSN 2168-0159. doi: 10.1002/sdtp.14852. URL `https://onlinelibrary.wiley.com/doi/abs/10.1002/sdtp.14852`. _eprint: https://onlinelibrary.wiley.com/doi/pdf/10.1002/sdtp.14852.

[8] Ni Zhao, Tim P. Osedach, Liang-Yi Chang, Scott M. Geyer, Darcy Wanger, Maddalena T. Binda, Alexi C. Arango, Moungi G. Bawendi, and Vladimir Bulovic. Colloidal PbS

Quantum Dot Solar Cells with High Fill Factor. *ACS Nano*, 4(7):3743–3752, July 2010. ISSN 1936-0851. doi: 10.1021/nn100129j. URL https://doi.org/10.1021/nn100129j. Publisher: American Chemical Society.

[9] Xin Tong, Jiang Wu, and Zhiming M. Wang, editors. *Quantum Dot Photodetectors*, volume 30 of *Lecture Notes in Nanoscale Science and Technology*. Springer International Publishing, Cham, 2021. ISBN 978-3-030-74269-0 978-3-030-74270-6. doi: 10.1007/978-3-030-74270-6. URL https://link.springer.com/10.1007/978-3-030-74270-6.

[10] Deep Chandra Upadhyay, Rishibrind Kumar Upadhyay, Abhinav Pratap Singh, and Satyabrata Jit. High-Performance Inverted Structure Broadband Photodetector Based on ZnO Nanorods/PCDTBT:PCBM:PbS QDs. *IEEE Transactions on Electron Devices*, 67(11): 4970–4976, November 2020. ISSN 0018-9383, 1557-9646. doi: 10.1109/TED.2020.3026984. URL https://ieeexplore.ieee.org/document/9217479/.

[11] Jianbo Gao, Craig L. Perkins, Joseph M. Luther, Mark C. Hanna, Hsiang-Yu Chen, Octavi E. Semonin, Arthur J. Nozik, Randy J. Ellingson, and Matthew C. Beard. n-Type Transition Metal Oxide as a Hole Extraction Layer in PbS Quantum Dot Solar Cells. *Nano Letters*, 11(8):3263–3266, August 2011. ISSN 1530-6984. doi: 10.1021/nl2015729. URL https://doi.org/10.1021/nl2015729. Publisher: American Chemical Society.

[12] Stefan Franzen. Surface Plasmon Polaritons and Screened Plasma Absorption in Indium Tin Oxide Compared to Silver and Gold. *The Journal of Physical Chemistry C*, 112 (15):6027–6032, April 2008. ISSN 1932-7447. doi: 10.1021/jp7097813. URL https://doi.org/10.1021/jp7097813. Publisher: American Chemical Society.

[13] Louis Jacques Mandé Daguerre and François Arago. *Historique et description des procédés du daguerréotype et du diorama*. Susse frères, éditeurs, 1839. Google-Books-ID: Ae4TAAAAQAAJ.

[14] François Arago. *Rapport de M. Arago sur le daguerréotype, lu à la séance de la Chambre des députés le 3 juillet 1839 et à l'Académie des sciences, séance du 19 août*. Bachelier, 1839. Google-Books-ID: ZiTrAAAAMAAJ.

[15] Edmond Becquerel. Comptes rendus hebdomadaires des séances de l'Académie des sciences / publiés... par MM. les secrétaires perpétuels, January 1848. URL https://gallica.bnf.fr/ark:/12148/bpt6k2983p.

[16] James Clerk Maxwell. Experiments on Colour, as perceived by the Eye, with Remarks on Colour-Blindness. *Earth and Environmental Science Transactions of The Royal Society of Edinburgh*, 21(2):275–298, March 1857. ISSN 2053-5945, 0080-4568. doi: 10.1017/S0080456800032117. URL https://www.cambridge.org/core/journals. Publisher: Royal Society of Edinburgh Scotland Foundation.

[17] Auguste Lumiere and Louis Lumiere. Les Autochromes - Brevet français n° 315.224, June 1903. URL https://www.institut-lumiere.org/musee/les-freres-lumiere-et-leurs-inventions/autochromes.html.

[18] Leopold D. Mannes and Jr Leopold Godowsky. Color photography, November 1936. URL https://patents.google.com/patent/US2059884A/en.

[19] R. A. Kirsch, L. Cahn, C. Ray, and G. H. Urban. Experiments in processing pictorial information with a digital computer. In *Papers and discussions presented at the December 9-13, 1957, eastern joint computer conference: Computers with deadlines to meet*, IRE-ACM-AIEE '57 (Eastern), pages 221–229, New York, NY, USA, December 1957. Association

for Computing Machinery. ISBN 978-1-4503-7862-8. doi: 10.1145/1457720.1457763. URL https://dl.acm.org/doi/10.1145/1457720.1457763.

[20] W. S. Boyle and G. E. Smith. Charge Coupled Semiconductor Devices. *Bell System Technical Journal*, 49(4):587–593, 1970. ISSN 1538-7305. doi: 10.1002/j.1538-7305.1970.tb01790.x. URL https://onlinelibrary.wiley.com/doi/abs/10.1002/j.1538-7305.1970.tb01790.x. _eprint: https://onlinelibrary.wiley.com/doi/pdf/10.1002/j.1538-7305.1970.tb01790.x.

[21] Gareth A. Lloyd and Steven J. Sasson. Electronic still camera, December 1978. URL https://patents.google.com/patent/US4131919A/en.

[22] Mohamed M. Atalla and Dawon Kahng. The mos transistor – the enabling technology of the future. *Proceedings of the IEEE*, 49(5):665–686, 1960.

[23] E.R. Fossum. CMOS image sensors: electronic camera-on-a-chip. *IEEE Transactions on Electron Devices*, 44(10):1689–1698, October 1997. ISSN 00189383. doi: 10.1109/16.628824. URL http://ieeexplore.ieee.org/document/628824/.

[24] Christopher N. LaFratta, John T. Fourkas, Tommaso Baldacchini, and Richard A. Farrer. Multiphoton Fabrication. *Angewandte Chemie International Edition*, 46(33):6238–6258, 2007. ISSN 1521-3773. doi: 10.1002/anie.200603995. URL https://onlinelibrary.wiley.com/doi/abs/10.1002/anie.200603995. _eprint: https://onlinelibrary.wiley.com/doi/pdf/10.1002/anie.200603995.

[25] Manijeh Razeghi, editor. *Fundamentals of Solid State Engineering*. Springer, 2012.

[26] Antoni Rogalski. Infrared detectors: status and trends. *Progress in Quantum Electronics*, 37(3):152–236, 2013.

[27] Antoni Rogalski. *Infrared Detectors*. CRC Press, 2011.

[28] Maria Hadjipanayi and Anthony J. Bell. Quantum-dot infrared photodetectors: advances and applications. *Journal of Nanophotonics*, 8(1):083083, 2014.

[29] F. Pelayo García de Arquer, Dmitri V. Talapin, Victor I. Klimov, Yasuhiko Arakawa, Manfred Bayer, and Edward H. Sargent. Semiconductor quantum dots: Technological progress and future challenges. *Science*, 373(6555):eaaz8541, August 2021. doi: 10.1126/science.aaz8541. URL https://www.science.org/doi/full/10.1126/science.aaz8541. Publisher: American Association for the Advancement of Science.

[30] Prashant Nagpal and Victor I. Klimov. Role of mid-gap states in charge transport and photoconductivity in semiconductor nanocrystal films. *Nature Communications*, 2:486, September 2011. ISSN 2041-1723. doi: 10.1038/ncomms1492.

[31] Sangyeon Pak, Yuljae Cho, John Hong, Juwon Lee, Sanghyo Lee, Bo Hou, Geon-Hyoung An, Young-Woo Lee, Jae Eun Jang, Hyunsik Im, Stephen M. Morris, Jung Inn Sohn, SeungNam Cha, and Jong Min Kim. Consecutive Junction-Induced Efficient Charge Separation Mechanisms for High-Performance MoS2/Quantum Dot Phototransistors. *ACS Applied Materials & Interfaces*, 10(44):38264–38271, November 2018. ISSN 1944-8244. doi: 10.1021/acsami.8b14408. URL https://doi.org/10.1021/acsami.8b14408. Publisher: American Chemical Society.

[32] Vlad Sukhovatkin, Sean Hinds, Lukasz Brzozowski, and Edward H. Sargent. Colloidal Quantum-Dot Photodetectors Exploiting Multiexciton Generation. *Science*, 324(5934): 1542–1544, June 2009. doi: 10.1126/science.1173812. URL https://www.science.org/

doi/10.1126/science.1173812. Publisher: American Association for the Advancement of Science.

[33] Octavi E. Semonin, Joseph M. Luther, Sukgeun Choi, Hsiang-Yu Chen, Jianbo Gao, Arthur J. Nozik, and Matthew C. Beard. Peak External Photocurrent Quantum Efficiency Exceeding 100% via MEG in a Quantum Dot Solar Cell. *Science*, 334(6062):1530–1533, December 2011. ISSN 0036-8075, 1095-9203. doi: 10.1126/science.1209845. URL https://science.sciencemag.org/content/334/6062/1530. Publisher: American Association for the Advancement of Science Section: Report.

[34] R. Clark Jones. Phenomenological Description of the Response and Detecting Ability of Radiation Detectors. *Proceedings of the IRE*, 47(9):1495–1502, September 1959. ISSN 2162-6634. doi: 10.1109/JRPROC.1959.287047. Conference Name: Proceedings of the IRE.

[35] Jianguang Jia, Lianjun Jia, Liangliang Wang, Yuan Lin, and Xiaowen Zhou. Enhanced film quality of PbS QD solid by Eliminating the oxide traps through an in-situ surface etching and passivation. *Dalton Transactions*, December 2022. ISSN 1477-9234. doi: 10.1039/D2DT03238D. URL https://pubs.rsc.org/en/content/articlelanding/2023/dt/d2dt03238d. Publisher: The Royal Society of Chemistry.

[36] Byung-Ryool Hyun, A. C. Bartnik, Liangfeng Sun, Tobias Hanrath, and F. W. Wise. Control of Electron Transfer from Lead-Salt Nanocrystals to TiO2. *Nano Letters*, 11(5): 2126–2132, May 2011. ISSN 1530-6984. doi: 10.1021/nl200718w. URL https://doi.org/10.1021/nl200718w. Publisher: American Chemical Society.

[37] Chia-Hao M. Chuang, Patrick R. Brown, Vladimir Bulović, and Moungi G. Bawendi. Improved performance and stability in quantum dot solar cells through band alignment engineering. *Nature Materials*, 13(8):796–801, August 2014. ISSN 1476-1122. doi: 10.1038/nmat3984.

[38] Min-Jae Choi, Jihun Oh, Jung-Keun Yoo, Jaesuk Choi, Dong Min Sim, and Yeon Sik Jung. Tailoring of the PbS/metal interface in colloidal quantum dot solar cells for improvements of performance and air stability. *Energy & Environmental Science*, 7(9):3052, June 2014. ISSN 1754-5692, 1754-5706. doi: 10.1039/C4EE00502C. URL http://xlink.rsc.org/?DOI=C4EE00502C.

[39] Patrick R. Brown, Richard R. Lunt, Ni Zhao, Timothy P. Osedach, Darcy D. Wanger, Liang-Yi Chang, Moungi G. Bawendi, and Vladimir Bulović. Improved Current Extraction from ZnO/PbS Quantum Dot Heterojunction Photovoltaics Using a MoO3 Interfacial Layer. *Nano Letters*, 11(7):2955–2961, July 2011. ISSN 1530-6984. doi: 10.1021/nl201472u. URL https://doi.org/10.1021/nl201472u. Publisher: American Chemical Society.

[40] Epimitheas Georgitzikis, Pawel E. Malinowski, Yunlong Li, Jorick Maes, Luis Moreno Hagelsieb, Stefano Guerrieri, Zeger Hens, Paul Heremans, and David Cheyns. Integration of PbS Quantum Dot Photodiodes on Silicon for NIR Imaging. *IEEE Sensors Journal*, 20 (13):6841–6848, July 2020. ISSN 1558-1748. doi: 10.1109/JSEN.2019.2933741. Conference Name: IEEE Sensors Journal.

[41] Chien-Sing Poon, Benjamin Rinehart, Dharminder S. Langri, Timothy M. Rambo, Aaron J. Miller, Brandon Foreman, and Ulas Sunar. Noninvasive Optical Monitoring of Cerebral Blood Flow and EEG Spectral Responses after Severe Traumatic Brain Injury: A Case Report. *Brain Sciences*, 11(8):1093, August 2021. ISSN 2076-3425. doi: 10.3390/brainsci11081093. URL https://www.mdpi.com/2076-3425/11/8/1093. Number: 8 Publisher: Multidisciplinary Digital Publishing Institute.

[42] Satoru Tsuchikawa, Te Ma, and Tetsuya Inagaki. Application of near-infrared spectroscopy to agriculture and forestry. *Analytical Sciences*, 38(4):635–642, April 2022. ISSN 1348-2246. doi: 10.1007/s44211-022-00106-6. URL `https://doi.org/10.1007/s44211-022-00106-6`.

[43] Geonwoo Kim, Hoonsoo Lee, Insuck Baek, Byoung-Kwan Cho, and Moon S. Kim. Short-Wave Infrared Hyperspectral Imaging System for Nondestructive Evaluation of Powdered Food. *Journal of Biosystems Engineering*, 47(2):223–232, June 2022. ISSN 2234-1862. doi: 10.1007/s42853-022-00141-1. URL `https://doi.org/10.1007/s42853-022-00141-1`.

[44] Qihao Weng. Thermal infrared remote sensing for urban climate and environmental studies: Methods, applications, and trends. *ISPRS Journal of Photogrammetry and Remote Sensing*, 64(4):335–344, July 2009. ISSN 0924-2716. doi: 10.1016/j.isprsjprs.2009.03.007. URL `https://www.sciencedirect.com/science/article/pii/S092427160900046X`.

[45] Muhammad Ali Farooq, Waseem Shariff, David O'callaghan, Arcangelo Merla, and Peter Corcoran. On the Role of Thermal Imaging in Automotive Applications: A Critical Review. *IEEE Access*, 11:25152–25173, 2023. ISSN 2169-3536. doi: 10.1109/ACCESS.2023.3255110. Conference Name: IEEE Access.

[46] Miloš S. Pavlović, Petar D. Milanović, Miloš S. Stanković, Dragana B. Perić, Ilija V. Popadić, and Miroslav V. Perić. Deep Learning Based SWIR Object Detection in Long-Range Surveillance Systems: An Automated Cross-Spectral Approach. *Sensors*, 22(7): 2562, January 2022. ISSN 1424-8220. doi: 10.3390/s22072562. URL `https://www.mdpi.com/1424-8220/22/7/2562`. Number: 7 Publisher: Multidisciplinary Digital Publishing Institute.

[47] A. Rogalski. Recent progress in infrared detector technologies. *Infrared Physics & Technology*, 54(3):136–154, May 2011. ISSN 1350-4495. doi: 10.1016/j.infrared.2010.12.003. URL `https://www.sciencedirect.com/science/article/pii/S1350449510001040`.

[48] Rubén Usamentiaga and Daniel Fernando García. Infrared Thermography Sensor for Temperature and Speed Measurement of Moving Material. *Sensors (Basel, Switzerland)*, 17(5):1157, May 2017. ISSN 1424-8220. doi: 10.3390/s17051157. URL `https://www.ncbi.nlm.nih.gov/pmc/articles/PMC5470903/`.

[49] Joseph A. Shaw and Paul W. Nugent. Physics principles in radiometric infrared imaging of clouds in the atmosphere. *European Journal of Physics*, 34(6):S111, October 2013. ISSN 0143-0807. doi: 10.1088/0143-0807/34/6/S111. URL `https://dx.doi.org/10.1088/0143-0807/34/6/S111`. Publisher: IOP Publishing.

[50] Elijah Thimsen, Bryce Sadtler, and Mikhail Y. Berezin. Shortwave-infrared (SWIR) emitters for biological imaging: a review of challenges and opportunities. *Nanophotonics*, 6(5): 1043–1054, September 2017. ISSN 2192-8614. doi: 10.1515/nanoph-2017-0039. URL `https://www.degruyter.com/document/doi/10.1515/nanoph-2017-0039/html`. Publisher: De Gruyter.

[51] Amin Morteza Najarian, Maral Vafaie, Andrew Johnston, Tong Zhu, Mingyang Wei, Makhsud I. Saidaminov, Yi Hou, Sjoerd Hoogland, F. Pelayo García de Arquer, and Edward H. Sargent. Sub-millimetre light detection and ranging using perovskites. *Nature Electronics*, pages 1–8, July 2022. ISSN 2520-1131. doi: 10.1038/s41928-022-00799-7. URL `https://www.nature.com/articles/s41928-022-00799-7`. Publisher: Nature Publishing Group.

[52] Vasanthi Sivaprakasam, Di Lin, Michael K. Yetzbacher, Heath E. Gemar, Joel M. Portier, and Abbie T. Watnik. Multi-spectral SWIR lidar for imaging and spectral discrimination through partial obscurations. *Optics Express*, 31(4):5443–5457, February 2023. ISSN 1094-4087. doi: 10.1364/OE.477499.

[53] Hiroshi Watanabe, Kohei SUGAHARA, and Takatoshi Kato. Optical sensor, September 2022. URL `https://patents.google.com/patent/US20220276405A1/en`.

[54] L. E. Brus. Electron-electron and electron-hole interactions in small semiconductor crystallites: The size dependence of the lowest excited electronic state. *Journal of Chemical Physics*, 80:4403–4409, May 1984. ISSN 0021-96060301-0104. doi: 10.1063/1.447218. URL `https://ui.adsabs.harvard.edu/abs/1984JChPh..80.4403B`. ADS Bibcode: 1984JChPh..80.4403B.

[55] Mark C. Weidman, Megan E. Beck, Rachel S. Hoffman, Ferry Prins, and William A. Tisdale. Monodisperse, Air-Stable PbS Nanocrystals via Precursor Stoichiometry Control. *ACS Nano*, 8(6):6363–6371, June 2014. ISSN 1936-0851. doi: 10.1021/nn5018654. URL `https://doi.org/10.1021/nn5018654`. Publisher: American Chemical Society.

[56] Carlo Giansante, Ivan Infante, Eduardo Fabiano, Roberto Grisorio, Gian Paolo Suranna, and Giuseppe Gigli. “Darker-than-Black” PbS Quantum Dots: Enhancing Optical Absorption of Colloidal Semiconductor Nanocrystals via Short Conjugated Ligands. *Journal of the American Chemical Society*, 137(5):1875–1886, February 2015. ISSN 0002-7863. doi: 10.1021/ja510739q. URL `https://doi.org/10.1021/ja510739q`. Publisher: American Chemical Society.

[57] Philippe Guyot-Sionnest. Electrical Transport in Colloidal Quantum Dot Films. *The Journal of Physical Chemistry Letters*, 3(9):1169–1175, May 2012. doi: 10.1021/jz300048y. URL `https://doi.org/10.1021/jz300048y`. Publisher: American Chemical Society.

[58] Dong Yu, Congjun Wang, and Philippe Guyot-Sionnest. n-Type conducting CdSe nanocrystal solids. *Science (New York, N.Y.)*, 300(5623):1277–1280, May 2003. ISSN 1095-9203. doi: 10.1126/science.1084424.

[59] Nevill Mott. *Metal-Insulator Transitions*. CRC Press, London, August 1990. ISBN 978-0-429-09488-0. doi: 10.1201/b12795.

[60] Ad Lagendijk, Bart van Tiggelen, and Diederik S. Wiersma. Fifty years of Anderson localization. *Physics Today*, 62(8):24–29, August 2009. ISSN 0031-9228. doi: 10.1063/1.3206091. URL `https://doi.org/10.1063/1.3206091`.

[61] Dmitri V. Talapin, Jong-Soo Lee, Maksym V. Kovalenko, and Elena V. Shevchenko. Prospects of Colloidal Nanocrystals for Electronic and Optoelectronic Applications. *Chemical Reviews*, 110(1):389–458, January 2010. ISSN 0009-2665, 1520-6890. doi: 10.1021/cr900137k. URL `https://pubs.acs.org/doi/10.1021/cr900137k`.

[62] Patrick R. Brown, Donghun Kim, Richard R. Lunt, Ni Zhao, Moungi G. Bawendi, Jeffrey C. Grossman, and Vladimir Bulović. Energy Level Modification in Lead Sulfide Quantum Dot Thin Films through Ligand Exchange. *ACS Nano*, 8(6):5863–5872, June 2014. ISSN 1936-0851, 1936-086X. doi: 10.1021/nn500897c. URL `https://pubs.acs.org/doi/10.1021/nn500897c`.

[63] Cherie R. Kagan and Christopher B. Murray. Charge transport in strongly coupled quantum dot solids. *Nature Nanotechnology*, 10(12):1013–1026, December 2015. ISSN 1748-3395. doi: 10.1038/nnano.2015.247. URL `https://www.nature.com/articles/nnano.2015.247`. Number: 12 Publisher: Nature Publishing Group.

[64] Danylo Zherebetskyy, Marcus Scheele, Yingjie Zhang, Noah Bronstein, Christopher Thompson, David Britt, Miquel Salmeron, Paul Alivisatos, and Lin-Wang Wang. Hydroxylation of the surface of PbS nanocrystals passivated with oleic acid. *Science*, 344(6190): 1380–1384, June 2014. ISSN 0036-8075, 1095-9203. doi: 10.1126/science.1252727. URL `https://www.science.org/doi/10.1126/science.1252727`.

[65] David Zhitomirsky, Oleksandr Voznyy, Larissa Levina, Sjoerd Hoogland, Kyle W. Kemp, Alexander H. Ip, Susanna M. Thon, and Edward H. Sargent. Engineering colloidal quantum dot solids within and beyond the mobility-invariant regime. *Nature Communications*, 5(1): 3803, May 2014. ISSN 2041-1723. doi: 10.1038/ncomms4803. URL `https://www.nature.com/articles/ncomms4803`. Number: 1 Publisher: Nature Publishing Group.

[66] Ruili Wang, Yuequn Shang, Pongsakorn Kanjanaboos, Wenjia Zhou, Zhijun Ning, and Edward H. Sargent. Colloidal quantum dot ligand engineering for high performance solar cells. *Energy & Environmental Science*, 9(4):1130–1143, 2016. ISSN 1754-5692, 1754-5706. doi: 10.1039/C5EE03887A. URL `http://xlink.rsc.org/?DOI=C5EE03887A`.

[67] Mengxia Liu, Nuri Yazdani, Maksym Yarema, Maximilian Jansen, Vanessa Wood, and Edward H. Sargent. Colloidal quantum dot electronics. *Nature Electronics*, 4(8):548–558, August 2021. ISSN 2520-1131. doi: 10.1038/s41928-021-00632-7. URL `https://www.nature.com/articles/s41928-021-00632-7`. Number: 8 Publisher: Nature Publishing Group.

[68] Yingjie Zhang, Danylo Zherebetskyy, Noah D. Bronstein, Sara Barja, Leonid Lichtenstein, A. Paul Alivisatos, Lin-Wang Wang, and Miquel Salmeron. Molecular Oxygen Induced in-Gap States in PbS Quantum Dots. *ACS Nano*, 9(10):10445–10452, October 2015. ISSN 1936-0851. doi: 10.1021/acsnano.5b04677. URL `https://doi.org/10.1021/acsnano.5b04677`. Publisher: American Chemical Society.

[69] C. G. Granqvist and A. Hultåker. Transparent and conducting ITO films: new developments and applications. *Thin Solid Films*, 411(1):1–5, May 2002. ISSN 0040-6090. doi: 10.1016/S0040-6090(02)00163-3. URL `https://www.sciencedirect.com/science/article/pii/S0040609002001633`.

[70] Claes G. Granqvist. Transparent conductors as solar energy materials: A panoramic review. *Solar Energy Materials and Solar Cells*, 91(17):1529–1598, October 2007. ISSN 0927-0248. doi: 10.1016/j.solmat.2007.04.031. URL `https://www.sciencedirect.com/science/article/pii/S092702480700205X`.

[71] Cheng Zhang, Chengang Ji, Yong-Bum Park, and L. Jay Guo. Thin-Metal-Film-Based Transparent Conductors: Material Preparation, Optical Design, and Device Applications. *Advanced Optical Materials*, 9(3):2001298, February 2021. ISSN 2195-1071, 2195-1071. doi: 10.1002/adom.202001298. URL `https://onlinelibrary.wiley.com/doi/10.1002/adom.202001298`.

[72] K. Bädeker. Über die elektrische Leitfähigkeit und die thermoelektrische Kraft einiger Schwermetallverbindungen. *Annalen der Physik*, 327(4):749–766, 1907. ISSN 1521-3889. doi: 10.1002/andp.19073270409. URL `https://onlinelibrary.wiley.com/doi/abs/10.1002/andp.19073270409`. _eprint: https://onlinelibrary.wiley.com/doi/pdf/10.1002/andp.19073270409.

[73] H. A. McMaster. U.s. patent 2,429,420, 1947.

[74] J. M. Mochel. U.s. patent 2,564,706, 1947.

[75] M. J. Zunick. U.s. patent 2,516,663, 1947.

[76] Toshio Hada, Kiyotaka Wasa, and Shigeru Hayakawa. Structures and electrical properties of zinc oxide films prepared by low pressure sputtering system. *Thin Solid Films*, 7(2): 135–145, February 1971. ISSN 0040-6090. doi: 10.1016/0040-6090(71)90032-0. URL https://www.sciencedirect.com/science/article/pii/0040609071900320.

[77] Hideo Hosono, David C. Paine, and David Ginley, editors. *Handbook of Transparent Conductors*. Springer US, 2011. ISBN 978-1-4419-1637-2. doi: 10.1007/978-1-4419-1638-9. URL https://www.springer.com/gp/book/9781441916372.

[78] Tadatsugu Minami. New n-Type Transparent Conducting Oxides. *MRS Bulletin*, 25(8): 38–44, August 2000. ISSN 1938-1425. doi: 10.1557/mrs2000.149. URL https://doi.org/10.1557/mrs2000.149.

[79] David S. Ginley and Clark Bright. Transparent Conducting Oxides. *MRS Bulletin*, 25(8):15–18, August 2000. ISSN 1938-1425. doi: 10.1557/mrs2000.256. URL https://doi.org/10.1557/mrs2000.256.

[80] Aomar Hadjadj and Mickaël Gilliot. Recent Advances in Functional Transparent Semiconductor Films and Coatings. *Coatings*, 13(2):307, February 2023. ISSN 2079-6412. doi: 10.3390/coatings13020307. URL https://www.mdpi.com/2079-6412/13/2/307. Number: 2 Publisher: Multidisciplinary Digital Publishing Institute.

[81] P. P. Edwards, A. Porch, M. O. Jones, D. V. Morgan, and R. M. Perks. Basic materials physics of transparent conducting oxides. *Dalton Transactions*, (19):2995–3002, September 2004. ISSN 1477-9234. doi: 10.1039/B408864F. URL https://pubs.rsc.org/en/content/articlelanding/2004/dt/b408864f.

[82] D. Bruce Buchholz, Qing Ma, Diego Alducin, Arturo Ponce, Miguel Jose-Yacaman, Rabi Khanal, Julia E. Medvedeva, and Robert P. H. Chang. The Structure and Properties of Amorphous Indium Oxide. *Chemistry of Materials*, 26(18):5401–5411, September 2014. ISSN 0897-4756, 1520-5002. doi: 10.1021/cm502689x. URL https://pubs.acs.org/doi/10.1021/cm502689x.

[83] M. Marezio. Refinement of the crystal structure of In2O3 at two wavelengths. *Acta Crystallographica*, 20(6):723–728, 1966. ISSN 0365-110X. doi: 10.1107/S0365110X66001749. URL https://onlinelibrary.wiley.com/doi/abs/10.1107/S0365110X66001749. _eprint: https://onlinelibrary.wiley.com/doi/pdf/10.1107/S0365110X66001749.

[84] G. Frank and H. Köstlin. Electrical properties and defect model of tin-doped indium oxide layers. *Applied Physics A*, 27(4):197–206, April 1982. ISSN 1432-0630. doi: 10.1007/BF00619080. URL https://doi.org/10.1007/BF00619080.

[85] John C. C. Fan and John B. Goodenough. X-ray photoemission spectroscopy studies of Sn-doped indium-oxide films. *Journal of Applied Physics*, 48(8):3524–3531, August 1977. ISSN 0021-8979. doi: 10.1063/1.324149. URL https://aip.scitation.org/doi/10.1063/1.324149.

[86] B. J. Ingram, G. B. Gonzalez, D. R. Kammler, M. I. Bertoni, and T. O. Mason. Chemical and Structural Factors Governing Transparent Conductivity in Oxides. *Journal of Electroceramics*, 13(1):167–175, July 2004. ISSN 1573-8663. doi: 10.1007/s10832-004-5094-y. URL https://doi.org/10.1007/s10832-004-5094-y.

[87] John Y. W. Seto. The electrical properties of polycrystalline silicon films. *Journal of Applied Physics*, 46(12):5247–5254, September 1975. ISSN 0021-8979. doi: 10.1063/1.321593. URL https://doi.org/10.1063/1.321593.

[88] D. H. Zhang and H. L. Ma. Scattering mechanisms of charge carriers in transparent conducting oxide films. *Applied Physics A*, 62(5):487–492, May 1996. ISSN 1432-0630. doi: 10.1007/BF01567122. URL https://doi.org/10.1007/BF01567122.

[89] S. A. Knickerbocker and A. K. Kulkarni. Estimation and verification of the optical properties of indium tin oxide based on the energy band diagram. *Journal of Vacuum Science & Technology A*, 14(3):757–761, May 1996. ISSN 0734-2101. doi: 10.1116/1.580384. URL https://doi.org/10.1116/1.580384.

[90] T. Pisarkiewicz, K. Zakrzewska, and E. Leja. Scattering of charge carriers in transparent and conducting thin oxide films with a non-parabolic conduction band. *Thin Solid Films*, 174:217–223, July 1989. ISSN 0040-6090. doi: 10.1016/0040-6090(89)90892-4. URL https://www.sciencedirect.com/science/article/pii/0040609089908924.

[91] J. R. Bellingham, W. A. Phillips, and C. J. Adkins. Intrinsic performance limits in transparent conducting oxides. *Journal of Materials Science Letters*, 11(5):263–265, January 1992. ISSN 1573-4811. doi: 10.1007/BF00729407. URL https://doi.org/10.1007/BF00729407.

[92] D. Mergel, M. Schenkel, M. Ghebre, and M. Sulkowski. Structural and electrical properties of In2O3:Sn films prepared by radio-frequency sputtering. *Thin Solid Films*, 392(1): 91–97, July 2001. ISSN 0040-6090. doi: 10.1016/S0040-6090(01)01013-6. URL https://www.sciencedirect.com/science/article/pii/S0040609001010136.

[93] K. Utsumi, H. Iigusa, R. Tokumaru, P. K. Song, and Y. Shigesato. Study on In2O3–SnO2 transparent and conductive films prepared by d.c. sputtering using high density ceramic targets. *Thin Solid Films*, 445(2):229–234, December 2003. ISSN 0040-6090. doi: 10.1016/S0040-6090(03)01167-2. URL https://www.sciencedirect.com/science/article/pii/S0040609003011672.

[94] Yan Jiang, Thomas Feurer, Romain Carron, Galo Torres Sevilla, Thierry Moser, Stefano Pisoni, Rolf Erni, Marta D. Rossell, Mario Ochoa, Ramis Hertwig, Ayodhya N. Tiwari, and Fan Fu. High-Mobility In2O3:H Electrodes for Four-Terminal Perovskite/CuInSe2 Tandem Solar Cells. *ACS Nano*, 14(6):7502–7512, June 2020. ISSN 1936-0851. doi: 10.1021/acsnano.0c03265. URL https://doi.org/10.1021/acsnano.0c03265. Publisher: American Chemical Society.

[95] H. Köstlin, R. Jost, and W. Lems. Optical and electrical properties of doped In2O3 films. *physica status solidi (a)*, 29(1):87–93, 1975. ISSN 1521-396X. doi: 10.1002/pssa.2210290110. URL https://onlinelibrary.wiley.com/doi/abs/10.1002/pssa.2210290110. _eprint: https://onlinelibrary.wiley.com/doi/pdf/10.1002/pssa.2210290110.

[96] Cavid Erginsoy. Neutral Impurity Scattering in Semiconductors. *Physical Review*, 79(6): 1013–1014, September 1950. doi: 10.1103/PhysRev.79.1013. URL https://link.aps.org/doi/10.1103/PhysRev.79.1013. Publisher: American Physical Society.

[97] Yuzo Shigesato and David C. Paine. Study of the effect of Sn doping on the electronic transport properties of thin film indium oxide. *Applied Physics Letters*, 62(11):1268–1270, March 1993. ISSN 0003-6951, 1077-3118. doi: 10.1063/1.108703. URL https://pubs.aip.org/aip/apl/article/62/11/1268-1270/61541.

[98] F. Simonis, M. van der Leij, and C. J. Hoogendoorn. Physics of doped tin dioxide films for spectral-selective surfaces. *Solar Energy Materials*, 1(3):221–231, March 1979. ISSN 0165-1633. doi: 10.1016/0165-1633(79)90040-6. URL https://www.sciencedirect.com/science/article/pii/0165163379900406.

[99] Hyun Suk Jung, Gill Sang Han, Nam-Gyu Park, and Min Jae Ko. Flexible Perovskite Solar Cells. *Joule*, 3(8):1850–1880, August 2019. ISSN 2542-4351. doi: 10.1016/j.joule.2019.07.023. URL `https://www.sciencedirect.com/science/article/pii/S2542435119303678`.

[100] I. Hamberg and C. G. Granqvist. Evaporated Sn-doped In $_2$ O $_3$ films: Basic optical properties and applications to energy-efficient windows. *Journal of Applied Physics*, 60 (11):R123–R160, December 1986. ISSN 0021-8979, 1089-7550. doi: 10.1063/1.337534. URL `http://aip.scitation.org/doi/10.1063/1.337534`.

[101] Elias Burstein. Anomalous Optical Absorption Limit in InSb. *Physical Review*, 93(3): 632–633, February 1954. doi: 10.1103/PhysRev.93.632. URL `https://link.aps.org/doi/10.1103/PhysRev.93.632`. Publisher: American Physical Society.

[102] Sebastian C. Dixon, David O. Scanlon, Claire J. Carmalt, and Ivan P. Parkin. n-Type doped transparent conducting binary oxides: an overview. *Journal of Materials Chemistry C*, 4(29):6946–6961, July 2016. ISSN 2050-7534. doi: 10.1039/C6TC01881E. URL `https://pubs.rsc.org/en/content/articlelanding/2016/tc/c6tc01881e`. Publisher: The Royal Society of Chemistry.

[103] Alain P. Roth, James B. Webb, and Digby F. Williams. Band-gap narrowing in heavily defect-doped ZnO. *Physical Review B*, 25(12):7836–7839, June 1982. ISSN 0163-1829. doi: 10.1103/PhysRevB.25.7836. URL `https://link.aps.org/doi/10.1103/PhysRevB.25.7836`.

[104] H. Han, J. W. Mayer, and T. L. Alford. Band gap shift in the indium-tin-oxide films on polyethylene napthalate after thermal annealing in air. *Journal of Applied Physics*, 100(8):083715, October 2006. ISSN 0021-8979. doi: 10.1063/1.2357647. URL `https://aip.scitation.org/doi/full/10.1063/1.2357647`. Publisher: American Institute of Physics.

[105] Aron Walsh, Juarez L. F. Da Silva, Su-Huai Wei, C. Körber, A. Klein, L. F. J. Piper, Alex DeMasi, Kevin E. Smith, G. Panaccione, P. Torelli, D. J. Payne, A. Bourlange, and R. G. Egdell. Nature of the band gap of In2O3 revealed by first-principles calculations and x-ray spectroscopy. *Physical Review Letters*, 100(16):167402, April 2008. ISSN 0031-9007. doi: 10.1103/PhysRevLett.100.167402.

[106] Swati Ray, Ratnabali Banerjee, N. Basu, A. K. Batabyal, and A. K. Barua. Properties of tin doped indium oxide thin films prepared by magnetron sputtering. *Journal of Applied Physics*, 54(6):3497–3501, June 1983. ISSN 0021-8979. doi: 10.1063/1.332415. URL `https://doi.org/10.1063/1.332415`.

[107] J. Tauc, R. Grigorovici, and A. Vancu. Optical Properties and Electronic Structure of Amorphous Germanium. *physica status solidi (b)*, 15(2): 627–637, 1966. ISSN 1521-3951. doi: 10.1002/pssb.19660150224. URL `https://onlinelibrary.wiley.com/doi/abs/10.1002/pssb.19660150224`. _eprint: https://onlinelibrary.wiley.com/doi/pdf/10.1002/pssb.19660150224.

[108] Hiromichi Ohta, Masahiro Orita, Masahiro Hirano, Hiroaki Tanji, Hiroshi Kawazoe, and Hideo Hosono. Highly electrically conductive indium–tin–oxide thin films epitaxially grown on yttria-stabilized zirconia (100) by pulsed-laser deposition. *Applied Physics Letters*, 76(19):2740–2742, May 2000. ISSN 0003-6951. doi: 10.1063/1.126461. URL `https://doi.org/10.1063/1.126461`.

[109] M. Nisha, S. Anusha, Aldrin Antony, R. Manoj, and M. K. Jayaraj. Effect of substrate temperature on the growth of ITO thin films. *Applied Surface Science*, 252(5):1430–1435, December 2005. ISSN 0169-4332. doi: 10.1016/j.apsusc.2005.02.115. URL `https://www.sciencedirect.com/science/article/pii/S0169433205004976`.

[110] G. Haacke. New figure of merit for transparent conductors. *Journal of Applied Physics*, 47 (9):4086–4089, 1976. ISSN 0021-8979. doi: 10.1063/1.323240. URL `https://doi.org/10.1063/1.323240`.

[111] Roy G. Gordon. Criteria for Choosing Transparent Conductors. *MRS Bulletin*, 25(8):52–57, August 2000. ISSN 1938-1425, 0883-7694. doi: 10.1557/mrs2000.151. URL `https://www.cambridge.org/core/journals/mrs-bulletin/article/criteria-for-choosing-transparent-conductors/A8FFCAA119DBA7A19D040E2B6B6ED964`. Publisher: Cambridge University Press.

[112] Zhangxian Chen, Wanchao Li, Ran Li, Yunfeng Zhang, Guoqin Xu, and Hansong Cheng. Fabrication of highly transparent and conductive indium-tin oxide thin films with a high figure of merit via solution processing. *Langmuir: the ACS journal of surfaces and colloids*, 29(45):13836–13842, November 2013. ISSN 1520-5827. doi: 10.1021/la4033282.

[113] Jephias Gwamuri, Murugesan Marikkannan, Jeyanthinath Mayandi, Patrick K. Bowen, and Joshua M. Pearce. Influence of Oxygen Concentration on the Performance of Ultra-Thin RF Magnetron Sputter Deposited Indium Tin Oxide Films as a Top Electrode for Photovoltaic Devices. *Materials*, 9(1):63, January 2016. ISSN 1996-1944. doi: 10.3390/ma9010063. URL `https://www.mdpi.com/1996-1944/9/1/63`. Number: 1 Publisher: Multidisciplinary Digital Publishing Institute.

[114] Michiko Yoshitake. *Work Function and Band Alignment of Electrode Materials*. Springer, Tsukuba, Japan, September 2020. ISBN 978-4-431-56896-4. URL `https://doi.org/10.1007/978-4-431-56898-8`.

[115] Jens Meyer, Sami Hamwi, Michael Kröger, Wolfgang Kowalsky, Thomas Riedl, and Antoine Kahn. Transition Metal Oxides for Organic Electronics: Energetics, Device Physics and Applications. *Advanced Materials*, 24(40):5408–5427, 2012. ISSN 1521-4095. doi: https://doi.org/10.1002/adma.201201630. URL `https://onlinelibrary.wiley.com/doi/abs/10.1002/adma.201201630`. _eprint: https://onlinelibrary.wiley.com/doi/pdf/10.1002/adma.201201630.

[116] Qi Wang, Yuchuan Shao, Qingfeng Dong, Zhengguo Xiao, Yongbo Yuan, and Jinsong Huang. Large fill-factor bilayer iodine perovskite solar cells fabricated by a low-temperature solution-process. *Energy & Environmental Science*, 7(7):2359–2365, June 2014. ISSN 1754-5706. doi: 10.1039/C4EE00233D. URL `https://pubs.rsc.org/en/content/articlelanding/2014/ee/c4ee00233d`. Publisher: The Royal Society of Chemistry.

[117] Jangwon Seo, Sangman Park, Young Chan Kim, Nam Joong Jeon, Jun Hong Noh, Sung Cheol Yoon, and Sang Il Seok. Benefits of very thin PCBM and LiF layers for solution-processed p–i–n perovskite solar cells. *Energy & Environmental Science*, 7(8):2642–2646, July 2014. ISSN 1754-5706. doi: 10.1039/C4EE01216J. URL `https://pubs.rsc.org/en/content/articlelanding/2014/ee/c4ee01216j`. Publisher: The Royal Society of Chemistry.

[118] Qin Wang, Chu-Chen Chueh, Morteza Eslamian, and Alex K.-Y. Jen. Modulation of PEDOT:PSS pH for Efficient Inverted Perovskite Solar Cells with Reduced Potential Loss and Enhanced Stability. *ACS Applied Materials & Interfaces*, 8(46):32068–32076, November 2016. ISSN 1944-8244. doi: 10.1021/acsami.6b11757. URL `https://doi.org/10.1021/acsami.6b11757`. Publisher: American Chemical Society.

[119] Wei-Yi Chen, Lin-Long Deng, Si-Min Dai, Xin Wang, Cheng-Bo Tian, Xin-Xing Zhan, Su-Yuan Xie, Rong-Bin Huang, and Lan-Sun Zheng. Low-cost solution-processed copper iodide as an alternative to PEDOT:PSS hole transport layer for efficient and stable inverted planar heterojunction perovskite solar cells. *Journal of Materials Chemistry A*, 3(38):19353–19359, September 2015. ISSN 2050-7496. doi: 10.1039/C5TA05286F. URL https://pubs.rsc.org/en/content/articlelanding/2015/ta/c5ta05286f. Publisher: The Royal Society of Chemistry.

[120] Ryan W. Crisp, Daniel M. Kroupa, Ashley R. Marshall, Elisa M. Miller, Jianbing Zhang, Matthew C. Beard, and Joseph M. Luther. Metal Halide Solid-State Surface Treatment for High Efficiency PbS and PbSe QD Solar Cells. *Scientific Reports*, 5(1):9945, April 2015. ISSN 2045-2322. doi: 10.1038/srep09945. URL https://www.nature.com/articles/srep09945. Number: 1 Publisher: Nature Publishing Group.

[121] Wang Xing, Yusheng Chen, Xinlong Wang, Lei Lv, Xinhua Ouyang, Ziyi Ge, and Hui Huang. MoS2 Quantum Dots with a Tunable Work Function for High-Performance Organic Solar Cells. *ACS Applied Materials & Interfaces*, 8(40):26916–26923, October 2016. ISSN 1944-8244. doi: 10.1021/acsami.6b06081. URL https://doi.org/10.1021/acsami.6b06081. Publisher: American Chemical Society.

[122] Kyung-Geun Lim, Soyeong Ahn, Young-Hoon Kim, Yabing Qi, and Tae-Woo Lee. Universal energy level tailoring of self-organized hole extraction layers in organic solar cells and organic–inorganic hybrid perovskite solar cells. *Energy & Environmental Science*, 9(3):932–939, March 2016. ISSN 1754-5706. doi: 10.1039/C5EE03560K. URL https://pubs.rsc.org/en/content/articlelanding/2016/ee/c5ee03560k. Publisher: The Royal Society of Chemistry.

[123] Fuhua Hou, Zisheng Su, Fangming Jin, Xingwu Yan, Lidan Wang, Haifeng Zhao, Jianzhuo Zhu, Bei Chu, and Wenlian Li. Efficient and stable planar heterojunction perovskite solar cells with an MoO3/PEDOT:PSS hole transporting layer. *Nanoscale*, 7(21):9427–9432, May 2015. ISSN 2040-3372. doi: 10.1039/C5NR01864A. URL https://pubs.rsc.org/en/content/articlelanding/2015/nr/c5nr01864a. Publisher: The Royal Society of Chemistry.

[124] Mark T. Greiner, Michael G. Helander, Wing-Man Tang, Zhi-Bin Wang, Jacky Qiu, and Zheng-Hong Lu. Universal energy-level alignment of molecules on metal oxides. *Nature Materials*, 11(1):76–81, January 2012. ISSN 1476-4660. doi: 10.1038/nmat3159. URL https://www.nature.com/articles/nmat3159. Number: 1 Publisher: Nature Publishing Group.

[125] H. Ishii and K. Seki. Energy level alignment at organic/metal interfaces studied by UV photoemission: breakdown of traditional assumption of a common vacuum level at the interface. *IEEE Transactions on Electron Devices*, 44(8):1295–1301, August 1997. ISSN 1557-9646. doi: 10.1109/16.605471. Conference Name: IEEE Transactions on Electron Devices.

[126] Xavier Crispin, Victor Geskin, Annica Crispin, Jérôme Cornil, Roberto Lazzaroni, William R. Salaneck, and Jean-Luc Brédas. Characterization of the Interface Dipole at Organic/ Metal Interfaces. *Journal of the American Chemical Society*, 124(27):8131–8141, July 2002. ISSN 0002-7863. doi: 10.1021/ja025673r. URL https://doi.org/10.1021/ja025673r. Publisher: American Chemical Society.

[127] H. Vázquez, Y. J. Dappe, J. Ortega, and F. Flores. Energy level alignment at metal/organic semiconductor interfaces: “Pillow” effect, induced density of interface states, and charge

neutrality level. *The Journal of Chemical Physics*, 126(14):144703, April 2007. ISSN 0021-9606. doi: 10.1063/1.2717165. URL https://aip.scitation.org/doi/full/10.1063/1.2717165. Publisher: American Institute of Physics.

[128] H. Vázquez, W. Gao, F. Flores, and A. Kahn. Energy level alignment at organic heterojunctions: Role of the charge neutrality level. *Physical Review B*, 71(4):041306, January 2005. doi: 10.1103/PhysRevB.71.041306. URL https://link.aps.org/doi/10.1103/PhysRevB.71.041306. Publisher: American Physical Society.

[129] Carl Tengstedt, Wojciech Osikowicz, William R. Salaneck, Ian D. Parker, Che-H. Hsu, and Mats Fahlman. Fermi-level pinning at conjugated polymer interfaces. *Applied Physics Letters*, 88(5):053502, January 2006. ISSN 0003-6951. doi: 10.1063/1.2168515. URL https://aip.scitation.org/doi/10.1063/1.2168515. Publisher: American Institute of Physics.

[130] Michele Sessolo and Henk J. Bolink. Hybrid Organic–Inorganic Light-Emitting Diodes. *Advanced Materials*, 23(16):1829–1845, 2011. ISSN 1521-4095. doi: https://doi.org/10.1002/adma.201004324. URL https://onlinelibrary.wiley.com/doi/abs/10.1002/adma.201004324. _eprint: https://www.onlinelibrary.wiley.com/doi/pdf/10.1002/adma.201004324.

[131] M. Kröger, S. Hamwi, J. Meyer, T. Riedl, W. Kowalsky, and A. Kahn. Role of the deep-lying electronic states of MoO3 in the enhancement of hole-injection in organic thin films. *Applied Physics Letters*, 95(12):123301, September 2009. ISSN 0003-6951. doi: 10.1063/1.3231928. URL https://aip.scitation.org/doi/10.1063/1.3231928. Publisher: American Institute of Physics.

[132] Mikio Taguchi, Akira Terakawa, Eiji Maruyama, and Makoto Tanaka. Obtaining a higher Voc in HIT cells. *Progress in Photovoltaics: Research and Applications*, 13(6):481–488, 2005. ISSN 1099-159X. doi: https://doi.org/10.1002/pip.646. URL https://onlinelibrary.wiley.com/doi/abs/10.1002/pip.646. _eprint: https://onlinelibrary.wiley.com/doi/pdf/10.1002/pip.646.

[133] Mark T. Greiner, Lily Chai, Michael G. Helander, Wing-Man Tang, and Zheng-Hong Lu. Transition Metal Oxide Work Functions: The Influence of Cation Oxidation State and Oxygen Vacancies. *Advanced Functional Materials*, 22(21):4557–4568, 2012. ISSN 1616-3028. doi: https://doi.org/10.1002/adfm.201200615. URL https://onlinelibrary.wiley.com/doi/abs/10.1002/adfm.201200615. _eprint: https://onlinelibrary.wiley.com/doi/pdf/10.1002/adfm.201200615.

[134] Kyung-Geun Lim, Soyeong Ahn, Young-Hoon Kim, Yabing Qi, and Tae-Woo Lee. Universal energy level tailoring of self-organized hole extraction layers in organic solar cells and organic–inorganic hybrid perovskite solar cells. *Energy & Environmental Science*, 9(3):932–939, March 2016. ISSN 1754-5706. doi: 10.1039/C5EE03560K. URL https://pubs.rsc.org/en/content/articlelanding/2016/ee/c5ee03560k. Publisher: The Royal Society of Chemistry.

[135] David O. Scanlon, Graeme W. Watson, D. J. Payne, G. R. Atkinson, R. G. Egdell, and D. S. L. Law. Theoretical and Experimental Study of the Electronic Structures of MoO3 and MoO2. *The Journal of Physical Chemistry C*, 114(10):4636–4645, March 2010. ISSN 1932-7447. doi: 10.1021/jp9093172. URL https://doi.org/10.1021/jp9093172. Publisher: American Chemical Society.

[136] N. F. Mott. On the Transition to Metallic Conduction in Semiconductors. *Canadian Journal of Physics*, 34:1356–1368, January 1956. ISSN 0008-4204. doi: 10.1139/p56-151. URL

https://ui.adsabs.harvard.edu/abs/1956CaJPh..34.1356M. ADS Bibcode: 1956CaJPh..34.1356M.

[137] Masatoshi Imada, Atsushi Fujimori, and Yoshinori Tokura. Metal-insulator transitions. *Reviews of Modern Physics*, 70(4):1039–1263, October 1998. doi: 10.1103/RevModPhys.70.1039. URL https://link.aps.org/doi/10.1103/RevModPhys.70.1039. Publisher: American Physical Society.

[138] Michael Nolan and Simon D. Elliott. The p-type conduction mechanism in Cu2O: a first principles study. *Physical Chemistry Chemical Physics*, 8(45):5350–5358, November 2006. ISSN 1463-9084. doi: 10.1039/B611969G. URL https://pubs.rsc.org/en/content/articlelanding/2006/cp/b611969g. Publisher: The Royal Society of Chemistry.

[139] Mark T. Greiner and Zheng-Hong Lu. Thin-film metal oxides in organic semiconductor devices: their electronic structures, work functions and interfaces. *NPG Asia Materials*, 5(7):e55–e55, July 2013. ISSN 1884-4057. doi: 10.1038/am.2013.29. URL https://www.nature.com/articles/am201329. Number: 7 Publisher: Nature Publishing Group.

[140] Kourosh Kalantar-zadeh, Jianshi Tang, Minsheng Wang, Kang L. Wang, Alexandros Shailos, Kosmas Galatsis, Robert Kojima, Veronica Strong, Andrew Lech, Wojtek Wlodarski, and Richard B. Kaner. Synthesis of nanometre-thick MoO3 sheets. *Nanoscale*, 2(3):429–433, March 2010. ISSN 2040-3372. doi: 10.1039/B9NR00320G. URL https://pubs.rsc.org/en/content/articlelanding/2010/nr/b9nr00320g. Publisher: The Royal Society of Chemistry.

[141] Ryota Shimizu, Kuniko Yamamoto, Tohru Suzuki, Takeo Ohsawa, Susumu Shiraki, and Taro Hitosugi. Low-temperature deposition of meta-stable β-MoO3(011) epitaxial thin films using step-and-terrace substrates. *Thin Solid Films*, 595:153–156, November 2015. ISSN 0040-6090. doi: 10.1016/j.tsf.2015.10.066. URL https://www.sciencedirect.com/science/article/pii/S0040609015010597.

[142] Corsin Battaglia, Xingtian Yin, Maxwell Zheng, Ian D. Sharp, Teresa Chen, Stephen McDonnell, Angelica Azcatl, Carlo Carraro, Biwu Ma, Roya Maboudian, Robert. M. Wallace, and Ali Javey. Hole Selective MoO $_x$ Contact for Silicon Solar Cells. *Nano Letters*, 14(2):967–971, February 2014. ISSN 1530-6984, 1530-6992. doi: 10.1021/nl404389u. URL https://pubs.acs.org/doi/10.1021/nl404389u.

[143] H. R. Zeller and H. U. Beyeler. Electrochromism and local order in amorphous WO3. *Applied physics*, 13(3):231–237, July 1977. ISSN 1432-0630. doi: 10.1007/BF00882886. URL https://doi.org/10.1007/BF00882886.

[144] M. T. Greiner, M. G. Helander, Z. B. Wang, W. M. Tang, J. Qiu, and Z. H. Lu. A metallic molybdenum suboxide buffer layer for organic electronic devices. *Applied Physics Letters*, 96(21):213302, May 2010. ISSN 0003-6951, 1077-3118. doi: 10.1063/1.3432447. URL http://aip.scitation.org/doi/10.1063/1.3432447.

[145] Arne Magnéli, Birgitta Blomberg-Hansson, Lars Kihlborg, and Gustav Sundkvist. Studies on Molybdenum and Molybdenum Wolfram Oxides of the Homologous Series Me(n)O(3n-1). *Acta Chemica Scandinavica*, 9:1382–1390, 1955. ISSN 0904-213X. doi: 10.3891/acta.chem.scand.09-1382. URL http://actachemscand.org/doi/10.3891/acta.chem.scand.09-1382.

[146] Quntao Tang and Hanyu Yao. Efficiency enhancement of TiOx electron-transporting layer-based ultrathin p-type c-Si solar cell by reactive sputtering of backside MoOx hole-transporting contact. *Journal of Materials Science: Materials in Electronics*, 31(8):

6406–6417, April 2020. ISSN 1573-482X. doi: 10.1007/s10854-020-03197-x. URL https://doi.org/10.1007/s10854-020-03197-x.

[147] Liang Huang, Bin Yao, Jiyu Sun, Xiang Gao, Jiabin Wu, Jun Wan, Tianqi Li, Zhimi Hu, and Jun Zhou. Highly conductive and flexible molybdenum oxide nanopaper for high volumetric supercapacitor electrode. *Journal of Materials Chemistry A*, 5(6):2897–2903, February 2017. ISSN 2050-7496. doi: 10.1039/C6TA10433A. URL https://pubs.rsc.org/en/content/articlelanding/2017/ta/c6ta10433a. Publisher: The Royal Society of Chemistry.

[148] Kuniko Yamamoto, Ryota Shimizu, Susumu Shiraki, and Taro Hitosugi. Transparent conducting properties of Re-doped β-MoO3 films. *APL Materials*, 4(9):096104, September 2016. ISSN 2166-532X. doi: 10.1063/1.4963154. URL https://doi.org/10.1063/1.4963154.

[149] Richard J. Colton, Alberto M. Guzman, and J. Wayne Rabalais. Photochromism and electrochromism in amorphous transition metal oxide films. *Accounts of Chemical Research*, 11(4):170–176, April 1978. ISSN 0001-4842. doi: 10.1021/ar50124a008. URL https://doi.org/10.1021/ar50124a008. Publisher: American Chemical Society.

[150] S. A. Tomás, M. A. Arvizu, O. Zelaya-Angel, and P. Rodríguez. Effect of ZnSe doping on the photochromic and thermochromic properties of MoO3 thin films. *Thin Solid Films*, 518(4):1332–1336, December 2009. ISSN 0040-6090. doi: 10.1016/j.tsf.2009.05.054. URL https://www.sciencedirect.com/science/article/pii/S0040609009010268.

[151] Lars Berggren, Andris Azens, and Gunnar A. Niklasson. Polaron absorption in amorphous tungsten oxide films. *Journal of Applied Physics*, 90(4):1860–1863, August 2001. ISSN 0021-8979. doi: 10.1063/1.1384853. URL https://doi.org/10.1063/1.1384853.

[152] Zahid Hussain. Optical and electrochromic properties of heated and annealed MoO3 thin films. *Journal of Materials Research*, 16(9):2695–2708, September 2001. ISSN 2044-5326. doi: 10.1557/JMR.2001.0369. URL https://doi.org/10.1557/JMR.2001.0369.

[153] Irfan, Huanjun Ding, Yongli Gao, Cephas Small, Do Young Kim, Jegadesan Subbiah, and Franky So. Energy level evolution of air and oxygen exposed molybdenum trioxide films. *Applied Physics Letters*, 96(24):243307, June 2010. ISSN 0003-6951. doi: 10.1063/1.3454779. URL https://aip.scitation.org/doi/abs/10.1063/1.3454779. Publisher: American Institute of Physics.

[154] J. Meyer, A. Shu, M. Kröger, and A. Kahn. Effect of contamination on the electronic structure and hole-injection properties of MoO3/organic semiconductor interfaces. *Applied Physics Letters*, 96(13):133308, March 2010. ISSN 0003-6951. doi: 10.1063/1.3374333. URL https://aip.scitation.org/doi/abs/10.1063/1.3374333. Publisher: American Institute of Physics.

[155] Hong Zhang, Chenxu Zhao, Jianxi Yao, and Wallace C. H. Choy. Dopant-free NiOx Nanocrystals: A Low-cost and Stable Hole Transport Material for Commercializing Perovskite Optoelectronics. *Angewandte Chemie International Edition*, 62(24):e202219307, 2023. ISSN 1521-3773. doi: 10.1002/anie.202219307. URL https://onlinelibrary.wiley.com/doi/abs/10.1002/anie.202219307. _eprint: https://onlinelibrary.wiley.com/doi/pdf/10.1002/anie.202219307.

[156] Jun-Yuan Jeng, Kuo-Cheng Chen, Tsung-Yu Chiang, Pei-Ying Lin, Tzung-Da Tsai, Yun-Chorng Chang, Tzung-Fang Guo, Peter Chen, Ten-Chin Wen, and Yao-Jane Hsu. Nickel oxide electrode interlayer in CH3 NH3 PbI3 perovskite/PCBM planar-heterojunction hybrid

solar cells. *Advanced Materials (Deerfield Beach, Fla.)*, 26(24):4107–4113, June 2014. ISSN 1521-4095. doi: 10.1002/adma.201306217.

[157] Xiaolu Zheng, Zhaoning Song, Zhiliang Chen, Sandip Singh Bista, Pengbin Gui, Niraj Shrestha, Cong Chen, Chongwen Li, Xinxing Yin, Rasha A. Awni, Hongwei Lei, Chen Tao, Randy J. Ellingson, Yanfa Yan, and Guojia Fang. Interface modification of sputtered NiO $_x$ as the hole-transporting layer for efficient inverted planar perovskite solar cells. *Journal of Materials Chemistry C*, 8(6):1972–1980, 2020. ISSN 2050-7526, 2050-7534. doi: 10.1039/C9TC05759E. URL http://xlink.rsc.org/?DOI=C9TC05759E.

[158] Sajid Sajid, Ahmed Mourtada Elseman, Hao Huang, Jun Ji, Shangyi Dou, Haoran Jiang, Xin Liu, Dong Wei, Peng Cui, and Meicheng Li. Breakthroughs in NiOx-HTMs towards stable, low-cost and efficient perovskite solar cells. *Nano Energy*, 51:408–424, September 2018. ISSN 22112855. doi: 10.1016/j.nanoen.2018.06.082. URL https://linkinghub.elsevier.com/retrieve/pii/S2211285518304774.

[159] L. F. Mattheiss. Electronic Structure of the $3d$ Transition-Metal Monoxides. I. Energy-Band Results. *Physical Review B*, 5(2):290–306, January 1972. doi: 10.1103/PhysRevB.5.290. URL https://link.aps.org/doi/10.1103/PhysRevB.5.290. Publisher: American Physical Society.

[160] E. Engel and R. N. Schmid. Insulating Ground States of Transition-Metal Monoxides from Exact Exchange. *Physical Review Letters*, 103(3):036404, July 2009. doi: 10.1103/PhysRevLett.103.036404. URL https://link.aps.org/doi/10.1103/PhysRevLett.103.036404. Publisher: American Physical Society.

[161] X. Ren, I. Leonov, G. Keller, M. Kollar, I. Nekrasov, and D. Vollhardt. $\mathrm{LDA}+\mathrm{DMFT}$ computation of the electronic spectrum of NiO. *Physical Review B*, 74(19):195114, November 2006. doi: 10.1103/PhysRevB.74.195114. URL https://link.aps.org/doi/10.1103/PhysRevB.74.195114. Publisher: American Physical Society.

[162] Fabien Tran and Peter Blaha. Accurate Band Gaps of Semiconductors and Insulators with a Semilocal Exchange-Correlation Potential. *Physical Review Letters*, 102(22):226401, June 2009. doi: 10.1103/PhysRevLett.102.226401. URL https://link.aps.org/doi/10.1103/PhysRevLett.102.226401. Publisher: American Physical Society.

[163] J. Kuneš, V. I. Anisimov, A. V. Lukoyanov, and D. Vollhardt. Local correlations and hole doping in NiO: A dynamical mean-field study. *Physical Review B*, 75(16):165115, April 2007. ISSN 1098-0121, 1550-235X. doi: 10.1103/PhysRevB.75.165115. URL https://link.aps.org/doi/10.1103/PhysRevB.75.165115.

[164] Alessio Filippetti and Nicola A. Spaldin. Self-interaction-corrected pseudopotential scheme for magnetic and strongly-correlated systems. *Physical Review B*, 67(12):125109, March 2003. doi: 10.1103/PhysRevB.67.125109. URL https://link.aps.org/doi/10.1103/PhysRevB.67.125109. Publisher: American Physical Society.

[165] G. A. Sawatzky and J. W. Allen. Magnitude and Origin of the Band Gap in NiO. *Physical Review Letters*, 53(24):2339–2342, December 1984. ISSN 0031-9007. doi: 10.1103/PhysRevLett.53.2339. URL https://link.aps.org/doi/10.1103/PhysRevLett.53.2339.

[166] Daniel I. Khomskii. *Basic Aspects of the Quantum Theory of Solids: Order and Elementary Excitations*. Cambridge University Press, September 2010. ISBN 978-0-521-83521-3 978-0-521-54292-0 978-0-511-78027-1. doi: 10.1017/CBO9780511780271. URL https:

//www.cambridge.org/core/product/identifier/9780511780271/type/book. Edition: 1.

[167] Atsushi Fujimori and Fujio Minami. Valence-band photoemission and optical absorption in nickel compounds. *Physical Review B*, 30(2):957–971, July 1984. doi: 10.1103/PhysRevB.30.957. URL https://link.aps.org/doi/10.1103/PhysRevB.30.957. Publisher: American Physical Society.

[168] J. Zaanen, G. A. Sawatzky, and J. W. Allen. Band gaps and electronic structure of transition-metal compounds. *Physical Review Letters*, 55(4):418–421, July 1985. doi: 10.1103/PhysRevLett.55.418. URL https://link.aps.org/doi/10.1103/PhysRevLett.55.418. Publisher: American Physical Society.

[169] Maria Isabel Pintor-Monroy, Bayron L. Murillo-Borjas, Massimo Catalano, and Manuel A. Quevedo-Lopez. Controlling Carrier Type and Concentration in NiO Films To Enable in Situ PN Homojunctions. *ACS Applied Materials & Interfaces*, 11(30):27048–27056, July 2019. ISSN 1944-8244. doi: 10.1021/acsami.9b04380. URL https://doi.org/10.1021/acsami.9b04380. Publisher: American Chemical Society.

[170] F. J. Morin. Electrical Properties of NiO. *Physical Review*, 93(6):1199–1204, March 1954. doi: 10.1103/PhysRev.93.1199. URL https://link.aps.org/doi/10.1103/PhysRev.93.1199. Publisher: American Physical Society.

[171] K. Terakura, A. R. Williams, T. Oguchi, and J. Kübler. Transition-Metal Monoxides: Band or Mott Insulators. *Physical Review Letters*, 52(20):1830–1833, May 1984. doi: 10.1103/PhysRevLett.52.1830. URL https://link.aps.org/doi/10.1103/PhysRevLett.52.1830. Publisher: American Physical Society.

[172] R. Merlin. Electronic Structure of NiO. *Physical Review Letters*, 54(25):2727–2727, June 1985. doi: 10.1103/PhysRevLett.54.2727. URL https://link.aps.org/doi/10.1103/PhysRevLett.54.2727. Publisher: American Physical Society.

[173] Badih El-Kareh and Lou N. Hutter. *Fundamentals of Semiconductor Processing Technology*. Springer Science & Business Media, December 2012. ISBN 978-1-4615-2209-6.

[174] Robert Eason. Pulsed Laser Deposition of Thin Films: Applications-Led Growth of Functional Materials. January 2007. ISSN 9780471447092. doi: 10.1002/0470052120.

[175] P. R. Willmott and J. R. Huber. Pulsed laser vaporization and deposition. *Reviews of Modern Physics*, 72(1):315–328, January 2000. ISSN 0034-6861, 1539-0756. doi: 10.1103/RevModPhys.72.315. URL https://link.aps.org/doi/10.1103/RevModPhys.72.315.

[176] Henry Mathieu, Thierry Bretagnon, and Pierre Lefebvre. *Physique des Semiconducteurs et des Composants Electroniques - Problèmes Résolus*. Collection Sciences Sup. Dunod, April 2001. URL https://hal.science/hal-01306435.

[177] A. Y. Cho and J. R. Arthur. Molecular beam epitaxy. *Progress in Solid State Chemistry*, 10:157–191, January 1975. ISSN 0079-6786. doi: 10.1016/0079-6786(75)90005-9. URL https://www.sciencedirect.com/science/article/pii/0079678675900059.

[178] Steven M. George. Atomic Layer Deposition: An Overview. *Chemical Reviews*, 110 (1):111–131, January 2010. ISSN 0009-2665, 1520-6890. doi: 10.1021/cr900056b. URL https://pubs.acs.org/doi/10.1021/cr900056b.

[179] C. A. Pan and T. P. Ma. Evaporation of High Quality In2 O 3 Films from In2 O 3 / In Source—Evaporation Chemistry and Thermodynamics. *Journal of The Electrochemical*

Society, 128(9):1953, September 1981. ISSN 1945-7111. doi: 10.1149/1.2127773. URL https://iopscience.iop.org/article/10.1149/1.2127773/meta. Publisher: IOP Publishing.

[180] F. O. Adurodija, H. Izumi, T. Ishihara, H. Yoshioka, M. Motoyama, and K. Murai. Influence of substrate temperature on the properties of indium oxide thin films. *Journal of Vacuum Science & Technology A*, 18(3):814–818, May 2000. ISSN 0734-2101. doi: 10.1116/1.582260. URL https://doi.org/10.1116/1.582260.

[181] Toshiro Maruyama and Kunihiro Fukui. Indium-tin oxide thin films prepared by chemical vapor deposition. *Journal of Applied Physics*, 70(7):3848–3851, October 1991. ISSN 0021-8979, 1089-7550. doi: 10.1063/1.349189. URL https://pubs.aip.org/jap/article/70/7/3848/500060/Indium-tin-oxide-thin-films-prepared-by-chemical.

[182] H. Kim, J. S. Horwitz, W. H. Kim, A. J. Mäkinen, Z. H. Kafafi, and D. B. Chrisey. Doped ZnO thin films as anode materials for organic light-emitting diodes. *Thin Solid Films*, 420-421:539–543, December 2002. ISSN 0040-6090. doi: 10.1016/S0040-6090(02)00836-2. URL https://www.sciencedirect.com/science/article/pii/S0040609002008362.

[183] Akio Suzuki, Tatsuhiko Matsushita, Takanori Aoki, Akihito Mori, and Masahiro Okuda. Highly conducting transparent indium tin oxide films prepared by pulsed laser deposition. *Thin Solid Films*, 411:23–27, May 2002. doi: 10.1016/S0040-6090(02)00167-0.

[184] K. Sreenivas, T. Sudersena Rao, Abhai Mansingh, and Subhash Chandra. Preparation and characterization of rf sputtered indium tin oxide films. *Journal of Applied Physics*, 57(2):384–392, January 1985. ISSN 0021-8979. doi: 10.1063/1.335481. URL https://doi.org/10.1063/1.335481.

[185] Jeffrey W. Elam, David A. Baker, Alex B. F. Martinson, Michael J. Pellin, and Joseph T. Hupp. Atomic Layer Deposition of Indium Tin Oxide Thin Films Using Nonhalogenated Precursors. *The Journal of Physical Chemistry C*, 112(6):1938–1945, February 2008. ISSN 1932-7447. doi: 10.1021/jp7097312. URL https://doi.org/10.1021/jp7097312. Publisher: American Chemical Society.

[186] Hossein Salami, Alan Uy, Aarathi Vadapalli, Corinne Grob, Vivek Dwivedi, and Raymond A. Adomaitis. Atomic layer deposition of ultrathin indium oxide and indium tin oxide films using a trimethylindium, tetrakis(dimethylamino)tin, and ozone precursor system. *Journal of Vacuum Science & Technology A*, 37(1):010905, December 2018. ISSN 0734-2101. doi: 10.1116/1.5058171. URL https://doi.org/10.1116/1.5058171.

[187] W. R. Grove. On the Electro-Chemical Polarity of Gases. *Philosophical Transactions of the Royal Society of London*, 142:87–101, 1852. ISSN 0261-0523. URL https://www.jstor.org/stable/108536. Publisher: The Royal Society.

[188] Alain Billard and Frédéric Perry. Pulvérisation cathodique magnétron. *Traitements des métaux*, December 2005. doi: 10.51257/a-v1-m1654. URL https://www.techniques-ingenieur.fr/doi/10.51257/a/v1/m1654.

[189] Olivier Tosoni. *Conception, élaboration et intégration d'électrodes transparentes optimisées pour l'extraction des charges dans des dispositifs photovoltaïques.* PhD thesis. URL https://theses.hal.science/tel-00955867/.

[190] P. J Kelly and R. D Arnell. Magnetron sputtering: a review of recent developments and applications. *Vacuum*, 56(3):159–172, March 2000. ISSN 0042-207X. doi: 10.1016/S0042-207X(99)00189-X. URL https://www.sciencedirect.com/science/article/pii/S0042207X9900189X.

[191] P. J. Kelly, P. S. Henderson, R. D. Arnell, G. A. Roche, and D. Carter. Reactive pulsed magnetron sputtering process for alumina films. *Journal of Vacuum Science & Technology A*, 18(6):2890–2896, November 2000. ISSN 0734-2101. doi: 10.1116/1.1319679. URL https://doi.org/10.1116/1.1319679.

[192] Yunfang Gui. *Mise au point par pulvérisation cathodique magnétron en condition réactive et caractérisations mécaniques et tribologiques de revêtements de phases Magnéli de titane (TinO2n-1)*. These de doctorat, Belfort-Montbéliard, July 2014. URL https://www.theses.fr/2014BELF0235.

[193] H. Báránková, S. Berg, P. Carlsson, and C. Nender. Hysteresis effects in the sputtering process using two reactive gases. *Thin Solid Films*, 260(2):181–186, May 1995. ISSN 0040-6090. doi: 10.1016/0040-6090(94)06501-2. URL https://www.sciencedirect.com/science/article/pii/0040609094065012.

[194] Muhammad Arif and C. Eisenmenger-Sittner. In situ assessment of target poisoning evolution in magnetron sputtering. *Surface and Coatings Technology*, 324:345–352, September 2017. ISSN 02578972. doi: 10.1016/j.surfcoat.2017.05.047. URL https://linkinghub.elsevier.com/retrieve/pii/S0257897217305261.

[195] D. Mercs, F. Lapostolle, F. Perry, A. Billard, and C. Frantz. Enhanced deposition rate of high quality stoichiometric ceramic compounds reactively sputter deposited at low pressure by modulating the discharge current at low frequency. *Surface and Coatings Technology*, 116-119:916–921, September 1999. ISSN 0257-8972. doi: 10.1016/S0257-8972(99)00262-5. URL https://www.sciencedirect.com/science/article/pii/S0257897299002625.

[196] J A Thornton. High Rate Thick Film Growth. *Annual Review of Materials Science*, 7(1): 239–260, August 1977. ISSN 0084-6600. doi: 10.1146/annurev.ms.07.080177.001323. URL https://www.annualreviews.org/doi/10.1146/annurev.ms.07.080177.001323.

[197] André Anders. A structure zone diagram including plasma-based deposition and ion etching. *Thin Solid Films*, 518(15):4087–4090, May 2010. ISSN 0040-6090. doi: 10.1016/j.tsf.2009.10.145. URL https://www.sciencedirect.com/science/article/pii/S0040609009018288.

[198] Miho Yasaka. X-ray thin-film measurement techniques. 2010.

[199] Dieter K. Schroder. *Semiconductor Material and Device Characterization*. Wiley, 1 edition, October 2005. ISBN 978-0-471-73906-7 978-0-471-74909-7. doi: 10.1002/0471749095. URL https://onlinelibrary.wiley.com/doi/book/10.1002/0471749095.

[200] N. Ghellai, A. Benmansour, and N.-E. Chabane Sari. Ellipsométrie spectroscopique. *Photoniques*, (51):22–27, January 2011. ISSN 1629-4475, 2269-8418. doi: 10.1051/photon/20115122. URL https://www.photoniques.com/articles/photon/abs/2011/01/photon201151p22/photon201151p22.html. Number: 51 Publisher: EDP Sciences.

[201] E. H. Hall. On a New Action of the Magnet on Electric Currents. *American Journal of Mathematics*, 2(3):287–292, 1879. ISSN 0002-9327. doi: 10.2307/2369245. URL https://www.jstor.org/stable/2369245. Publisher: Johns Hopkins University Press.

[202] Fred A. Stevie and Carrie L. Donley. Introduction to x-ray photoelectron spectroscopy. *Journal of Vacuum Science & Technology A: Vacuum, Surfaces, and Films*, 38(6):063204, December 2020. ISSN 0734-2101, 1520-8559. doi: 10.1116/6.0000412. URL https://pubs.aip.org/jva/article/38/6/063204/1024200/Introduction-to-x-ray-photoelectron-spectroscopy.

[203] Jonas Baltrusaitis, Beatriz Mendoza-Sanchez, Vincent Fernandez, Rick Veenstra, Nijole Dukstiene, Adam Roberts, and Neal Fairley. Generalized molybdenum oxide surface chemical state XPS determination via informed amorphous sample model. *Applied Surface Science*, 326:151–161, January 2015. ISSN 0169-4332. doi: 10.1016/j.apsusc.2014.11.077. URL `http://www.sciencedirect.com/science/article/pii/S0169433214025586`.

[204] Grzegorz Greczynski and Lars Hultman. A step-by-step guide to perform x-ray photoelectron spectroscopy. *Journal of Applied Physics*, 132(1):011101, July 2022. ISSN 0021-8979. doi: 10.1063/5.0086359. URL `https://doi.org/10.1063/5.0086359`.

[205] G. Greczynski and L. Hultman. X-ray photoelectron spectroscopy: Towards reliable binding energy referencing. *Progress in Materials Science*, 107:100591, January 2020. ISSN 0079-6425. doi: 10.1016/j.pmatsci.2019.100591. URL `https://www.sciencedirect.com/science/article/pii/S0079642519300738`.

[206] Donald R. Baer, Kateryna Artyushkova, Christopher Richard Brundle, James E. Castle, Mark H. Engelhard, Karen J. Gaskell, John T. Grant, Richard T. Haasch, Matthew R. Linford, Cedric J. Powell, Alexander G. Shard, Peter M. A. Sherwood, and Vincent S. Smentkowski. Practical guides for x-ray photoelectron spectroscopy: First steps in planning, conducting, and reporting XPS measurements. *Journal of Vacuum Science & Technology A: Vacuum, Surfaces, and Films*, 37(3):031401, May 2019. ISSN 0734-2101, 1520-8559. doi: 10.1116/1.5065501. URL `https://pubs.aip.org/jva/article/37/3/031401/910789/Practical-guides-for-x-ray-photoelectron`.

[207] Dhruv Shah, Dhananjay I. Patel, Tuhin Roychowdhury, G. Bruce Rayner, Noel O'Toole, Donald R. Baer, and Matthew R. Linford. Tutorial on interpreting x-ray photoelectron spectroscopy survey spectra: Questions and answers on spectra from the atomic layer deposition of Al2O3 on silicon. *Journal of Vacuum Science & Technology B*, 36(6):062902, November 2018. ISSN 2166-2746. doi: 10.1116/1.5043297. URL `https://doi.org/10.1116/1.5043297`.

[208] Neal Fairley, Vincent Fernandez, Mireille Richard-Plouet, Catherine Guillot-Deudon, John Walton, Emily Smith, Delphine Flahaut, Mark Greiner, Mark Biesinger, Sven Tougaard, David Morgan, and Jonas Baltrusaitis. Systematic and collaborative approach to problem solving using X-ray photoelectron spectroscopy. *Applied Surface Science Advances*, 5:100112, September 2021. ISSN 2666-5239. doi: 10.1016/j.apsadv.2021.100112. URL `https://www.sciencedirect.com/science/article/pii/S2666523921000581`.

[209] M. P. Seah. A review of the analysis of surfaces and thin films by AES and XPS. *Vacuum*, 34(3):463–478, March 1984. ISSN 0042-207X. doi: 10.1016/0042-207X(84)90084-8. URL `https://www.sciencedirect.com/science/article/pii/0042207X84900848`.

[210] J. M. Ribeiro, F. C. Correia, P. B. Salvador, L. Rebouta, L. C. Alves, E. Alves, N. P. Barradas, A. Mendes, and C. J. Tavares. Compositional analysis by RBS, XPS and EDX of ZnO:Al,Bi and ZnO:Ga,Bi thin films deposited by d.c. magnetron sputtering. *Vacuum*, 161:268–275, March 2019. ISSN 0042-207X. doi: 10.1016/j.vacuum.2018.12.038. URL `https://www.sciencedirect.com/science/article/pii/S0042207X1832164X`.

[211] Babak Bakhit, Daniel Primetzhofer, Eduardo Pitthan, Mauricio A. Sortica, Eleni Ntemou, Johanna Rosen, Lars Hultman, Ivan Petrov, and Grzegorz Greczynski. Systematic compositional analysis of sputter-deposited boron-containing thin films. *Journal of Vacuum Science & Technology A*, 39(6):063408, September 2021. ISSN 0734-2101. doi: 10.1116/6.0001234. URL `https://doi.org/10.1116/6.0001234`.

[212] Da Li, Xiaodong Fang, Zanhong Deng, Weiwei Dong, Ruhua Tao, Shu Zhou, Jinmei Wang, Tao Wang, Yiping Zhao, and Xuebin Zhu. Characteristics of CuCr1-xMgxO2 films prepared by pulsed laser deposition. *Journal of Alloys and Compounds*, 486(1): 462–467, November 2009. ISSN 0925-8388. doi: 10.1016/j.jallcom.2009.06.174. URL `https://www.sciencedirect.com/science/article/pii/S0925838809013309`.

[213] L. J. Brillson. Surface photovoltage measurements and Fermi level pinning: comments on "development and confirmation of the unified model for Schottky barrier formation and MOS interface states on III-V compounds". *Thin Solid Films*, 89(4):L27–L33, March 1982. ISSN 0040-6090. doi: 10.1016/0040-6090(82)90328-5. URL `https://www.sciencedirect.com/science/article/pii/0040609082903285`.

[214] E. H. Nicollian and J. R. Brews. *MOS (Metal Oxide Semiconductor) Physics and Technology*. December 2002. ISBN 978-0-471-43079-7. URL `https://www.wiley.com/en-be/MOS+%28Metal+Oxide+Semiconductor%29+Physics+and+Technology-p-9780471430797`.

[215] S. M. Sze and K. Ng Kwok. *Physics of Semiconductor Devices*. John wiley & sons, ltd edition, April 2006. ISBN 978-0-471-14323-9. URL `https://www.wiley.com/en-us/Physics+of+Semiconductor+Devices%2C+3rd+Edition-p-9780470068328`.

[216] Charles Leroux, Gérard Ghibaudo, and Gilles Reimbold. Accurate determination of flat band voltage in advanced MOS structure. *Microelectronics Reliability*, 47(4):660–664, April 2007. ISSN 0026-2714. doi: 10.1016/j.microrel.2007.01.033. URL `https://www.sciencedirect.com/science/article/pii/S002627140700039X`.

[217] R. Castagné and A. Vapaille. Description of the SiO2?Si interface properties by means of very low frequency MOS capacitance measurements. *Surface Science*, 28(1):157–193, November 1971. ISSN 0039-6028. doi: 10.1016/0039-6028(71)90092-6. URL `https://www.sciencedirect.com/science/article/pii/0039602871900926`.

[218] C. J Huang, Y. K Su, and S. L Wu. The effect of solvent on the etching of ITO electrode. *Materials Chemistry and Physics*, 84(1):146–150, March 2004. ISSN 0254-0584. doi: 10.1016/j.matchemphys.2003.11.021. URL `https://www.sciencedirect.com/science/article/pii/S0254058403005406`.

[219] J. H. Hwang, D. D. Edwards, D. R. Kammler, and T. O. Mason. Point defects and electrical properties of Sn-doped In-based transparent conducting oxides. *Solid State Ionics*, 129 (1):135–144, April 2000. ISSN 0167-2738. doi: 10.1016/S0167-2738(99)00321-5. URL `https://www.sciencedirect.com/science/article/pii/S0167273899003215`.

[220] V. Sivaji Reddy, K. Das, A. Dhar, and S. K. Ray. The effect of substrate temperature on the properties of ITO thin films for OLED applications. *Semiconductor Science and Technology*, 21(12):1747, November 2006. ISSN 0268-1242. doi: 10.1088/0268-1242/21/12/043. URL `https://dx.doi.org/10.1088/0268-1242/21/12/043`.

[221] Ocal Tuna, Yusuf Selamet, Gulnur Aygun, and Lutfi Ozyuzer. High quality ITO thin films grown by dc and RF sputtering without oxygen. *Journal of Physics D: Applied Physics*, 43 (5):055402, January 2010. ISSN 0022-3727. doi: 10.1088/0022-3727/43/5/055402. URL `https://dx.doi.org/10.1088/0022-3727/43/5/055402`.

[222] S. Ishibashi, Y. Higuchi, Y. Ota, and K. Nakamura. Low resistivity indium–tin oxide transparent conductive films. I. Effect of introducing H2O gas or H2 gas during direct current magnetron sputtering. *Journal of Vacuum Science & Technology A*, 8(3):1399–1402, May 1990. ISSN 0734-2101. doi: 10.1116/1.576889. URL `https://doi.org/10.1116/1.576889`.

[223] Xiaonan Li, Brian Keyes, Sally Asher, S. B. Zhang, Su-Huai Wei, Timothy J. Coutts, Sukit Limpijumnong, and Chris G. Van de Walle. Hydrogen passivation effect in nitrogen-doped ZnO thin films. *Applied Physics Letters*, 86(12):122107, March 2005. ISSN 0003-6951. doi: 10.1063/1.1886256. URL https://doi.org/10.1063/1.1886256.

[224] Takashi Koida, Hiroyuki Fujiwara, and Michio Kondo. Hydrogen-doped In2O3 as High-mobility Transparent Conductive Oxide. *Japanese Journal of Applied Physics*, 46(7L):L685, July 2007. ISSN 1347-4065. doi: 10.1143/JJAP.46.L685. URL https://iopscience.iop.org/article/10.1143/JJAP.46.L685/meta. Publisher: IOP Publishing.

[225] L. Barraud, Z. C. Holman, N. Badel, P. Reiss, A. Descoeudres, C. Battaglia, S. De Wolf, and C. Ballif. Hydrogen-doped indium oxide/indium tin oxide bilayers for high-efficiency silicon heterojunction solar cells. *Solar Energy Materials and Solar Cells*, 115:151–156, August 2013. ISSN 0927-0248. doi: 10.1016/j.solmat.2013.03.024. URL https://www.sciencedirect.com/science/article/pii/S0927024813001372.

[226] Jan M. Dekkers. *Transparent conducting oxides on polymeric substrates by pulsed laser deposition*. PhD thesis, March 2007. URL https://research.utwente.nl/en/publications/transparent-conducting-oxides-on-polymeric-substrates-by-pulsed-l.

[227] Sukit Limpijumnong, Pakpoom Reunchan, Anderson Janotti, and Chris G. Van de Walle. Hydrogen doping in indium oxide: An ab initio study. *Physical Review B*, 80(19):193202, November 2009. doi: 10.1103/PhysRevB.80.193202. URL https://link.aps.org/doi/10.1103/PhysRevB.80.193202. Publisher: American Physical Society.

[228] T. Koida, H. Fujiwara, and M. Kondo. High-mobility hydrogen-doped In2O3 transparent conductive oxide for a-Si:H/c-Si heterojunction solar cells. *Solar Energy Materials and Solar Cells*, 93(6):851–854, June 2009. ISSN 0927-0248. doi: 10.1016/j.solmat.2008.09.047. URL https://www.sciencedirect.com/science/article/pii/S0927024808003395.

[229] Thanaporn Tohsophon, Ali Dabirian, Stefaan De Wolf, Monica Morales-Masis, and Christophe Ballif. Environmental stability of high-mobility indium-oxide based transparent electrodes. *APL Materials*, 3(11):116105, November 2015. ISSN 2166-532X. doi: 10.1063/1.4935125. URL https://doi.org/10.1063/1.4935125.

[230] B. Macco, H.C.M. Knoops, and W.M.M. Kessels. Electron scattering and doping mechanisms in solid-phase-crystallized ln2O3:H prepared by atomic layer deposition. *ACS Applied Materials & Interfaces*, 7(30):16723–16729, August 2015. ISSN 1944-8244. doi: 10.1021/acsami.5b04420.

[231] Hans F. Wardenga, Mareike V. Frischbier, Monica Morales-Masis, and Andreas Klein. In Situ Hall Effect Monitoring of Vacuum Annealing of In2O3:H Thin Films. *Materials*, 8(2):561–574, February 2015. ISSN 1996-1944. doi: 10.3390/ma8020561. URL https://www.mdpi.com/1996-1944/8/2/561. Number: 2 Publisher: Multidisciplinary Digital Publishing Institute.

[232] Gabrielle C. E. Jost, Alexander N. Hamri, Florian Köhler, and Jürgen Hüpkes. Reliability aspects of hydrogen-doped indium oxide. *physica status solidi (a)*, 213(7):1751–1759, 2016. ISSN 1862-6319. doi: 10.1002/pssa.201532806. URL https://onlinelibrary.wiley.com/doi/abs/10.1002/pssa.201532806. _eprint: https://onlinelibrary.wiley.com/doi/pdf/10.1002/pssa.201532806.

[233] J. H. Park, C. Buurma, S. Sivananthan, R. Kodama, W. Gao, and T. A. Gessert. The effect of post-annealing on Indium Tin Oxide thin films by magnetron sputtering method. *Applied Surface Science*, 307:388–392, July 2014. ISSN 0169-4332. doi: 10.1016/j.apsusc.2014.04.042. URL https://www.sciencedirect.com/science/article/pii/S016943321400806X.

[234] Ramachandran Ammapet Vijayan, Stephanie Essig, Stefaan De Wolf, Bairava Ganesh Ramanathan, Philipp Löper, Christophe Ballif, and Muthubalan Varadharajaperumal. Hole-Collection Mechanism in Passivating Metal-Oxide Contacts on Si Solar Cells: Insights From Numerical Simulations. *IEEE Journal of Photovoltaics*, 8(2):473–482, March 2018. ISSN 2156-3403. doi: 10.1109/JPHOTOV.2018.2796131. Conference Name: IEEE Journal of Photovoltaics.

[235] Ahmad Hadi Ali, Zainuriah Hassan, and Ahmad Shuhaimi. Enhancement of optical transmittance and electrical resistivity of post-annealed ITO thin films RF sputtered on Si. *Applied Surface Science*, 443:544–547, June 2018. ISSN 0169-4332. doi: 10.1016/j.apsusc.2018.03.024. URL `https://www.sciencedirect.com/science/article/pii/S0169433218306846`.

[236] T. Kamioka, Y. Hayashi, Y. Isogai, K. Nakamura, and Y. Ohshita. Analysis of interface workfunction and process-induced damage of reactive-plasma-deposited ITO/SiO2/Si stack. *AIP Advances*, 7(9):095212, September 2017. doi: 10.1063/1.4997495. URL `https://aip.scitation.org/doi/full/10.1063/1.4997495`. Publisher: American Institute of Physics.

[237] Raphaël Lachaume. *Contribution à la caractérisation électrique et à la simulation numérique des cellules photovoltaïques silicium à hétérojonction.* These de doctorat, Grenoble, May 2014. URL `https://www.theses.fr/2014GRENT028`.

[238] Y. Park, V. Choong, Y. Gao, B. R. Hsieh, and C. W. Tang. Work function of indium tin oxide transparent conductor measured by photoelectron spectroscopy. *Applied Physics Letters*, 68(19):2699–2701, May 1996. ISSN 0003-6951. doi: 10.1063/1.116313. URL `https://aip.scitation.org/doi/10.1063/1.116313`.

[239] T. Kamioka, Y. Hayashi, Yukie Isogai, Kyotaro Nakamura, Y. Ohshita, and A. Ogura. Effect of ITO Capping Layer on Interface Workfunction of MoOx in ITO/MoOx/SiO2/Si Contacts. *2018 IEEE 7th World Conference on Photovoltaic Energy Conversion (WCPEC) (A Joint Conference of 45th IEEE PVSC, 28th PVSEC & 34th EU PVSEC)*, 2018. doi: 10.1109/PVSC.2018.8547885.

[240] R. J. Powell and G. F. Derbenwick. Vacuum Ultraviolet Radiation Effects in SiO2. *IEEE Transactions on Nuclear Science*, 18(6):99–105, December 1971. ISSN 1558-1578. doi: 10.1109/TNS.1971.4326419. URL `https://ieeexplore.ieee.org/document/4326419`. Conference Name: IEEE Transactions on Nuclear Science.

[241] Christoph Messmer, Martin Bivour, Jonas Schön, and Martin Hermle. Requirements for efficient hole extraction in transition metal oxide-based silicon heterojunction solar cells. *Journal of Applied Physics*, 124(8):085702, August 2018. ISSN 0021-8979. doi: 10.1063/1.5045250. URL `https://doi.org/10.1063/1.5045250`.

[242] Irfan Irfan, Alexander James Turinske, Zhenan Bao, and Yongli Gao. Work function recovery of air exposed molybdenum oxide thin films. *Applied Physics Letters*, 101(9):093305, August 2012. ISSN 0003-6951. doi: 10.1063/1.4748978. URL `https://aip.scitation.org/doi/full/10.1063/1.4748978`. Publisher: American Institute of Physics.

[243] Lisa Neusel, Martin Bivour, and Martin Hermle. Selectivity issues of MoOx based hole contacts. *Energy Procedia*, 124:425–434, September 2017. ISSN 1876-6102. doi: 10.1016/j.egypro.2017.09.268. URL `https://www.sciencedirect.com/science/article/pii/S1876610217341991`.

[244] Jitendra Kumar Jha, Reinaldo Santos-Ortiz, Jincheng Du, and Nigel D. Shepherd. The influence of MoOx gap states on hole injection from aluminum doped zinc oxide with nanoscale MoOx surface layer anodes for organic light emitting diodes. *Journal of Applied Physics*, 118(6):065304, August 2015. ISSN 0021-8979. doi: 10.1063/1.4928171. URL `https://aip.scitation.org/doi/full/10.1063/1.4928171`. Publisher: American Institute of Physics.

[245] André L. F. Cauduro, Roberto dos Reis, Gong Chen, Andreas K. Schmid, Christophe Méthivier, Horst-Günter Rubahn, Léo Bossard-Giannesini, Hervé Cruguel, Nadine Witkowski, and Morten Madsen. Crystalline Molybdenum Oxide Thin-Films for Application as Interfacial Layers in Optoelectronic Devices. *ACS Applied Materials & Interfaces*, 9(8):7717–7724, March 2017. ISSN 1944-8244. doi: 10.1021/acsami.6b14228. URL `https://doi.org/10.1021/acsami.6b14228`. Publisher: American Chemical Society.

[246] Mark T. Greiner, Lily Chai, Michael G. Helander, Wing-Man Tang, and Zheng-Hong Lu. Metal/Metal-Oxide Interfaces: How Metal Contacts Affect the Work Function and Band Structure of MoO3. *Advanced Functional Materials*, 23(2): 215–226, 2013. ISSN 1616-3028. doi: https://doi.org/10.1002/adfm.201200993. URL `https://onlinelibrary.wiley.com/doi/abs/10.1002/adfm.201200993`. _eprint: https://onlinelibrary.wiley.com/doi/pdf/10.1002/adfm.201200993.

[247] F. Werfel and E. Minni. Photoemission study of the electronic structure of Mo and Mo oxides. *Journal of Physics C: Solid State Physics*, 16(31):6091, November 1983. ISSN 0022-3719. doi: 10.1088/0022-3719/16/31/022. URL `https://dx.doi.org/10.1088/0022-3719/16/31/022`.

[248] Megan L. Hoey, J. B. Carlson, R. M. Osgood, B. Kimball, and W. Buchwald. rf plasma oxidation of Ni thin films sputter deposited to generate thin nickel oxide layers. *Applied Physics Letters*, 97(15):153104, October 2010. ISSN 0003-6951. doi: 10.1063/1.3499661. URL `https://aip.scitation.org/doi/full/10.1063/1.3499661`. Publisher: American Institute of Physics.

[249] T. Ressler, J. Wienold, R. E. Jentoft, and T. Neisius. Bulk Structural Investigation of the Reduction of MoO3 with Propene and the Oxidation of MoO2 with Oxygen. *Journal of Catalysis*, 210(1):67–83, August 2002. ISSN 0021-9517. doi: 10.1006/jcat.2002.3659. URL `https://www.sciencedirect.com/science/article/pii/S0021951702936596`.

[250] Jiung Jang, Yeonsu Kang, Danyoung Cha, Junyoung Bae, and Sungsik Lee. Thin-Film Optical Devices Based on Transparent Conducting Oxides: Physical Mechanisms and Applications. *Crystals*, 9(4):192, April 2019. ISSN 2073-4352. doi: 10.3390/cryst9040192. URL `https://www.mdpi.com/2073-4352/9/4/192`. Number: 4 Publisher: Multidisciplinary Digital Publishing Institute.

[251] Philip Schulz, Jan O. Tiepelt, Jeffrey A. Christians, Igal Levine, Eran Edri, Erin M. Sanehira, Gary Hodes, David Cahen, and Antoine Kahn. High-Work-Function Molybdenum Oxide Hole Extraction Contacts in Hybrid Organic–Inorganic Perovskite Solar Cells. *ACS Applied Materials & Interfaces*, 8(46):31491–31499, November 2016. ISSN 1944-8244, 1944-8252. doi: 10.1021/acsami.6b10898. URL `https://pubs.acs.org/doi/10.1021/acsami.6b10898`.

[252] T. Ressler, R. E. Jentoft, J. Wienold, M. M. Günter, and O. Timpe. In Situ XAS and XRD Studies on the Formation of Mo Suboxides during Reduction of MoO3. *The Journal of Physical Chemistry B*, 104(27):6360–6370, July 2000. ISSN 1520-6106. doi: 10.1021/jp000690t. URL `https://doi.org/10.1021/jp000690t`. Publisher: American Chemical Society.

[253] H. Sato, T. Minami, S. Takata, and T. Yamada. Transparent conducting p-type NiO thin films prepared by magnetron sputtering. *Thin Solid Films*, 236(1):27–31, December 1993. ISSN 0040-6090. doi: 10.1016/0040-6090(93)90636-4. URL https://www.sciencedirect.com/science/article/pii/0040609093906364.

[254] Guibin Shen, Hongye Dong, Fan Yang, Xin Ren Ng, Xin Li, Fen Lin, and Cheng Mu. Application of an amphipathic molecule at the NiOx/perovskite interface for improving the efficiency and long-term stability of the inverted perovskite solar cells. *Journal of Energy Chemistry*, 78:454–462, March 2023. ISSN 2095-4956. doi: 10.1016/j.jechem.2022.12.015. URL https://www.sciencedirect.com/science/article/pii/S2095495622006805.

[255] P. Puspharajah, S. Radhakrishna, and A. K. Arof. Transparent conducting lithium-doped nickel oxide thin films by spray pyrolysis technique. *Journal of Materials Science*, 32(11):3001–3006, June 1997. ISSN 1573-4803. doi: 10.1023/A:1018657424566. URL https://doi.org/10.1023/A:1018657424566.

[256] Hao-Long Chen, Yang-Ming Lu, and Weng-Sing Hwang. Characterization of sputtered NiO thin films. *Surface and Coatings Technology*, 198(1):138–142, August 2005. ISSN 0257-8972. doi: 10.1016/j.surfcoat.2004.10.032. URL https://www.sciencedirect.com/science/article/pii/S0257897204010229.

[257] Seongrok Seo, Ik Jae Park, Myungjun Kim, Seonhee Lee, Changdeuck Bae, Hyun Suk Jung, Nam-Gyu Park, Jin Young Kim, and Hyunjung Shin. An ultra-thin, un-doped NiO hole transporting layer of highly efficient (16.4%) organic–inorganic hybrid perovskite solar cells. *Nanoscale*, 8(22):11403–11412, June 2016. ISSN 2040-3372. doi: 10.1039/C6NR01601D. URL https://pubs.rsc.org/en/content/articlelanding/2016/nr/c6nr01601d. Publisher: The Royal Society of Chemistry.

[258] Dongmei Dong, Wenwen Wang, Guobo Dong, Yuliang Zhou, Zhonghou Wu, Mei Wang, Famin Liu, and Xungang Diao. Electrochromic properties of NiOx:H films deposited by DC magnetron sputtering for ITO/NiOx:H/ZrO2/WO3/ITO device. *Applied Surface Science*, 357:799–805, December 2015. ISSN 0169-4332. doi: 10.1016/j.apsusc.2015.09.056. URL https://www.sciencedirect.com/science/article/pii/S0169433215021509.

[259] T. F. Chen, A. J. Wang, B. Y. Shang, Z. L. Wu, Y. L. Li, and Y. S. Wang. Property modulation of NiO films grown by radio frequency magnetron sputtering. *Journal of Alloys and Compounds*, 643:167–173, September 2015. ISSN 0925-8388. doi: 10.1016/j.jallcom.2015.04.139. URL https://www.sciencedirect.com/science/article/pii/S0925838815011639.

[260] A. U. Chavan, L. D. Jadhav, A. P. Jamale, S. P. Patil, C. H. Bhosale, S. R. Bharadwaj, and P. S. Patil. Effect of variation of NiO on properties of NiO/GDC (gadolinium doped ceria) nano-composites. *Ceramics International*, 38(4):3191–3196, May 2012. ISSN 0272-8842. doi: 10.1016/j.ceramint.2011.12.023. URL https://www.sciencedirect.com/science/article/pii/S027288421101090X.

[261] Yaxiong Guo, Junjie Ma, Haibing Wang, Feihong Ye, Liangbin Xiong, Hongwei Lei, and Zuojun Tan. Overcoming Ni3+-Induced Non-Radiative Recombination at Perovskite-Nickel Oxide Interfaces to Boost Voltages in Perovskite Solar Cells. *Advanced Materials Interfaces*, 8(16):2100920, 2021. ISSN 2196-7350. doi: 10.1002/admi.202100920. URL https://onlinelibrary.wiley.com/doi/abs/10.1002/admi.202100920. _eprint: https://onlinelibrary.wiley.com/doi/pdf/10.1002/admi.202100920.

[262] Juan Tirado, Manuel Vásquez-Montoya, Cristina Roldán-Carmona, Maryline Ralaiarisoa, Norbert Koch, Mohammad Khaja Nazeeruddin, and Franklin Jaramillo. Air-Stable n–i–p

Planar Perovskite Solar Cells Using Nickel Oxide Nanocrystals as Sole Hole-Transporting Material. *ACS Applied Energy Materials*, 2(7):4890–4899, July 2019. doi: 10.1021/acsaem.9b00603. URL https://doi.org/10.1021/acsaem.9b00603. Publisher: American Chemical Society.

[263] Erkan Aydin, Joel Troughton, Michele De Bastiani, Esma Ugur, Muhammad Sajjad, Areej Alzahrani, Marios Neophytou, Udo Schwingenschlögl, Frédéric Laquai, Derya Baran, and Stefaan De Wolf. Room-Temperature-Sputtered Nanocrystalline Nickel Oxide as Hole Transport Layer for p–i–n Perovskite Solar Cells. *ACS Applied Energy Materials*, 1(11): 6227–6233, November 2018. doi: 10.1021/acsaem.8b01263. URL https://doi.org/10.1021/acsaem.8b01263. Publisher: American Chemical Society.

[264] Mark T. Greiner, Michael G. Helander, Zhi-Bin Wang, Wing-Man Tang, and Zheng-Hong Lu. Effects of Processing Conditions on the Work Function and Energy-Level Alignment of NiO Thin Films. *The Journal of Physical Chemistry C*, 114(46):19777–19781, November 2010. ISSN 1932-7447. doi: 10.1021/jp108281m. URL https://doi.org/10.1021/jp108281m. Publisher: American Chemical Society.

[265] Xin Yan, Jianghui Zheng, LingLing Zheng, Guanhua Lin, Huangding Lin, Guo Chen, Binbin Du, and Fengyan Zhang. Optimization of sputtering NiOx films for perovskite solar cell applications. *Materials Research Bulletin*, 103:150–157, July 2018. ISSN 0025-5408. doi: 10.1016/j.materresbull.2018.03.027. URL https://www.sciencedirect.com/science/article/pii/S0025540817344306.

[266] Andrea De Iacovo, Carlo Venettacci, Lorenzo Colace, Leonardo Scopa, and Sabrina Foglia. PbS Colloidal Quantum Dot Photodetectors operating in the near infrared. *Scientific Reports*, 6(1):37913, November 2016. ISSN 2045-2322. doi: 10.1038/srep37913. URL https://www.nature.com/articles/srep37913. Number: 1 Publisher: Nature Publishing Group.

[267] Martijn J. R. Heck, Jared F. Bauters, Michael L. Davenport, Jonathan K. Doylend, Siddharth Jain, Géza Kurczveil, Sudharsanan Srinivasan, Yongbo Tang, and John E. Bowers. Hybrid Silicon Photonic Integrated Circuit Technology. *IEEE Journal of Selected Topics in Quantum Electronics*, 19(4):6100117–6100117, July 2013. ISSN 1558-4542. doi: 10.1109/JSTQE.2012.2235413. Conference Name: IEEE Journal of Selected Topics in Quantum Electronics.

[268] Andreas Mandelis, Lilei Hu, and Jing Wang. Quantitative measurements of charge carrier hopping transport properties in depleted-heterojunction PbS colloidal quantum dot solar cells from temperature dependent current–voltage characteristics. *RSC Advances*, 6(95): 93180–93194, 2016. ISSN 2046-2069. doi: 10.1039/C6RA22645K. URL http://xlink.rsc.org/?DOI=C6RA22645K.

[269] F. Menchini, L. Serenelli, L. Martini, M. Izzi, G. Stracci, P. Mangiapane, E. Salza, and M. Tucci. Transparent hole-collecting and buffer layers for heterojunction solar cells based on n-type-doped silicon. *Applied Physics A*, 124(7):489, July 2018. ISSN 0947-8396, 1432-0630. doi: 10.1007/s00339-018-1903-z. URL http://link.springer.com/10.1007/s00339-018-1903-z.

[270] Ankit Kumar, Srinivas Sista, and Yang Yang. Dipole induced anomalous S-shape I-V curves in polymer solar cells. *Journal of Applied Physics*, 105(9):094512, May 2009. ISSN 0021-8979. doi: 10.1063/1.3117513. URL https://aip.scitation.org/doi/10.1063/1.3117513. Publisher: American Institute of Physics.

[271] Kaname Kanai, Kenji Koizumi, Satoru Ouchi, Yoshiaki Tsukamoto, Kei Sakanoue, Yukio Ouchi, and Kazuhiko Seki. Electronic structure of anode interface with molybdenum oxide buffer layer. *Organic Electronics*, 11(2):188–194, February 2010. ISSN 1566-1199. doi: 10.1016/j.orgel.2009.10.013. URL `http://www.sciencedirect.com/science/article/pii/S1566119909003048`.

[272] Dong-Ho Kang and Nam-Gyu Park. On the Current–Voltage Hysteresis in Perovskite Solar Cells: Dependence on Perovskite Composition and Methods to Remove Hysteresis. *Advanced Materials*, 31(34):1805214, 2019. ISSN 1521-4095. doi: 10.1002/adma.201805214. URL `https://onlinelibrary.wiley.com/doi/abs/10.1002/adma.201805214`. _eprint: https://onlinelibrary.wiley.com/doi/pdf/10.1002/adma.201805214.

[273] Sander J. W. Vonk, Magnus B. Fridriksson, Stijn O. M. Hinterding, Mark J. J. Mangnus, Thomas P. van Swieten, Ferdinand C. Grozema, Freddy T. Rabouw, and Ward van der Stam. Trapping and Detrapping in Colloidal Perovskite Nanoplatelets: Elucidation and Prevention of Nonradiative Processes through Chemical Treatment. *The Journal of Physical Chemistry C*, 124(14):8047–8054, April 2020. ISSN 1932-7447. doi: 10.1021/acs.jpcc.0c02287. URL `https://doi.org/10.1021/acs.jpcc.0c02287`. Publisher: American Chemical Society.